

Technische Universität München
Institut für Energietechnik

Lehrstuhl für Thermodynamik

Experimental and Numerical Analysis of a PCM-Supported Humidification-Dehumidification Solar Desalination System

Abdel Hakim M. A. Hassabou

Vollständiger Abdruck der von der Fakultät für Maschinenwesen der
Technischen Universität München zur Erlangung des akademischen Grades eines

DOKTOR – INGENIEURS

genehmigten Dissertation.

Vorsitzender:

Univ.-Prof. Dr.-Ing. Dirk Weuster-Botz

Prüfer der Dissertation:

1. Univ.-Prof. Wolfgang H. Polifke, Ph. D. (CCNY)

2. Prof. Abdalla Hanafi, Ph. D.,
University of Kairo / Ägypten

Die Dissertation wurde am 27.09.2011 bei der Technischen Universität München eingereicht und
durch die Fakultät für Maschinenwesen am 10.11.2011 angenommen.

Preface

First and foremost I thank the Greatest Creator for his countless blessings and neat creation: “He sends down rain from the sky and with it gives life to the earth after it is dead: Verily in that are signs for those who are wise.” [Al- Qur’aan 30:24]. “It is He Who has let free the two bodies of flowing water: one palatable and sweet, and the other salty and bitter; yet has He made a barrier between them, and a partition that is forbidden to be passed.” [Al-Qur’aan 25:53]. “It is He Who created The Night and the Day, and the sun and the moon: All (the celestial bodies) Swim along, each in its rounded course.” [Al-Qur’aan 21:33]. “It is not permitted to the Sun to catch up the Moon, nor can the Night outstrip the Day: Each (just) swims along in (its own) orbit (According to Law).” [Al-Qur’aan 36:40].

I would like to express my deep appreciation and gratitude to my advisors: Prof. Wolfgang Polifke, Dr-Eng. Markus Spinnler, Lehrstuhl für Thermodynamik, Technische Universität München (TUM), Germany, and Prof. Abdalla Hanafi, Faculty of Engineering Cairo University, for their continuous guidance, support, advices, and valuable time. I thank Allah for blessing me with such great advisors.

I’m deeply grateful to Prof. Polifke for his brilliant insights and many inspiring ideas which helped me to develop better understanding and careful numerical and theoretical analysis. I have learned a great deal from him how to buildup argumentations and maintain a clear sense of purpose. My appreciation for him as a scientist and as a person outpaces the limits of acknowledgement words. I would like to thank prof. Hanafi for his support and encouragement to apply for the Ph.D. scholarship and conduct my research abroad. I appreciate the time, guidance, and efforts Prof. Hanafi provided to my research from preliminary stages to the conclusion. I also thank Prof. Hanafi for teaching me the Computational and Numerical Methods in Heat Transfer and Fluid Mechanics in my post graduate studies.

A very special word of thanks goes to Dr. Markus Spinnler; Head of the Solar Research Center at TUM for making my research as smooth as possible. His early and continued technical and administrative supports were invaluable. He formulated the research proposal of my Ph.D. study and was leading the technical and administrative correspondences of my scholarship for securing the financial means and laboratory facilities. He also was very helpful in advising and discussing lab problems and experimental analysis as well proof reading of the dissertation and providing many valuable comments in concluding the study. His sense of humour and friendliness hospitality for me and my family in Germany were enjoyable and will never be forgotten.

It is my pleasure to thank Prof. Thomas Sattelmayer, Head of the Lehrstuhl für Thermodynamik, TUM and all the administrative and supporting staff, who were abundantly helpful and offered invaluable assistance, and great hospitality. I would like to express my deep thanking to my colleague, Dipl.-Eng. Burkhard Seifert for his support and valuable discussions during the course of the study.

This research project is co-funded by the Middle East Desalination Research Center (MEDRC) through the Ph.D. scholarship grant number 05-AS-003, and TUM, Germany. The financial support of MEDRC and TUM is gratefully acknowledged and appreciated.

I'm fully indebted to my great parents for their unconditional loving and support throughout my whole life. I cherish the support in all life situations and friendship of my brothers and sister; Gamal, Usama, and Walaa.

I am heartily thankful to Dr-Eng. Jürgen Blumenberg and his wife; Mrs. Gaby. Their great friendship and close social relationships made my family stay in Germany very pleasant. Thanks for never letting us feel that there was a long distance between us and our dear friends and families in our home country; Egypt.

Last but not least, I owe my deepest gratitude to my lovely wife Abear for her patience, providing a supportive environment for me, and taking over major responsibilities of our kids. The long trip would have been very harsh and I could not have achieved as much as I did without her enduring support. Finally I can not describe how appreciative I'm to my three kids; my daughter Salma, my son Noureldin, and my little daughter Manar. The innocent smiley faces were always motivating and triggering my advancement. Whatever I achieve will be dedicated to make your future bright.

München, September 2011

Abdel Hakim Hassabou

Abstract

This work discusses the results of experimental and theoretical studies on a humidification-dehumidification (HDH) water desalination system equipped with phase change material (PCM) as a packing media in all its main components. The PCM-supported HDH system consists of an evaporator and condenser comprised by two cylindrical direct-contact packed beds filled with spherical PCM packing elements. Moreover, a solar collector and an external PCM thermal storage are used to drive the HDH plant. The external PCM thermal storage is used to guarantee continuous operation of the plant day and night round the clock under the transient behaviour of solar irradiation.

The objective of using PCM elements in the evaporator and condenser was for heat storage as a back up during cloudy hours or for part-time night operation. During analysis of steady state conditions, it was discovered that the PCM packing media seem to enhance their thermal performance through locally establishing multiple-effects of heating/humidification (MEHH) and cooling/dehumidification (MECD) while air passing through the successive packing layers in the evaporator and condenser respectively. The multiple-effect phenomena are attributed solely to existence of conductive packing media, which act as heat and mass exchangers. Thus, the focus of the study lies on the thermal conductivity rather than the thermal capacity or solid-liquid phase change processes of the packing in the two columns.

The major aim of this study is to examine systematically the effect of MEHH and MECD at enhanced thermal conductivity of the filling material and to determine the technical and economic feasibility of applying these concepts in HDH desalination plants under steady state operation conditions.

Transient simulation models for the individual components in the HDH system have been established and validated against experimental measurements. Using both experiment and simulation, a detailed heat and mass transfer analysis for the performance of the evaporator and condenser over a wide range of operation conditions under steady state has been performed using different types of packing materials. Furthermore, a yearly parametric analysis for the whole HDH plant has been performed under real weather conditions for two locations in Egypt. The overall performance analysis focuses on the optimum operation conditions of the HDH system, with optimum conductive filling material, with and without external PCM thermal buffer. Special attention is paid to the effect of climatic conditions and comparison between PCM and water as storage media in the external thermal storage.

Contents

List of figures	viii
List of Tables	xi
List of Frames	xi
1 Introduction.....	1
1.1 Fresh water challenges.....	1
1.2 Desalination option	2
1.3 Overview on desalination processes.....	2
1.3.1 Energy requirements and water cost	4
1.3.2 Selection criteria of desalination technology	5
1.3.3 Coupling desalination plants with power plants.....	6
1.3.4 Coupling renewable energies with desalination technologies	6
1.3.5 Barriers and limitations of RE-desalination	8
1.4 Solar desalination	9
1.4.1 Conventional solar stills	9
1.4.2 Humidification-Dehumidification technique	10
1.5 Aim of the work	11
1.6 Dissertation Overview	12
2 Literature Survey	13
2.1 Introduction	13
2.2 Importance of solar energy storage	13
2.3 Thermo-Chemical Energy Storage.....	14
2.4 Sensible heat energy storage (SHES)	15
2.5 Latent heat energy storage (LHES)	15
2.5.1 Concept of Phase Change Energy Storage	15
2.5.2 Advantages of LHES.....	17
2.5.3 Solid-Solid Phase Change Storages.....	17
2.5.4 Solid-Liquid-Vapour Phase Change Storages.....	18
2.5.5 Solid-Liquid Phase Change Storages	18
2.6 Classification of Phase Change Materials.....	19
2.6.1 Organic Phase Change Materials	20
2.6.2 Inorganic Phase Change Materials	21
2.6.3 Eutectics	22
2.6.4 Salt Mixtures	23
2.6.5 Multi Grade Phase Change Materials	24
2.7 Heat transfer in PCM regenerators	25
2.8 Desalination with humidification-dehumidification technique	27
2.8.1 Classification of HDH systems	28
2.8.2 Principles of operation	29
2.8.3 Lumped model analysis	31
2.8.4 Review of Performance	36
2.8.4.1 Effect of feed seawater mass flow rate	36
2.8.4.2 Effect of air to water mass flow ratio	39

2.8.4.3	Effect of air heating	40
2.8.4.4	Effect of packing height.....	42
2.8.4.5	Type of carrier gas	46
2.8.5	Air dehumidification.....	46
2.8.6	Solar collectors	50
2.8.7	Thermal storage.....	51
2.8.8	Summary of the literature on HDH systems	53
2.8.9	Conclusion and spot light.....	54
3	Scope of the Study	55
3.1	Scope of the study	55
3.2	Proposed system and operation cycle	55
3.3	Concept of Multi-Effects of Heating and Humidification (MEHH)	57
3.3.1	Micro scale level	57
3.3.2	Macro scale level	59
3.4	Concept of Multi-Effects of Cooling and Condensation (MECC).....	61
3.5	Study objectives and methodology	61
4	Theoretical Analysis and Modeling	63
4.1	System variables.....	63
4.2	Mathematical Modeling	64
4.2.1	Model assumptions	66
4.2.2	Flow in the external heat storage	68
4.2.3	Two phase flow in dual phase change regenerators.....	71
4.2.4	Closure relationships	79
4.3	Hydrodynamic analysis	87
4.3.1	Gas-liquid interaction	87
4.3.2	Column Sizing.....	88
4.4	Modeling solid-liquid phase change	89
4.5	Macro-dynamic performance analysis of the HDH system	92
4.5.1	Cooling tower performance	92
4.5.2	Humidifier efficiency.....	92
4.5.3	Dehumidifier efficiency.....	93
4.5.4	Productivity factor (<i>PF</i>).....	95
4.5.5	Efficiency of the solar collector.....	95
4.5.6	Energy balance on heat exchangers.....	96
4.5.7	Overall system performance	97
4.5.8	Salt and mass flow balances	98
4.6	Representation of the MEHH and MECD phenomena	99
4.6.1	Fundamental points	99
4.6.2	Capturing the MEHH and MECD phenomena	100
5	Experimental Analysis	103
5.1	Experimental setup and procedures	103
5.1.1	Design objectives.....	103
5.1.2	Experimental Facility.....	104
5.2	Measuring Techniques.....	105

5.3	Functional description	107
5.4	Design of experiments and potential influences of boundary conditions.....	108
5.5	Results and discussions	111
5.5.1	Behavior of the PCM-supported HDH cycle.....	113
5.5.2	Comparison between conductive and non conductive packing.....	117
5.5.3	Effect of packing specific area	121
5.6	Conclusions	123
6	Model Implementation and Validation.....	125
6.1	Implementation of the evaporator model with MATLAB	125
6.2	Solution of the HDH plant lumped model	127
6.3	Model validation	128
6.4	Sample of simulation results	136
6.5	Conclusions	137
7	Parameters Analysis of the Evaporator and Condenser.....	141
7.1	Boundary conditions	141
7.2	Evaporator Performance.....	142
7.2.1	Effect of packing size	142
7.2.2	Effect of column aspect ratio.....	145
7.2.3	Effect of inlet hot water temperature	147
7.2.4	Effect of inlet saturated air temperature	148
7.2.5	Effect of water to air flow ratio.....	149
7.2.6	Effect of packing thermal conductivity	150
7.2.7	Concluding remarks	154
7.3	Condenser Performance.....	154
7.3.1	Effect of inlet cooling water temperature	154
7.3.2	Effect of inlet saturated air temperature	155
7.3.3	Effect of cooling water to air mass flow ratio	156
7.3.4	Effect of packing thermal conductivity	157
7.3.7	Concluding remarks	160
7.4	Conclusions	161
8	Optimization of HDH plant.....	163
8.1	Geographical locations	163
8.2	Boundary conditions and input parameters.....	163
8.3	Parametric Analysis	164
8.3.1	Effect of brine concentration factor (r_c).....	166
8.3.2	Effect of thermal buffer storage capacity.....	167
8.3.3	Effect of solar collector area	168
8.3.4	Effect of hot water flow rate	169
8.3.5	Effect of cooling water flow rate	170
8.3.6	Effect of storage medium type	170
8.3.7	Effect of PCM melting temperature (T_m)	174
8.4	Conclusions	176
9	Summary and conclusions	177
9.1	Summary	177

9.2 Conclusions	178
References	180
Appendices.....	191
Appendix A	191
A1. PCM Thermo-physical properties	191
A2. Factorial design of experiments and experimental plan.....	192
A3. Constants and Thermo-physical properties of air and water	193
Appendix B	194
B1. Pressure drop calculations (Stichlmair et al. [29]).....	194
Appendix C	196
C1. Literature correlations for heat transfer coefficient between bed packing and working fluid	196
C2. Summary of some heat transfer coefficient correlations between fluids and packed beds	199
Appendix D	201
D1. Cooling tower theory and performance	201

List of Figures

Figure 1.1: Cost breakdown of desalinated water	2
Figure 1.2: Overview and energy classification of desalination processes	3
Figure 1.3: Flow scheme of energy, water, and money	4
Figure 1.4: Feasible couplings between renewable energy and desalination technologies	7
Figure 1.5: Basin type solar still	10
Figure 1.6: Schematic diagram of a HDH desalination cycle	11
Figure 2.1: Phase change behavior of solid-liquid latent heat storage systems; (a) melting at a sharp point, (b) melting over a temperature range	16
Figure 2.2: Classification of energy storage materials	19
Figure 2.3: Energy released versus time for different geometries	26
Figure 2.4: Schematic of the solar-driven HDH process without thermal storage	30
Figure 2.5: Finite element at the liquid-air interface in direct contact heat and mass exchangers	31
Figure 2.6: Effect of the feed seawater flow-rate on inlet hot water temperature and GOR	34
Figure 2.7: Effect of the seawater flow-rate on the collector area and air mass flow rate under constant specific heat input per unit mass of seawater	35
Figure 2.8: Effect of the feed seawater flow-rate on the air to water mass flow rate ratio and humidifier size factor (NTU)	36
Figure 2.9: Effect of the feed water flow-rate on the daily production of the HDH desalination unit	37
Figure 2.10: Variation of distillate flow rate as a function of the water flow rate: (a) air flow rate, (b) cooling water temperature, (c) hot water temperature	38
Figure 2.11: Schematic of HDD system by Abdel-Monem	41
Figure 2.12: Representation of multi effect of heating and humidification by Chafik on the psychrometric chart	42
Figure 2.13: Multi effect of heating and humidification of the HDH desalination unit by Chafik	43
Figure 2.14: Specific water cost produced by the solar HDH desalination unit by Chafik	43
Figure 2.15: Height versus air temperature for EnviPac	45
Figure 2.16: Height vs Vapor Production for EnviPac filling	45
Figure 2.17: A schematic direct contact spray condensers	48
Figure 2.18: Schematics of the radiative cooled solar still	50
Figure 2.19: Schematic illustration of hybrid latent heat storage and spray flash evaporation system	53
Figure 3.1: Schematic layout of the PCM-Supported HDH desalination unit (AquaTube)	56
Figure 3.2: Illustration of local heat and mass transfer flow between different components in the evaporator; (a) one packing element, (b) finite element	58

Figure 3.3: Sketch of the locally established multi-effects of heating and humidification in the evaporator	58
Figure 3.4: Dependency of air moisture carrying capacity on the temperature	59
Figure 4.1: Schematic layout of the PCM-Supported HDH desalination unit (AquaTube) and operation cycle	64
Figure 4.2: illustration of heat and mass transfer flow between different components on one packing element; (a) Evaporator, (b) Condenser, (c) External PCM thermal buffer	65
Figure 4.3: Schematic of heat transfer in the external PCM thermal buffer; (a) Layout of the PCM packed bed, (b) energy balance over a control volume	68
Figure 4.4: Schematic of heat and mass transfer in the evaporator; (a) Layout of the evaporator, (b) energy balance over a control volume	72
Figure 4.5: Schematic of heat and mass transfer in the condenser; (a) Layout of the condenser, (b) energy and mass balance over a control volume	78
Figure 4.6: Effective heat transfer coefficients obtained with different Nusselt number correlations.	86
Figure 4.7. Schematic of a semi-infinite domain undergoing phase change	90
Figure 4.8: Linearization of air saturation enthalpy	94
Figure 4.9: Counter current cooling tower operating lines	94
Figure 5.1: Block diagram for the test setup	105
Figure 5.2: Test apparatus and prototype of PCM based HDH system	105
Figure 5.3: Locations of measured parameters	106
Figure 5.4: Thermal behavior of PCM system, top: evaporator, bottom: condenser	112
Figure 5.5: Thermal behavior of empty spheres system, top: evaporator, bottom: condenser	112
Figure 5.6: Qualitative illustration of temperature profiles in the evaporator	116
Figure 5.7: Qualitative illustration of ideal temperature profiles, left: evaporator, right: condenser	116
Figure 5.8: Average inlet and outlet liquid and gas temperatures for experiment type (1), Top: Evaporator, Bottom: Condenser	117
Figure 5.9: Evolution of productivity and GOR for PCM and Empty balls packing elements	118
Figure 5.10: Comparative productivity; (a) 78cm packed height, (b) 39cm packed height and Comparative GOR; (c) 78cm packed height, (d) 39cm packed height	120
Figure 5.11: Comparative productivities for PCM, Empty spheres, and Hiflow rings packing media for 0.38m packing height (for two hours of steady state operation)	122
Figure 6.1: Flow diagram and control logic of the simulation model	129
Figure 6.2: Evolution of inlet and outlet liquid and gas temperatures for PCM packing height 78cm; Top: evaporator, (b) Bottom: condenser	133
Figure 6.3: Evolution of solid phase temperatures for PCM packing height	134

78cm; Top: Evaporator, Bottom: Condenser	
Figure 6.4: Evolution of inlet and outlet liquid and gas temperatures for empty spheres packing height 78cm; Top: Evaporator, Bottom: Condenser	135
Figure 6.5: Comparison between measured and simulated accumulated hourly productivities	136
Figure 6.6: Time evolution of PCM temperature along the packed height	138
Figure 6.7: Evolution of liquid temperature along the packed height	139
Figure 6.8: Time evolution of gas temperature along the packed height	139
Figure 6.9: Time evolution of water vapor concentration along the packed height	140
Figure 7.1: Effect of packing size on the evaporation rate	143
Figure 7.2: Effect of packing size on specific surface area of the packed bed	143
Figure 7.3: Effect of packing size on the pressure drop of the gas	144
Figure 7.4: Effect of column aspect ratio on the evaporation rate, $V_{bed}=\text{const.}$	146
Figure 7.6: Effect of column aspect ratio on the evaporation rate, $H= 2\text{m}$	147
Figure 7.5: Effect of column aspect ratio on the evaporation rate, $H= 1\text{m}$	148
Figure 7.7: Effect of inlet hot water temperature on the evaporation rate	149
Figure 7.8: Effect of inlet air temperature on the evaporation rate	150
Figure 7.9: Effect of air/water mass flow ratio on the evaporation rate	151
Figure 7.10: Effect of packing media properties on the evaporation rate	153
Figure 7.11: Effect of hot water flow rate on the evaporation rate of different packing media	153
Figure 7.12: Effect of inlet cooling water temperature on the condensation rate	155
Figure 7.13: Effect of inlet air temperature on the condensation rate	156
Figure 7.14: Effect of water to air mass flow ratio on the PF productivity factor and NTU	157
Figure 7.15: Effect of air to water mass flow ratio on the condensation rate	158
Figure 7.16: Effect of solid packing media on hourly productivity	159
Figure 7.17: Effect of PCM thermal conductivity on condensation rate under different cooling water mass flow rates	160
Figure 7.18: Effect of PCM thermal conductivity on condensation rate under different inlet cooling water	161
Figure 8.1: Selected geographical locations in Egypt	163
Figure 8.2: Daily and seasonal variations of weather conditions in Al-Arsh and Al-Kharga, Egypt	164
Figure 8.3: Effect of brine concentration ratio on the average-yearly distillate rate and GOR	166
Figure 8.4: Effect of PCM thermal buffer volume on the average-yearly daily distillate for Al-Arsh	167
Figure 8.5: Effect of PCM thermal buffer volume on the average-yearly daily distillate for Al-Kharga	168
Figure 8.6: Effect of solar collector area on the average-yearly daily distillate rate under different climatic conditions	168

Figure 8.7: Effect of air to hot water mass flow rate ratio on the average-yearly daily distillate rate and GOR	169
Figure 8.8: Effect of cooling water to air flow rate ratio on the average-yearly hourly distillate production and GOR	170
Figure 8.9: Comparison between water and PCM as a storage medium	171
Figure 8.10: Effect of operational temperature range on sensible and latent heat storage	172
Figure 8.11: Histogram of hourly variation of inlet water temperature to the PCM-storage over one year for Al-Arish city with 3m ³ thermal storage	173
Figure 8.12: Effect PCM melting temperature in the external thermal buffer	174

List of Tables

Table 1.1: Characteristics for various desalination Technologies	5
Table 1.2: Type of renewable energy supply system and specific water cost	8
Table 2.1: Design parameters range of AQUASOL II	44
Table 5.1: Chosen variable parameters for experiments and range of values	110
Table 5.2: Basic sets of designed experiments according to boundary conditions	110
Table 5.3: Average values for inlet and outlet liquid and gas temperatures and productivities during steady state operation conditions	114
Table 6.1: Implementation of energy and mass balance equations using the "pdepe" MATLAB function	130
Table 6.2: Specified boundary and operating conditions for model validation	131
Table 6.3: Measured and simulated total productivities	132
Table 6.4: Inlet and geometrical parameters within a sample simulation run	137
Table 7.1: Reference boundary conditions for the evaporator and condenser	142
Table 7.2: Effect of different packing media on the evaporation rate (M _{hw} =1000 [l/h])	152
Table 7.3: Effect of different packing media on the condensation rate (M _{cw} =1000 [l/h])	159
Table 7.4: Design recommendations for the evaporator and condenser to produce 1000 [l/day] fresh water, inlet hot water temperature= 83°C	162
Table 8.1: Specified baseline boundary and operating conditions	165

List of Frames

Frame 2.1: Desirable properties of latent heat storage materials	23
--	----

Nomenclature

A	Area, [m ²]
A_{st}	Cross-sectional area of storage container; [m ²]
a	Specific area of the packing, (packing area per unit volume of the packed column); [m ² .m ⁻³]
a_s	Specific area of the packing per unit area of the solid, (packing area per unit volume of the solid elements); [m ² .m ⁻³]
a_e	Effective liquid-gas interfacial area of the packing [per unit volume of the packed column) ; [m ² .m ⁻³]
a_w	Wetted area of the packing [per unit volume of the packed column); [m ² .m ⁻³]
a_{gs}	Dry area of the packing at the interface between gas and solid [per unit volume of the packed column); [m ² .m ⁻³]
Bi	Biot number, dimensionless, [= $h l_0/k$]
c	Specific heat, [J.kg ⁻¹ .K ⁻¹]
c	Concentration, [mol.m ⁻³]
c_p	Specific heat at constant pressure; [kJ/kg . K]
c_{app}	Apparent specific heat capacity for PCM; [kJ. kg ⁻¹ .K ⁻¹]
D	Diffusion coefficient; [m ² .s ⁻¹]
$D_{st} \& d_{st}$	Packed column diameter; [m]
$d \& d_p$	Particle diameter; [m]
f_a	packing shape factor
G	Air mass flux; [kg.m ⁻² .s ⁻¹]
Gr	Grashof number
Gr_t	Thermal Grashof number
Gr_w	Diffusional or mass transfer Grashof number
ΔH_m	Specific fusion enthalpy of phase change material; [J.kg ⁻¹]
H	Packing height; [m]
h	Heat transfer coefficient; [W.m ⁻² .K ⁻¹]
$h_{fg} \& \Delta H_{fg}$	Latent heat of vaporization; [J.mol ⁻¹]
h_l	Liquid holdup
I	Solar irradiation; [W.m ⁻²]
k	Thermal conductivity; [W.m ⁻¹ .K ⁻¹]
K	Permeability; [m ²]
K	Mass transfer coefficient; [m. s ⁻¹]
K_i	Overall mass transfer coefficient based on the enthalpy difference; [m. s ⁻¹]
L_{st}	Packing height; [m]
L	liquid mass flux; [kg. m ⁻² .s ⁻¹]
l_0	Characteristic length; [m]
M	Mass flow rate; [kg.s ⁻¹]
m	Mass flow rate; [kg.s ⁻¹]
m	Mass; [kg]

\dot{m}	Mass flow rate; [kg.s ⁻¹]
\dot{m}_{evap}	Evaporation rate; [mol.s ⁻¹]
\dot{m}_{cond}	Condensation rate; [mol.s ⁻¹]
N	Evaporative mass flux; [mol.m ⁻² .s ⁻¹]
\dot{n}	Evaporative mass flux; [mol.m ⁻² .s ⁻¹]
Nu	Nusselt number, dimensionless [= $h L_{st} / k$]
NTU	Number of transfer units
$P \& p$	Pressure; [N.m ⁻²]
Pr	Prandtl number; dimensionless [$\mu C_p / k$]
Pe	Péclet number; dimensionless
Q	Amount of heat transfer; [J]
Q	Heat flow; [W]
q''	Heat flux; [W.m ⁻²]
R	universal gas constant; [8.314 J.mol ⁻¹ .K ⁻¹]
r_c	Brine concentration factor; dimensionless
Re	Reynolds number; dimensionless [$v D / \nu$]
Re_o	Superficial Reynolds number; dimensionless [= $V d / \nu$]
Sh	Sherwood number; dimensionless [= $K L_{st} / D$]
S	Saturation
S	Shape factor
Ste	Stefan number, dimensionless
T	Temperature; [K]
T_a	Ambient temperature; [K]
T_{g_in}	Inlet gas temperature (evaporator or condenser); [K]
T_{g_out}	Outlet gas temperature (evaporator or condenser); [K]
T_{a1}	Bottom air temperature; [K]
T_{a2}	Top air temperature; [K]
T_{L_in}	Inlet water temperature (evaporator or condenser); [K]
T_{L_out}	Outlet water temperature (evaporator or condenser); [K]
T_{w1}	Outlet brine water temperature from the evaporator; [K]
T_{w2}	Inlet hot water temperature to the evaporator; [K]
T_{w3}	Inlet cooling water temperature to the condenser; [K]
T_{w4}	Outlet cooling water temperature from the condenser; [K]
T_m	Melting temperature; [K]
T_{pcm1}	Surface (wall) temperature of phase change material cell; [K]
T_1	Initial temperature; [K]
T_2	Final temperature; [K]
t	Time; [sec]
ΔP	Pressure drop ; [N.m ⁻²]
ΔT	Temperature difference; [K]
$\Delta T_m, \Delta T_t$	Half width of melting temperatures range; [K]
ΔT_{LM}	Logarithmic mean temperatures difference; [-]

U	Overall heat transfer coefficient between gas and liquid; [$W.m^{-2}.K^{-1}$]
U_0	Superficial velocity; [$m.s^{-1}$]
u, v	Mean axial velocity in the packed bed; [$m.s^{-1}$]
v_p	Average pore velocity of the fluid (bulk mean velocity); [$m.s^{-1}$]
u_D	Darcian velocity of the fluid; [$m.s^{-1}$]
V	Superficial velocity; [$m.s^{-1}$]
V	Volume; [m^3]
v	Velocity; [$m.s^{-1}$]
v_{sup}	Superficial velocity; $m.s^{-1}$
w	Mass fraction of water vapor in air or absolute humidity ratio; [kg/kg air]
y	Mol fraction of water vapor in gas mixture
Z	Coordinate of the axial direction or packing height; [m]

Greek Letter Symbols

α	Thermal diffusivity; [$m^2.s^{-1}$]
β_t	Volumetric thermal expansion coefficient; [K^{-1}]
β_c	Volumetric diffusion expansion coefficient; [$m^3.mol^{-1}$]
ϕ	Phase fraction
ϕ	Relative humidity [%]
μ	Dynamic viscosity; [$N.s.m^{-2}$]
ν	Kinematic viscosity; [$m^2.s^{-1}$]
ρ	Density; [$kg.m^{-3}$]
τ	Time; [s]
ϵ	Porosity, dimensionless
ϵ_l	Liquid holdup, liquid fraction in a unit volume of packed column
ϵ_g	Gas holdup, gas fraction in a unit volume of packed column
ϵ_s	Solid fraction in a unit volume of packed column
σ	Surface tension; [$J.m^{-2}$]
δ	Liquid film thickness, [m]
ψ	Relative humidity; [%]
ψ	Accumulation parameter; dimensionless
δ	Liquid film thickness; [m]
η	Efficiency
ζ	Effectiveness

Subscripts

a	Air
act	Actual
atm	Atmospheric
amb	Ambient
$ball$	The packing sphere or ball

<i>bed</i>	The packed bed
<i>c</i>	Critical
<i>coll</i>	Solar collector
<i>cond</i>	Condenser/condensation
<i>cw</i>	Cooling water (on the condenser side)
<i>d</i>	Distillate
<i>d</i>	Dry
<i>e or eff</i>	Effective
<i>evap</i>	Evaporator/Evaporation
<i>f</i>	Fluid
<i>g</i>	Gas (air-vapor mixture)
<i>gs</i>	Gas-solid
<i>HE</i>	Heat exchanger
<i>hw</i>	Hot water (on the evaporator side)
<i>incident</i>	Incident solar irradiation
<i>initial & 0</i>	Initial (temperature)
<i>inter</i>	Interfacial (water-gas interface)
<i>irr</i>	Irrigated
<i>l</i>	Liquid state
<i>lg</i>	Liquid-gas
<i>ls</i>	Liquid-solid
<i>min</i>	Minimum
<i>max</i>	Maximum
<i>p</i>	Packing or particle
<i>ref</i>	Reference conditions
<i>rel</i>	Relative
<i>s</i>	Solid state and (PCM)
<i>sat</i>	Saturation conditions
<i>st</i>	Storage (packed column)
<i>sup & 0</i>	Superficial
<i>v</i>	vapor
<i>w</i>	Water
<i>w</i>	Wetted
<i>PCM</i>	Phase change material

Glossary

<i>AHE</i>	Heat exchanger area
<i>CS</i>	Continuous solid model
<i>d</i>	day
<i>DOE</i>	Design of experiment
<i>ETC</i>	Evacuated tube collector
<i>ED</i>	Electro Dialysis desalination technology
<i>FPC</i>	Flat plate collector

<i>GOR</i>	Gained output ratio
<i>h</i>	Hour
<i>HE</i>	Heat exchanger
<i>HDH</i>	Humidification-dehumidification
<i>HDPE</i>	High-density Polyethylene
<i>LHES</i>	Latent heat energy storage
<i>MSF</i>	Multi-Stage Flash desalination technology
<i>MED</i>	Multi-Effect Distillation technology
<i>PCM</i>	Phase change material/s
<i>PCR</i>	Phase change regenerator
<i>PDEs</i>	Partial differential equations
<i>PP</i>	Polypropylene
<i>PV</i>	Photovoltaic cells
<i>RE</i>	Renewable energy
<i>RO</i>	Reverse Osmosis desalination technology
<i>SHES</i>	Sensible heat energy storage

1 Introduction

The first part of this chapter discusses drinking water scarcity and quality degradation problem, which will get worse in the future globally, especially in Middle East and North Africa (MENA) region. The role of desalination to mitigate this problem, intensive energy consumption of desalination technologies, and mutual interdependency between energy and desalinated water production is highlighted. Research and development efforts to increase the energy efficiency of desalination and to integrate it with renewable energy (RE) sources are summarized. In the second part, the scope and objectives of the present study are presented.

1.1 Fresh water challenges

Water is the essence of life and touches every aspect of our life. Fresh water represents a significant constituent of the human body, plants and animals. Water is abundantly available on the earth and covers more than 70% of its surface. Fresh water comprises only 3% out of the total volume of water, while 97% is saline, undrinkable water in oceans and seas. Yet almost all of the fresh water is effectively locked away in the ice caps of Antarctica and Greenland and in deep underground aquifer, which remain technologically or economically beyond our reach [63]. The net amount of fresh water available for the bulk of our usable supply is very limited to just 0.3% (less than 100,000 km³) of the fresh water reserves on the globe.

Globally, uneven distribution of fresh water resources both geographically and temporally is the main cause of water scarcity in many parts of the world. Irrational use of water resources, non-conservative disposal of untreated industrial waste effluents into surface and underground water bodies, climate change and global warming, population growth, and accelerated industrialization and urbanization rates scale up the problem and add other dimensions to its complexity.

Some 88 developing countries that are home of about 50% of the world's population are affected by serious water shortages. Water-borne diseases (WBD) represent 80-90% of all diseases and 30% of all deaths result from poor water quality in these countries. This problem necessitates taking a decisive step to setup new strategies for facing such a rapid increase in WBD, which affects human health and their mental and physical abilities. Furthermore, over the next 25 years, the number of people affected by severe water shortages is expected to increase fourfold [64]. The unprecedented rapid increase of water shortage and rising conflicts between neighboring countries about trans-boundary water resources make the water problem more sensitive today than at any time in the past.

To help mitigate this destabilizing trend and the consequences of the current and impending crisis, three major kinds of resources have to be committed: low cost

seawater desalination, upgrading water quality of surface and contaminated underground water, and intensification of wastewater regeneration and reuse.

1.2 Desalination option

Water desalination is the process that removes dissolved minerals and other pollutants from seawater, brackish water, or treated wastewater to produce fresh potable water. Water desalination is a technically mature technology to provide renewable and reliable water supplies and has been practiced regularly over the last 50 years in different parts of the world. Most of the desalination plants in operation are located in the driest part of the world; Middle East and North Africa (MENA) region. Nearly more than 15 thousand desalination plants (of a unit size of 100 m³/day or more) with cumulative capacity of approximately 65.2 Million m³/day have been installed or contracted around the world by the end of 2010.

The three factors that have the largest effect on the cost of desalination per unit of fresh water produced are the feed water salinity level, energy cost, and plant size which show economies of scale [65]. Intensive energy requirement stands as a major contributor to -the relatively- high cost of desalinated water. It has been estimated by Kalogirou [66] that the production of 1000 m³ per day of fresh water requires 10000 tons of oil per year.

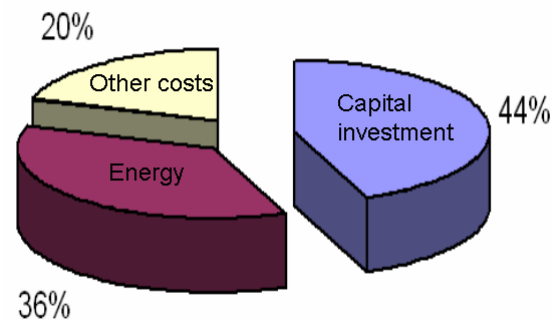


Figure 1.1: Cost breakdown of desalinated water, adopted from Abdel Gawad [5]

Fortunately, desalination cost declines steadily over time and becomes more competitive compared with conventional water resources. Nevertheless there are still some potential and necessity for bringing the cost down. While cost cannot be overlooked, there is compelling evidence that desalination will have to be adopted as the only acceptable way to provide potable water in some developing countries, particularly in the MENA region [68]. Reducing the cost of desalinated water, therefore, has been and will continue to be a crucial issue to be explored.

1.3 Overview on desalination processes

Depending on the transport phenomena involved in the separation process, desalination systems are broadly categorized under two main groups, which survived the crucial evolution of desalination technology, namely; thermal (or phase change) and membrane techniques. Several treatment and desalination technologies that vary in nature, efficiency, and energy requirements are

summarized in figure (1.2).

Thermal technologies (or distillation) are based on liquid-vapor phase change due to addition of heat to drive the process. In the distillation process, seawater is heated to evaporate the water partially and the generated vapor is then condensed back into fresh water, leaving behind high concentrated salts in the waste brine. Evaporation heat is retained by the generated vapor as latent heat. When the vapor is condensed, it releases its latent heat, which can either be used to preheat feed seawater or evaporate water in a next stage. This process produces highly purified fresh water of better quality than the membrane processes.

Distillation processes are divided into mainly three methods, multiple effect distillation (MED), multistage flash (MSF), and vapor compression (VC) as well as solar distillation techniques (e.g. basin-type solar distillers and HDH technique).

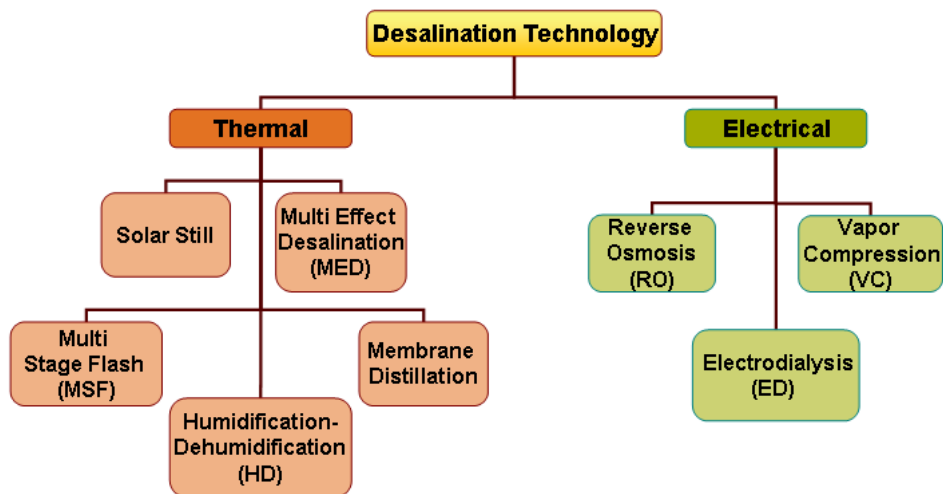


Figure 1.2: Overview and energy classification of desalination processes

In **membrane technologies**, the separation is realized by selectively passing fresh water or salt ions through semi-permeable membranes. The former process is called reverse osmosis (RO) where the separation is realized by applying high pressure difference on the membrane to outbalance the osmotic pressure. The later is called electro dialysis (ED) where an electrolytic charge difference on a pair of separation membranes is used as the driving force. In such processes no phase change takes place and, therefore, the energy consumption is lower than that of thermal processes for producing the same amount of fresh water. Other types such as micro and nano filtration membranes are used for water quality improvement and wastewater treatment.

1.3.1 Energy requirements and water cost

Desalination processes, require mainly either low temperature steam or sensible heat for thermal distillation processes and electrical power for membrane systems. Electrical power is also necessary in thermal desalination plants for driving mechanical components such as pumps. The majority of desalination plants acquire their electric power requirements either directly from a public grid or from co-located power plant. The flow diagram of energy, water, and money for desalination process is illustrated in figure (1.3).

Traditionally, fossil fuels such as oil and gas have been the major energy sources. However, sustainability of this resource in the long term is a vital issue to be addressed in view of the limited fossil fuels, prices volatility, and their negative impact on the global environment. Sustainability assurance of energy and water supply in the long term is prompting consideration of alternative renewable energy sources for seawater desalination.

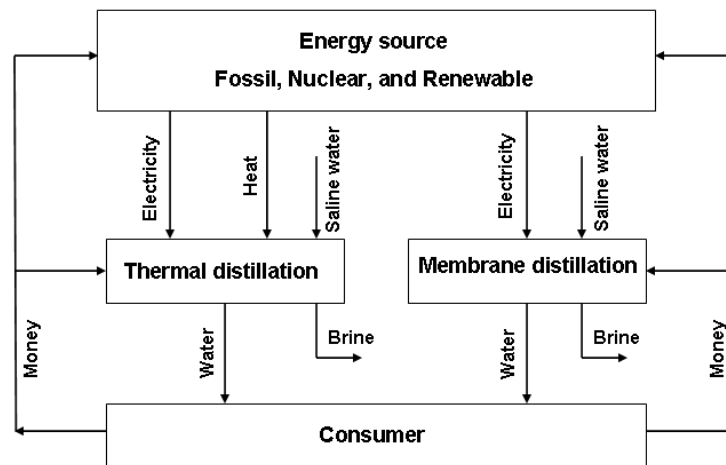


Figure 1.3: Flow scheme of energy, water, and money; adopted from [158]

The theoretical absolute minimum energy required for water desalination is about 0.8 kWh/m^3 ($\approx 2.88 \text{ kJ/kg}$) of water produced, depending solely on feed water salinity regardless of the technology and configuration of the desalination scheme [70]. This value represents the reversible, isothermal work for any steady state separation process. This figure is practically unrealistic not only because it assumes complete reversibility of all operations, but also because it would involve pumping an infinite amount of feed water and the pumping work would then be infinity [71]. The practically minimum energy consumption to produce fresh water is approximately 5 kWh/m^3 for RO as a membrane process and 50 kWh/m^3 for MED as a distillation process.

1.3.2 Selection criteria of desalination technology

The right selection of desalination technology depends on several factors and, to a great extent, can be considered as case specific. The most influential aspects are the type of feed water, the required quality of produced water, the plant capacity, the local available energy source and its cost, and the availability of skilled human resources. Table (1.1) compares between the main streams of commercial desalination technologies in common use worldwide.

Membrane processes, mainly reverse osmosis (RO), is currently the predominant technology due to its low specific energy consumption compared to thermal processes. However, membrane technologies are less tolerant to source water turbidity, require highly skilled personnel for operation and maintenance, and have comparatively high operation and maintenance costs. Moreover, membrane technologies are very sensitive to feed water quality and therefore require intensive feed water pretreatment. Thermal desalination technologies are, by default, more technically adopted to be integrated with thermal power plants for cogeneration of electricity and water.

Table 1.1: Characteristics for various desalination Technologies [72]

Feature	MSF	MED	RO
Global energy consumption	high	medium	low
Adaptability to high sea water turbidity	excellent	medium	low
Adaptability to high sea water salinity	high	medium	low
Need of a co-generating power plant	high	medium	low
Product water quality	very high (2-5 ppm)	very high (2-5 ppm)	drinking (300-400 ppm)
Maintenance costs	low	low	high
Easy of operation	good	good	medium
Investment costs	medium/high	medium	low

Even though currently practiced desalination of brackish or seawater may be economically efficient in large scale facilities, it is less suitable for the decentralised water supply, as it is needed for small communities in remote developing regions. Thus, desalting processes, which are appropriate for decentralised use, should be technically simple in order to reduce capital and maintenance costs and to provide an application which can be operated without specialised knowledge. It is also highly desired to operate these units by renewable energies, especially solar systems since solar energy is often abundantly available in water-scarce regions.

1.3.3 Coupling desalination plants with power plants

Since thermal desalination technologies utilize heat energy as the main driving force, co-location with power plants is an attractive option for cogeneration of water and power at competitive economies. Co-location of power plants and thermal desalination plants has been considered the most desirable setup since it provides many advantages over the displaced plants:

- better overall thermal efficiency due to recovery and utilization of latent heat of condensation in the power plant as an energy source for the desalination plant
- cost saving through common use of infrastructure for both plants (e.g. the intake and outfall, and using the power plant condenser as a brine heater of the desalination plant)
- minimizes energy transportation losses and costs, better land use, and less man power is required for operation and maintenance of both plants

Moreover, conventional electrical power production requires a sustainable source of water, while desalination technology requires a substantial power supply. This mutual interdependency implies that the sustainable solutions should be found in the autonomous systems which simultaneously produce both electrical power and desalinated water within the same scheme.

1.3.4 Coupling renewable energies with desalination technologies

Renewable energy (RE) technologies such as solar thermal, photovoltaic (PV), wind energy, and biomass have reached a level of maturity that makes them reliable sources of energy for driving desalination processes. It is agreed that the economic feasibility of the desalination industry will depend greatly on technology development of renewable energies [73]. Recently, considerable attention has been given to the use of renewable energies for desalination plants, especially in remote areas and islands.

Coupling renewable energy systems with the desalination technologies takes place at an interface between both of them, where the energy generated by the RE system is utilized by the desalination plant. This energy can be in different forms such as thermal energy, electricity or shaft power. Owing to the variety of desalination processes and required form of power, there are a number of coupling schemes with power generation systems. Plausible couplings are depicted in the form of a tree in figure (1.4).

However, the two common features which characterize RE sources are the intermittence and continuous variation in intensity over time. In other words, RE systems are characterized by a transient behaviour and time mismatch between the demand and availability of energy supply. These handicaps require either some form

of energy storage or hybridization with other energy sources. Due to energy storage and hybrid operation with bio or fossil fuel, RE systems can provide continuous operation capacity for desalination processes.

Wind power has become very competitive to conventional fossil fuel power plants. Nevertheless, wind power can only be economically viable in limited sites where wind speed is greater than 6 m/s and can be reliable to meet only a small fraction of the base load all over the year. Solar photovoltaic (PV) technology has the advantage of direct conversion of sun's light into electricity. However, it has low conversion efficiency; approximately 12-16%. The overall conversion efficiency even decreases further to less than 10% when storing to batteries.

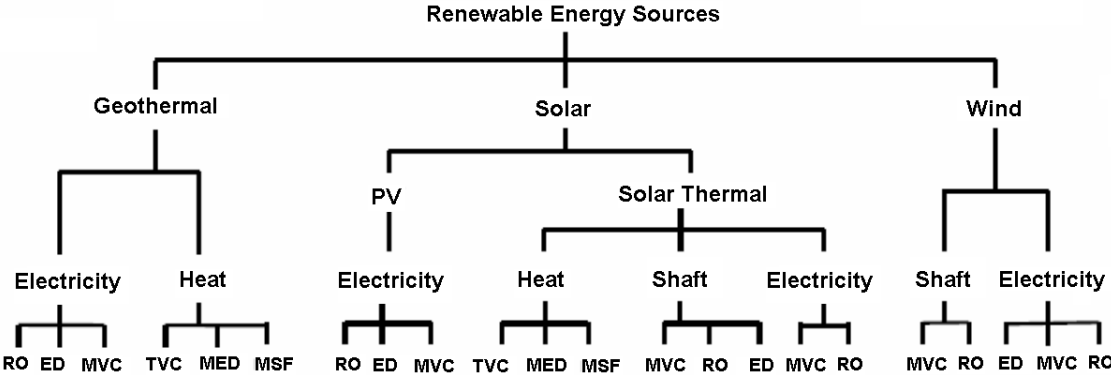


Figure 1.4: Feasible couplings between renewable energy and desalination technologies [72]

Low and medium temperature solar thermal applications in addition to high temperature steam and electricity generation using solar concentrators are well developed and in the focus of contemporary research studies. Furthermore, biomass technologies are expanding and developing more robustly for producing both heat and electricity and can be used either separately or in combination with solar concentrating systems for powering desalination plants.

From the traditional perspective, renewable energy sources are ideally suited for small-scale decentralized desalination plants in remote areas. Nevertheless, it is more emphasized nowadays that solar technologies could drive different types of water desalination technologies of different capacities with the emerging concentrating solar power technology on a commercial scale.

The viability of any RE desalination combination at a particular site depends mainly on: the renewable energy potential and form, required desalination capacity, availability of spare parts and skilled personnel for plant operation and maintenance,

and the total system cost [70]. As a matter of fact, it could easily be understood that the cost of water produced from desalination systems using a conventional source of energy, (gas, oil, electricity) is much lower than that obtained by RE sources. Table (1.2) presents a comparison between water cost for those technologies which use a conventional source of energy and those powered by renewable energy sources. The specific water cost from RE-desalination depending on the used technologies, plant capacity, salinity of feed water, and other site specific factors such as land cost and time availability of renewable energy and its intensity.

Table 1.2: Type of renewable energy supply system and specific water cost [74]

Type of feedwater	Type of energy used	Cost (per m ³)
Brackish	Conventional	0.21€–1.06€ (0.26\$–1.33\$)
	Photovoltaics	4.50€–10.32€
	Geothermal	2.00€
Seawater	Conventional	0.35€–2.70€
	Wind	1.00€–5.00€
	Photovoltaics	3.14€–9.00€
	Solar collectors	3.50€–8.00€

For brackish water and conventional source of energy, the cost ranges between 0.21 €/m³ and 1.06 €/m³ when very small units are used. Similarly, seawater desalination cost varies between 0.35 €/m³ and 2.7 €/m³ and only when the desalination unit is very small (2–3 m³ daily production) the cost can increase to approximately 5.50 €/m³ [74].

1.3.5 Barriers and limitations of RE-desalination

Several technical, institutional, economic and social barriers, which hinder the widespread application of RE-D, are discussed extensively by ProDes project [75]. In summary, the high water production cost for RE-D, as a main barrier, is attributed (but not limited) to the following reasons [75]:

- There is no development of complete optimized RE-D as a single system but only as separate component parts.
- Current desalination technology has been designed requiring a constant energy supply, whilst most RE systems provide a variable energy supply due to their transient nature. This results in increased specific capital and maintenance costs

- Desalination development focuses on ever larger systems, not the smaller scale typical of RE-D, which causes a lack of standard (i.e. cheap) components appropriate for small scale desalination plants.
- Lack of supporting policies to promote the penetration of RE-D in the market, which make it cheaper.

1.4 Solar desalination

Solar distillation can be classified into two main categories based on the plant setup. The first is the basin-type (or direct type) solar stills in which the solar collector is integrated in the still, such that solar irradiation is directly used to evaporate water. In the second class, which is called indirect type solar still, the solar collecting device is separated from the evaporator. As an indirect type solar distiller, humidification-dehumidification (HDH) technique using fixed packed beds was introduced as a promising technique as early as 1950's. As reported by Huges [1], a solar operated HDH process can yield 5 times as much fresh water as a solar still of the same solar collecting area can produce.

1.4.1 Conventional solar stills

Solar stills are a simple method for desalinating water as they mimic the hydrological cycle in the nature. Solar stills utilize the fact that water left exposed to air will tend to evaporate. The function of the still is to capture this evaporating water and condense it on a cold surface, thus providing potable water. The solar still consists of a black colored pan (to maximize the absorbed energy) containing water, this pan is then covered with a glass sheet or translucent plastic, which allows the admission of solar energy. This cover also acts as a condensing surface for the evaporated water. The cover is tilted towards the fresh water collector (Figure 1.5).

Conventional **basin-type solar stills** have low efficiency as there is no real possibility to recover the latent heat of condensation, which is wasted to the environment. This type obviously suffers from low productivity and requires large land areas. The low daily productivity along with the high cost of water produced by this method are the main obstacles to utilize the huge solar energy resource in water distillation. The problem of low daily productivity of solar stills triggered scientists to investigate various means of improving still productivity and thermal efficiency for minimum water production cost. These means include various passive and active methods for single effect stills.

Different techniques, configurations, and developments that have been introduced in literature to improve the single effect stills are enormous and were highlighted in Fath [77] and Tiwari, and Yadav [79]. Solar distillation is usually suitable for small-scale applications in remote areas, where abundant solar radiation and low cost land are available. Fath [77] concluded that the development of solar distillation has demonstrated its suitability for saline water desalination when the weather conditions

are favorable and the demand is not too large, i.e., less than 200 m³/d. As a consequence, the so called **humidification-dehumidification (HDH)** technique using fixed packed beds was introduced as a promising technique as early as in the 1950's.

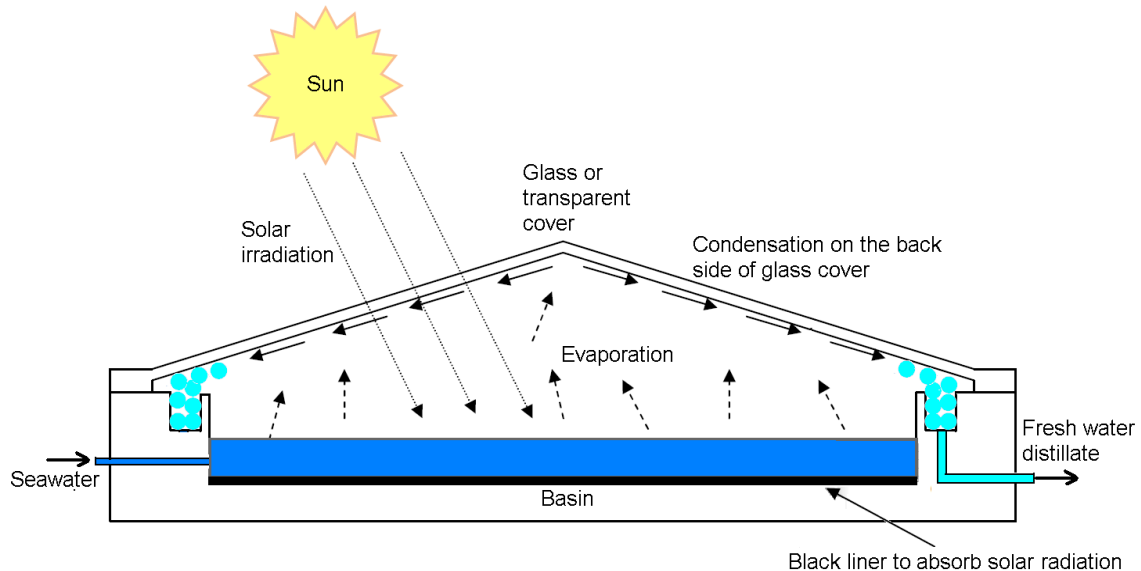


Figure 1.5: Basin type solar still

1.4.2 Humidification-Dehumidification technique

The basic components of a conventional HDH desalination unit as illustrated in Figure (1.6) are: the evaporator, the condenser, and the heat supply system combining solar collector with/without hot water storage tank. The HDH cycle can be described simply as a process of bringing warm unsaturated air into direct contact with warm saline water. Under such conditions desired humidity content in the air is reached. Then, this is followed by stripping out the vapour from the humidified air by passing it through a condenser.

It is often referred to this process as Multiple-Effect Humidification-dehumidification (MEHD) cycle. In fact, the multi-effect term doesn't refer to a number of successive stages but rather to a multiple recycle and reuse of the input heat in the process. The multi-effects can be achieved in different ways, brine recirculation, air recirculation, recovery of latent heat of condensation (while preheating the feed seawater in the condenser as displayed in figure (1.6)), or any combinations of them. The brine is heated up further through a solar collector during the day time. An external thermal buffer may be used to support the plant during the night time or in bad weather times.

Introduction of the indirect type solar desalination process based on the (HDH) principle led to a major improvement in the efficiency and reduction in the specific collector area. This is due to energy recovery mechanisms, extended evaporation surfaces, and enhanced heat and mass transfer coefficients due to the turbulent flow between air and water. Therefore, combining the principle of humidification-dehumidification with solar desalination appears to be an attractive method of water desalination with solar energy. The HDH technique is especially

suited for seawater desalination when the demand for water is decentralized. Advantages of this technique include flexibility in capacity, moderate installation and operating costs, simplicity, and possibility of using low temperature energy (solar, geothermal, recovered energy or cogeneration) [2].

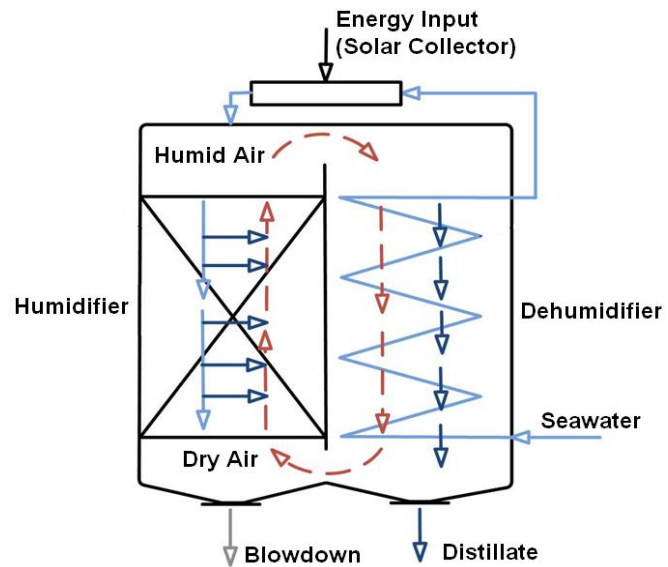


Figure 1.6: Schematic diagram of a HDH desalination cycle

1.5 Aim of the work

The major aim of this study is to examine, characterize, and optimize the performance of an innovative “**PCM-supported HDH system**” utilizing spherical capsules of Phase Change Materials (PCM) as a packing media in the evaporator, and condenser. The system configuration comprises a closed air loop between the evaporator and condenser. The condenser is of direct contact type in a concurrent flow regime between cooling fresh water and humid air. Moreover, a solar thermal power supply, which consists of a solar collector and an external thermal storage is used to drive the HDH plant. The thermal storage is accomplished by storing to PCM with melting point around the required output temperature to guarantee 24 hours of operation. The PCM elements will be integrated in the hot water storage tank in order to reduce its volume, cost, and heat losses.

The objective of integration of PCM packing in the HDH process is for improving the thermal performance of the evaporator and condenser and not for thermal energy storage. Under steady state conditions, the main difference between PCM packing and other commercially available bed filling materials such as Raschig Rings, Pall Rings, Berl Saddles or Intalox Saddles, is the thermal conductivity of PCM, but not its thermal storage capacity or solid-liquid phase change. Thus this study focuses on

using a conductive filling media to achieve multiple-effects of heating/humidification (MEHH) and cooling/dehumidification (MECD) while air passing through the successive PCM layers in the evaporator and condenser respectively. These phenomena are foreseen to enhance the heat and mass exchange processes and will be described in detail and focused throughout the present analysis.

The study has been accomplished through comprehensive experimental and numerical investigations on the PCM-supported HDH system. A mixed micro-macro balance transient simulation model has been established and validated against experimental measurements using COMSOL Multiphysics and MATLAB for solving fluid flow and heat and mass transfer phenomena in one spatial dimension for different components in such a loop. The model is fairly general and simple, yet sufficiently accurate to be applied as a design and optimization tool for HDH plants integrated with different types of packing materials and external thermal storage systems. Using both experimental and simulation tools, a detailed heat and mass transfer analysis for the performance of the evaporator and condenser over a wide range of operation conditions under steady state has been performed and clearly documented using different types of packing materials.

The dynamic performance of the PCM-supported HDH system over a wide range of operation conditions will be presented and analyzed on a macro-scale level under varying weather conditions over one year for Al-Arish City on the eastern north coast of Egypt. The analysis will focus on the optimum operation conditions of the system with and without external PCM thermal buffer. Special attention shall be paid to the effect of climatic conditions and comparison between PCM and water as storage media in the external thermal storage.

1.6 Dissertation Overview

The dissertation contains 9 main chapters. Chapter 2 presents the state of the art of solar desalination by HDH technique, and thermal energy storage methods and media. In chapter 3 the proposed HDH system is introduced and scope of the present work is outlined. Chapter 4 discusses the theoretical background, underlying physics of the proposed system components, and mathematical modeling development for individual components and for the HDH system as a whole. Chapter 5 discusses the experimental results and analysis of the PCM-supported HDH cycle. The chapter 6 deals with the numerical simulation and validation of single components models as well as the HDH cycle. In Chapter 7 the simulation results and parametric analysis of the main single components (i.e. the evaporator and condenser) are discussed. Chapter 8 focuses on the numerical optimization of the HDHD system as a whole including the solar collector field and the external PCM thermal energy storage. Finally, chapter 9 summarizes and concludes the study activities and proposes future work needed for improving and implementation of the proposed system.

2 Literature Survey

2.1 Introduction

As the proposed system in the present study incorporates phase-change energy storage materials (PCM) in small-scale desalination units, the relevant basics and developments of PCM thermal energy storage systems will be helpful for designing the main system components and selection of the appropriate storage medium. The first part of this chapter provides a comprehensive literature on PCM, covering almost all potential PCMs that could be used for thermal storage at the different operating temperatures and also discussing problems associated with the application of these materials in practical energy storage systems.

In order to gain a wide and concrete knowledge on small-scale desalination units working with humidification-dehumidification technique (HDH), it is essential to review the real projects in the field under real working conditions including all the crucial and important influencing operating parameters. Elaborated review covering the above mentioned areas of interest is presented in the second part of this chapter. Learned lessons, and gained experiences will be extracted intending to identify scope of the work, proposed system, and study methodology which will be presented in chapter 3.

2.2 Importance of solar energy storage

Efficient and reliable thermal energy storage systems have applications whenever there is a temporal difference between energy supply and demand. Thermal energy storage can also be used to reduce the mass of the heat rejection system. Waste heat generated during high-power sprint mode operation is absorbed by the thermal storage unit and then later dissipated over a much longer non-operation period [127]. Solar energy as a renewable source of energy is available in abundance in many parts of the world, and its advantages are self-evident in our times of global energy shortage and unsteady increase in the price of world oil. With the breakdown of effecting stabilizing factors, oil prices have become impossible to predict. However the disadvantages are equally obvious; solar energy is an intermittent and dilute source of energy. Its availability varies with geographical location, clock time, season or time of the year, and according to the extent of cloudiness, fog, or haze. These problems invited scientists to investigate various means of improving solar energy collection efficiency, and developing efficient and economical heat energy storages in order to launch widespread utilization of solar energy for low and high temperature thermal applications.

The functions of heat storage units in a solar energy system are to store the excess energy at daytime or when it is in abundance, so that it can be regenerated and used

according to the demand at night as well as cloudy hours and rainy days. How to store energy is one of the most important issues in a solar energy system. The general characteristics of energy storages may be summarized in three aspects [85]. The first is the time period during which energy can be stored. The second aspect is the volumetric energy capacity for the same amount of energy, the smaller the volume of energy storage, the better the storage is. The last aspect is that energy can conveniently be added and withdrawn from the storage system. For instance, a large heat transfer surface area should be required for storages. Basically, solar energy could be stored in three forms; sensible heat, latent heat, and thermo-chemical heat or a combination of them.

2.3 Thermo-Chemical Energy Storage

Thermo-chemical storage offers an order of magnitude larger heat storage capacity over sensible storage. This type of energy storage, rely on the energy absorbed and released in breaking and reforming molecular bonds in a completely reversible endothermic chemical reaction, such as it can be reversed upon demand to release back the heat. In this case, the heat stored depends on the amount of storage material, the endothermic heat of reaction, and the extent of conversion. Thermo-chemical energy storages also have the advantage of a long-term storage with low losses. However, the chemical reactions employed must be completely reversible.

One concept is using a salt, such as sodium sulphide and water. The salt can be dried using for instance solar heat. This will accumulate thermal energy, and this energy can be recovered by adding water vapor to the salt. This concept works “on paper” and in the lab, but there are problems with corrosion and air tightness, since the dry salt must be stored in an evacuated (airless) environment [103]. Reactions like these are combined with a heat pumping effect. Energy at a low temperature level has to be provided in order to discharge the storage, for instance vaporisation of water. At the charging process energy is withdrawn from the system for instance by condensing water.

Another form of latent heat storage is the physical adsorption of water vapor from the atmosphere at the surface of a highly porous solid like zeolite. When dry zeolite material adsorbs water vapor, the heat of condensation is released in the adsorption process, while the porous media is saturated with water. Then the water can be driven off (desorbed) again by heating the porous media to more than 100 °C and thereby storing the thermal energy. While desorbing water, the saturation of the porous media decreases again, which means regeneration of the zeolite.

The adsorption/desorption processes can be repeated (almost) indefinitely without any significant deterioration of the zeolite material [26]. This process is being used in a heating/cooling plant in some buildings in Munich. Drying of the zeolite material is done by cheap, off-peak heat from the district heating system [104].

There is actually a commercial product based on zeolite/water adsorption available, also in Germany, namely self-cooling beer kegs. The user just turns a handle and waits for about ten minutes. Then he/she can serve 20 liters of cold beer to guests. The empty kegs are returned to the factory, recharged by heating, and filled with beer again. Air humidification/cooling and dehumidification/heating are being used to cool the beer glasses and recharge the empty kegs, respectively. Since its introduction in 2001, about 20,000 kegs are in regular use [105].

Thermochemical reactions have the potential to store up to $1 \text{ MWh}\cdot\text{m}^{-3}$, depending of course upon the actual reaction [103]. However, they are more complex than other thermal energy storage systems, and still in the development phase, but they are also more flexible [98].

2.4 Sensible heat energy storage (SHES)

In sensible heat storage (SHES), temperature of the storage material varies with the amount of heat energy stored. SHES system utilizes the heat capacity (c) and the change in temperature ΔT of the material during charging and discharging processes. The amount of stored heat depends on specific heat of the medium, the temperature change, and the amount of storage material.

$$Q = \int_{T_1}^{T_2} m \cdot c \cdot dT \quad (2.1)$$

Most SHS use water, stone, iron, earth, or ceramic bricks as the thermal storage material, and air, water, or oil as the heat transfer fluid. The high heat capacity of water often makes water tanks logical choice for thermal energy storage systems that operate in a temperature needed for heating and cooling applications, but the low density of water requires large volumes. In desalination technology, water storage tanks are highly recommended for 24 hours operation of humidification-dehumidification solar desalination units [87]. The relatively low heat capacity of thermal storage materials such as rock and ceramics is somewhat offset by the large temperature difference possible by these materials and their relatively high densities [88].

2.5 Latent heat energy storage (LHES)

2.5.1 Concept of Phase Change Energy Storage

The latent heat storage (LHES) or phase change materials (PCM) absorb and release heat as it undergoes a change in phase from solid to solid, solid to liquid or

liquid to gas or reverse. The phase change involved takes place without a change in the temperature of the material itself. Figure (2.1) depicts the mechanisms of heat absorption and release in LHES materials. During the heat transfer to the solid phase, as long as the matrix structure is strong enough to stand the rising kinetic energy due to the higher oscillation amplitude of each element in the matrix; the matrix structures does not change and the change of internal energy can be monitored by a rise of temperature. Therefore, initially solid-liquid PCM perform like conventional storage materials; their temperature rises as they absorb heat, then change has yet a sensible component.

At the melting point there is a change to the next higher level of entropy, the binding forces in the matrix are no longer strong enough to stand the risen kinetic energy of its elements. As the temperature of the PCM rises, their chemical bonds break up gradually as the material changes phase from solid to liquid. The phase change is a heat seeking (endothermic) process and therefore, the PCM absorbs large amount of heat without getting hotter, i.e. while storing heat, the temperature of the PCM stays nearly constant until the melting process is completed.

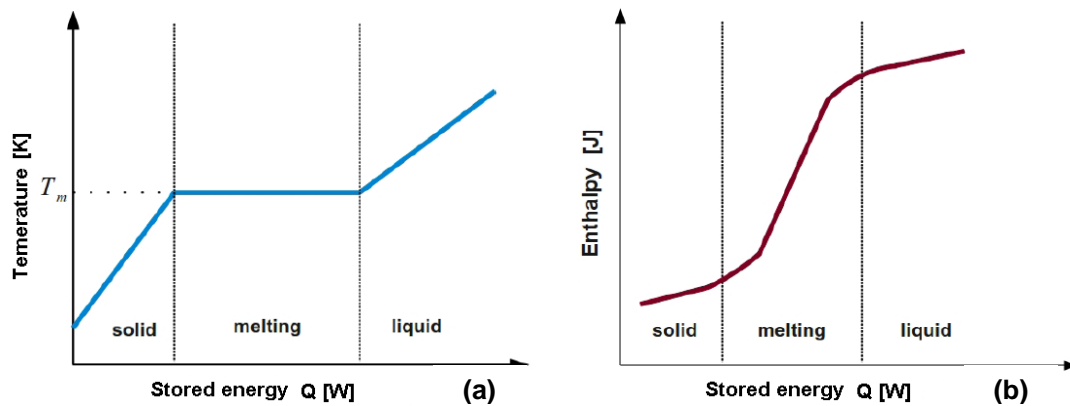


Figure 2.1: Phase change behavior of solid-liquid latent heat storage systems; (a) melting at a sharp point, (b) melting over a temperature range

The energy stored during the phase change process is called “latent heat” or “heat of fusion”. As the materials cool off (at night or on cloudy days) they subsequently release the stored heat while solidifying in the same fashion.

The storage capacity of the LHES system with a PCM medium is defined by the following equation:

$$Q = \int_{T_1}^{T_m} c_s (T_m - T_1) + m\Delta H_m + \int_{T_m}^{T_2} c_l (T_2 - T_m)$$

$$Q = m[\Delta H_m + c_s(T_m - T_1) + c_l(T_2 - T_m)] \quad (2.2)$$

where ΔH_m is the latent heat of melting and c_s and c_l the are specific heats of the solid and liquid phase, respectively.

2.5.2 Advantages of LHES

The main advantages of LHES over other storage systems may be summarized in the following:

- a) Higher energy density per unit mass and per unit volume, resulting in reduction of mass and volume of the storage unit. It has been reported [86] that phase change materials store 5 to 14 times more heat per unit volume than sensible heat storages such as water, masonry, or rock.
- b) The PCM temperature remains nearly constant during the phase change, which is useful for smoothing temperature variations, then keeping the subject at uniform temperature. In other words, heat extraction and storage take place at (nominally) constant temperature corresponding to the phase change temperature.
- c) Lower storage temperatures, which reduce the heat loss.

Latent heat energy storage media are confined in three basic forms; solid-solid, solid-liquid, and solid-liquid-vapour phase change.

2.5.3 Solid-Solid Phase Change Storages

The challenges to widespread use of PCM are their packaging or capsulation, high cost, and lake of technical knowledge among potential customers and users. For solid-solid phase transformation the need for encapsulation of phase change material is eliminated. This enables the high capacity properties of phase change to be exploited without the additional thermal resistance and the associated costs due to the encapsulation. In solid-solid transitions, heat is stored when the material is transformed from one crystalline structure to another. Generally, the latent heat of transformation for this transition is smaller than that of the solid-liquid phase change materials. However, there are some of them having high capacity, form-stable, that can be used as direct contact thermal storage systems in many applications in industry and in commercial and residential heating. Some of the most promising materials for solid-solid PCM are the commercially available vinyl silane graft copolymer, a polysiloxane [88], and organic solid solution of pentaerythritol, pentaglycerine, Li_2SO_4 , and KHF_2 [92].

Some investigations that have dealt with the Polysiloxane, as a promising form-stable candidate for thermal energy storage proved that it has high latent heat of

fusion and relatively low cost [88-91]. Such form-stable systems have many advantages over conventional phase change storage systems. For example, conventional phase change storage systems for steam applications would be larger, less efficient, and would require an intermediate working fluid since most encapsulation materials corrode in steam environment. Due to low thermal resistance, the direct contact form-stable system is also particularly suited for low grade waste energy recovery such as from industrial processes where the flow gases are between 100 and 200 °C [88].

Commercially available polymers such as high density polyethylene (HDPE) have to be usually *cross-linked* to make them form-stable with the help of a catalyst or by more sophisticated method. The *cross-linked* storage units can use the granular form that is usually available, or can utilize other shapes such as rods or other geometries [88]. High density polyethylene offers definite advantages as potential thermal energy storage material if it is rendered form-stable by cross-linking [101]. Kamamoto et al. [6] concluded that cross-linked HDPE is an excellent thermal energy storage material and can be used in direct thermal contact with ethylene glycol and silicon oil. Sharma et al. [98] reported that their operating temperatures of 110 to 140°C are too high for some applications such as space and water heating, and according to his knowledge no company has commercially developed cross-linked polyethylene for heat storage applications at this time.

2.5.4 Solid-Liquid-Vapour Phase Change Storages

The use of a complete solid-liquid-vapor phase change cycle will further increase the storage density, but large volume changes cause problems regarding the containment of such materials, and then rule out their potential application in thermal storage systems. Indeed, such systems are technically feasible, but quite more complicated than the simple (and passive) solid-liquid-solid cycle [103]. Furthermore, changes of phase from liquid to gas involve large changes in volume of the material and so are difficult to make practical in a closed compact solar seawater desalination and hot water storage systems. Indeed, no single attempt to use solid-liquid-gas phase change for PCM storage has been found in the literature.

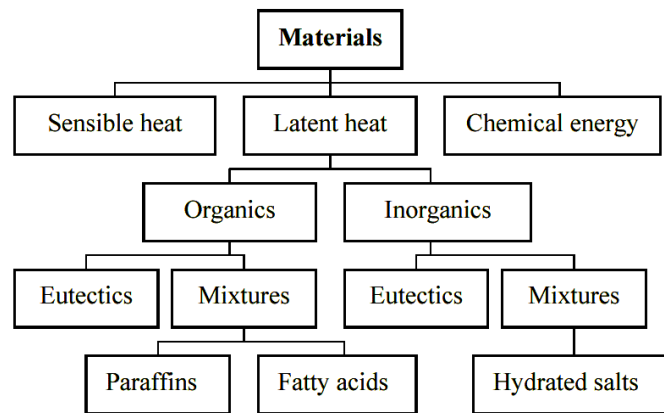
2.5.5 Solid-Liquid Phase Change Storages

Solid-liquid transformations are most commonly employed due to small changes in volume and high heats of fusion. It is also possible to choose a melting temperature in a wide range from a large amount of solid-liquid phase change materials. A wide variety of solid-liquid phase change materials is commercially available with temperature ranges from – 21 °C (sodium chloride solution) to more than + 200 °C (salts and eutectic salt mixtures). Phase change materials can therefore be used as a thermal storage medium for both heating and cooling. Phase change materials

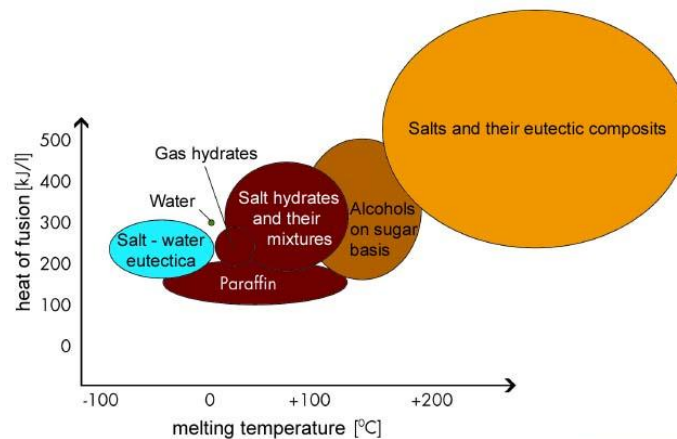
(solid–liquid) have a storage density in the order of 0.1 MWh/m³ [103]. This study now focuses on solid/liquid phase change materials that have a characteristic melting temperature in the range 40-90 °C.

2.6 Classification of Phase Change Materials

Phase change materials are classified into two main categories; organic compounds and inorganic (salts), figure (2.2a) shows a classification of existing materials which can be used for thermal energy storage. Figure (2.2b) gives an overview on different phase change storage materials and sorts them according to their melting temperature and latent heat of fusion. More detailed description of the properties of these materials are given below.



(a) According to type of thermal energy storage media [93]



(b) According to melting temperature and heat of fusion (ZAE Bayern)

Figure 2.2: Classification of energy storage materials

As the thermal and chemical behaviour of each subgroup is greatly different, the properties of each subgroup are to be discussed in some detail. However, these PCM to be used in the design of thermal storage systems should exhibit certain desirable thermo physical, kinetic, and chemical properties, which are listed in frame (1). In addition, economic competitiveness and large-scale availability of these materials should be considered.

2.6.1 Organic Phase Change Materials

Paraffins: Some of the more popular and easy to use products are various paraffin and these can be made with melting points between $-20\text{ }^{\circ}\text{C}$ and $120\text{ }^{\circ}\text{C}$ [103]. Paraffins are non-toxic, ecologically harmless, and chemically inert to nearly all materials, and this means that there will be no corrosion in energy storage systems. Paraffin waxes are normally mineral oil products of type $\text{C}_n\text{H}_{2n+2}$, which are a family of saturated hydrocarbons with very similar properties. Paraffins between C_5 and C_{15} are liquids, and the rest are waxy solids. They consist of a mixture of mostly straight-chain paraffins, or normal alkanes, their melting temperatures are strongly influenced by the length of the chain of the alkanes, and ranges between 23 and $67\text{ }^{\circ}\text{C}$ [97]. Generally, the longer the average length of the chain, the higher the melting temperature and heat of fusion [96].

Numerous investigations show that paraffin waxes present many desirable characteristics of a PCM for heat storage purposes such as:

- (i) High heat of fusion, good self-nucleating properties, and no tendency of phase segregation on melting
- (ii) Chemically stable, safe, and non-reactive, good kinetic properties for the phase transition, therefore only a low or no supercooling effect
- (iii) Compatible with all metal containers and easily incorporated into heat storage systems. Care however should be taken when using plastic containers as paraffins have a tendency to infiltrate and soften some plastics [99]
- (iv) Easily available commercially from many manufacturers in various grades with reasonable prices

However, the main drawbacks are equally addressed as:

- (i) Low thermal conductivity in solid state, which presents a problem when high heat transfer rates are required during the freezing cycle. Therefore, special considerations are required for the heat exchanger in order to overcome this problem. The most sound solutions to enhance the thermal conductivity of paraffins are to use finned containers and metallic fillers or through combination latent/sensible storage systems [100]. Aluminum honeycombs has been found to improve system performance [86].
- (ii) In addition, pure paraffin waxes are very expensive therefore economics only permit the use of technical quality paraffin waxes, which do not have

a sharp melting temperature. Commercial grade paraffin wax is obtained from petroleum distillation and is not a pure substance, but a combination of different hydrocarbons.

- (iii) Paraffin waxes have a large volume change between the solid and liquid stages. This causes many problems in container design [101].

Non-paraffins: Other organics, for example, number of esters, fatty acids, satiric acid, plasmatic acid, alcohols, and glycols suitable for energy storages, are also available for latent heat storage use. Non-paraffin organics is the largest category of common materials for phase change storage that have a wide variety of melting points and heats of fusion. Hale et al. [86] reported around 70 non-paraffin organics that have melting points in the range of 7 to 187 °C, and heats of fusion in the range of 42 to 250 kJ/kg. Fatty acids have melting points suitable for heating applications and have heat of fusion values comparable to those of paraffins and salt hydrates. They exhibit excellent melting/freezing characteristics without any supercooling. Their major drawback is their cost which is about three times higher than paraffins [101]. One of the most promising organic phase change materials is the high density polyethylene (HDPE), which is manufactured by polymerization of ethylene gas [85].

2.6.2 Inorganic Phase Change Materials

Salt hydrates are some of the oldest and most extensively studied group of PCM for their use in latent heat thermal energy storage systems. They consist of salt and water which combine in a crystalline matrix when the material solidifies. There are many different materials that have melting ranges from 15 to 117 °C [98]. Salt hydrates have three modes of melting; congruent, incongruent, and semi-congruent. The most attractive properties of salt hydrates are:

- (i) High heat of fusion
- (ii) Small change of volume during phase transition
- (iii) Sharp well-defined melting points, this maximizes the efficiency of a heat storage system
- (iv) Relatively high thermal conductivities compared to organic PCM. This could increase heat transfer inside and outside the storage unit
- (v) Moreover, salt hydrates are generally compatible with plastic containers, except that most plastics are not serviceable at the melting point of some of the high-melting PCM, and
- (vi) Low cost and easy availability of salt hydrates make them commercially attractive for heat storage applications. Two of the least expensive and most available salt hydrates are $\text{CaCl}_2 \cdot 6\text{H}_2\text{O}$ and $\text{Na}_2\text{SO}_4 \cdot 10\text{H}_2\text{O}$. Many salt hydrates are sufficiently inexpensive for the use in storage [98].

On the other side, three major problems with most of these materials have been reported as:

- (i) One problem is segregation due to incongruent melting. Segregation is formation of other hydrates or dehydrated salts that tend to settle out and reduce the active volume available for heat storage. This problem could be eliminated by several techniques, such as use of gelled or thickening agents [102] though this process negatively impacts the heat storage characteristics of the mixture and the mixture still degrades with time [97], rotating storage devices for stirring, direct contact heat transfer [101], and encapsulation of the PCM in a small volume to reduce separation. The mechanism of such phenomena is that water of crystallization released during thawing is not sufficient to dissolve the solid present (the resulting solution is supersaturated at the melting temperature). The solid settles down at the bottom of the container due to its higher density. During the reverse process, i.e. crystallization, a substantial part of the settled salt is unable to come into contact with water required for its crystallization. Therefore, the compound of the solid is not the same as that of the liquid. The energy density of the storage reduces after several charge and discharge cycles due to this phenomenon of incongruent melting.
- (ii) Supercooling is the second problem common to many salt hydrates. During cooling, the solidification does not take place at the melting temperature due to the low rate of crystal formation. Consequently, the solution has to be supercooled, i.e. cooled below the melting temperature by several degrees, until a reasonable rate of nucleation is achieved. Due to supercooling, the PCM does not discharge the stored thermal energy at the melting temperature as expected. This problem has been avoided in several salt hydrates through promoting nucleation by one of the following means: adding small quantities of a nucleating material so that crystals may start growing around it; mechanical means such as a rough container walls to promote heterogeneous nucleation; and keeping in the PCM a "cold finger" or a region which is allowed to remain cool when the rest of the PCM has melt. Lane [102] offers a comprehensive listing of nucleating materials for most common salt hydrates.
- (iii) Another problem of salt hydrates is their tendency to cause corrosion in metal containers that are commonly used in thermal storage systems [97]. Compatibility of PCM and container should always be checked before use.

2.6.3 Eutectics

Eutectics are mixtures of two or more salts which have definite melting/freezing points, and they can be classified as organic, inorganic, and organic-inorganic eutectics. Their behaviour is analogous to congruent melting salt hydrates, and has great potential for thermal energy storage applications [101]. Eutectics nearly always

melt and freeze without segregation since they freeze to an intimate mixture of crystals, leaving little opportunity for the components to separate [98].

Frame 2.1: Desirable properties of latent heat storage materials [94, 95]

Thermo physical properties

- Melting temperature in the desired operating temperature range
- High latent heat of fusion per unit volume, so that less volume of the container is required for storing a given amount of energy
- High density, so that a smaller amount of PCM can be used.
- High specific heat to provide for additional significant sensible heat storage effects
- High thermal conductivity of both solid and liquid phases, so that the temperature gradients required for charging and discharging the storage material are small
- Small volume change, on phase transformation and small vapour pressure at operating temperatures to reduce the containment problems
- Congruent melting, the material should melt completely so that the solid and liquid phases are identical in composition. Otherwise, the difference in density between solid and liquid may cause segregation resulting in changes in the chemical composition of the material

Kinetic properties

- High nucleation rate to avoid super cooling of the liquid phase i.e. the melt should crystallise at its thermodynamic freezing point. At times, the super cooling may be superposed by introducing nucleating agent or a "cold finger" in the storage material
- High rate of crystals growth, so that the system can meet demands of heat recovery from the storage system

Chemical properties

- Chemical stability
- Complete reversible freezing/melting cycle
- No degradation after a large number of freezing/melting cycles
- Non-corrosiveness to construction materials
- Non-toxic, non-flammable and non-explosive materials for safety

2.6.4 Salt Mixtures

The composite salt/ceramic thermal energy storage media concept offers the potential of using PCM via direct contact heat exchange and, therefore, the potential of significant cost improvement through elimination of heat exchange materials, and reduction of storage material and containment vessel size. This salt ceramic approach may be explained as micro-encapsulation of a PCM within the submicron pores of a ceramic matrix [101]. The liquid salt is retained within the solid ceramic

network by surface tension and capillary forces. Heat storage occurs as latent heat of the PCM and as sensible heat of the basic ceramic material and PCM. Therefore, the use of salt/ceramic materials represents not a pure latent heat but a latent/sensible hybrid storage concept [101]. A novel energy storage system consists of n-octadecane retained by capillary forces in a porous silica support [83]. This configuration eliminates the expensive heat exchange surface, provides higher energy density, and gives higher rates of energy storage and release [98].

2.6.5 Multi Grade Phase Change Materials

Sometimes the isothermal storage level might be disadvantageous such as the following cases [112]:

- 1) If the energy to be stored is available at much higher temperature level than the melting point of the heat storage material, the storage occurs at lower temperature level than that of the source.
- 2) A worse case may occur if the melting point of the PCM is higher than the temperature level of the energy source. Then there is no latent heat storage and a large amount of heat may be lost.

These cases may occur during solar energy storage when the temperature of the heat transfer medium from the solar collector is higher than the melting point of the PCM applied (the storage is realized at not sufficiently high temperature) or the temperature of the transporting medium is lower than the melting temperature of the PCM (there is no storage). There are three possibilities to overcome these problems [112]:

- 1) Application of materials with high specific heat. The average specific heat of solid material is $3 \text{ (kJ.kg}^{-1}.\text{K}^{-1})$, the specific heat of water is $4.18 \text{ (kJ.kg}^{-1}.\text{K}^{-1})$, therefore, a large volume must be involved in the storage process
- 2) Application of two phase change materials; one with a lower melting point, and other with a higher melting point, then the storage volume can be reduced but two separate storage tanks are necessary
- 3) Application of crystal hydrates which crystallizes in two different hydrate forms and the two forms have different melting points which are called two grade phase change materials

Calcium chloride may be a promising material to accomplish the third way mentioned above. Calcium chloride forms different crystal hydrates ($\text{CaCl}_2.6\text{H}_2\text{O}$, $\text{CaCl}_2.4\text{H}_2\text{O}$, $\text{CaCl}_2.2\text{H}_2\text{O}$) and they have different melting points of 29.9, 43.3, and 130 °C respectively [112]. If a PCM of low phase change temperature is selected the process of phase change will take place even at low solar gain. Thus the number of days, when the latent heat storage can be used will be high during the year.

However, the stored heat is less valuable, due to the low temperature level. Selecting a higher phase change temperature, the process of phase change will take place only at a higher solar gain. The number of days, with higher solar gain is less, thus the period in which latent heat storage can be used is short. On the other hand, the stored heat is much more valuable, due to the high temperature level. A double grade phase change materials combines the advantages of both versions.

Another novel approach that has been suggested by Watanbe et al. [116] includes the use of three types of PCM with different melting temperatures. This allows for maximum use of the heat transfer medium energy.

2.7 Heat transfer in PCM regenerators

The heat transfer process between the latent heat storage units and the heat transfer fluid during charging and discharging cycles greatly depends -among several other factors- on the type of heat exchanging surface. The crystallising (nucleating) and thickening agents, which are added to some PCM to prevent supercooling and phase segregation, lower the thermal conductivity of the PCM and increase the viscosity which inhibits convection motion in the liquid PCM [100, 106]. Therefore, an important disadvantage of the common materials used in solid-liquid phase change (paraffin, hydrated salts) is their low thermal conductivity which makes them act as self-insulator materials. That is; PCM solidifies on the interfacial heat transfer surface with the working fluid during the discharging process and acts as self-insulator. Enormous amount of research effort so far has been devoted to overcome the inherent handicaps mentioned above via some kind of heat transfer enhancement techniques:

- (a) Active methods such as agitators/vibrators, scrapers and slurries [102]
- (b) Using microencapsulated PCM.
- (c) Using PCM containing dispersed high conductivity particles or Lessing rings [108]
- (d) Using PCM graphite composite material [107]
- (e) Using extended surfaces such as fins and honeycombs [100, 109, 110]
- (f) An efficient configuration of PCM is encapsulation in hollow shells (e.g. tubes, pipes, spheres, cans with small dimensions), which are then used in a packed or fluidized bed configuration. Using such passive heat exchangers that typically consist of a large number of encapsulated elements increases the effective heat transfer area, then enhances the heat transfer rate, and a great thermal stratification in the storage could be achieved. These benefits are more obvious when the dimensions of the elements are small [85]. Phase change materials perform best in containers that –when combined PCM- total one inch (25.4 mm) in diameter or width [111], however, this statement can not

be generalized. Steel and polyethylene are common packaging materials,

- (g) Using the composite salt/ceramic thermal energy storage media concept which offers the potential of using PCM via direct contact heat exchange. A direct contact heat exchanger with an immiscible heat transfer fluid moving in the PCM has eliminated the permanent heat exchange surface and has been confirmed to prevent phase separation of the PCM [113, 114].
- (h) Using a porous metal matrix such as aluminum matrix [115] as a way of improving the performance of the storage system, enhancing heat conduction without reducing significantly the stored energy

The type of heat exchanger surface strongly influences the temperature gradients of the PCM in the charging and discharging of the storage. Proper designing of latent heat energy storage systems require quantitative information about the heat transfer and phase change processes inside the PCM units. Among different geometrical configurations of the PCM capsules, it is found that spherical shape has received the utmost attention of research work in literature. Some authors attributed their interest in spherical capsules to the fact that the sphere has the largest volume to surface area ratio [126], although self-insulation during solidification might hinder full exploitation of the storage, which is rather in favor of large surface area per unit volume. Hence sphere size should not be too large as mentioned earlier. Further considerations for optimum sphere size depend on handling, energy density, and pressure drop [126]. Singh et al. [121] have clarified experimentally that if packing of spherical and other shapes like cubes and tubes are compared physically, it appears that during fluid flow in the bed, fluid film may remain in contact with the maximum portion of the surface area of spherical elements as compared to other shapes. In the case of non-spherical shapes, as the working fluid strikes the surface, it may get detached from the packing surface due to presence of sharp corners and edges. Therefore lesser contact area may be available for heat transfer for non-spherical shapes.

Besides, non-spherical shapes have also surface contact between material elements which reduces the area available for heat transfer. Therefore lower values of heat transfer may be expected for other non-spherical configurations as compared to the spherical material elements. Singh et al. [121] have conducted an extensive experimentation to investigate the effect of the system and operating

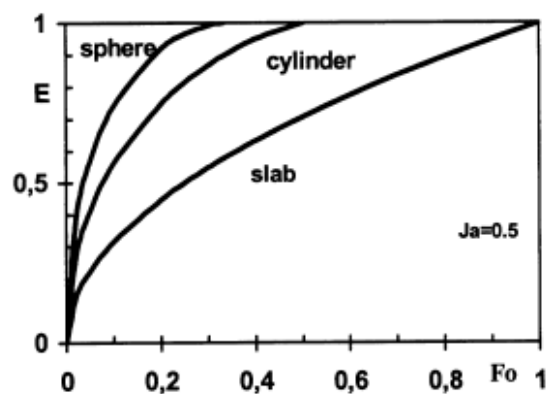


Figure 2.3: Energy released versus time for different geometries [124]

parameters on the heat transfer and pressure drop characteristics of packed bed solar energy storage system with large sized elements as a storage material of five different shapes. It was clear from the experimental results that the spherical shape has the highest heat transfer coefficient and the second lowest friction factor coefficient amongst the other five shapes.

Standish and Drinkwater [122] reported that the element shape is a significant variable in gas liquid flooding in packed column. Gauvin and Katta [123] emphasized that the major operating cost in packed bed system is directly related to the pressure drop in the bed, which can not be predicted with reliability when the elements in the bed depart from the spherical shape. Barba and Spiga [124] analyzed the behavior of encapsulated salt hydrates, used as latent energy storage in a domestic hot water tank. The discharge process of the (PCM) was analyzed for three different geometrical configurations, i.e. considering the PCM encapsulated in slab, cylindrical or spherical polyethylene containers. The influence of the geometry and the Jacob number which is defined as:

$$Ja = c_s (T_m - T_{pcm}) / H \quad (2.3)$$

where T_{pcm} is the wall temperature of the cooled PCM cell surface, on the ending time of solidification were investigated. Spherical capsules, operating with high Jacob numbers (not too high to compromise the efficiency of the latent heat storage system) exhibited the largest energy density and the most rapid charge and release times as shown in figure (2.3).

2.8 Desalination with humidification-dehumidification technique

Basin type solar stills exhibit two main draw backs. The first is the combined loss of evaporation, convection and radiation energy received by the condenser, which accounts for most of the energy lost to the surroundings. Partial recovery of this heat for feed preheating or to be stored for extending plant the production after sun-set has been an essential approach for enhancing the performance of solar distillers. Practically full recovery is almost impossible due to thermodynamic irreversibilities. The technical and economical viability of the energy recovery system should be justified with the additional yield gain.

The second drawback is the transient trend of water production and long idleness of the plant after sunset and during cloudy periods when the ambient temperature is low and the heat sink is promising (i.e. cooling seawater temperature in the condenser is low). The limited heat capacities of these distillation systems can not support the plant operation during night or cloud periods. This drawback can be

overcome by applying a thermal storage capacity to the system. Likely, the technical and economical viability of energy storage (e.g. sensible or latent heat storage) in comparison with only daily production has to be justified with the additional yield gain.

A break through in solar desalination was introduced based on the humidification-dehumidification (HDH) principle. The humid air distillation process has already been developed and introduced first by the University of Arizona through a pilot plant work performed from 1956 to 1963, which led to construction of an experimental pilot solar energy multiple-effect humidification (MEH) plant in 1963. Multi-Effect Humidification (MEH) process was further developed over the years and a few units were constructed and tested in different countries [2].

This technique leads to a major improvement in the efficiency and compactness of solar desalination units. The efficiency of energy utilization is increased in HDH technology due to the better control over the evaporation and condensation operations. There are several advantages of HDH process as a small-scale desalination system. It is simple, modular and flexible in scale-up, works under atmospheric pressure with below-boiling temperatures, ideal for utilization of low-grade energy and waste heat resources, can follow a highly varying input thermal power supply without upset, inexpensive construction materials can be used, and requires moderate investment and operation costs as well as low technical skills for operation and maintenance.

Khedr [130] performed a techno-economical investigation on HDH desalination process and compared it with other conventional processes. The results showed that the economics of the process is quite satisfactory for capacities of more than 10 m³/day, which is suitable for remote arid areas. Garg et al [131] reported that the HDH technique is suitable up to 90-m³/day capacity, and can be developed in coastal arid zones of the country where industrial development is impeded by inadequate or unreliable water supplies.

An extensive review of the literature on HDH systems was reported by Al-Hallaj and Selman [2] Bourouni et al [129], and Narayan et al [149]. It is meaningless to repeat the previous review, thus the present study uses the previously mentioned literature surveys as its point of departure and consequently will focus on abstracting the important results for the present work and to discuss the design limitations and problems experienced with the HDH system components and potential improvements.

2.8.1 Classification of HDH systems

The solar humidification-dehumidification (HDH) processes, also called the multiple-effect humidification-dehumidification processes (MEH) fall under three main

categories. The first category is based on the cycle configuration; (a) closed-water open-air (CWOA) cycle, in which ambient fresh air is withdrawn and discharged to the surroundings for each HDH cycle, while feed brine is recirculated and concentrated, or (b) closed-air open-water cycle (CAOW), wherein air is recirculated in a closed loop through the evaporator and condenser, while feed saline water is withdrawn and discharged to the surroundings for each HDH cycle as shown in figure (2.4). The air can either be circulated by natural convection or forced convection, which is the classification basis for the second category. The third classification category distinguishes between HDH systems based on the type of working medium to be heated whether water or air.

2.8.2 Principles of operation

Figure (2.4) shows a schematic diagram of a solar-driven humid air distillation plant. The evaporation, condensation, and heating processes in HDH technique are separated in three main components; humidifier (or evaporator), dehumidifier (or condenser), and external thermal energy source, such as solar flat plate collector or waste heat recovery. In HDH systems, air continuously flows in closed/open loop cycles, as a carrier medium, to transfer the generated water vapour from the evaporator to the condenser, where it is condensed back into highly purified fresh water. Usually, HDH plants operate at ambient pressure. By this means, simple and robust design for decentralised applications is guaranteed. Moreover, capital as well as maintenance costs are thus reduced.

In the humidifier, which is working on the cooling tower theory, the hot water from the storage tank or flat plate collector is gently sprayed, in tiny droplets, over the top of the humidifier and trickles down by the gravitational force to the brine collecting basin. Due to spreading of hot water over the packing elements surfaces while flowing down, its surface area in contact with countercurrent flowing air is greatly increased. The water transfers part of its heat and mass to the rising air, which becomes humid and hot, while water cools down through the column. The hot humid air is directed to a cooling surface or the condenser to be partly dehumidified and cooled, while preheating the feed saline water through a heat exchanger arrangement.

The air is circulated between evaporator and condenser by natural or forced convection. As humid air is less dense than dry air, natural convection operation is possible under the action of both temperature and humidity gradients along the column height in both evaporator and condenser. The concentrated brine may be recirculated to the storage tank or mixed with the saline feed water to recover its sensible thermal energy content. The feed water temperature is further increased to 80-85 °C at the inlet of the packed column through an external heat source. As the external heat needed is relatively low due to recovery of both latent heat of condensation and part of the concentrated brine thermal heat content, the external

heat source can be from solar flat plate collector or from waste heat to compensate for the sensible heat losses in the cycle.

The Gain Output Ratio (GOR) which is defined as the ratio of the energy consumed in the production of the condensate to the energy input by external heat source is always used as a measure of the overall performance of HDH units.

$$GOR = \frac{\dot{m}_d \cdot h_{fg}}{\dot{m}_{sw} \cdot c_{sw} \cdot \Delta T_{coll}} \quad (2.4)$$

where h_{fg} is the latent heat of condensation, and the subscript “sw” stands for feed seawater. Since the latent heat of condensation is recovered through the condenser

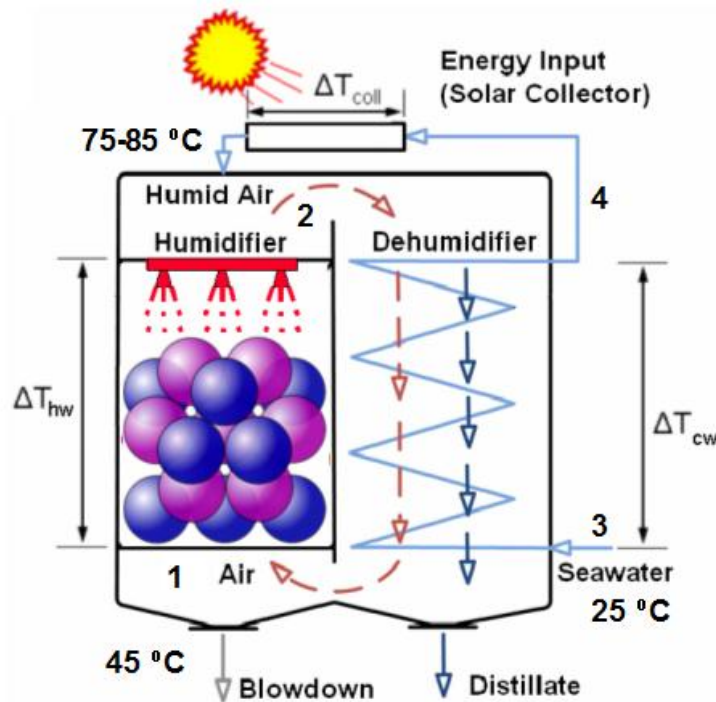


Figure 2.4: Schematic of the solar-driven HDH process without thermal storage

for preheating of the feed seawater, GOR should be greater than unity. The term “multiple effect humidification” used for these cycles is not in reference to the number of constructed stages, but to the ratio of heat input to heat utilized for distillate production (GOR>1) [2]. Typical GOR values for HDH systems range between 1.2 and 4.5, which correspond to specific energy consumption rates of 140

to 550 kWh/m³ of distilled water and 4 to 12 l/m².day of solar collector area, as reported by Narayan et al [149].

GOR is directly proportional to heat and mass transfer effectiveness in the evaporator and condenser or both the temperature drop of hot water in the evaporator (ΔT_{hw}) and temperature rise of feed seawater in the condenser (ΔT_{cw}) and inversely to the temperature jump in the solar collector (ΔT_{coll}). When the HDH system works efficiently, both the temperature drop in the evaporator and temperature rise through the condenser become high, which reduces the required temperature jump in the collector, i.e. the required energy input to produce same amount of distillate.

The heat and mass transfer rates in the evaporator and condenser depend on the following parameters, see the finite element illustration in figure (2.5):

1. heat and mass transfer coefficients
2. gas-liquid contact area
3. driving forces for heat and mass transfer (i.e. temperature difference ΔT , and water vapor concentration difference ΔC)

The driving force for heat transfer is the temperature difference between the liquid film and the bulk of the carrier gas. For mass transfer, it is due to the difference in water vapor pressure (or vapor concentration C) on the liquid film surface and partial pressure of water vapor in the bulk gas. The gas liquid contact area is a function of the geometric configuration of the exchanger, packing shape and size, and liquid and gas flow rates.

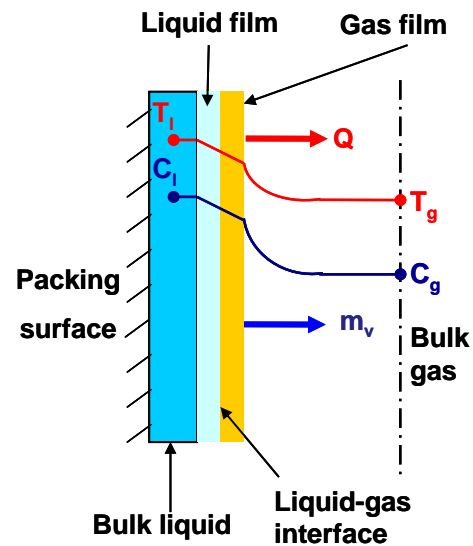


Figure 2.5: Finite element at the liquid-air interface in direct contact heat and mass exchangers

2.8.3 Lumped model analysis

In this section a simplified lumped model of a HDH system as shown in Figure (2.4) will be developed to explain how it works. Such a framework might help in interpretation and making sense of literature results, which will be presented in the following parts of this chapter.

2.8.3.1 Heat and mass balances

Applying thermodynamic laws on the evaporator, condenser, and solar heater as shown in figure (2.4) and assuming no heat losses in the HDH cycle, the heat and mass balances can be written as:

Humidifier

$$\text{Mass balance:} \quad \dot{m}_{sw} + \dot{m}_a \cdot w_{a1} = \dot{m}_b + \dot{m}_a \cdot w_{a2} \quad (2.5)$$

$$\text{Heat balance:} \quad \dot{m}_{sw} \cdot h_{sw2} + \dot{m}_a \cdot h_{a1} = \dot{m}_b \cdot h_{sw1} + \dot{m}_a \cdot h_{a2} \quad (2.6)$$

Where the subscripts a , b , 1 , and 2 stand for air, brine or blow down, bottom and top of the evaporator/condenser respectively, while w_{a2} and w_{a1} are the moisture contents of the air entering and leaving the condenser respectively.

Dehumidifier

$$\text{Mass balance:} \quad \dot{m}_{dist} = \dot{m}_a (w_{a2} - w_{a1}) \quad (2.7)$$

$$\text{Heat balance:} \quad \dot{m}_a \cdot (h_{a2} - h_{a1}) + \dot{m}_{sw} \cdot (h_{cw4} - h_{cw3}) = \dot{m}_{dist} \cdot h_{dist} \quad (2.8)$$

where the subscript “ $dist$ ” stands for distilled water, while h_{cw3} and h_{cw4} are the enthalpies of the cooling seawater water entering and leaving the condenser respectively.

Solar heater

Heat balance: The useful energy obtained from the collector can be written in the form:

$$\dot{Q}_{in} = \dot{m}_{sw} \cdot c_{sw} \cdot \Delta T_{coll} = I_T \cdot A_{coll} \cdot \eta_{coll} \quad (2.9)$$

Where I_T represents the solar global irradiation intensity (W/m^2), A_{coll} is the collector area (m^2), and η_{coll} is the collector thermal efficiency. Based on various commercial collectors performance data, the efficiency is assumed to be represented as:

$$\eta_{coll} = 0.75 - 0.025 \left(\frac{T_4 - T_{amb}}{I} \right) \quad (2.10)$$

The enthalpy and humidity of the saturated air depend on its temperature at constant pressure and can be calculated using the following empirical correlation [132];

$$h_a = 0.00585T_a^3 - 0.497T_a^2 + 19.87T_a - 207.61 \quad (2.10)$$

$$w_a = 2.19 \cdot 10^{-6}T_a^3 - 1.85 \cdot 10^{-4}T_a^2 + 7.06 \cdot 10^{-3}T_a - 0.077 \quad (2.11)$$

where T_a is the saturated air temperature in °C.

HDH unit sizing

As a common practice, the number of transfer units (NTU) will be used as a measure for the humidifier size (see appendix D1), while the condenser is assumed to have the same size as the humidifier for symmetrical design of the HDH unit. The NTU can be related to the performance characteristic (KaV/L) (see appendix D1). Based on the steady state experimental analysis, Nawayseh et al. [159] has developed the following correlation for forced convection:

$$KaV / L = 0.52(L/G)^{-0.16} \quad \text{for forced draft} \quad 0.1 < L/G < 2 \quad (2.12)$$

It has been reported by Al-Hallaj and Selman [2] that this empirical correlation was found to describe the mass transfer well in different humidifiers constructed in Jordan and Malaysia, and therefore will be used for the lumped simulations presented in this section.

Assumptions

For solving the lumped model, the following assumptions were made:

- All the energy consumed in the evaporator is utilized for water evaporation
- All the evaporated water is condensed in the condenser and the latent heat of condensation is recovered by the feed seawater, hence the temperature rise of feed seawater in the condenser is equal to the temperature fall in the evaporator
- The outlet water temperature from the evaporator is constant at 45°C, this implies that the evaporator size will be adopted to maintain this temperature constant under different boundary conditions
- The outlet air temperature from the evaporator (inlet to the condenser) is the mean value between inlet and outlet hot water temperatures
- The outlet air temperature from the condenser (inlet to the evaporator) is 3°C higher than the inlet cooling seawater temperature to the condenser

- Air circulates in a closed loop, hence is assumed to be fully saturated with water vapor at local temperatures
- Feed seawater is equal to ambient temperature and it is constant at 25°C
- Fresh water production rate is prescribed at a constant value of 1000 l/ day, while the HDH unit size, air flow rate, and solar collector area have to be adopted to obtain same distillate rate under different boundary conditions
- Solar irradiation intensity is constant at 800 W/m²
- The solar collector area will be varied to maintain constant specific heat input per unit of feed seawater flow under different mass flow rates, i.e. constant temperature jump of feed seawater through the collector

2.8.3.2 Results of lumped model

All calculations of this simplified model were done using Excel. Figure (2.6) shows the influence of hot feed seawater mass flow rate on the inlet hot water temperature and GOR. As the seawater flow rate increases the inlet hot water temperature entering the evaporator (T_2) decreases (i.e. , as the outlet water temperature from the condenser decreases with increasing mass flow rate due to the assumption of constant distillation/condensation rate. To maintain constant distillation rate with decreasing the inlet hot water temperature, this is compensated by increasing the air mass flow rate, while keeping the water temperature jump through the collector constant by increasing the collector area linearly with the water mass flow rate, as shown in figure (2.7). Since the specific heat input per liter of water mass flow is constant, GOR decreases with decreasing the water mass flow rate, as the energy input to the system increases at a constant distillation rate.

However, since the outlet air temperature from the evaporator and its humidity content depend on the inlet hot water temperature, for obtaining a constant distillate rate the air mass flow rate should be increased with increasing seawater mass flow rate to substitute the temperature fall of inlet hot water. This fact is described by equation (2.7) and shown in figure (2.7).

Following equation (2.12), the effect of feed seawater mass flow rate on the NTU is shown in figure (2.8) as a function of air to water mass flow ratio. Results show that the performance of the unit (in terms of low NTU) increases with inlet hot water mass flow rate below 850 l/m²/h under the prescribed boundary conditions. Beyond this limit, it is observed that the performance of the unit decreases when the hot liquid flow rate increases. A critical air to water mass flow rate corresponding to the minimum NTU can be determined from the plot, as the humidity content is varying exponentially with air temperature (see figure 3.4). At this value, a maximum amount of evaporated water can be obtained at a water recovery ratio of 5% (the ratio between distillate rate and feed seawater mass flow rate).

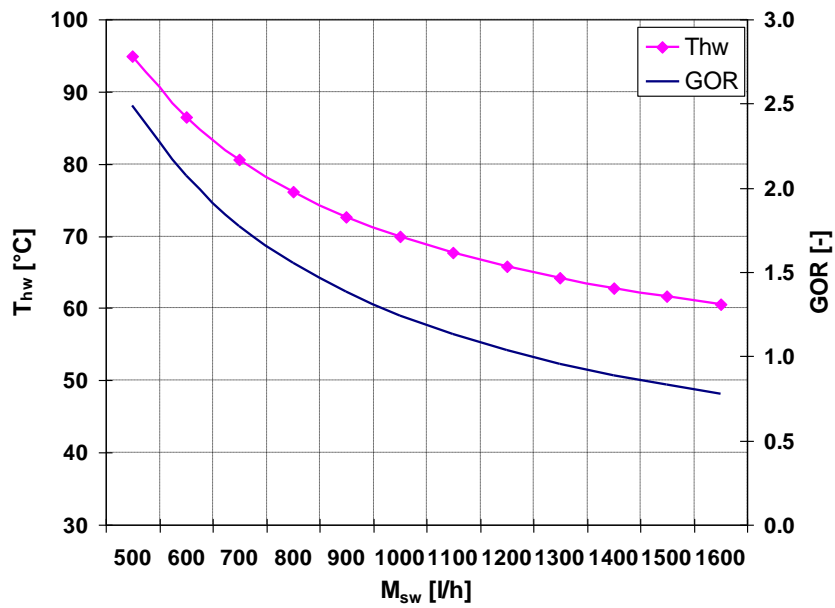


Figure 2.6: Effect of the feed seawater flow-rate on inlet hot water temperature and GOR

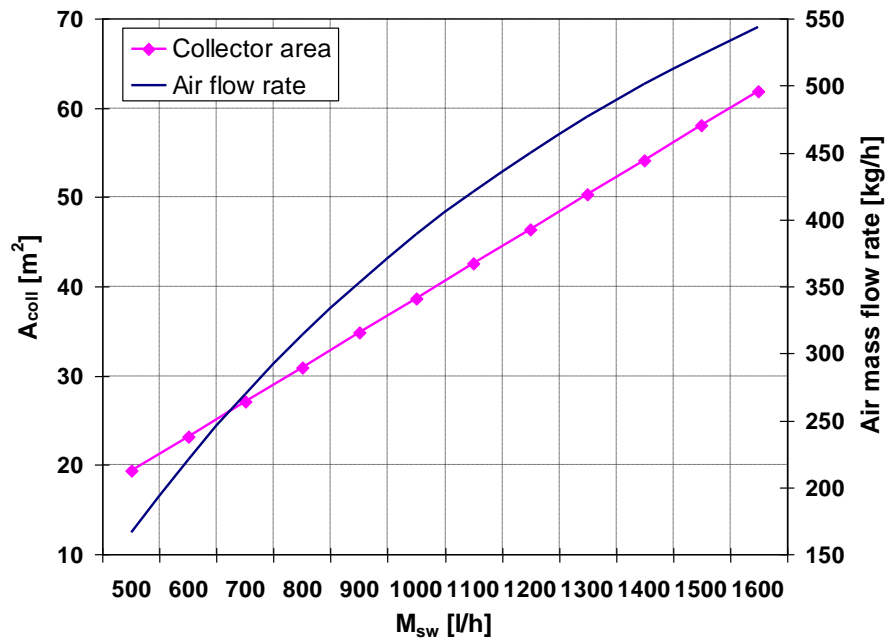


Figure 2.7: Effect of the seawater flow-rate on the collector area and air mass flow rate under constant specific heat input per unit mass of seawater

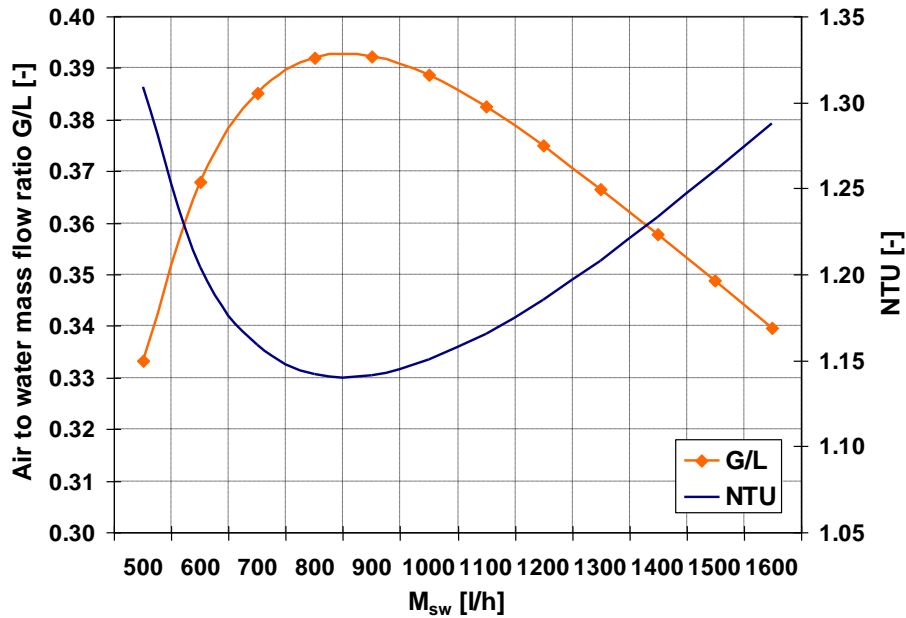


Figure 2.8: Effect of the feed seawater flow-rate on the air to water mass flow rate ratio and humidifier size factor (NTU)

2.8.4 Review of Performance

Different configurations of HDH systems have been developed and examined in the literature. It is essential to understand how specific parameters affect the cycle's performance and how to compromise between the efficiencies of different components in the system. Consequently, presentation of the influencing factors will be reported in the following section.

2.8.4.1 Effect of feed seawater mass flow rate

As mentioned above, the overall performance of the HDH system or GOR is not only dependent on the individual effectiveness of different single components but also on their mutual influences on each other. As noted earlier (in the lumped model analysis), the effect of feed water flow rate on the productivity of the HDH unit was shown by Al-Hallaj and Selman [2] to be complex due to its combined effects on the operating temperature and efficiency of the solar collector, humidifier, and condenser. Increasing feed flow rate reduces the operating temperature, which reduces the production of the unit. The heat and mass transfer rates in the humidifier and condenser decrease at low operating temperatures.

On the other hand, the efficiency of the collector, humidifier and condenser increase at higher feed flow rate. In the humidifier, higher water flow rate will improve both the mass transfer coefficient and the degree of wetting of the packing. Al-Hallaj and Selman [2] developed an analytical semi-empirical simulation model for the HDH system without thermal storage, and predicted its output in terms of the distillate rate. The simulation results have shown a maximum production rate at 0.013 kg/s of water flow rate, as shown in figure (2.9), due to combined effects of feed flow rate.

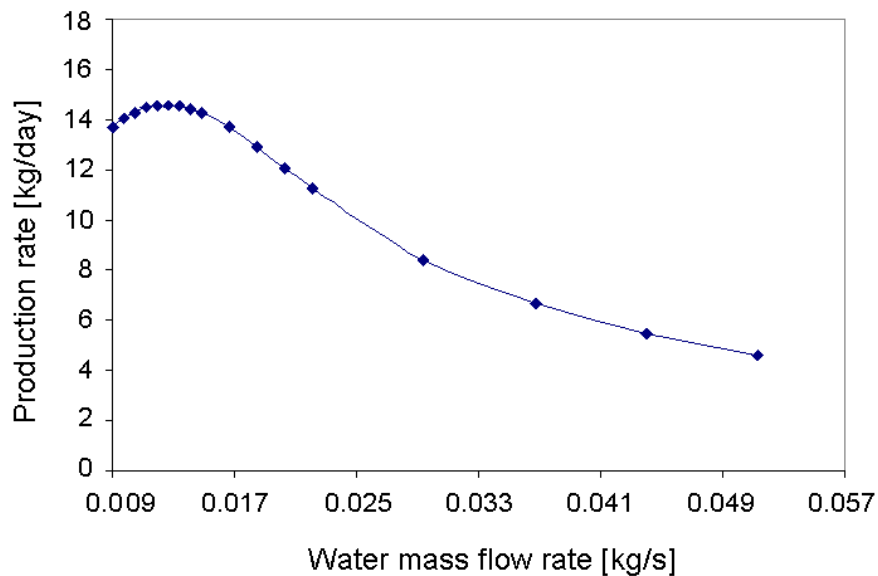


Figure 2.9: Effect of the feed water flow-rate on the daily production of the HDH desalination unit [132]

Al-Enezi et al [142] studied experimentally on a global level the characteristics of HDH process as a function of operating conditions. A small capacity experimental system composed of a packed bed humidifier, a double pipe glass condenser, a constant temperature water circulation tank and a chiller for cooling water was used for the study. As shown in figure (2.7), the water production was found to depend strongly on the hot water temperature. Also the water production was found to increase with the increase of air flow rate and the decrease of cooling water temperature. They emphasized that the distillate rate decreases with the increase in the feed seawater flow rate.

Al-Enezi et al [142] clarified that increasing the hot water flow rate has two opposite effects on the system performance. The first is the decrease in the system operating temperature due to the increase in water flow rate at constant input energy through the heat supply. This effect reduces the driving force for evaporation and, in return, the amount of product water. On the other hand, increasing the feed water flow rate

increases the heat and mass transfer coefficients and contact areas. The results shown in figure (2.10) indicate that this later effect is not as pronounced as the effect of reduction in the operating temperature caused by the increase in the feed water flow rate. The overall heat and mass transfer coefficients, as a function of the above mentioned parameters, were found to follow a similar pattern to the water production rate. These results come in agreement with the results of Al-Hallaj [2].

The given values for brine mass flow and both air and brine temperatures were determined for optimal operation of specific test stands of Al-Hallaj [2] and Al-Enezi et al [142]. The active surface of the used packing material plays an important role with a high dependency on brine mass flow and brine distribution over the given geometry. It is obvious that the brine mass flow must be reduced significantly to achieve satisfying GOR values. The theoretically optimal value would be a brine mass flow in the range of the distillate mass flow.

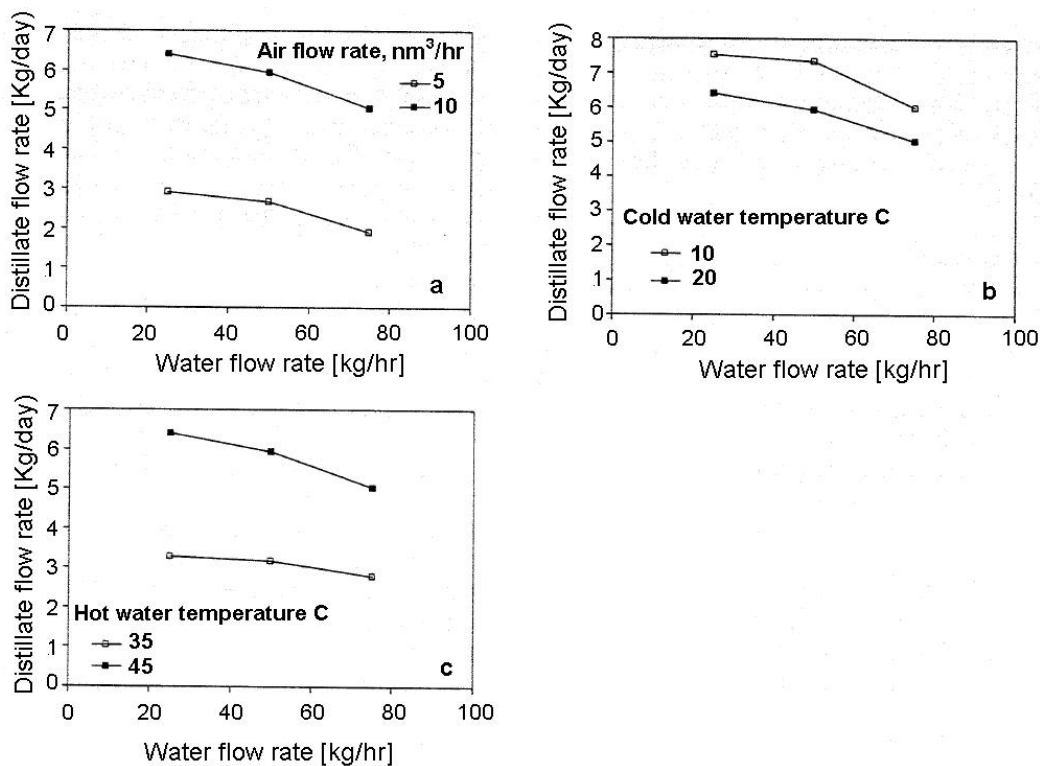


Figure 2.10: Variation of distillate flow rate as a function of the water flow rate: (a) air flow rate, (b) cooling water temperature, (c) hot water temperature [142]

2.8.4.2 Effect of air to water mass flow ratio

An important measure of HDH cycle performance is the *Terminal Temperature Difference* (TTD), which is the stream-to-stream temperature difference at both ends of the evaporator and condenser. Analysis based on the second law of thermodynamics reveals that by decreasing the TTD the plant performance is enhanced due to reducing entropy losses in the system. The TTD depends on the heat capacity flow rates of air and water in the system. It has been clearly observed from the lumped analysis in figure (2.8) that the air to water mass flow rate ratio strongly affects the system performance, as the heat recovery rate and inlet hot water temperature are drastically influenced by varying this ratio.

An interesting approach has been presented by Müller-Holst [5] to enhance heat recovery and reduce the TTD in the system. The system uses free convection between vertical fleece mats as evaporator and vertically hanging heat exchanger plates as a condenser. Here, a multi-stage behaviour is reported by means of different self-establishing convection vortices between evaporator and condenser by removing the partition between both chambers to allow the hot humidified air to cut across the separation gap and enter the condenser at multiple points along the packed height. This way, under the naturally induced flow, air is extracted at various points from the evaporator and supplied to the condenser at corresponding points. This enables continuous temperature stratification by dividing the large temperature gradient (in case of inserting a partition between the evaporator and condenser) into small intervals, resulting in small temperature gap (i.e. TTD) to keep the process running with minimizing entropy generation. This in turn results in a higher heat recovery from the dehumidifier [149]. In fact, most of the energy needed for the humidification process is regained from the dehumidifier bringing down the energy demand to a reported value of 120 kWh/m³. This system has been commercialized in different capacities ranging from 1 to 10 m³/day by a water management company; Tinox GmbH.

Based on this concept, a pilot plant with direct flow through the collectors has been working almost without any maintenance or repair for a period of more than seven years on the island of Fuerteventura. Results from Fuerteventura for a distillation unit without thermal storage showed that the daily averaged heat recovery factor (GOR) was between 3 and 4.5. It was reported that a similar distillation unit in the laboratory at ZAE Bayern yielded a GOR of more than 8 at steady state conditions. The optimized module produced 40 l/h of fresh water, but it was shown that a production of 1000 l/day is possible when the unit was operated continuously for 24 hours. Based on a collector area of 8.5 m², the productivity of the optimized module was 13 l/m².d for a 24 h operation. It was realized that an improvement of the overall system efficiency could be reached by adding a thermal storage as alternate heat source, to enable 24 h operation of the distillation module. This was achieved by using extra collectors and hot water storage tanks. A similar suggestion has been made to

extend the operation of the unit constructed in Jordan and Malaysia to be operated in 24-h/d period by both Al-Hallaj et al. [132] and Nawayseh et al. [134].

Another approach for forcing the TTD to get narrow has been presented by Brendel [154]. He used a forced convection in a multistage evaporator/condenser set-up similar to Müller-Holst's [5] concept but this system was run at different brine mass flows to balance the heat capacity flows and yielding approximately 300 l/d. However, this plant is far too costly and too complex for application in isolated arid regions in developing countries.

2.8.4.3 Effect of air heating

The performance of the HDH system depends greatly on whether air or water is heated [149]. It has been shown in the previous section that not only water heating is essential but also hot water quality (i.e. inlet hot water temperature) at the entrance of the evaporator plays the most important role in identifying the system performance. Nevertheless, fresh water production efficiency can be enhanced with air heating in addition to water heating. It has been experimentally observed by Klausner and Mei [137] that the fresh water production rate increases when air is heated prior to entering the diffusion tower. However, it is a well known fact that solar air heaters are less efficient and less mature than solar water heating devices, which is directly reflected on the specific cost of energy harnessed by each of them.

Also, from the various literature studies [149], it was observed that air-heated systems have higher energy consumption than water heated systems. This is because sensible heat content of water, which is supplied by air in the humidifier, is not subsequently recovered from the water, unlike in the water-heated cycle in which the energy transferred to air is recovered in the dehumidifier.

The air heated systems have been reported in the literature can be either single (e.g. Abdel-Monem [145]) or multi-stage (e.g. Chafik [155]). Abdel-Monem [145] have experimentally investigated the effect of heating water and air on the performance of the HDH system illustrated in figure (2.11). The main parts of the laboratory system are: air heater, water heater, cooling tower (humidifier), and air cooler (dehumidifier). Both the feeding air and water are heated before they enter into the humidifier.

Within the operation range used in the experimental study, it was found that: the inlet hot water temperature to the evaporator has the most important positive effect on the productivity. Increasing both the inlet water and air temperature to the humidifier was better than if each were increased individually; and increasing both water and air temperatures is preferable than increasing their flow rates through the system to increase the distillate rate. Increasing the cooling water to airflow rate ratio and decreasing inlet cooling water temperature through the dehumidifier increase the

distillate rate. The system was not tested at out door to examine its performance under actual weather conditions.

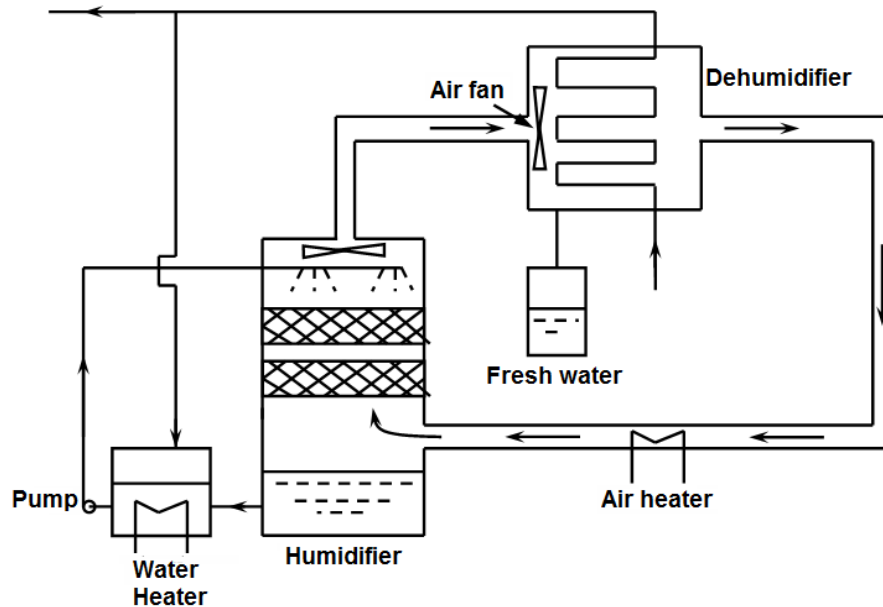


Figure 2.11: Schematic of HDD system by Abdel-Monem [145]

Chafik [155] developed a multiple effect heating-humidification (MEHH) solar desalination unit as shown in figures (2.12). The experimental setup integrates the solar air heater with a spray humidifier. A main feature of this desalination process is to conduct the heating/humidifying procedure in several stages in order to load the air with a high amount of water vapor and to reduce the volume of circulating air. The solar air heater and the humidifier were combined into a single multi-stage unit. After heating the air in the solar collector and humidified in the evaporator, it is passed through another stage for further heating and humidifying to attain higher humidity content. The air was recycled in a closed loop to increase the effectiveness of the system. In the multiple stages arrangement, absolute humidity values of 20% (by weight) and beyond can be attained in comparison with $< 6\%$ in a single stage process. Such a high concentration can be attainable in air heated up to 500°C , while it can be achieved in the MEHH process at operating temperatures less than 90°C . This process is represented on the psychrometric chart as depicted in figure (2.13). Air is heated in each stage, where at the end of the stage seawater is sprayed to humidify the air and bring it to the saturation condition. These processes of MEHH are represented by the zigzag lines. The highest red arrow on figure (2.13) represents the high temperature that has to be theoretically reached to attain the same humidity in a single stage cycle.

In comparison to other solar thermal multi-effect distillation processes, Chafik [155] reported that this unit is very costly while the integrated air collector-humidifier represents 40% of the total cost. The cost depends on the number of stages as shown in figure (2.14). It is worth to mention that the higher operating temperature has substantial negative influence on the solar collector efficiency. Moreover, we may expect that the heat and mass transfer coefficients between air and water are smaller than using a separated humidifier from the solar collector. This implies that multi-staging would have no significant impact on the energy efficiency of the system as the higher yield requires higher energy input as compared to single stage systems.

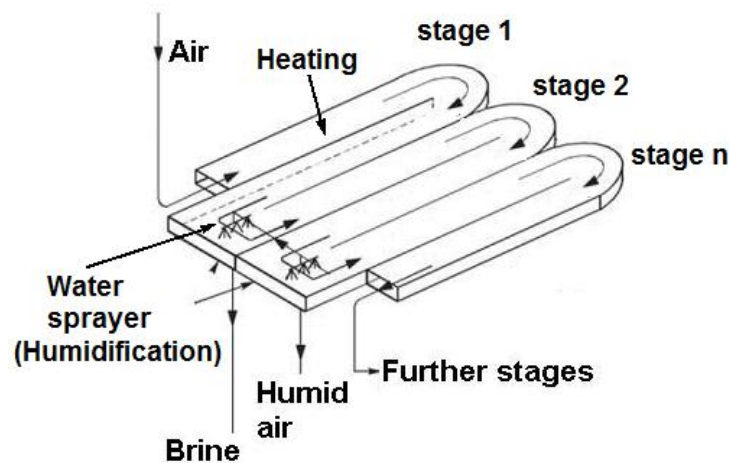


Figure 2.12: Multi effect of heating and humidification of the HDH desalination unit by Chafik [155] (modified)

2.8.4.4 Effect of packing height

At the Institute of Thermodynamics, Technische Universität München (TUM), in Munich, Germany, where most of the experimental and numerical investigations for the present work have been carried out, previous experimental studies based on an overall balances were done on small scale solar HDH desalination units; namely AQUASOL II.

Lex [143] has examined the use of modern industrial filling material in packed beds for a small-sized evaporation unit in solar desalination based on HDH technique under natural convection. In the framework of these investigations, a testing rig for porous evaporators was installed and a simulation model was developed. Detailed test series on both experimentation plant and simulation yielded useful results about the performance of the porous evaporator. The packing materials tested in this work

were; EnviPac Gr.1, \varnothing 32 mm, and VFF plastic Pall-Rings \varnothing 25 mm. Based on a parametrical study, Lex [143] summarized the results and design recommendations in table (2.1).

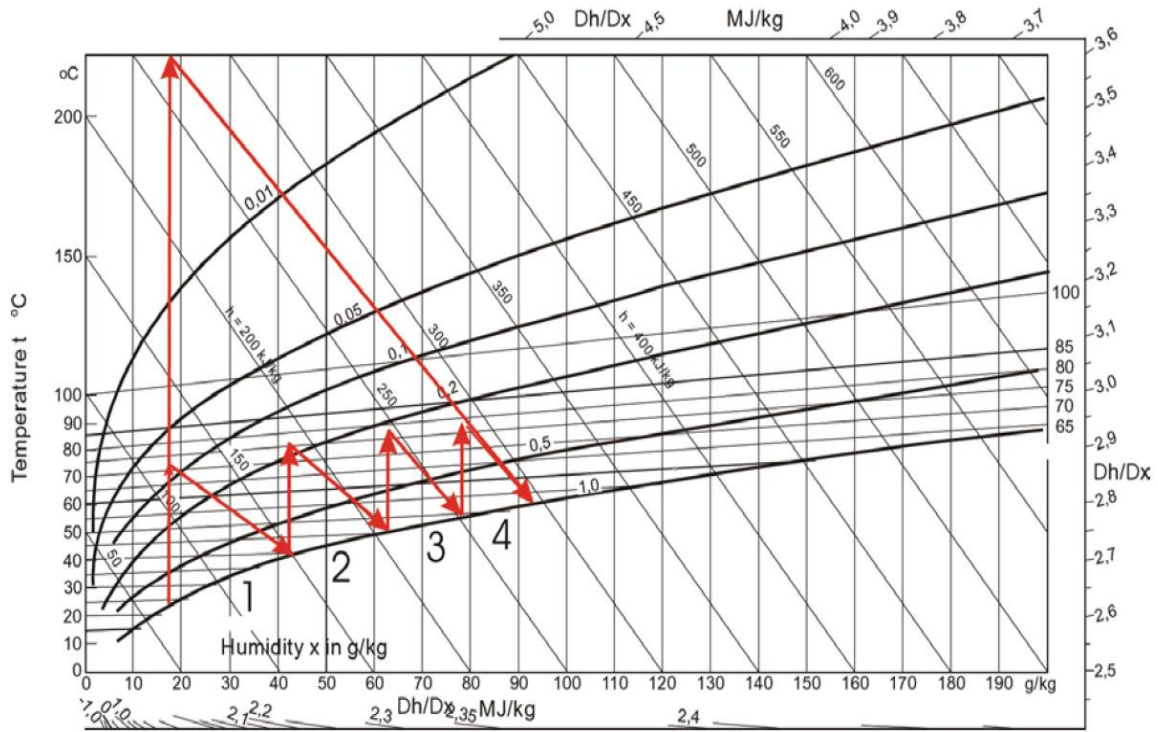


Figure 2.13: Representation of multi effect of heating and humidification by Chafik [155] on the psychrometric chart

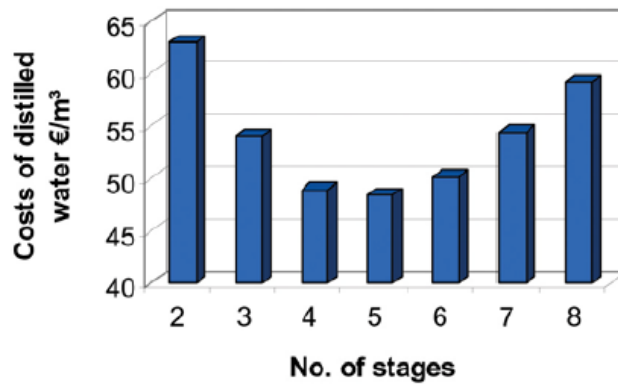


Figure 2.14: Specific water cost produced by the solar HDH desalination unit by Chafik [155]

The optimal value of feed water temperature was recommended as 85°C which also was confirmed in numerous preliminary tests for yielding optimal evaporation ratio at reduced calcination and gypsum formation effects. This range of water temperatures would enable using economical materials like polymers in construction of the units. As secondary effect the costs stay low.

The following figures (2.15) and (2.16) show temperature and evaporation rate dependency over the filling height of 300 mm for EnviPac at different brine temperatures, different inlet air temperatures, and a mass flow of 360 l/h. The dashed line delineates the evaporator outlet air temperature, hence temperature levels decrease over the evaporator outlet. Local temperature minima at a filling height of 200 mm depicts a local maximum in evaporation. Air develops a mass flow of 0,05 kg/s with an entrance relative humidity of 25 % and an outlet relative humidity of 95 %.

Table 2.1: Design parameters range of AQUASOL II [143]

Parameter	Range
Height of packing (H)	300 mm
Interfacial area	main factor to increase vapor production
Distribution system	nozzles
Brine inlet temperature	85 °C

For the temperature range given in this application a height of 300 mm was found to be ideal under natural draft operation. The irrigated area is variable and can be used as parameter to increase the humidity ratio in the exit air and hence its velocity. Indeed, the problem of pressure loss is evident and is leading to an optimum in filling height. The diagram in figure (2.16) shows the evaporation rate [l/h] at different filling heights with EnviPac filling material. It can be shown, that in this case, an optimum is achieved at 300 mm. These results reveal that free convection air flow in HDH units is very sensitive to the permeability of the bed. However, optimal filling height under forced convection with the same packing material would be significantly higher than with natural convection discussed above, as pressure loss may not be one of the main governing factors in the overall heat and mass balance.

It was reported that the distribution system was the main problem of the evaporation over the packed bed. The shower heads didn't show good results, the nozzles had good results in front of uniform irrigation. Against fouling and crystallization out of sea water they won't have a satisfying compartment in continuous use. The gutter distribution would have better properties in this point, but its fabrication cost was high. The realized distribution was irrigation by nozzles.

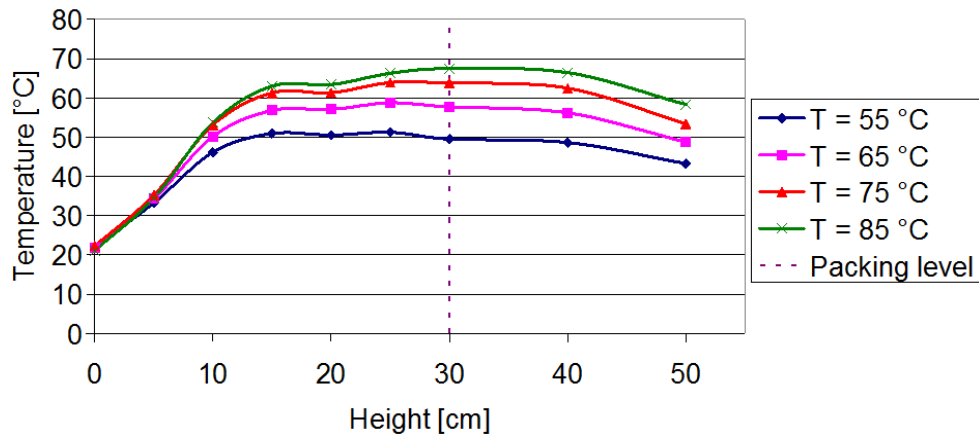


Figure 2.15: Height versus air temperature for EnviPac [128]

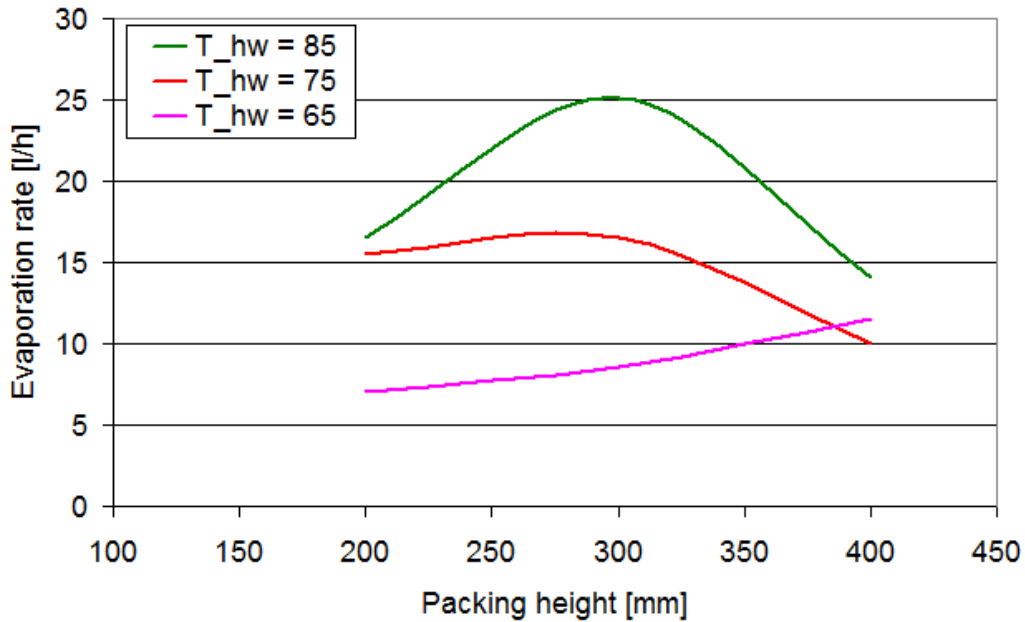


Figure 2.16: Height versus vapor production for EnviPac filling [128]

From previous sections it can be realized that the factors which influence the air HDH process are: the flow rate of air, the flow rate of water, the inlet temperature of water to the humidifier, the inlet temperature of air to the humidifier, the inlet temperature of cooling water to the dehumidifier, the flow rate of cooling water and water to air heat capacity flow rate ratio in the system. In the following subsections some of these parameters will be discussed entirely through discussing different

processes that take place in the HDH plant in light of previous investigations available in the open literature.

2.8.4.5 Type of carrier gas

A nonconventional approach for enhancing heat and mass transfer in both humidifier and condenser by using other carrier gases instead of air was reported by Abu Arabi and Reddy [133]. A lumped thermodynamic model analysis was performed on the effect of using different carrier gases besides air on the performance evaluation of HDH cycle. Hydrogen, helium, neon, nitrogen, oxygen, argon, and carbon dioxide were used. The investigations showed that hydrogen and helium give much better heat flux than air, while carbon dioxide and argon give much better mass flux. They concluded that carbon dioxide is recommended as a carrier gas in desalination units that based on HDH principle taking into account both heat and mass fluxes. Another advantage for using carbon dioxide is that it helps in reducing the calcium scale formation in these systems [133].

2.8.5 Air dehumidification

The condenser device may utilize either a direct contact heat exchanger between fresh cooling water and the humidified air, or condensation on a cooled surface, identical to a shell and tube heat exchanger, flat-plate heat exchangers and finned tube heat exchangers. Non-contact or surface type condensers have been widely used in HDH units for in-line preheating of feed seawater through recovery of latent heat of condensation. In this case, the cooling medium (i.e. feed seawater) flows counter-currently through a bank of tubes where it gets heated up by the condensed vapour upon the outer surface of the tubes. This design integrates both the condenser and pre-heater device in one heat exchanger, as the cooling medium is separated from the condensed vapour. However, due to existence of non-condensable gases, low effectiveness of this type of condensers may be cited as the major potential drawback.

Literature on HDH systems show that it is the condenser rather than the evaporator, which limits the productivity of these units, so more attention is needed on the proper design and selection of condenser. It was noticed by Gahin et al. [144] that, in open air / closed water HDH cycles, the water evaporated is almost double the water condensed. This leads to the consideration of the use of more than one effect or increase the heat transfer surface of the condenser. Recirculation of the air after leaving the condenser to the humidifier is another alternative [145]. It was reported by Kheder [146] that an air recycling system has the advantage of more than 20% reduction in packed height of the humidifier and more stable operation of the plant.

The performance of the condenser is mainly dependent, among other factors, on the temperature difference between the humid air mixture and the condenser surface, and the condensation surface area. The desired condenser design should enhance both above factors in addition to simplicity and economic considerations.

As a direct consequence, it is important to note that effective heat recovery in such type of condensers require a larger heat transfer area for improving the overall HDH system performance. For example, Bourouni et al. [128] used 3000 m length of polypropylene tubes in the condenser. In another design Orfi et al. [156] used a seawater cooled condenser that contains two rows of long copper cylinders where longitudinal fins were soldered to their outer surfaces. The feed seawater flows inside the cylinders while the water vapor condenses on the finned surfaces. The condenser has a heat-transfer surface area of 1.5 m² and a total length of 28 m of the coil. The multiple paths of the cooling medium inside tubes of small diameters increase both the pressure loss and scale formation, which makes the fouling tendency inherently high.

Furthermore, this configuration also has a rather restrictive coupling between the performance of the condenser and the performance of the whole system, since the mass flow rate of feed seawater (i.e. the condenser coolant) should be same as in other system components (i.e. evaporator, and solar collector). For a given solar collector area, increasing the mass flow rate of feed seawater increases the energy efficiency of both the condenser and solar collector, while decreases the evaporator effectiveness due to lowering its inlet hot water temperature. Due to existence of non-condensable gases, the condenser performs better at higher mass flow rates of cooling seawater than the optimum designed flow rate in the evaporator. The overall thermal performance of HDH system is therefore extremely restricted by such a kind of complex trade off.

Direct-contact condensers have several advantages that tend to alleviate these problems. This type of condensers makes use of spray columns or packed beds in countercurrent/concurrent flow regime to bring together the cooling medium (e.g. freshwater in HDH cycle) and humid air in direct contact along the bed height. On contrary to non-contact heat exchangers, direct contact condensers exhibit higher intensity of heat transfer without heat resistance through the tube walls and provide a large specific interfacial area with a minimum pressure loss. As a result, direct contact condensation technique is widely used in industrial processes, and in chemical and nuclear applications due to the required low driving potential and high efficiency.

Several research studies (136, 137, 147, 148) report that direct contact condensation of humid air is an attractive alternative for small-scale HDH desalination units. Dawoud et al. [148] argued that it is simple, inexpensive, not susceptible to fouling, and has relatively high heat transfer rate and low pressure

drop per unit volume. The direct contact spray condenser (DCSC) which is illustrated in figure (2.17) applies a direct heat and mass transfer between the humid air and a cooled (in an external heat exchanger) portion of condensate.

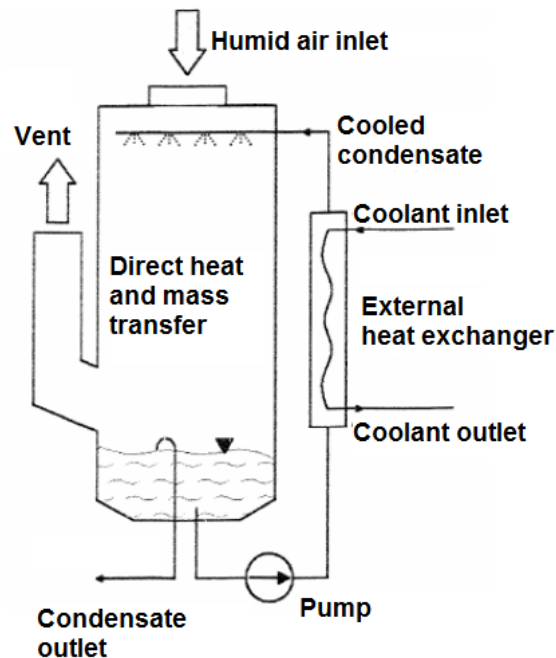


Figure 2.17: A schematic direct contact spray condensers [148]

Packed columns with liquid desiccant cooling is especially suitable to be driven by low temperature energy source such as solar energy and waste heat, because the energy for air dehumidification and cooling can be stored efficiently in liquid desiccants without considerable losses. Such desiccant cooling dehumidifiers require more heat exchangers and a thermal energy source for desiccant regeneration and fresh water condensate recovery. This displaces the system a way from simplicity and uneconomical for small scale category of desalination units of 1 m³/ day distillate.

In direct contact packed bed condensers, countercurrent operation provides the greatest efficiency because mass transfer driving forces are at a maximum [36]. However, for natural draft operation of HDH units, concurrent operation may be more advantageous as the pressure drop is less compared to countercurrent flow. Moreover, gas and liquid contact intensity is greatly increased at higher flow rates; thus mass transfer rates can be elevated in concurrent flow. Strigle [36] mentioned that, in those systems where there is practically no vapor pressure of a solute above the liquid phase, concurrent flow operation should be considered.

Klausner and Mei [136] described a diffusion driven desalination (DDD) process for mineralized water distillation. The investigations focused on optimization of the DDD system both experimentally and numerically. A practical difficulty that arises in film condensation is that heat transfer is tremendously degraded in the presence of non-condensable gases. In order to overcome this problem, they used a direct contact condenser. For this application the warm fresh water discharging the direct contact condenser is chilled in a conventional shell- and -tube heat exchanger using cooling seawater water. A portion of the chilled fresh water is directed back to the direct contact condenser. The distillate is discarded as the fresh water production.

Haddad et al. [140] presented another alternative condensing system for basin type solar stills as depicted in Figure (2.18). An external condenser, constructed as a packed bed storage tank filled with sensible heat storage material (rocks), was integrated with the still. The packed bed condenser was cooled during the night, using a radiative cooling panel by circulating water into the packed bed condenser and the radiative cooling panel.

The cooling panel utilized the cold effective sky temperature, which normally is 10-25°C lower than the ambient temperature, in order to cool the rock domain in the packed bed storage during the night. The packed bed tank is installed at a higher level than the solar still level and is connected to the solar still by a vertical duct. At the beginning of the day light, the tank temperature was lowered to nearly effective sky temperature and water was evacuated from the storage tank. By buoyancy forces and reduced back pressure created in the condenser, the vapor was sucked through the duct between the still and the condenser.

Several advantages were reported for this system. The heat loss was reduced since the temperature inside the still was lowered, the low temperature of the condenser enhanced the condensation rate, and consequently this lowered the vapor partial pressure in the still resulting in higher evaporation rate.

When humid air is fed into a dry porous medium which is at a lower temperature, the humidity condenses and the condensate trickles down by gravity. As elapsed time increases and a condensate is formed within the porous medium, the temperature difference between the humid air and porous medium decreases and the condensate flow rate diminishes.

Vafi and Sozen [13] developed a model for analyzing the behavior of a packed bed of encapsulated phase change material (PCM) and a condensing flow through it. Thermal charging of the packed bed was analyzed and compared for a sensible heat storage material as well as for different PCM storages. It was found that storage of thermal energy of condensation would be most efficient when a PCM with melting temperature close to the lower limit of the operation temperature range chosen. It was also found that for a given particle size and nominal particle Reynolds number,

the amount of condensation in the working fluid depends principally on the thermophysical properties of the solid phase (or PCM), namely, the thermal capacitance of the packed bed. The larger the thermal capacitance, the larger the amount of condensation in working fluid is.

Weislogel and Chung [127] reported that, a PCM packed bed with condensing working fluid passing through has many potential benefits. It will further enhance the condensation rate by using encapsulated PCM packing with large heat capacity and melting temperature close to the lower limit of the operation temperature range of the condenser. Thomas et al [57] indicated that the volumetric heat transfer coefficient for direct contact condensation of immiscible fluid in a packed bed is inversely proportional to the difference between the saturation temperature and the average bed temperature.

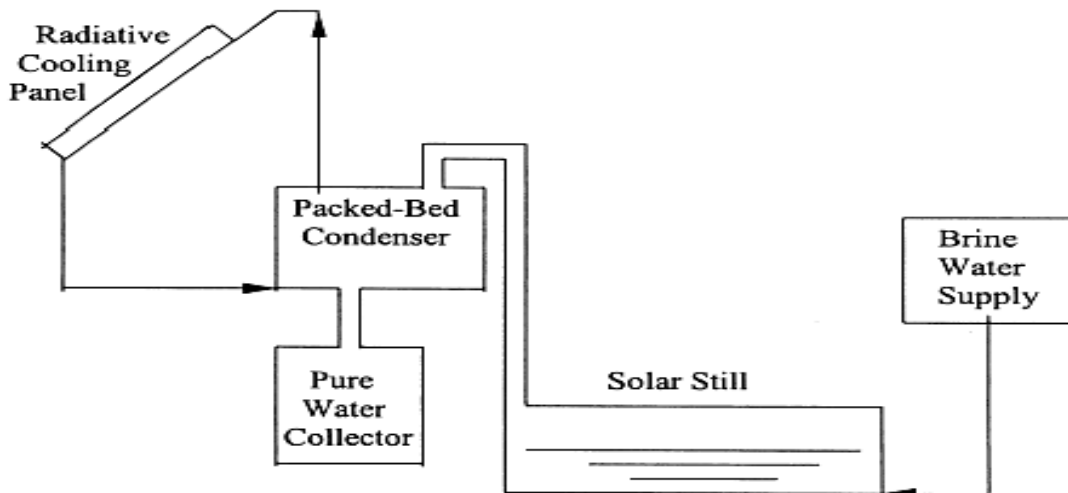


Figure 2.18: Schematics of the radiative cooled solar still [140]

2.8.6 Solar collectors

Bourouni et al., [129] stated that coupling HDH units with thermal solar collectors presents a very interesting solution; however, the water cost is relatively high. They attributed the higher production cost of HDH systems to two different reasons. One reason for this is that solar heating necessitates significant investment in solar collectors and land. Another is that very large amounts of air need to be recirculated because the quantity of water normally contained in saturated air is minimal. Thus, air pumping alone may represent a prohibitive energy cost.

The impact of the collector cost can be seen from the study by Samad [138], in which he describes the operational problems in solar desalination plants and suggests remedies to overcome such hurdles. In his study, it is mentioned that the minimum water cost is very sensitive to the collector cost, and that a drop in collector cost to 50% of its basic value could result in a drop in water cost from \$4.77/m³ to \$3.03/m³.

Flat plate collectors (FPC) are commercially produced in large quantities and in a wide variety of designs mainly for hot water production. Initial capital cost is not prohibitively high and ranges from \$80-250/m² [139], depending on the material used and the country of origin. FPC have low exit temperatures and are combined efficiently with solar stills, or may be combined with small capacity MED but efficiencies are low [2].

Evacuated tube collectors (ETC) are more suitable for conventional distillation plants, as MED or Thermal Vapor Compression (TVC). They are more expensive than FPC and range from \$300-550/m². Initial capital costs are high but operational costs are relatively low. These are more suitable for large capacities compared with low temperature FPC [8]. An alternative to the FPC could be a new convex type solar collector that has been mentioned earlier in this study and which could be more favorable to the flat plate collector. The use of the new tubeless collectors leads to 45% greater energy gain than the flat plate collectors. Therefore, it is important to find ways to reduce the collector cost and implement storage facility and find other methods to improve system efficiency in order to achieve cost reductions so that solar desalination could become competitive with conventional desalination techniques across the globe in the future and not merely for small capacity decentralized use in arid regions of the world [2].

2.8.7 Thermal storage

Work has been initiated to add thermal storage modules to the MEH units. Müller-Holst et al. [4-5] have theoretically and experimentally studied the effects of implementing a 24-hour operation with thermal storage in their investigations. They concluded that further cost reduction by at least half the original cost could be achievable by implementing thermal storage capabilities. Alternate sources of energy could be utilized to heat water stored for nocturnal use in a 24-hour operation. Waste heat from industry, waste heat from fuel cells are some sources of “free energy”, which could help increasing productivity of the MEH units at no additional expenditure except for the thermal storage units. Further studies and simulation and process improvement design of MEH units with a 24-hour operation and thermal storage modules should be considered in future, as a critical step for the commercialization of these units [2].

Many different types of hot water storage tanks are in use. Almost all solar heating systems for space heating and domestic hot water use water as storage medium in a buffer tank, hot water tank or combined tank. The availability, the harmlessness to the environment, the low price, the possibility to use the same medium in more than one circuit and the relatively high heat capacity of water are the main advantages of using water as the heat storage medium. The contemporary developments in design and operation of concentrating solar power systems and solar thermal desalination plants reveal the limitations of water as a storage medium. In order to achieve 24-hour operation of these systems, the heat storage capacity needs to be increased in order to store more energy during day time with minimized heat loss from the tanks. The physical properties of water allow only the use of its sensible heat in a temperature range below 95°C which imposes other limitation on such systems.

The total heat capacity of the storage can of course be increased by increasing the storage size, but this is often not economically feasible, since the additional cost of an enlargement of the storage is very high [6]. Latent heat storage systems using phase change material (PCM) are possibly attractive due to their high heat storage capacity and isothermal behaviour during charging and discharging. The main advantage of using latent thermal storage elements in solar distillation systems is to stabilize their thermal performance with a compact design compared to sensible heat storage such as water. The heat storage design can be improved and the installation can be easier with more compact systems. Nagano [8] reported that the size of PCM storage should be 30% of the water storage for the same capacity, although this is likely to be case specific and dependent upon the collector capacity [7].

A hybrid latent heat storage and spray flash evaporation for process steam generation and seawater desalination has been proposed by Miyatake et al. [141] as shown in figure (2.19). Form-stable cross-linked polymer pellets, which retain their shape even above their melting point, were used as the phase change material in the heat storage column, and aqueous NaCl solution is used as the working fluid.

The spray flash evaporation technique was adopted for the generation of process steam in which the hot working fluid from the heat storage column is injected directly into a low-pressure vapor zone inside the flash chamber through a tubular nozzle, and as the working fluid attains a superheated condition suddenly, a portion of it vaporizes to regain equilibrium and the steam is formed.

Miyatake et al. [141] reported experimental and numerical results of the transient characteristics of the hybrid system and its performance in utilizing the stored energy for generation of process steam and production of fresh water under various operating conditions. It has been revealed by the numerical analysis that the transient variations of the amount of generated steam and fresh water in the system can be predicted with sufficient accuracy, and it will facilitate the design of a practical desalination system. Obvious advantage of this system is the combining of both heat

exchanger and energy storage in one unit. The nature of both working fluids in gaseous immiscible state for charging and liquid state for discharging processes enables such compact design where both working fluids can flow in the same porous channels.

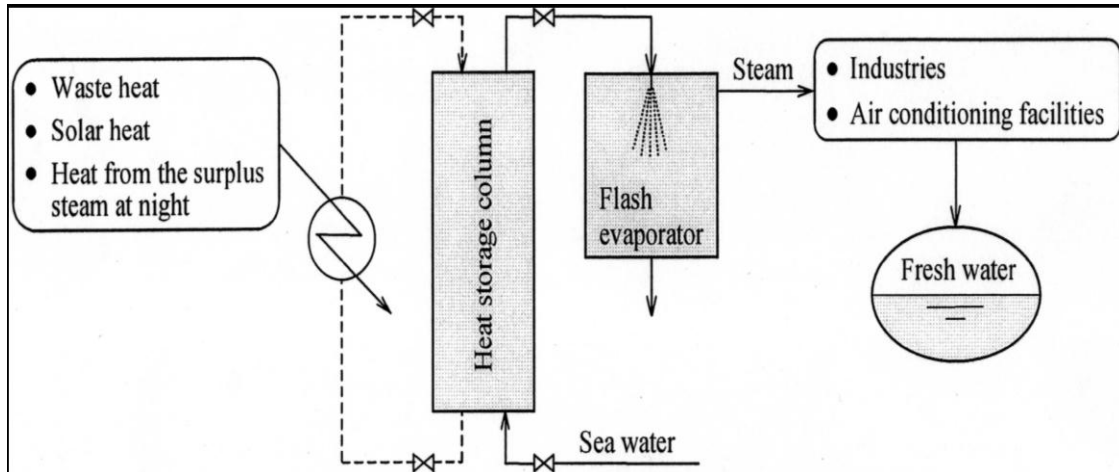


Figure 2.19: Schematic illustration of hybrid latent heat storage and spray flash evaporation system [141]

2.8.8 Summary of the literature on HDH systems

This section extracts and summarizes the important results and experiences of previous investigations in literature and focuses on some of the interesting developments. Different systems have been proposed in literature including open/closed water and air loops, with/without air heating, with/without water heating, and forced/ natural air circulation. In all cycles of HDH units, the latent heat of condensation is utilized in preheating the feed saline water in shell and tubes heat exchangers or direct contact condensation in packed columns.

The main axes in developing the humidifier and dehumidifier through various designs and configurations were focusing on improving the heat and mass transfer rates by increasing the gas-liquid interfacial area and achieving multi-stages or multi-effects. These developments are mainly classified as open-water/closed air (OWCA) cycle and open-air/closed water (OACW) cycle. OWCA systems are the most commonly used, more efficient, and hence they have been studied extensively in the literature.

Most of the realised approaches are using forced convection for actuating the air flow between evaporator and condenser. Various shapes of packing elements were used and investigated by different authors. The factors influencing the choice of a

packing are its heat and mass transfer performance, the quality of water, pressure drop, cost and durability [149]. Al-Hallaj and Selman [2] summarized the main technical results reported by various research groups. Almost all the investigators state that the effect of water flow rate on the performance of the unit is important. The effect of air flow rate on productivity is termed insignificant by all authors except Younis et al [135]. Also, all researchers express preference for natural convection since air flow rate has no significant effect on unit productivity. However, forced circulation could be feasible with another cost-effective source of energy such as wind energy. The effect of air flow rate is only noticeable at temperatures around 50°C, as reported by Al-Hallaj et al [132].

It is concluded that HDH technology has great promise for decentralized small-scale water production applications, although additional research and development is needed for improving system efficiency and reducing capital cost [149]. Al-Hallaj and Selman [2] attributed the higher production cost of HDH systems compared with reverse osmosis (RO) and multi-stage flash evaporation (MSF) units to three main reasons:

1. HDH units rely upon natural draft which results in low heat and mass transfer coefficients and a large surface area for the humidifier
2. The HDH systems are applied for small desalination capacities and scale economies can not be realized in capital investment
3. Film condensation over tubes is typically used, which is extremely inefficient when non condensable gases present. Thus, a much larger condenser area is required, and the condenser accounts for the majority of the capital cost.

2.8.9 Conclusion and spot light

The extensive literature on HDH systems reveals that in spite of the large and valuable amount of research and development effort invested, there is still room for development and optimization of such systems. To improve the performance of HDH systems, previous studies have investigated various configurations of the HDH cycle. These efforts focused on improving heat and mass exchanger designs or using multi effect humidification of air. A multitude of alternative water-heated HDH systems has been presented. However, few interesting approaches focused on direct air heating compared to direct water heating, which proved to be much more energy efficient than air heated systems. The multi effects of heating/humidification of air which was investigated by Chafik [155], the combination of air heating and water heating which was presented by Abdel-Monem [145], and the hybrid latent heat storage and spray flash evaporation which has been proposed by Miyatake et al. [141] are approaching the main interest of the present work. A novel approach for the multi effects of heating/humidification of air and improvement of the HDH cycle will be presented in the next chapter.

3 Scope of the Study

This chapter presents the features of the proposed PCM-Supported HDH system under focus of the present study. The predicted phenomena of multi-effect of heating/humidification (MEHH) in the evaporator and multi-effect of cooling/dehumidification (MECD) in the condenser are illustrated. The scope, objectives of the study, and the adopted methodology will be presented.

3.1 Scope of the study

As reported in the literature, thermal energy storage plays an important role in securing a high thermal performance of solar driven desalination units. A new approach in this context is the use of encapsulated phase change material (PCM) as packing media both in the evaporator and condenser while consequently applying free or forced convection. In the present study, an HDH system with fully integrated packed bed phase change regenerators in both evaporator and condenser has been proposed.

Moreover, a solar thermal power supply consists of a solar collector and an external thermal storage is used to drive the HDH plant. The thermal storage is accomplished by storing to PCM with melting point around the required output temperature to guarantee 24 hours of operation. The PCM elements will be integrated in the hot water storage tank in order to reduce storage tank volume, cost, and heat losses.

The main objective of using PCM elements in the evaporator and condenser was for heat storage as a backup during transient solar irradiation behavior for part-time night operation and cloudy hours. During analysis of steady state conditions, it was discovered that multiple-effects of heating/humidification (MEHH) and cooling/dehumidification (MECD) while air passing through the successive PCM layers in the evaporator and condenser respectively seem to play an important role in system efficiency. The multiple-effects phenomena are attributed to existence of conductive packing media which act as heat and mass exchangers in the two columns. Thus, the focus of the study lies on the thermal conductivity rather than the thermal capacity or solid-liquid phase change processes of the packing. However, these interesting phenomena will be discussed in detail in the next sections and throughout the experimental and numerical analysis in the next chapters.

3.2 Proposed system and operation cycle

The operation cycle and flow diagram of the proposed system and its processes is illustrated schematically in figure (3.1). The plant configuration comprises three closed loops; the air loop, the hot water loop, and the cooling water loop. Hot water is sprayed into the top of the evaporation tower to form a thin liquid film over the

spherical packing while in contact with low humidity counter current air stream. Partial evaporation and convective heat transfer cools the brine down, which leaves the evaporation unit concentrated at a lower temperature. Part of the outlet warm brine is blown down to keep the salinity concentration within a certain limit, while the other part is re-circulated back and mixed with the seawater makeup, and hence the cycle is repeated. The brine and seawater makeup is heated up through recovery of latent heat of condensation in a heat exchanger downstream of the condenser. The brine is then heated up further through a solar collector during the day time or bypassed to the external thermal buffer to avoid heat losses through the collector during the night time. The solar collector should be over designed to store the excessive energy during day time in the external thermal buffer to be utilized for night operation.

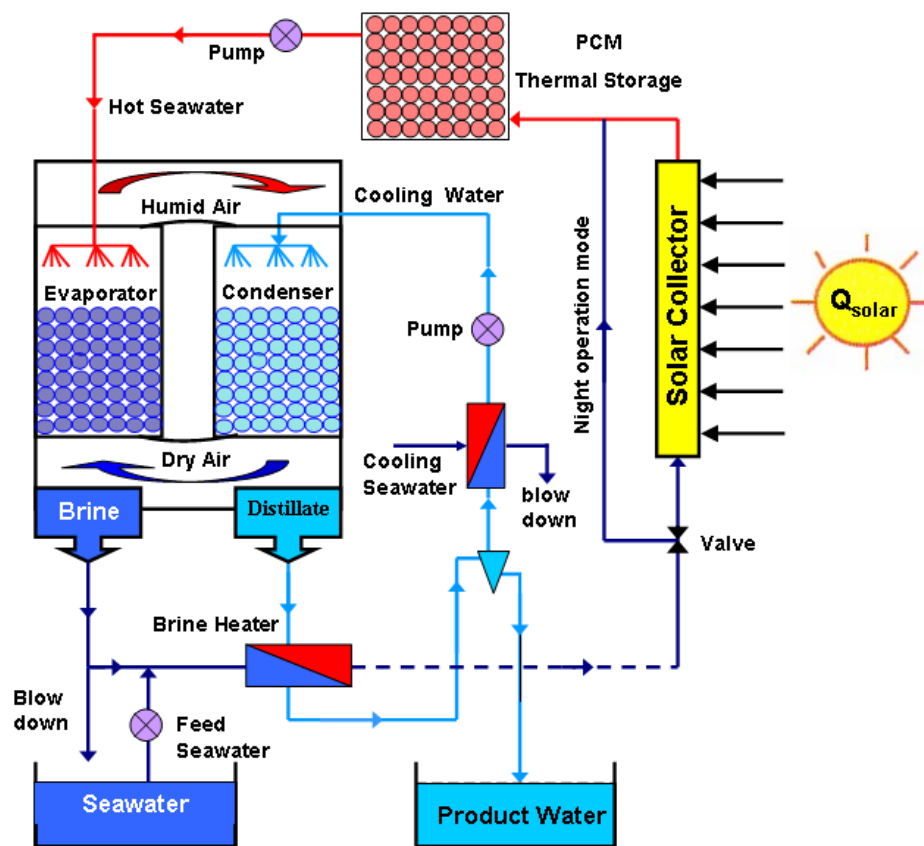


Figure 3.1: Schematic layout of the PCM-Supported HDH desalination unit (AquaTube)

The humidified air is guided by forced convection into the air cooler (dehumidifier) where the sub-cooled water is gently sprayed in tiny droplets at the top of the condenser and trickles downward by gravity concurrently with the hot humidified air. The liquid droplets eventually form a liquid film on the surface of the spherical

packing where it gets in direct contact with the concurrent flow of hot humid air at liquid-gas interface. The air continuously circulates in closed loop cycles, as a carrier medium, to transfer the generated water vapor from the evaporator to the condenser where it is condensed back into highly purified fresh water.

3.3 Concept of Multi-Effects of Heating and Humidification (MEHH)

The main physical difference between the two phase flow in the PCM evaporator and condenser investigated in the present study and a conventional packed bed is that the latter is equipped with a nearly non-conductive packing elements. The non-conductive packing usually has a negligible heat capacity. This implies that the energy balance and energy flow in the conventional packed beds are only governed by the interaction between both fluid phases (i.e. hot and cold streams).

On the other side, for the PCM (or any other conductive material) as packing media, the solid phase contributes to the energy balance and the interstitial energy flow between fluid phases. In the latter, since there are wetted areas and dry patches, there is simultaneous heat and mass transfer entirely between all phases in both evaporator and condenser. Therefore, the physical problem under investigation involves multiscales; on the pore scale level or the micro scale as well as on the macro scale level or the overall balance which mutually affects the sensible and latent heat components at different interfaces on the micro-scale level.

3.3.1 Micro scale level

Existence of PCM packing (or any conductive medium) in the evaporator and condenser creates a parallel path for heat and mass transfer between gas and liquid through the packing elements due to partial wetting of the packing surfaces as shown in figure 3.2. Let the subscript “s” identify the solid particles and subscripts “l” and “g” designate the liquid water and humid air (air-water vapor gas mixture) respectively.

Consider a rectangular finite slab which has thermal conductivity k covered on one of its sides by hot liquid water and subjected to ambient air on the other side as shown in figure (3.2b).

- Due to the higher liquid temperature, there will be two sensible heat transfer components between water and gas (Q_{lg}) and water and solid (Q_{ls}).
- The interaction between gas and solid phases (Q_{gs}) arises due to the temperature difference between both of them.
- At the liquid gas interface, the latent heat of vaporization becomes part of the energy balance, and the mass diffusion (m_v) caused by the vapor pressure gradient affects both heat and mass balances.

In fact there is a tradeoff between direct heat and mass transfer at the liquid-gas interface and the energy flow from liquid to gas across the solid medium which creates the multiple effects of heating and humidification (MEHH) in the evaporator and similarly multi-effects of cooling and dehumidification in the condenser (MECC).

3.3.2 Macro scale level

The change of PCM temperature and enthalpy is both space and time dependent as a result of the transient conduction inside the PCM beads, and thermal stratification in water and gas phases along the packing height. However, due to the stratification of the heat source temperature (i.e. the hot water), stratification exists along the packing height in the PCM layers. This in turn creates a multiple effect heating/humidification or cooling/dehumidification in the evaporator and condenser respectively. The MEHH in the evaporator is illustrated in figure (3.3).

The conductive packing media proposed theoretically serve as temporary heat exchangers that virtually increase the sensible and latent heat transfer interfacial area between water and air and create a multi-effect heating and humidification and multi-effect cooling and dehumidification along humid air passages in the evaporator and condenser, respectively. Such combined effects of creating additional parallel and serial interfaces for heat and mass transfer along the packing heights would increase the air carrying capacity for water vapor and maximize evaporation and condensation rates in the closed air loop cycle.

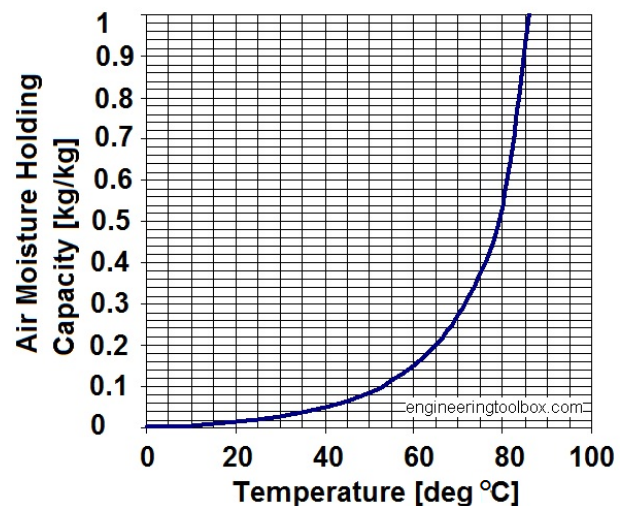


Figure 3.4: Dependency of air moisture carrying capacity on the temperature

When unsaturated airflow gets in contact with hot saline water, a certain quantity of water vapor diffuses from water into the air, which results in a temperature reduction of water as well as a higher salt concentration. The maximum amount of water vapor is limited by the saturation conditions of air, which is mainly dependent on its temperature under constant pressure. Once the air is saturated, it can not carry more water vapor unless its temperature is further increased. As a well known fact, the air carrying capacity for water vapor has an exponential dependence on its temperature. In order to achieve certain humidity content, the air temperature could

be increased at once to the corresponding temperature (as represented by the dashed arrow on figure (3.3) or in a multiple stages of heating and humidification as depicted by the successive red and blue solid arrows on figure (3.3). In the first case, the heat source is required to be available at a high temperature, which in turn will be reflected on increasing the collector area and hence the principle and operating costs. In the latter case the heat source can have a lower quality, such as a waste heat source or simple flat plate solar collector.

In order to achieve the maximum amount of water vapor in the evaporation chamber, the incoming water temperature should be at a temperature high enough so that the maximum amount of water can be evaporated to the surrounding air. The maximum temperature of the incoming water cannot exceed 85°C due to the high material costs associated with such high temperatures. Moreover, the carrying capacity of moist air approaches its highest at approximately 87 °C (see figure 3.4). Therefore it is not expected (in a water heated HDH system) that the air reaches its theoretical maximum carrying capacity at the outlet of the evaporator, since there is always a temperature difference between the hot and cold streams in a heat and mass exchanger.

This leads to the fact that if the air is to be heated alternatively or simultaneously with heating water, it may be theoretically possible to reach the maximum carrying capacity for humidity content. However, solar air collectors have low thermal efficiencies, especially at higher outlet air temperatures, considerably lower than that of the water solar heaters. Thus heating air requires larger solar collector fields, which will add a considerable fraction to the specific desalinated water cost. The resulting prohibitive cost renders this option almost impossible.

This particular problem inspired the concept of utilizing the a conductive packing media such as PCM capsules in the evaporator to create the MEHH locally (as illustrated by figure (3.3), without the need to extract air outside the evaporator at intermediate points, heat it in external air heaters and return it back to the same point, which would neither be technically nor economically feasible.

Moreover, on the macro scale the natural draught is driven by the temperature and density gradients along and between both the evaporator and condenser. The principle behind natural convective heat transfer in the evaporator and condenser is that systems which are influenced by gravity and have materials with different densities are subject to different rates of heat transfer due to uneven heating (i.e. stratification) of the materials present. As a result, particles which are less dense such as humid air rise up and displace the colder more dense air particles, which sink down. Such phenomenon induces air currents between the evaporator and condenser and can be utilized for self-propulsion of the air into the HDH system. Existence of thermal stratification and the MEHH and MECC could have an influence on boosting the natural convection flow, which in turn increases the distillation rate.

The energy flow between all and each pair of phases plays the major role in plotting the system behavior under each specific boundary and geometrical conditions. These particular characteristics have to be seen as the basic concept proposed in the present study for improving the performance of the HDH cycle.

The main advantages of integrating a conductive packing media in the HDH cycle can be summarized in the following points:

- High heat and mass transfer surface area per unit volume
- Self establishment of MEHH and MECC locally
- Air collector is not required
- Extension of the external heat storage capacity

3.4 Concept of Multi-Effects of Cooling and Condensation (MECC)

In the suggested PCM condenser, the physical phenomenon of direct contact condensation is characterized by the transport of heat and mass through the gas (i.e. humid air)-liquid interface as well as across the dry patches at the gas-PCM (or gas-solid) interface along the packing height. Due to continuous cooling of PCM elements by the subcooled liquid layer, supplementary cooling and condensation take place at the gas-solid interface simultaneously with that at the gas-liquid interface; as a result, heat and mass transfer rates are enhanced. Since axial stratification occurs entirely in all involved phases, the phase temperature is a function of distance and hence the PCM temperature profile plays an important role in the condenser performance. However, unlike the evaporator, the gas phase remains saturated at local temperatures throughout the MECC process since the condensation process takes place at both gas-liquid and gas-solid interfaces.

3.5 Study objectives and methodology

In order to solve the problems discussed in the literature concerning the continuous operation of the solar-driven HDH plants round the clock and the problems associated with achieving the MEHH as explained above, investigation of an innovative solution shall be the main task of the present work. Here, in both evaporator and condenser, a porous package of spherical filling material shall be applied yielding similar flow behaviour. In order to guarantee an enhanced thermal performance, the new system consequently is using internal heat exchangers as filling material for evaporator and condenser. These materials for the first time will be integrated in a thermal desalination process. In the framework of the present study, a new evaporator and condenser technology for solar humid air distillation incorporating conductive media such as PCM storages shall be examined.

The major objective of this study is to examine the innovative approach for locally creating MEHH and MECC and to determine the technical and economic feasibility of applying conductive components in HDH cycle and PCM storage in solar desalination plants under both steady state and transient operation conditions.

The study follows two main parallel lines through conducting comprehensive experimental analysis and numerical investigations on the PCM-supported HDH system. The main goals and scope of work to achieve the objectives of the study is as follows:

- A mixed micro-macro balance transient simulation model will be established and validated against experimental measurements using COMSOL Multiphysics and MATLAB for solving fluid flow and heat and mass transfer phenomena in one spatial dimension for different components in such a loop. The model is desired to be fairly general and simple, yet sufficiently accurate to be applied as a design and optimization tool for HDH plants integrated with different types of thermal storage systems.
- The thermal behavior of the new evaporator and condenser technology in the closed air loop distillation unit incorporating conductive packing under steady state conditions shall be discussed and analyzed both experimentally and numerically. Influence of using PCM and Non-PCM packing candidates on the plant performance has to be compiled and an optimal solution has to be integrated into the process.
- Effect of various influencing independent parameters on individual components and HDH plant performance and productivity will be investigated.
- The dynamic performance of the humid air distillation unit integrated with the PCM-thermal storage and solar flat plate collector will be discussed and analyzed. Comparative performance of HDH system is focused and clearly documented using PCM and water as a thermal storage media in the external thermal storage over a wide range of operation conditions. The overall analysis will be performed under real varying weather conditions over one year for a selected geographical location in Egypt. Special attention shall be paid to the heat recovery mechanisms and optimum coupling of the external thermal storage with the HDH cycle.
- Finally the numerical simulation model will be used to optimize the design characteristics of a small-scale HDH module with a production capacity of 1 m³/day.

4 Theoretical Analysis and Modeling

In this chapter, detailed thermodynamic and hydrodynamic modeling of various components of the proposed HDH system has been developed. Pertinent theories, several correlations, and closure models adopted from literature will be presented. A mixed micro-macro balance transient simulation model in one spatial dimension for capturing heat and mass transfer phenomena in the HDH plant as a whole has been established. The model is fairly general to be applied as a design and optimization tool for HDH plants with different types of packing and coupled to sensible or latent thermal storage systems.

4.1 System variables

The system overall setup and operation processes which have been used for developing the mathematical model are illustrated schematically in figure (4.1). The setup is typically the same as that of figure (3.1) but the main operation parameters of interest for the development of heat and mass balances in the following sections are depicted on figure (4.1) for ease of referencing. As described previously, the setup works on the same principle and contains two main sections; the distillation (HDH) cycle and the solar water heater. The later consists of a solar collector and PCM storage tank. A flat-plate solar collector (FPC) is proposed to provide the thermal power supply to the system.

In figure (4.1), it is assumed that part of the outlet brine is blown down to keep the salt concentration within a certain limit identified by the brine recirculation factor (r_c). The other part is blended with the seawater makeup and re-circulated through a heat exchanger (brine heater) downstream of the condenser where the latent heat of condensation is partly recovered by the warm brine blend.

The warm brine flow is heated further through the solar water collector and then passed through the external thermal storage and hence the cycle is repeated. The collected solar energy during day time will then be divided between the load and the storage tank. When solar energy is no longer available, the collector flow will be bypassed and the load is handled by discharging the thermal storage until either it is fully discharged (nightly part time operation) or solar energy again is available (24-hour operation). The above description assumes no heat losses during the fluid flows through piping and tube connections.

Existence of PCM packing (or any conductive medium) in the evaporator and condenser creates a parallel path for heat and mass transfer between gas and liquid through the packing elements due to partial wetting of the packing surfaces as shown in figure (4.2). Let the subscript “s” identify the solid particles and subscripts “l” and “g” designate the liquid water and humid air (air-water vapor gas mixture)

respectively. Because of the partial wetting in the evaporator and condenser, there is heat transfer (q_{lg}) between water and air, heat transfer (q_{ls}) between water and PCM beads (or solid phase), and heat transfer (q_{gs}) between gas and PCM beads. Moreover, there is direct condensation of water vapor on the dry patches of the packing spheres in the condenser.

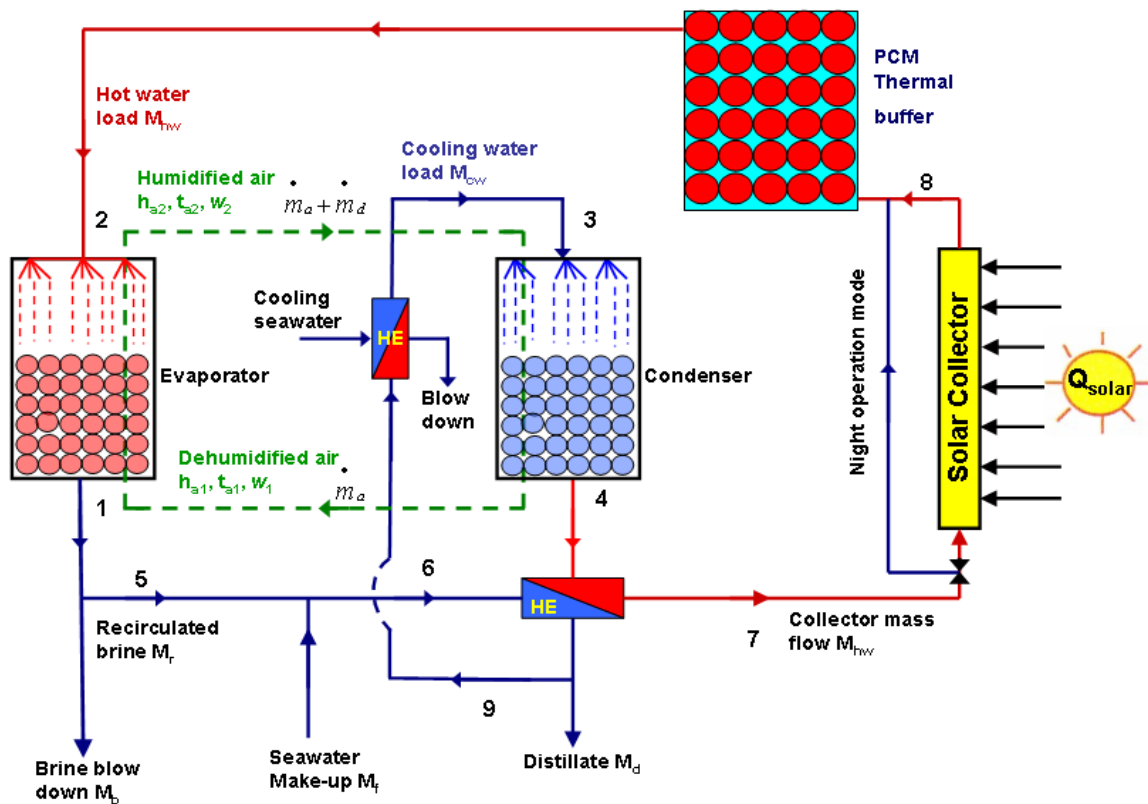


Figure 4.1: Schematic layout of the PCM-Supported HDH desalination unit (AquaTube) and operation cycle

4.2 Mathematical Modeling

A single phase model is commonly used for analyzing thermo-fluid flow in packed beds and porous media when fluid is moving relative to a solid matrix. This model assumes local thermal equilibrium between solid and fluid phases, where their temperatures are represented by a unique value. The assumption of local thermal equilibrium breaks down in certain physical situations. For example the temperature at the bounding surface changes significantly with respect to time, and when solid and fluid phases have significantly different heat capacities and thermal conductivities, the local rate of change of temperature for one phase differs significantly from that for the other phase [11].

The two-energy equation models which have been proposed by Schlünder [10] allow two distinct temperatures to determine the distribution of temperatures of solid and fluid phases. The governing equations for coupled heat and mass transfer processes in the three types of heat exchangers shown in figure (4.2) can be obtained following the two-energy equation models in the following form:

$$\varepsilon \rho_f c_f \left[\frac{\partial \langle T \rangle^f}{\partial t} + \langle \vec{v} \rangle^f \cdot \nabla \langle T \rangle^f \right] = \nabla \cdot \vec{k}_{eff}^f \cdot \nabla \langle T \rangle^f + h_{fs} a_{fs} (\langle T \rangle^s - \langle T \rangle^f) \quad (4.1)$$

$$(1 - \varepsilon) \rho_s c_s \frac{\partial \langle T \rangle^s}{\partial t} = \nabla \cdot \vec{k}_{eff}^s \cdot \nabla \langle T \rangle^s - h_{fs} a_{fs} (\langle T \rangle^s - \langle T \rangle^f) \quad (4.2)$$

where $\langle \vec{v} \rangle$ is the volume averaged velocity, $\langle T \rangle^f$ and $\langle T \rangle^s$ denote the intrinsically averaged temperature of fluid and solid phase respectively. The symbols ε , \vec{k}_{eff} , a_{fs} , and h_{fs} refer to the porosity, effective thermal conductivity tensor, specific surface area of packing, and interfacial convective heat transfer coefficient respectively. The heat transfer between solid and fluid phases is described by source and sink terms on the right hand side of the energy balance equations.

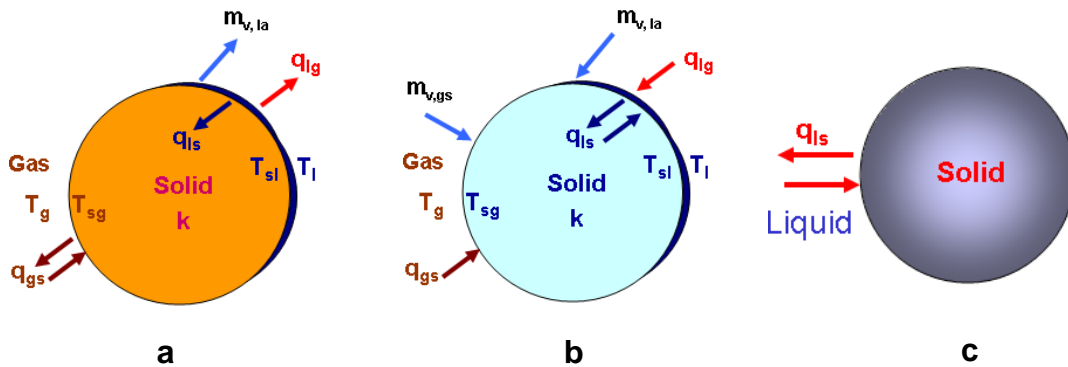


Figure 4.2: illustration of heat and mass transfer flow between different components on one packing element; (a) Evaporator, (b) Condenser, (c) External PCM thermal buffer

It is essential and customary to use local volume averaging techniques over a representative elementary volume V to rigorously describe the transport processes in porous media by a set of governing equations. There are two different averages of a quantity in the governing equations. These are the local volume average and the intrinsic phase average [13]. The intrinsic phase average refers to the average

properties that are associated with a single phase, such as the solid phase temperature, while the volume averaged properties are associated with the spatial average values of fluid motion, such as the superficial fluid velocity. It is extremely important to distinguish and make use of both types of averaging concepts in the model equations.

Because of the fact that PCM candidates usually exhibit low thermal conductivities and are available commercially encapsulated in relatively large containers, adopting the assumption of local thermal equilibrium can limit the validity and generality of the mathematical model. In addition, due to the complexity of coupled heat and mass transfer phenomena in the evaporator and condenser as described in figure (4.2), it is not a simple task to assess the validity of this assumption, since the temperature of the solid phase at the interface with the gas phase could be different from its temperature at the interface with the liquid phase.

Moreover, assuming the lumped capacitance is valid during the phase change process, the solid temperature inside the PCM beads varies between the liquid temperature, the gas temperature, and the melting temperature. Hence existence of deformable moving interface with its motion being not easily predicted and significant discontinuities of properties at the interface cause a complicated coupling between the field equations of each phase, which suggests that the use of a non-local thermal equilibrium assumption is a possible solution to the problem. Therefore, the non-local thermal equilibrium assumption or the two-energy equation models will be adopted for the present study.

In this study, a mathematical model and numerical procedures shall be proposed to determine the macroscopic transport and time history of the crucial field variables such as the temperature, evaporation and condensation rates, pressure, and velocities of the working fluids. These procedures will be developed first for the single phase flow problem (i.e. the external thermal buffer) and then will be extended to the multi-phase flow in the evaporator and condenser. Upon extending the mathematical model to the case of dual phase change regenerators, a macroscopic balance analysis for the whole plant with peripheries will be developed to couple the three heat exchangers with the solar collector field to conduct numerical experiments for a wide range of operation conditions and design features.

4.2.1 Model assumptions

Detailed pore scale modeling of momentum, heat, and mass transfer for the complex flow in porous media would be difficult and especially the process dynamics would be impracticable [12]. In all the physical systems under consideration, the phase change heat transfer takes place on the length scale of the encapsulated PCM spheres. In the evaporator and condenser, evaporation and condensation of water vapor at different interfaces with gas and solid phases occur simultaneously with the

solid-liquid phase change inside the PCM beads. However, the objective is to model the bulk heat and mass transfer in these systems with no interest in tracking the moving boundaries. Such microscopic details are neither easy to be captured nor needed, instead, the macroscopic aspects of the flow are much more interesting as an engineering problem. Therefore, dealing with such a multi-scale problem, a fundamental question arises as how to bridge the computational scale and reduce the problem to a simple form of solution. In order to establish a simplified mathematical treatment, the underlying assumptions will be given in the subsequent points and discussions.

- The column wall is assumed to be perfectly insulated (adiabatic)
- Thermal conductivity of PCM in the transverse direction is assumed to be infinite, i.e. one layer of PCM is assumed to have the same temperature over the cross section area of the tank. The thermal resistance of the spherical plastic shells was neglected, since they are very thin and have a thermal conductivity close to that of the PCM candidate. The heat flow inside the PCM beads is dominated by conduction, and the convection heat transfer induced by internal recirculation during the melting process was neglected.
- The spherical PCM capsules behave as a continuous medium (i.e. continuous solid model approach) with effective thermophysical properties, so that the liquid film and the gas mixture could keep continuous and uniform flows.
- The radial temperatures of liquid and gas phases are uniform (i.e. the transverse temperature gradients within each phase are neglected) and the velocity profiles are assumed to be fully developed and uniform at the entry point where heat and mass transfer start.
- Furthermore the wall effects on porosity, which may be present due to large packing-to-column diameter ratio and results in greater porosity near the wall than the central region of the column, are neglected for simplicity.
- The liquid and gas phase fractions are also assumed constant along the packed height since the evaporation and condensation rates are less than 5% of the feed seawater in HDH. This assumption is extremely important for model simplification otherwise another moving boundary between liquid and gas phases should be traced which renders the numerical solution extremely difficult to be attainable.
- Operating temperatures are below 85°C, and are therefore not high enough to appreciate radiation effects.
- Axial dispersion effects in the fluid which arise due to the mixing action within the fluid as a result of eddy currents created as the fluid flows through the complex porous passages are neglected.

The mathematical model is greatly simplified with these assumptions and leads to time dependent equations in one spatial dimension. In addition, the 1-dimensional formulation not only reduces the computational efforts, but also ensures more stability of the simulation model as any small perturbations in the transverse direction may cause large errors in the numerical solution.

4.2.2 Flow in the external heat storage

The system of latent heat storage (Fig. 4.3) consists of a vertical cylindrical tank, which is perfectly insulated, with seawater flowing relative to a spherical PCM packing. The derivation of energy balance equations in the packed bed assumes local thermal non-equilibrium as mentioned before and hence considers separate energy balance equations for solid and liquid phases. The classical form of equations (4.1) and (4.2) can be applied straightforward with empirical transport coefficients to describe the single phase flow in the external PCM thermal buffer.

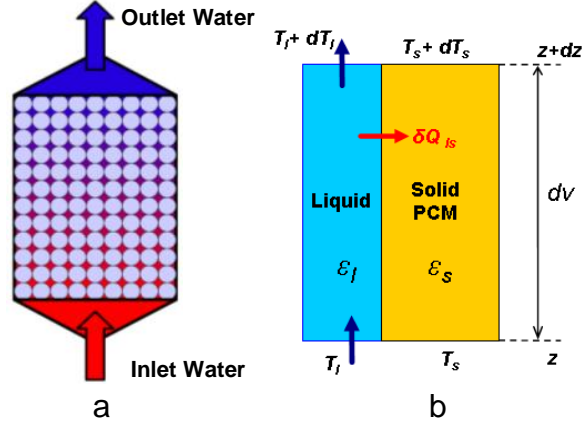


Figure 4.3: Schematic of heat transfer in the external PCM thermal buffer; (a) Layout of the PCM packed bed, (b) energy balance over a control volume

The volume averaging brackets in equations (4.1) and (4.2) will not appear in the subsequent developments of various mathematical models for simplicity.

There are basically three sub-models derived from the two-energy equation models. These sub-models include the “Continuous Solid Phase (CS) Model”, “Schumann’s Model”, and “Concentric Dispersion Model (or Model with Thermal Gradient within Solid Particles)”. An overview of all possible packed bed models is presented in Wakao and Kagueli [15], Kaviany [11], and Ismail and Stuginsky [16].

Schumann’s Model neglects the axial heat conduction in both fluid and solid phases as well as the transverse heat transfer in the bed. This simplification allows a one-dimensional formulation and drops the first term on the right hand side of the general equations (4.1) and (4.2).

$$\varphi_f c_f \left[\frac{\partial T_f}{\partial t} + u_f \cdot \nabla T_f \right] = h_{sf} a_{sf} (T_s - T_f) \quad (4.3)$$

$$(1 - \varepsilon) \rho_s c_s \frac{\partial T_s}{\partial t} = -h_{sf} a_{sf} (T_s - T_f) \quad (4.4)$$

It is worth mentioning that starting from equations (4.3) and (4.4), the averaging brackets in equations (4.1) and (4.2) will be dropped for simplicity, as the field variables are known to be intrinsic phase average by default unless stated. In the CS model, the solid phase is assumed to behave as a continuous medium, not as a medium composed of individual particles, while heat transfer in the packed bed is

assumed by conduction in both axial and radial directions [16]. The CS model retains the general formulation of equations (4.1) and (4.2).

In all models described previously no thermal gradient within the beads is considered. In the concentric dispersion model, thermal gradients within solid particles are considered while inter-particle heat transfer is neglected. Therefore the radial temperature profile will only be due to convective heat transfer between the fluid and solid phases at the particle's surface. In order to include the effect of limited thermal conductivity of the solid material which decreases the heat transfer and leads to a radial temperature gradient within the particle, the energy balance equation of the solid phase (i.e. equation (4.1)) must be replaced by a Fourier equation for heat conduction:

$$h_{fs} a_{fs} (T_f - T_{s,surface}) = \frac{\partial}{\partial r} (k_s T_{s,surface}) \quad (4.5)$$

where the convective heat transfer at the solid surface must be balanced by the transport of energy through heat conduction into the particle:

$$\rho_s c_s \frac{\partial T_s}{\partial t} = k_s \frac{1}{r^2} \frac{\partial}{\partial r} \left(r^2 \frac{\partial T_s}{\partial r} \right) \quad (4.6)$$

where r is the radius of the sphere. As mentioned earlier, since the temperature of the solid phase at the interface with the gas phase could be different from its temperature at the interface with the liquid phase, this model can not be adopted to describe the heat transfer in the evaporator and condenser components from the fundamental basis.

On an average level of complexity, reasonable accuracy and affordable computation time, and for seeking generality of the adopted mathematical formulation for all the main system components, the CS model has been selected and will be used throughout this study and subsequent analysis. The properties of each phase are determined by assuming a volume averaging described by the relative representation of each phase in the packed volume (i.e. based on the porosity and fluid hold up).

Conservation of Energy: Following the two-energy equation models and considering the assumptions and simplifications mentioned above, the one dimensional model can be written in the following form in the axial direction (z) for fluid and solid phases respectively:

$$\varepsilon_s \rho_s c_{app,s} \frac{\partial T_s}{\partial t} = k_{s,eff} \frac{\partial^2 T_s}{\partial z^2} + h_{ls,eff} a [T_l - T_s] \quad (4.7)$$

$$\varepsilon_l \rho_l c_l \frac{\partial T_l}{\partial t} + \varepsilon_l \rho_l c_l v_l \frac{\partial T_l}{\partial z} = \varepsilon_l k_l \frac{\partial^2 T_l}{\partial z^2} - h_{ls,eff} a [T_l - T_s] \quad (4.8)$$

In equations (4.7) and (4.8), subscripts s , l are standing for solid, and liquid respectively, while v denotes the interstitial flow velocity and a is the total specific surface area per unit volume of the packed column. The symbol ε_s , and ε_l denote the solid fraction and the liquid holdup in the bed respectively where the total porosity in the bed is $\varepsilon = \varepsilon_l = 1 - \varepsilon_s$.

In the above heat balance equation of the liquid phase (i.e. equation (4.8)), the first term on the left hand side represents the accumulation of energy in the fluid, and the second term represents the energy carried away by the fluid. On the right hand side, the first term represents the energy gain by conduction through the fluid, while the second term stands for the energy transfer with the solid phase. Similarly, for the heat balance of solid phase, the first term on the left hand side accounts for heat accumulation. On the right hand side, the first term accounts for heat gain by conduction through and between solid particles, and the second term accounts for heat gain from the fluid phase.

Generally, all PCM have low thermal conductivity (k). Paraffin waxes have thermal conductivity of the order of 0.2 W/m.K while hydrated salts have higher thermal conductivity but still relatively lower than 1.0 W/m.K. If the packing used are large spheres, the overall heat and mass transfer coefficients will be low due to the high internal thermal resistance in the PCM spheres (r/k). The thermal conduction resistance inside the PCM beads is included implicitly by introducing the Jefferson degradation factor [14] in the fluid-solid heat transfer coefficients in a one-dimensional CS model [section 4.3.3.5]. The effective heat transfer coefficients between gas/liquid and the PCM beads are then given by:

$$h_{fs,eff} = h_{fs} / (1.0 + 0.2Bi) \quad (4.9)$$

where $Bi = h_{fs} d_{ball} / (6k_s)$ is the Biot number and the term $1/(1+0.2Bi)$ represents the Jefferson degradation factor. This effect of temperature gradient inside the particles has to be considered in all the system components due to the relatively large size and low thermal conductivity of the PCM beads. In this analysis a readily encapsulated commercial PCM candidates were used as a packing media in the evaporator, condenser, and the external thermal buffer. Table (A1) in the Appendix presents the thermo-physical properties of the selected PCM candidates.

Pressure drop: It has been shown by Dullien [51] that the pressure drop in a porous bed can be calculated as a function of the flow rate by using the Ergun's equation [52], when the flow rate is outside the range of validity of Darcy's law (i.e. $Re > 10$). The Ergun equation, which is based on the particle's model, is suitable to calculate

the air pressure drop ΔP per unit bed height through a porous bed with relative uniform porosity:

$$\Delta P = 150 \frac{\mu_g (1-\varepsilon)^2 v_g}{d_p^2 \varepsilon^3} + 1.75 \frac{\rho_g (1-\varepsilon) v_g^2}{d_p \varepsilon^3} \quad (4.10)$$

Where d_p is the diameter of particles, and v_g is the superficial gas velocity.

4.2.3 Two phase flow in dual phase change regenerators

Modeling two phase flow in dual phase change regenerators is rarely presented in the literature for the condenser [17], but not a single analysis has been reported for the evaporator up to the best knowledge of the author. The underlying heat and mass transfer processes are complex and require the solution of highly nonlinear coupled partial differential equations for space and time varying flow characteristics and tracking the moving boundaries. Derivation of the governing equations to describe steady state and dynamic characteristics of multi-phase multi-component dual phase change regenerators of the evaporator and condenser is expected to be more complicated and should be clearly formulated on rational basis and supported by experimental validation.

4.2.2.1 Flow in the evaporator

Figure (4.4) shows a schematic of the evaporator chamber with its flow pattern and operation features. Warm salt water from the external PCM storage tank is gently sprayed in tiny droplets at the top of the evaporation tower and trickles downward by gravity where heat and mass transfer take place between sprayed droplets and a countercurrent dehumidified air leaving bottom of the condenser chamber.

Countercurrent air stream is heated and humidified in contact with the hot water film while hot water is cooled down and partly evaporated. On the other side, another binary heat transfer between solid PCM beads and both liquid water film and humid air (gas mixture) take place simultaneously. This is due to non-fully wetted surface area of packing elements.

The binary interactions between solid phase and both fluid phases are dependent on the interfacial areas and flow characteristics. The evaporated water leaves behind salts and other contaminations resulting in concentrated brine with lower temperature at the bottom of the evaporator. A mutual interdependency between heat and mass transfer and flow fields couples between hydrodynamics and thermodynamics.

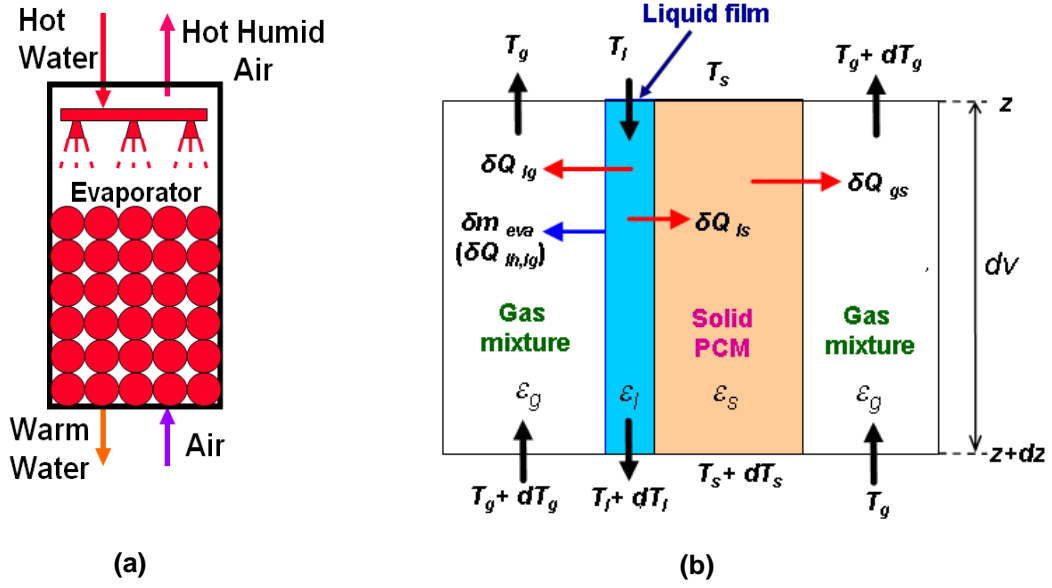


Figure 4.4: Schematic of heat and mass transfer in the evaporator; (a) Layout of the evaporator, (b) energy balance over a control volume

Conservation of energy: Applying the CS model on the control volume shown in Fig. 3.b., with the assumptions and simplifications mentioned previously and introducing latent heat terms, the energy equations for solid, liquid, and gas phases can be written in a one dimensional form respectively as:

$$\epsilon_s \rho_s c_{app,s} \frac{\partial T_s}{\partial t} = k_{s,eff} \frac{\partial^2 T_s}{\partial z^2} + h_{ls} a_w [T_l - T_s] + h_{gs} a_{gs} [T_g - T_s] \quad (4.11)$$

$$\epsilon_l \rho_l c_l \frac{\partial T_l}{\partial t} + \epsilon_l \rho_l c_l v_l \frac{\partial T_l}{\partial z} = \epsilon_l k_l \frac{\partial^2 T_l}{\partial z^2} - h_{ls,eff} a_w [T_l - T_s] - h_{lg,eff} a_e [T_l - T_g] - \dot{m}_{evap} h_{fg} \quad (4.12)$$

$$\epsilon_g c_{p,g} \frac{\partial (\rho_g T_g)}{\partial t} + \epsilon_g c_{p,g} \frac{\partial (\rho_g v_g T_g)}{\partial z} = \epsilon_g k_g \frac{\partial^2 T_g}{\partial z^2} - h_{gs,eff} a_{gs} [T_g - T_s] + h_{lg,eff} a_e [T_l - T_g] + \dot{m}_{evap} h_{fg} \quad (4.13)$$

In equations (4.11) – (4.13), subscripts s, l, g are standing for solid, liquid, and gas mixture respectively, while v denotes the interstitial flow velocity and \dot{m}_{evap} is the

evaporation rate per unit volume of the packed column. It is noted that a , a_{ls} , and a_{gs} are the total specific (per unit volume of the packed column), the wetted area (a_w) and the effective specific interfacial area (a_e) between liquid and gas respectively, where $a_{gs} = a - a_w$ is the specific gas-solid interfacial area. The symbols ε_s , ε_l , and ε_g denote the solid fraction in the bed, the liquid holdup, and the gas holdup respectively. From definition, $\varepsilon_s + \varepsilon_l + \varepsilon_g = 1$, the total porosity in the bed $\varepsilon = \varepsilon_l + \varepsilon_g$, and the solid fraction $\varepsilon_s = 1 - \varepsilon$.

In the above heat balance equations of fluid phases (i.e. equations (4.12) and (4.13)), the last term stands for latent heat transfer in the same direction of heat transfer from liquid to gas side assuming evaporation is the only mechanism of mass transfer in the evaporator chamber. All other terms can be described similarly to equations (4.7) and (4.8), for solid and fluid phases respectively.

The term Q , which appears on figure (4.4b) represents the energy flow by convection heat transfer between each pair of phases due to the temperature difference between them, and is represented in the energy equations by the last two terms for the solid phase and both second and third terms on the right hand side of equations (4.12)-(4.13) for liquid and gas phases respectively. The mass diffusion takes place at the gas/liquid interface. The evaporation rate \dot{m}_{evap} is expressed in $(\text{mol} \cdot \text{s}^{-1} \cdot \text{m}^{-3})$. The corresponding latent heat of evaporation is absorbed by the gas phase. At steady state conditions, the energy flow from liquid to solid phase equilibrates with the energy flow from solid to gas phase and the local temperatures of all phases remain constant. Any change of the operation and boundary conditions will break steady state equilibrium, and the local temperatures will change correspondingly.

When the working fluid undergoes phase change (evaporation or condensation), a rigorous model which couples the governing energy, mass and momentum balance equations above together with state variables and thermodynamic relationships has to be considered for simulating the system performance. Although it might be a satisfactory approach for the liquid phase to be treated as incompressible fluid, it is not so for the gas phase especially under natural draft operation or under high pressures. Applying the Oberbeck-Boussinesq approximation in which all properties of the gas mixture are assumed to be independent of the pressure and temperature except for the density is applied in equation (4.13) to capture this effect will be discussed in the momentum balance below. The solid-liquid phase change in PCM beads is captured by introducing an apparent heat capacity c_{app} in the one dimensional form of the solid phase energy balance equation following the apparent heat capacity approach [18].

Mass balance: The water vapor concentration gradient in the gas mixture at the bulk of the packed bed along the axial direction (z) can be described by the equation:

$$\varepsilon_g \frac{\partial c}{\partial t} = \varepsilon_g D \frac{\partial^2 c}{\partial z^2} - \varepsilon_g \frac{\partial (c v_g)}{\partial z} + \dot{m}_{evap,lg} \quad (4.14)$$

In the above equations, v_g is the average gas velocity in the pore along the axial direction, D denotes the diffusivity of the transported species, c is the water-vapor concentration (mol.m^{-3}). The last term in the above equation is the evaporation rate \dot{m}_{evap} per unit volume of the packed column (mol.s^{-1}). Liquid and gas phase continuity equations are given by:

$$\frac{\partial(\varepsilon_l \rho_l)}{\partial t} + \nabla(\varepsilon_l \rho_l u_l) = -\dot{m}_{evap} \quad (4.15)$$

$$\frac{\partial(\varepsilon_g \rho_g)}{\partial t} + \nabla(\varepsilon_g \rho_g u_g) = \dot{m}_{evap} \quad (4.16)$$

The model assumes homogeneous porous media and uniform flow distribution in a large diameter column. When it comes to the assumption that liquid and gas saturations (or holdups) do not vary (significantly) with the axial position due to evaporation and considering the average axial gas density and average axial gas velocity, the continuity equations for the gas and liquid phases under these conditions can be simplified to the form:

$$L = \varepsilon_l \rho_l v_l \quad (4.17)$$

$$G = \varepsilon_g \rho_g v_g \quad (4.18)$$

where L and G are the liquid and gas mass fluxes per unit cross sectional area of the packed column ($\text{kg. m}^{-2}.\text{s}^{-1}$) and v is the interstitial flow velocity. Given the mass flow rate of liquid and gas, the average pore velocities can be determined under forced draft operation where the effect of buoyancy forces in the gas mixture can be neglected.

Momentum balance: In the current application, the axial variation in density is of particular importance for a natural draft operation because it gives rise to buoyant forces, which are the main driving forces in this case and mutually dependent on heat and mass transfer rates. The gas density gradient is caused by both temperature and humidity gradients (double diffusive system) along the axial direction due to heat and mass transfer from the hot water film to the gas mixture. The gas density under the double diffusion effects can be calculated by [19, 20]:

$$\rho = \rho_{ref} [1 - \beta_t (T - T_{ref}) - \beta_c (c - c_{ref})] \quad (4.19)$$

where β_t , β_c , ρ_{ref} , c_{ref} , and T_{ref} are the volumetric thermal expansion coefficient, volumetric diffusion (concentration) expansion coefficient, reference density, reference concentration, and reference temperature respectively. Single phase flow in a dense porous medium with low flow velocity is typically governed by Darcy's law, which relates the fluid velocity v to the pressure drop ΔP over a distance ΔL , using the viscosity μ and the absolute permeability K of the medium as proportional constants.

$$v = -\frac{K \Delta P}{\mu \Delta L} \quad (4.20)$$

Ergun determined an empirical relationship between K , d , the pore size, and the void fraction ε for spherical particles:

$$K = -\frac{d^2 \varepsilon^3}{150(1-\varepsilon)^2} \quad (4.21)$$

It can also be derived from Karman-Kozeny's hydraulic radius theory [19]; in this case the constant is 180 instead of 150 and d represents the particle (bead) diameter. Darcy's law can then be used to derive relations between the velocity and the pressure gradient for each of the two fluid phases as follows, (Nield and Bejan [20]):

$$v_l = -\frac{K_{rl} K}{\mu_l} (\nabla P - \rho_l g) \quad (4.22)$$

$$v_g = -\frac{K_{rg} K}{\mu_g} (\nabla P - \rho_g g) \quad (4.23)$$

For the case of two phase flow in equations (4.22) and (4.23), the concept of relative permeability K_r has been introduced by Sáez and Carbonell [22] in momentum balance equations. The idea behind the concept of relative permeability is that an expression for the drag force for single-phase flow is used. However, this has to be altered (divided) by a certain parameter to take into account the presence of the second phase. This parameter is known as the relative permeability of a certain phase (k_{ra}). The relative permeability can in fact be viewed as the ratio between the effective permeability of a certain phase within two-phase flow ($k_{eff,\alpha}$) and the permeability of the bed (k). The relative permeabilities of the gas and liquid phases are normally assumed to be primarily a function of the saturation S of each phase [21]:

$$S_{\alpha} = \frac{\varepsilon_{\alpha}}{\varepsilon} \quad (4.24)$$

Sáez and Carbonell [22] analyzed data for liquid holdup and pressure drop available in the literature over a wide range of Reynolds and Galileo numbers in packed beds, to determine the dependence of the relative permeability on the saturation for each phase (Phase saturation refers to the phase volume per void volume). They correlated the available information in the form:

$$K_{rl} = \delta^{2.43} \quad (4.25)$$

$$K_{rg} = S_g^{2.43} \quad (4.26)$$

The quantity δ in Equation (4.25) is the reduced liquid saturation:

$$\delta = \frac{S_l - S_l^0}{1 - S_l^0} \quad (4.27)$$

where S_l^0 is the reduced liquid saturation, Expressing k_{rl} in this form suggests that the saturation corresponding to the static liquid holdup ($S_l^0 = \varepsilon_l^0 / \varepsilon_l$) consists of essentially stagnant liquid. The use of a reduced liquid saturation in the formula for the liquid phase relative permeability is common practice in two-phase flow analyses [21].

In the first attempt to use the so called slit model (one of the porous media flow models) to correlate experimental data, Holub et al. [23] analysis were identical in form to equations (4.25) and (4.26), but with relative permeability functions for the gas and liquid phases with a cubic dependence on saturation:

$$K_{rl} = S_l^3 \quad (4.28)$$

$$K_{rg} = S_g^3 \quad (4.29)$$

Holub et al. [23] compared the relative permeability functions in equations (4.31) and (4.29) to the empirically determined results in equations (4.25), (4.26). They were successful in fitting holdup and pressure drop data in the literature, provided that Ergun's constants were set to the values measured experimentally in each case [21].

For the laminar mixed or free convection flow induced by the combined thermal and mass buoyancy forces, there is a buoyant force on the gas phase and also an acceleration term, which should be included in Darcy's law. Taking all of these flow characteristics into consideration, we finally reach a form similar to Brinkman equation. Brinkman equation extends Darcy's law to include a term that accounts for

the viscous transport and introduces velocities in special directions as dependent variables. The flow field can be determined by solving the Brinkman equation for the momentum balance in combination with the continuity equation. Applying Brinkman equation on two phase flow by using the relative permeability K_r , the gas phase momentum balance equation reads:

$$\rho \frac{\partial v_g}{\partial t} = (-\nabla p + \rho g) - \frac{\mu_g}{KK_{rg}} v_g + \mu_g \nabla v_g \quad (4.30)$$

where μ is the dynamic viscosity, K is the permeability, ∇p is the pressure gradient, and ρ is the varying gas density. The buoyant force appears automatically when an equation of state is inserted into the equation of motion (4.30) in the (ρg) term (but not into the acceleration term $(\rho \partial v / \partial t)$).

$$\rho \frac{\partial v}{\partial t} = (-\nabla p + \rho_{ref} g) - \frac{\mu_g}{KK_{rel,g}} v_g + \mu_g \nabla v_g - \rho_{ref} g [\beta_t (T - T_{ref}) + \beta_c (c - c_{ref})] \quad (4.31)$$

The form of equation (4.31) is similar to the Boussinesq equation for forced and free convection in non-isothermal flow in free (non-porous media) flow when the second and third term on the right hand side can be omitted. Therefore, this form of the equation of motion is very useful for heat and mass transfer analysis. For forced convection the buoyant term $\rho_{ref} g [\beta_t (T - T_{ref}) + \beta_c (c - c_{ref})]$, which represents the momentum transfer caused by the combined buoyancy forces, can be neglected while for free convection the term $(-\nabla p + \rho_{ref} g)$ is small and omitting it is usually appropriate [19]. It is also customary [19] to replace ρ on the left side of equation (4.31) by the gas density at inlet conditions. This substitution has been successful for free convection at moderate temperature differences. Under these conditions the fluid motion is slow, and the acceleration term $\partial v / \partial t$ is small compared to g [19].

4.2.2.2 Flow in the condenser

Figure 4.5a shows the physical system of direct contact condensation in the PCM condenser. Figure 4.5b shows a schematic illustration of energy and mass flow in a rectangular finite element of the packed bed. Comparing figure (4.5) and figure (4.4), due to similarity between the evaporator and condenser designs, a similar set of coupled partial differential equations (4.11) – (4.18) as well as other state variable equations are found to represent heat and mass balances for the condenser. Altering the signs of the last two terms in both equations (4.12) and (4.13), the same form of the energy and mass balance equations could be applied on the condensation bed, with some modifications to take into account the condensation on the solid surface that might take place in parallel with the absorption of water vapor

on the falling liquid film. All other equations remain the same as the evaporator model.

$$\varepsilon_s \rho_s c_{app,s} \frac{\partial T_s}{\partial t} = k_{s,eff} \frac{\partial^2 T_s}{\partial z^2} + h_{ls,eff} a_w [T_l - T_s] + h_{gs,eff} a_{gs} [T_g - T_s] + \dot{m}_{cond,gs} h_{fg} \quad (4.32)$$

$$\varepsilon_l \rho_l c_l \frac{\partial T_l}{\partial t} + \varepsilon_l \rho_l c_l v_l \frac{\partial T_l}{\partial z} = \varepsilon_l k_l \frac{\partial^2 T_l}{\partial z^2} - h_{ls} a_w [T_l - T_s] - h_{lg} a_e [T_l - T_g] + \dot{m}_{cond,lg} h_{fg} \quad (4.33)$$

$$\begin{aligned} \varepsilon_g c_{p,g} \frac{\partial(\rho_g T_g)}{\partial t} + \varepsilon_g c_{p,g} \frac{\partial(\rho_g v_g T_g)}{\partial z} &= \varepsilon_g k_g \frac{\partial^2 T_g}{\partial z^2} - h_{gs,eff} a_{gs} [T_g - T_s] - h_{lg,eff} a_e [T_g - T_l] \\ &- \dot{m}_{cond,lg} h_{fg} - \dot{m}_{cond,gs} h_{fg} \end{aligned} \quad (4.34)$$

$$\varepsilon_g \frac{\partial c}{\partial t} = \varepsilon_g D \frac{\partial^2 c}{\partial z^2} + \varepsilon_g \frac{\partial(c v_g)}{\partial z} - \dot{m}_{cond,lg} - \dot{m}_{cond,gs} \quad (4.35)$$

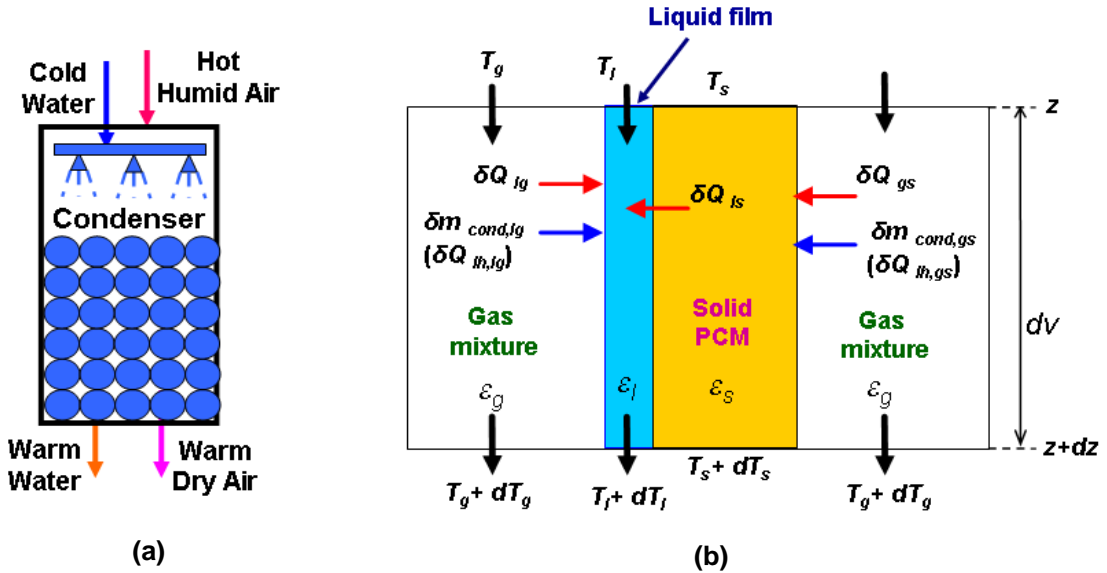


Figure 4.5: Schematic of heat and mass transfer in the condenser; (a) Layout of the condenser, (b) energy and mass balance over a control volume

The vapor condensation takes place at two interfaces: gas/liquid interface and gas/solid interface. The condensation mass flow rate m_{cond} is expressed in $(\text{mol} \cdot \text{s}^{-1} \cdot \text{m}^{-3})$. The corresponding latent heat of condensation $Q_{lh,lg}$ and $Q_{lh,gs}$ is absorbed by the

liquid and solid phases, respectively. At steady state conditions, the energy flow from gas to solid phase equilibrates with the energy flow from solid to liquid phase and the local temperatures of all phases remain constant. Any change of the system parameters will break steady state conditions, and the local temperatures will change.

The condensation rate depends mainly on the vapor pressure gradient between the bulk gas phase from one side and both the gas-liquid interface and the gas-solid interface from the other side. The vapor pressure is a direct function of the respective local temperatures, assuming saturation conditions in closed loop cycles. However, the sensible energy flow components also affect the film temperature at gas-liquid interface and gas-solid interface, which indirectly affects the condensation rate. On the other hand, condensation contributes a considerable fraction of latent heat to the liquid and solid phases and leads to rising their temperatures, which in turn affects both heat and mass balances. In fact, the microscopic analysis of the condensation process is much more complicated than the described macroscopic analysis, while the later is sufficiently accurate for the present application and range of operation conditions in comparison with the experimental measurements as will be presented later.

4.2.4 Closure relationships

Predictive models for packed column performance incorporate macroscopic properties of the entire column based on volume or spatial averaging technique which was developed by Slattery [26], rather than focusing rigorously on underlying local variations of momentum, heat, and mass transfer processes. Hence, closure models have to be provided in the numerical scheme to capture the information that is lost in the averaging process. Careful selection of the appropriate closure relationships from literature is therefore a fundamental factor for achieving high accuracy of the simulation model. Modeling and design of a randomly packed distillation column requires a reliable specification of effective interfacial areas, phase fractions, heat and mass transfer coefficients, and pressure drop. The next sections will be devoted to the adopted modeling procedures and calculations of such critical parameters.

4.2.3.1 Evaporation and condensation rates

The evaporation rate, the condensation rates at the gas/liquid interface and the gas/solid interface can be written respectively as a function of the difference between the vapor pressure or vapor concentration at these interfaces and the vapor pressure or vapor concentration at the bulk gas:

$$\dot{m}_{evap} = k_g a_e (c_{inter}(T_l) - c) \quad (4.36)$$

$$\dot{m}_{cond,gl} = k_g a_e (c - c_{inter}(T_l)) \quad (4.37)$$

$$\dot{m}_{cond,gs} = k_{gs} a_{gs} (P_v - P_{v,inter}(T_s)) \quad (4.38)$$

Where P_v is the saturation vapor pressure (pa), $P_{v,inter}(T_s)$ is the saturation vapor pressure at the interface as a function of the particle temperature, c is the water vapor concentration (mol/m^3), and $c_{inter}(T_l)$ is the interfacial water vapor concentration at the liquid water temperature. As the liquid side heat transfer coefficient is generally much greater than that of the gas side, the temperature difference between the interface and bulk liquid is very slight, the interfacial temperatures are assumed equal to the liquid temperature.

The interfacial concentration can be expressed as a function of the interface temperature (T_{inter}) by combining the Clapeyron equation, which represents the dependence of saturation pressure on saturation temperature, and the ideal gas equation of state:

$$c_{inter}(T_{inter}) = \frac{P_{ref}}{RT_{inter}} \exp \left[\frac{-h_{fg}}{R} \left(\frac{1}{T_{inter}} - \frac{1}{T_{ref}} \right) \right] \quad (4.39)$$

where the reference pressure $p_{ref}=618.9\text{Pa}$, the universal gas constant $R=8.314\text{J}/\text{mol}/\text{K}$, latent heat of condensation $h_{fg}=45050\text{J}/\text{mol}$, and the reference temperature $T_{ref}=273.15\text{K}$. Thermodynamic relationships are used to evaluate the phases partial pressures and other thermophysical properties of humid air as presented in Appendix D.

4.2.3.2 Void fraction and specific packing area

The void fraction is defined as the ratio of the volume of voids to the overall volume of a packing. It is not only strongly dependent on the method by which the container is packed but also on the ratio of the container diameter to the diameter of the packing particle (d_{bed}/d_p). An empirical relationship between the void fraction for randomly packed uniform spheres in a cylindrical bed was derived by Torab and Beasley [27] from real data as follows:

$$\varepsilon = \varepsilon_l + \varepsilon_g = 0.4272 - 4.516 \times 10^{-3} (d_{bed}/d_p) + 7.881 \times 10^{-5} (d_{bed}/d_p)^2 \quad (4.40)$$

This relation can be used to predict the void fraction as a function of (d_{bed}/d_p) for modeling and optimization of schemes for values of (d_{bed}/d_p) < 28. For values of (d_{bed}/d_p) > 28 the void fraction is 0.3625 [27]. The solid fraction in the packed bed can be directly determined:

$$\varepsilon_s = 1 - \varepsilon \quad (4.41)$$

4.2.3.3 Liquid and gas hold-ups

Liquid hold-up is the liquid present in the void spaces of the packing. Total liquid hold-up is usually divided into two components: dynamic and static. Static hold-up is the liquid remaining on the packing after it has been fully wetted and drained for a long time. It depends on several variables: geometry and size of the particles, method of packing of the column, physical properties of the liquid and the surface of the solid, capillary and gravitational forces, and physical and thermodynamic properties of the solid-liquid-gas system. Viscosity has been mentioned by several authors as a factor that can have a direct impact on the static liquid hold-up. Shulman et al. [38] correlated their experimental data with an expression that included the viscosity and this model is recommended [38] for calculation of static liquid hold-up. Normally this static hold-up is not large and thus not of great significance [36].

This is important for the present study as it has direct effect on the available area for heat and mass transfer (dry or wetted areas) as well as pressure drop, especially so in naturally drafted operation, which is very sensitive to small values of pressure loss. Reasonable amount of liquid hold-up is necessary for good mass transfer and efficient tower operation.

High hold-up increases pressure drop in the column [32]. By increasing the liquid flow rate, the liquid holdup grows steadily. After reaching the loading point (the flow rate at which the vapor phase begins to interact with the liquid phase to increase the interfacial area in the packed bed, see section (3.6), the holdup increases significantly and reaches its maximum at the flooding point. At this point the countercurrent flow of gas and liquid breaks down [33]. Below the loading point the holdup is a function only of the liquid rate; above the loading point the holdup also depends on the gas rate. The region where there is an influence of gas rate is commonly known as the loading region [29].

As the liquid hold-up increases with increasing liquid viscosity, usual liquid hold-up graphs [36] for an air/water system apply to a liquid viscosity of about $0.001 \text{ kg}\cdot\text{m}^{-1}\cdot\text{s}^{-1}$. It is recommended [36] that only 3.8 cm (1.5 inch) and larger size packings be used for handling liquids of $0.05 \text{ kg}\cdot\text{m}^{-1}\cdot\text{s}^{-1}$ or higher viscosities.

Stichlmair et al [29] developed a model based on the particle model to study the liquid holdup and gas pressure drop in beds of random or structured packing. Among various models that were examined throughout this study, Stichlmair et al [29] model was the simplest and most reliable model for spherical packing when predicted friction factor and pressure drop were evaluated against experimental data presented by Bauer [30], see figure (B.1) in Appendix (B) and against other experimental data listed in Klerk [31]. The model of Stichlmair et al. [29] was considered by Kister [32] to be the most fundamental model available, since it

includes the determination of liquid holdup both below and above the loading point. This model will be shortly described to the extent that is only needed for determination of liquid and gas holdups as closure relationships, while calculation procedures for estimation of the pressure drop are presented in Appendix (B). Holdup measurements for eight different types of packing have been correlated by Stichlmair et al [29] as follows:

$$h_l = \varepsilon_l = 0.555 Fr_l^{1/3} \quad (4.42)$$

Where h_l (or ε_l in energy and mass balance equations) is a function of Froude number, which is defined as:

$$Fr_l = v_{l,\text{sup}}^2 \frac{a}{g \varepsilon^{4.65}} \quad (4.43)$$

where $v_{l,\text{sup}}$ is the superficial liquid velocity. The gas fraction can be determined as:

$$\varepsilon_g = \varepsilon - \varepsilon_l \quad (4.44)$$

Where in conventional particle bed, the specific packing area per unit volume a is directly related to the porosity ε through the following equation:

$$a = \frac{6(1 - \varepsilon)}{d_p} \quad (4.45)$$

It is interesting to mention that although the Brinkman equation can be used to model the flow field, Stichlmair et al [29] model will be used for determination of the liquid and gas holdup (which are fundamental parameters for modeling heat and mass transfer) and can also be used for calculation of pressure drop along the packed bed under forced draft where the influence of buoyant forces can be neglected.

4.2.3.4 Interfacial areas

Generalized methods for predicting the mass-transfer performance of larger-scale packed distillation columns have been reviewed by Kister [32]. For random packing, only four methods have been thought to be general and reliable enough to merit serious consideration for commercial design [40]. Namely, Cornell et al. [42], Onda et al. [35], Bolles and Fair [44], and Bravo and Fair [43]. Additionally, based on the integrative approach to the pressure drop and liquid holdup model of Stichlmair et al [29], Wagner et al. [40] developed a new model to provide a correlation for effective interfacial area in randomly packed columns.

Several models and approaches for mass transfer coefficients on both the gas and liquid sides are presented by Wagner et al. [40]. Various approaches and models for determination of the wetted and effective interfacial areas for mass transfer presented by Kister [32] and Gandhidasan [41] were preliminary examined and compared against each other.

One particular problem to address here is the significant discrepancies between the predicted values of mass transfer coefficients between various approaches and models. It is observed that many researchers have used Onda et al. [35] model to describe the liquid-gas interfacial areas and mass transfer coefficient in distillation columns. Klausner et al. [45] have already developed a detailed heat and mass transfer analysis for a HDH system called the diffusion driven desalination (DDD) process. They extensively tested Onda et al. [35] correlations and used it to evaluate the mass transfer coefficients on the liquid and gas sides. They reported that excellent results were obtained against experimentation measurements [47]; thus the same approach will be applied here.

Nevertheless, Klausner and Mei [45-46] modified Onda et al. [35] model described by equations (4.46-4.47) by introducing a constant of 2.2 instead of 1.45 for calculating the wetted interfacial area in the (DDD) system. They argued that the model underestimates the wetted surface area of the packing and this was the reason behind this modification in equation (4.47). The model is based on the concept of wetted packing area as a geometric parameter in determining the Reynolds number for the liquid as opposed to the interfacial area.

$$\frac{a_e}{a} = 1 - \exp \left[-1.45 \left(\frac{\sigma_c}{\sigma_l} \right)^{0.75} (\text{Re}_l)^{0.1} (\text{We}_l)^{0.2} (\text{Fr}_l)^{-0.05} \right] \quad (4.46)$$

$$a_w = a \left\{ 1 - \exp \left[-2.2 \left(\frac{\sigma_c}{\sigma_L} \right)^{0.75} (\text{Re}_{LA})^{0.5} (\text{We}_L)^{0.2} (\text{Fr}_L)^{-0.05} \right] \right\} \quad (4.47)$$

Therefore, this modification could be even more crucial for the present analysis due to the existence of conductive packing media or a solid phase in the energy and mass balances. However, their predicted performance using this modified correlation is always higher than their experimental measurements in terms of the outlet air humidity content, outlet water temperature, and outlet air temperature.

In the original model, Onda et al. [35] assumed the wetted area was equal to the effective interfacial area. The total wetted surface area in the irrigated column is expected to be greater than the effective area for mass transfer due to existence of static liquid holdup which contributes little to heat and mass transfer. This finding has been ascertained during the course of preliminary calculations of the effective

interfacial area, when Onda model results nearly coincide with that of the conservative model of Shi and Mersmann [34]. Another important finding that has been discovered in the course of the present analysis is that the predicted wetted area by the modified Onda et al.'s correlation nearly coincides with that of Wagner et al. [40]. Based on these findings, the original and modified Onda et al.'s correlations will be used for describing the effective interfacial area and total wetted surface area in the column, respectively.

4.2.3.5 Liquid-gas heat and mass transport coefficients

Following the methodology of Klausner et al. [45], Individual mass transfer coefficients for liquid and gas sides are evaluated using Onda et al.'s [35] correlations. Applying analogy between heat and mass transfer, the individual and overall heat transfer coefficients at the gas-liquid interface have been formulated based on the two resistance theory [45] as follows:.

$$K_l = 0.0051 \left(\frac{L}{a_w \mu_l} \right)^{2/3} \left(\frac{\mu_l g}{\rho_l} \right)^{1/3} \left(\frac{\rho_l D_l}{\mu_l} \right)^{-0.5} (ad_p)^{0.4} \quad (4.48)$$

$$K_g = C \left(\frac{G}{a \mu_g} \right)^{0.7} \left(\frac{\mu_g}{\rho_g D_g} \right)^{1/3} (ad_p)^{-2} a D_g \quad C = \begin{cases} 5.23 & d_p > 0.015 \\ 2 & d_p \leq 0.015 \end{cases} \quad (4.49)$$

Where K_l and K_g are mass transfer coefficients on the liquid and gas sides respectively. Using analogy between heat and mass transfer, the heat transfer coefficients on each side (U_l and U_g) and the overall heat transfer coefficient h_{lg} are computed as follows [45]:

$$U_l = K_L (\rho_l c_{pl} k_l / D_l)^{1/2} \quad (4.50)$$

$$U_g = K_g (\rho_g c_{pg})^{1/3} (k_g / D_g)^{2/3} \quad (4.51)$$

$$U = h_{gl} = (U_l^{-1} + U_g^{-1})^{-1} \quad (4.52)$$

A general empirical correlation for the condensation mass transfer coefficient at the gas-solid interface (i.e. condensation on dry PCM patches), which was originally developed by Sun and Besant [50] to calculate the adsorption rate of water vapor in a desiccant bed of silica gel particles, has been modified and introduced heuristically in the present model:

$$k_{gs} = 0.048 \text{Re}_g^{-0.3} \cdot \frac{G}{M_g P_a (\mu_g / \rho_g D_g)^{2/3}} \quad (4.53)$$

where $G=\rho U_d/\varepsilon_g$ is the pore mass flux of the gas phase, $Re=4r_h G/\mu_g$ is Reynolds number, M_g is the molecular weight of gas (g/mol), P_a is the dry air pressure (pa), U_d is the Darcian velocity of gas, and $r_h=\varepsilon_g/a$ is the hydraulic radius for gas flow in the porous medium.

4.2.3.6 Fluid-particle heat transfer coefficient

The interfacial convective heat transfer coefficient for fluid flow in fixed packed beds (thermal regenerators), which is needed when the local thermal equilibrium between the fluid and solid phases breaks down, is a very important factor in the heat transfer performance of the storage medium. It is known that the heat transfer performance of thermal regenerators is dependent upon many other factors, for example, the heat exchanger design, the physical properties of the heat transfer fluid, etc. Among them, the heat transfer coefficient between the packing (solid phase) and the heat transfer fluid (h_{sf}) is one of the most important factors, which may strongly influence the heat transfer performance of the regenerator. Therefore, careful selection of the heat transfer coefficient correlation from literature is important. Various approaches and correlations for determining the interfacial convective heat transfer coefficient between the bed packing and the working fluid are discussed and compared in Appendix (C).

The correlation of Wakao and Kaguei [15] was used for the fluid/solid heat transfer coefficient in both the single and two phase flow regenerators, where “fluid” stands for either liquid or gas phase. Wakao and Kaguei [15] have experimentally examined the results on h_{sf} for both steady and transient behaviors and reached to a reliable correlation. They have found the following correlation for h_{sf} for spherical particles (or the dimensionless form of it; the Nusselt number):

$$Nu_d = \frac{h_{sf} d_p}{k_f} = 2.0 + 1.1 Re^{0.6} Pr^{\frac{1}{3}} \quad (4.54)$$

Where $Re=\varepsilon u_p d_p/\nu = u_D d_p/\nu$, where u_p and u_D are the average pore velocity (bulk mean velocity) and the Darcian velocity of the fluid respectively. However, Wakao and Kaguei correlation neglects the axial diffusion effects and is valid only for packed beds with ($\varepsilon \approx 0.4$). The Jefferson degradation factor [14] was introduced in the fluid-solid heat transfer coefficients to account for the conduction resistance inside the PCM spheres while using a one-dimensional model for the packed bed as mentioned earlier and described by equation (4.9).

Figure (4.6) compares the values of effective heat transfer coefficients obtained with four different Nusselt correlations (described in appendix C) for the flow through a spherical packing in dependency on the Reynolds Number. The values differ significantly from each other, which could be due to differences in experimental boundary conditions under which these correlations were determined. The

correlation of Wakao and Kaguei [15], which gives a rather lower value, proved to match the experimental measurements very well as will be shown in chapter 6.

4.2.3.7 Evaluation of effective thermal properties

According to the volume averaging concept, effective thermal properties should be used in the energy and mass balance equations rather than the real properties of pure components. The effective thermal conductivity k_{eff} characterizes the heat transfer properties in a fixed bed regenerator containing multi-components and multi-phases. The heat transfer properties include conduction through the solid beads, conduction across the contact points of solid particles, film convection through the fluid layer involving the solid particles, possibly radiation, and others [16]. These mechanisms of heat transfer are generally included in one single parameter called the “effective thermal conductivity” [16].

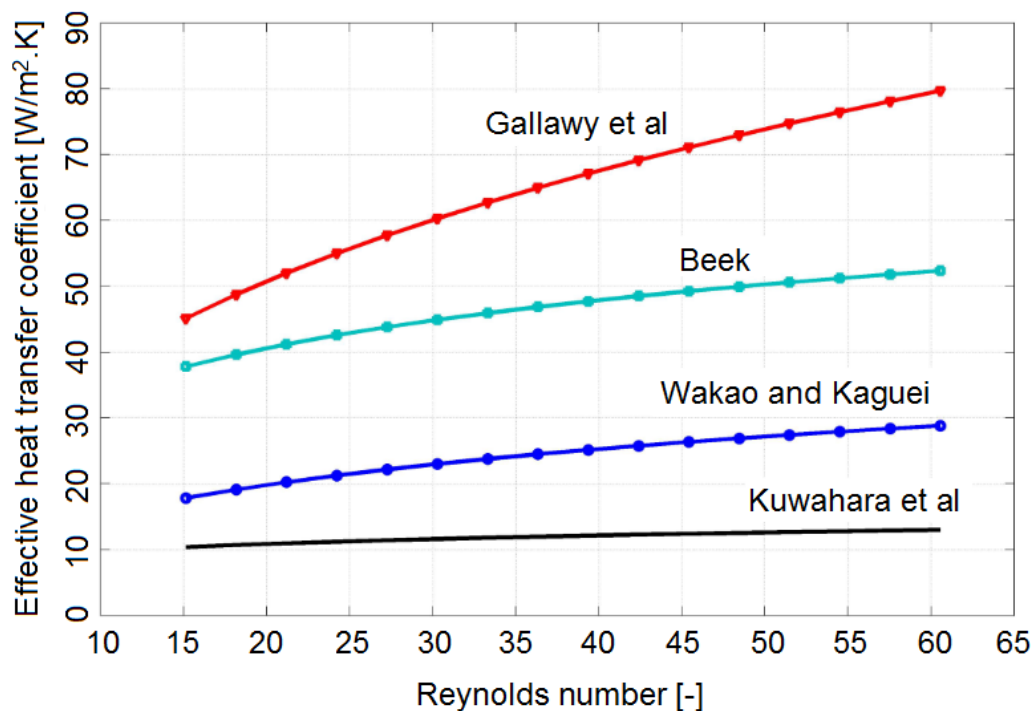


Figure 4.6: Effective heat transfer coefficients obtained with different Nusselt number correlations.

Kaviany [11], Wakao and Kaguei [15], and Bird et al. [19] presented different approaches to model the thermal conductivity for a single and two phase flow from the conductivities of the fluid k_f and solid k_s phases. However, for a packed bed of spherical particles, the following correlation has been adopted from Bauer [30] for arbitrary pore shapes and concentrations.

$$\frac{k_{eff}}{k_s} = (1 - \varepsilon)^{3/2} \quad (4.55)$$

This correlation has been examined and it was found that although simple, it accurately produces very similar results as the other complex correlations presented in the literature. The effective densities and specific heats of the fluid and solid phases are calculated as follows [15]:

$$\rho_{f,eff} = \varepsilon_f \rho_f \quad \rho_{s,eff} = (1 - \varepsilon) \rho_s \quad (4.56)$$

$$c_{f,eff} = \varepsilon_f c_f \quad c_{s,eff} = (1 - \varepsilon) c_s \quad (4.57)$$

4.3 Hydrodynamic analysis

4.3.1 Gas-liquid interaction

The countercurrent flow of gas and liquid in a packed column is characterized by two operating points: loading and flooding. The gas-liquid interaction is one of the essential factors affecting pressure drop in countercurrent two phase flow in packed beds. It can be assumed [37] that the increasing velocity difference of the two phases leads to a number of effects on the liquid film. The interface will first become increasingly wavy, after which the gas entrains droplets and finally forces the liquid film upwards. These effects will lead to an increase of the pressure drop, which represents the extra energy dissipation in the gas phase. Therefore, Strigle [36] gives two definitions for the lower loading point, which is the highest flow rate at which the pressure drop is proportional to the square of the gas flow rate, and the loading point, which is the flow rate at which the vapor phase begins to interact with the liquid phase to increase the interfacial area in the packed bed. Above this gas flow rate, the column will reach a maximum capacity that will be determined either by massive liquid entrainment in the gas phase or by excessive liquid hold up in the packed bed.

At high liquid flow rate, depending on the size of the packing, the packed bed voids largely tend to be filled with liquid, and some of the gas phase actually is aspirated down the column in the liquid phase. A sufficient liquid retention time in the base of the column will permit these aspirated gas bubbles to rise to the surface of the liquid pool and escape back into the gas phase. Strigle [80] emphasized that prudent designer will use a large enough packing to avoid this area of operation. For example, 5 cm (2 inch) packings don't exhibit this phenomenon below a liquid rate of 88.6 ton.hr⁻¹.m⁻², and 8.85 cm (3.5 inch) packings have been operated at liquid rates as high as 158 ton.hr⁻¹.m⁻². The foregoing maximum design liquid rates are based on a liquid viscosity no higher than 1 cps for 2.5 cm size packing, 0.0018 kg.m⁻¹.s⁻¹ for 3.8 cm size packing, and 0.0032 kg.m⁻¹.s⁻¹ for 5 cm size packing.

At flooding, essentially all the voids are filled with liquid. The flooding point can be described in a number of ways, but the clearest definition [39] is the point where at a certain gas flow, flow reversal of the liquid occurs and the liquid is unable to flow through the packing and collects on the top of the bed. The pressure drop per unit height increases rapidly due to this liquid accumulation. This point is the operating limit for counter-current flow of gas and liquid through solid packing. Flooding is a kind of hydrodynamic phenomenon to be prevented in the operation of packed columns, which are extensively used in absorption and distillation, and in empty tubes mainly used in reflux condensers, where the condensate moves downward counter-currently with respect to the uprising vapor. Kister and Gill [32] applied the principle that the packing pressure drop at flooding point increases as the packing capacity increases to derive a simple flood point correlation.

$$\Delta P_{Fl} = 0.115 F_p^{0.7} \quad (4.58)$$

Equation (4.58) expresses the pressure drop at the flood point as a function of the packing factor (F_p) alone. It is recommended [32] to use this correlation for flood point prediction if pressure drop data are available or when pressure drop can be reliably predicted.

Flooding is not often of significant importance for small schemes with relatively low gas flow rates, such as small scale HDH system proposed in the present study. On contrary, as the HDH systems are usually operated at relatively low liquid loads, the minimum wetting rate becomes significantly more important than the flooding rate. The minimum wetting rate (MWR) is the lower stability limit of packing. It is the liquid load below which the falling liquid film breaks up, and the liquid storage causes dewetting of the packing surface [32]. Kister [32] presented various correlations and commonly known rules of thumb for estimating the MWR and recommends a simple correlation/rule of thumb:

$$L_{MW} = L \times (60/a)^{0.5} \quad (4.59)$$

where L is a reference minimum wetting rate based on an average value of a about 60 gpm.ft⁻². Values of L for different packing materials are tabulated in Kister [32], for PVC and Polypropylene L is 1.4 and 1.6 gpm.ft⁻² (~ 950.5 – 1086.3 l.m⁻².h⁻¹) respectively.

4.3.2 Column Sizing

Three different techniques are being used for tower sizing; the flooding point, the maximum operation capacity (MOC), and the maximum pressure drop criteria. In flooding point criterion, packed towers are usually designed at 70 to 80 percent of the flood point flow velocity. This practice provides sufficient margin to allow for

uncertainties associated with the flood-point concept and prediction and to keep the design point away from the region at which efficiency rapidly diminishes (just below the flood point) [32]. Strigle [36] recommended designing packed towers with a 10 to 20 percent margin from the maximum operational capacity. Since MOC is usually about 5 percent below the flood point, the Strigle's criterion is equivalent to designing at 76 to 86 percent of flood point velocity. This criterion is therefore less conservative than the flood point criterion [32].

Packed towers are also designed that the pressure drop at any point in the tower does not exceed a recommended maximum value. Maximum pressure drop criteria for packed towers are listed by Kister [32]. The generalized pressure drop correlation (GPDC) is the classic sizing method for packed towers and is used in many industries. It is, however, based mostly on the small pilot tower data. As long as the correlation is applied to small packing, it appears to give reasonable results, but when the performance of large packing in large towers is assessed, then the results appear overly optimistic [89]. The majority of designers prefer the flood point criterion over the MOC [32]. For more conservative designs, the maximum pressure drop criterion is recommended [32] to be used with the flood point criterion or MOC criterion.

Strigle [36] stated that the use of random dumped tower packing is not customary in water cooling towers. Because of the pressure drop available, the maximum packed depth for large size plastic packings is under 1.8 m. Some figures are provided for the height of gas phase transfer unit for random packing cooling towers. The average values for packing sizes 2.5, 3.8, 5, and 7.75 or 8.9 cm, are 0.4, 0.46, 0.56, and 0.76m respectively. In addition, the average packed depths specified must make allowance of around 20% to 40% greater than these values for large size tower packings to account for lower quality distribution of both liquid and gas [36]. He added that, cooling towers which operated with natural draft are hyperbolic and may require an overall height of 67m. The fill that used in such a column must be quite open to avoid any significant pressure drop. Such fill can have a T- or V- shape cross section molded from perforated plastic sheets. Corrugated sheets made of asbestos and cement are popular in large natural draft towers, noting that asbestos is banned for its carcinogenic effects. A ceramic cellular block that is stacked into the tower also is used. However, these fills provide a small interfacial area per unit volume so mass transfer is rather low per unit of packed depth.

4.4 Modeling solid-liquid phase change

Typically, three methods have been developed for fixed domain class solid-liquid phase change problems: temperature based method, the enthalpy-based method, and the apparent heat capacity [18].

The apparent heat capacity method is adopted in this study, since the temperature field is the primary dependent variable that can be derived directly from the solution. The apparent heat capacity assumes that the phase change occurs over a small temperature interval rather than at a sharp melting temperature. However, in the present study, all the three types of PCM packing media have a melting temperature interval of 2°C around the specified melting points according to the manufacturer's data. Civan and Sliepcevich [18] have formulated the energy equation for a two-phase system of a pure substance in a semi-infinite media undergoing phase change, as depicted in figure (4.7), as follows:

$$\left\{ \frac{\partial(\rho_2 h_2)}{\partial T} + \left[\frac{\partial(\rho_1 h_1)}{\partial T} - \frac{\partial(\rho_2 h_2)}{\partial T} \right] \varphi_1 + (\rho_1 h_1 - \rho_2 h_2) \left(\frac{d\varphi_1}{dT} \right) \right\} \frac{\partial T}{\partial t} + \nabla \cdot \{ (\rho_1 h_1 V_1 + \rho_2 h_2 V_2) - [k_2 + (k_1 - k_2) \varphi_1] \cdot \nabla T \} - \frac{Dp}{Dt} = 0 \quad (4.60)$$

The energy equation in the form of equation (4.60) is called an apparent heat capacity formulation in which the quantities enclosed in the braces preceding $\partial T/\partial t$ represent an "apparent" volumetric heat capacity. Since the volumetric latent heat effect of phase change, $(\rho_1 h_1 - \rho_2 h_2)$, is included in the apparent volumetric heat capacity definition, this formulation allows for a continuous treatment of a system involving phase transfer. In addition, it doesn't require the solution of separate, single-phase equations for each of the phases.

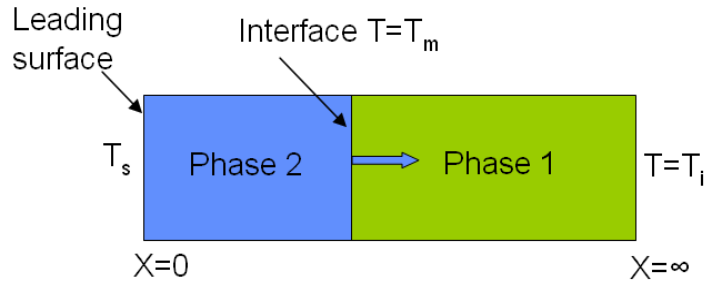


Figure 4.7: Schematic of a semi-infinite domain undergoing phase change

For simplification Civan and Sliepcevich [18] assumed that the pressure is constant, the phases are isotropic and homogeneous, the phase densities are equal, and there is no motion in either of the phases. Accordingly, equation (4.60) reduces to:

$$\rho c \left(\frac{\partial T}{\partial t} \right) = \left(\frac{\partial}{\partial x} \right) \left(k \frac{\partial T}{\partial x} \right) \quad (4.61)$$

in which

$$\rho = \rho_1 = \rho_2 \quad (4.62)$$

$$c_{app} = c_2 + (c_1 - c_2)\varphi_1 + \Delta H_m \frac{d\varphi_1}{dT} \quad (4.63)$$

$$k = k_2 + (k_1 - k_2)\varphi_1 \quad (4.64)$$

In equation (4.63), c_{app} denotes the specific apparent heat capacity and ΔH_m the specific latent heat for change from phase 2 to phase 1, which are determined according to the specific enthalpies of phases 1 and 2, respectively. If the phase transition takes place instantaneously at a fixed temperature, then a mathematical function such as:

$$\varphi_1 = U(T - T_t) \quad (4.65)$$

is representative of the volumetric fraction of the phase 1, where U is a step function whose value is zero when $T < T_t$ but equals one otherwise. Its derivative, i.e., the variation of the phase 1 fraction with temperature is:

$$\frac{d\varphi_1}{dT} = \delta(T - T_t) \quad (4.66)$$

in which $\delta(T - T_t)$ is the Dirac delta function whose value is infinity at the transition temperature, T_t , but is zero at all other temperatures. To alleviate this singularity the Dirac delta function can be approximated by a uniform distribution over a finite temperature interval, thus equation (4.66) is replaced by:

$$\frac{d\varphi_1}{dT} = 1/(2\Delta T_t) \quad (4.67)$$

Alternatively a normal smooth distribution function can be used as a smooth variation,

$$\frac{d\varphi_1}{dT} = (\Gamma \pi^{-1/2}) \exp[-\Gamma^2(T - T_t)^2] \quad (4.68)$$

in which Γ is so chosen that $erf(\Gamma \Delta T_t) = 1.0 - \lambda$, where ΔT_t is one-half of the assumed phase change interval and λ is a sufficiently small positive number. Consequently, the integrals of equations (4.66) and (4.67) yield the linear and the error function approximations, respectively, for the phase 1 fraction. With conventional finite difference and finite element methods the phase 1 fraction derived from equations (4.67) or (4.68) by integration should be used to avoid the numerical instabilities arising from the jump in the values of the volumetric fraction of phase 1 from zero to one. It has been shown from the numerical solutions carried out by Civan and Sliepcevich [18] that the results obtained by approximating the phase change at a

fixed temperature by a gradual change over a small temperature interval should be acceptable if $(2\Delta T_i)/(T_i - T_s) < 0.1$. Through the use of Equation (4.63), the transient model is applicable anywhere in the storage medium. This model removes the necessity of tracking the moving phase change boundary and generally simplifies the numerical solution.

4.5 Macro-dynamic performance analysis of the HDH system

4.5.1 Cooling tower performance

In comparison with the two phase flow in the PCM-packed columns (i.e. the evaporator and condenser), the energy balance for a conventional cooling tower which is packed with nonconductive media doesn't include the solid sub-domain. Thus, this results in two energy balance equations for both liquid and gas phases instead of three for the case of PCM packing. Though the cooling tower theory is basically different from the developed mathematical modeling approach, it is indeed useful for defining and identifying the crucial indicative parameters for addressing the system performance. Since operation and design theory of evaporative coolers and direct contact condensers is closely related, these parameters can serve both of them. The practical theory of cooling towers operation was, perhaps, first developed by Merkel [54]. This theory has been presented and discussed in detail throughout numerous heat and mass transfer textbooks as the basis of most cooling tower analysis and design rating. Appendix (D) covers the theoretical development and analysis of Merkel's equation, which is extremely important to develop a common understanding of the performance measures in the subsequent discussions.

4.5.2 Humidifier efficiency

The performance of a humidification column can be evaluated by Braun's [58] effectiveness model for a counter flow cooling tower. This model was based on Merkel's assumptions which neglect the effect of the water loss due to evaporation and set the Lewis number to unity. Braun defines air-side effectiveness, ζ_a as the ratio of the actual heat transfer to the maximum possible air-side heat transfer that would occur if the exiting air stream were saturated at the temperature of the inlet hot water (i.e., $h_{a2} = h_{s,w2}$ with reference to figure (4.1) for the present study);

$$\zeta_{evap} = \frac{Q_{g,actual}}{Q_{g,maximum}} = \frac{Q_{g,actual}}{\dot{m}_g (h_{s,w2} - h_{g1})} \Bigg|_{evap} \quad (4.69)$$

where $h_{s,w2}$ is the saturated air enthalpy at inlet water conditions, and h_{a1} is the enthalpy of the inlet air. Analogously to a dry counter flow heat exchanger, Braun

[58] evaluated the cooling tower air-side effectiveness ζ_{evap} in terms of a saturation specific heat capacity C_s :

$$\zeta_{evap} = \frac{1 - \exp[-NTU(1 - C_{r,evap})]}{1 - C_{r,evap} \exp[-NTU(1 - C_{r,evap})]} \quad (4.70)$$

where $C_{r,evap}$ is the gas to water heat capacity flow ratios;

$$C_{r,evap} = \frac{C_{\min}}{C_{\max}} = \frac{\dot{m}_g C_{s,evap}}{\dot{m}_{hw} C_w} \quad (4.71)$$

Braun [58] linearized the air saturation enthalpy over the temperature, as depicted in figure (4.8) below, for analytical determination of the exit conditions from the cooling tower. Then, he estimated an average value of saturation specific heat C_s as the average slope between the inlet and outlet water states;

$$C_{s,evap} = \frac{(h_{s,w2} - h_{s,w1})}{(T_{w2} - T_{w1})} \quad (4.72)$$

where $h_{s,w1}$ is the enthalpy of saturated air at exit water conditions.

Figure (4.9) [Singham (56)] illustrates the effect of water film temperature on the enthalpy difference between the bulk air and saturated air at the interface along the axial direction of a counter flow cooling tower ($h_s - h_g$). The air operating line begins at a point having an enthalpy ($h_{g,in}$) corresponding to the inlet wet bulb temperature T_{WB} . The vertical distance between the two operating lines represents graphically the enthalpy difference ($h_s - h_g$) (as in the integrand of equation (D.4) in Appendix D). According to the air-side effectiveness, ζ_a definition, the maximum possible air-side heat transfer would occur when the vertical distance ($h_s - h_g$) at the air exit approaches zero.

4.5.3 Dehumidifier efficiency

Since the humidifier and condenser are very similar, it is not surprising that the condenser effectiveness ζ_{cond} can be defined in a fashion similar to its counterpart evaporative cooler. When the condenser is regarded as a parallel heat exchanger, its effectiveness can be expressed as:

$$\zeta_{cond} = \frac{Q_{g,actual}}{Q_{g,maximum}} = \frac{Q_{g,actual}}{\dot{m}_g (h_{g2} - h_{s,w3})}_{cond} \quad (4.73)$$

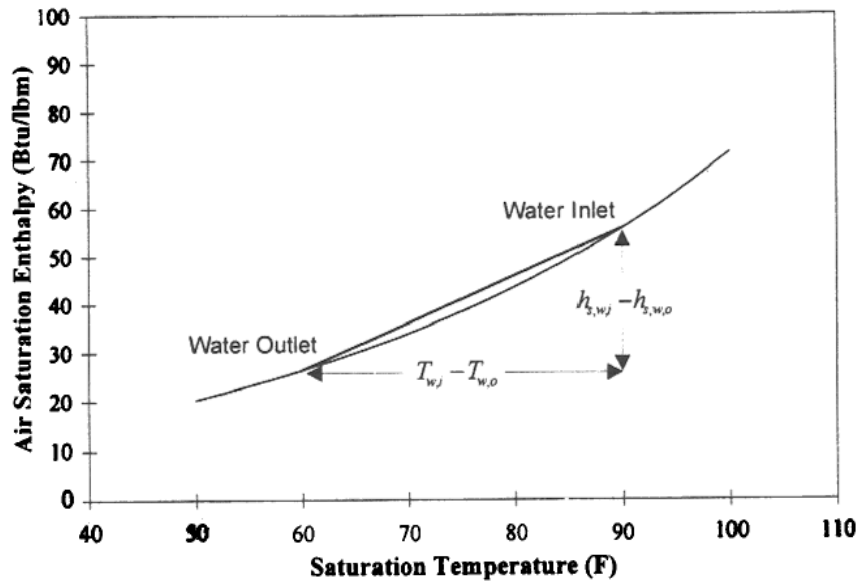


Figure 4.8: Linearization of air saturation enthalpy [58]

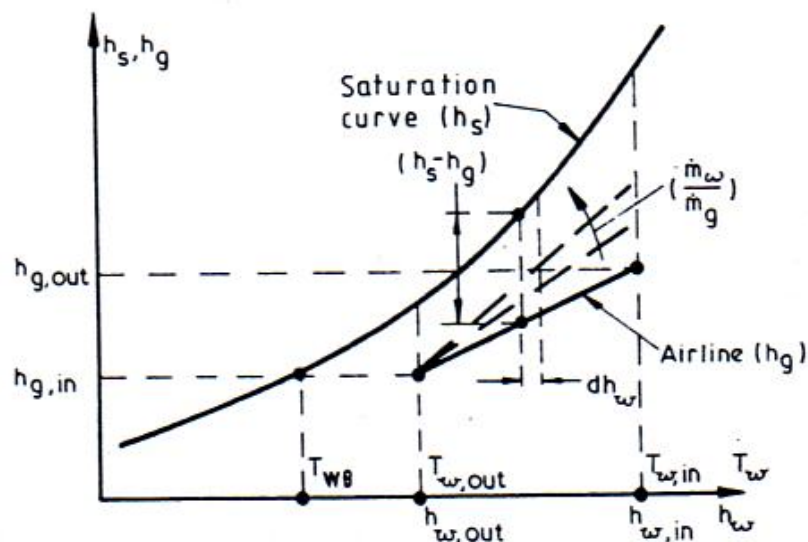


Figure 4.9: Counter current cooling tower operating lines [56]

$$\zeta_{cond} = \frac{1 - \exp[-NTU(1 + C_{r,cond})]}{[1 + C_{r,cond}]} \quad (4.74)$$

If the heat capacity flow of the gas phase is lesser than that of the liquid phase, then:

$$C_{r,cond} = \frac{C_{\min}}{C_{\max}} = \frac{\dot{m}_g C_{s,cond}}{\dot{m}_{cw} C_w} \quad (4.75)$$

$$C_{s,cond} = \frac{(h_{s,w4} - h_{s,w3})}{(T_{w4} - T_{w3})} \quad (4.76)$$

where $h_{s,w3}$ and $h_{s,w4}$ are the enthalpies of saturated air at inlet and exit water conditions respectively. The maximum heat and mass transfer and humidity change would be achieved when air is cooled down to the inlet cooling water temperature. In this idealized situation, the partial vapor pressure of the air at the outlet is equal to the saturation pressure of the liquid solution at the inlet of the column.

4.5.4 Productivity factor (PF)

This factor is a measure of how much condensation rate can be gained per unit mass transfer potential ($K_i A$) in the evaporator or condenser. It is defined as [62]:

$$PF = \frac{M_d}{K_i A} = \frac{M_d}{M_a} \times \frac{1}{NTU} \quad (4.77)$$

where M_d and M_a are the distillate rate and air mass flow rate ($\text{kg}\cdot\text{s}^{-1}$) respectively, K_i is the mean value for the overall mass transfer coefficient between water and air based on the enthalpy difference ($\text{kg}\cdot\text{m}^{-2}\cdot\text{s}^{-1}$), and A is the mass transfer surface area associated with K_i in m^2 .

4.5.5 Efficiency of the solar collector

The instantaneous overall energy balance of the solar water heater (which comprises a solar flat plate collector (FPC) and a thermal buffer) is an important consideration in the numerical prediction of the HDH system's thermal performance. The performance of the FPC is estimated using an empirical relation available in the literature [59] as a function of the inlet water temperature to the collector T_7 , the incident global solar irradiation $I_{incident}$, and the ambient temperature and:

$$\eta_{col} = 0.60 - 0.0078 \left(\frac{T_7 - T_{amb}}{I_{incident}} \right) \quad (4.78)$$

The above efficiency includes the heat losses through the connecting pipes and the flow mal-distribution in the collector absorber due to low water flow rate used [2]. The FPC efficiencies available in the market nowadays are usually higher than those given by equation (4.78). However, this might provide conservative values of fresh water production, especially as this equation was developed under the climatic conditions of Jordan in the Middle East.

Like any kind of energy conversion devices, the efficiency of a solar collector resembles the ratio between the rate of thermal energy extracted by the working medium (usable output heat) \dot{Q}_u and the incident solar irradiation $I_{incident}$ (W.m^{-2}) crossing the aperture area (A_{col}) of the collector:

$$\eta_{col} = \frac{\dot{Q}_u}{\dot{Q}_{in,col}} = \frac{\dot{Q}_u}{I_{incident} A_{col}} \quad (4.79)$$

The rate of input thermal energy through the solar collector determines the inlet temperature to the thermal buffer T_{w8} (i.e. the outlet water temperature from the FPC) under transient conditions:

$$\dot{Q}_{in,col} = \eta_{col} A_{col} I_{incident} = M_{hw} c_w (T_{w8} - T_{w7}) \quad (4.80)$$

4.5.6 Energy balance on heat exchangers

For both heat exchangers involved in the HDH process as depicted in figure 1 (i.e. the brine heater and water cooler in the condenser closed cycle) the energy balance calculations follow the same approach as Polifke and Kopitz [60]. In both cases a countercurrent regime is chosen due to its high effectiveness. In fact the brine heater has a direct influence on the recovery rate of latent heat of condensation while the water cooler has a high influence on the condenser performance. Moreover, the two heat exchangers implicitly have mutual influences on each other.

In the brine heater, the margin between the outlet hot stream temperature and the outlet cold stream temperature ($T_{w9} - T_{w7}$) is assumed to be 3K for simplification. For the water cooler, the temperature of the fresh cold water at the top of the condenser is not allowed to be more than $(T_{amb} + 3)$ K. Thus, the design of the heat exchangers is confined in determining the maximum heat transfer surface area on yearly basis under transient operation conditions:

$$A_{HE} = \frac{\dot{Q}_{HE}}{U_{HE} \Delta T_{LM}} \quad (4.81)$$

Where \dot{Q}_{HE} is the cooling duty, U_{HE} is the mean overall heat transfer coefficient, and ΔT_{LM} is the logarithmic mean temperature difference between hot and cold fluids. The heat transfer coefficient is assumed to be constant although it is strongly dependent on the mass flow rate for seek of simplicity. The value of U_{HE} is approximately estimated as $2837.7 \text{ W.m}^{-2}.\text{K}^{-1}$ for design purposes of water-aqueous solutions exchangers [61]. Real operation behaviour of the system probably could not be well reflected at this point, but it may provide reasonable qualitative and quantitative approximation of the system performance under different operation strategies.

4.5.7 Overall system performance

The overall efficiency of thermal desalination systems is commonly determined by its gained output ratio (*GOR*), illustrating how much energy that desalinated water can be produced from saline or contaminated water for each unit of energy expended. It is a measure of energy efficient utilization and recovery of the thermal heat consumption of the plant. It simply indicates the ratio of the mass of water actually produced to that produced without heat recovery for given heat input to the plant. It is defined as the ratio between the latent heat of condensation for a specific quantity of seawater to the actual external energy needed for distillation.

$$GOR = \frac{\dot{Q}_{cond}}{\dot{Q}_{in}} = \frac{\dot{m}_d h_{fg}}{\dot{Q}_{in}} \quad (4.82)$$

where h_{fg} is the latent heat of condensation. The *GOR* can be written differently, depending on the number of units of driving energy. The Performance Ratio (*PR*) is a frequently used definition for *GOR*, which is defined based on the amount of water produced in (kg) per one million Joules of heat supplied to the system. Typical *GOR* values for large-scale MSF plants range between 8 and 10 correspond to *PR* between 3.5 and 4.5 kg/MJ. This can be quite confusing and great care should be taken when dealing with technical specifications of commercial desalination plants and reviewing literature.

The input mechanical energy to the system is neglected in the calculation of *GOR* by equation (4.82) as it is assumed to be too small compared with the thermal energy input. Referring to the system closed cycle shown in figure (4.1), the rate of fresh distillate product can be calculated as follows:

$$\dot{m}_d = \dot{m}_a(w_2 - w_1) \quad (4.83)$$

where w_2 and w_1 are the moisture contents of the air entering and leaving the condenser respectively (kg_w/kg_{air}).

As mentioned earlier, the usable output heat during day time is broken down into input heat which is supplied to the HDH system and stored heat for night time operation or during cloudy hours. The quantity and quality of energy input to the HDH cycle is directly related to the storage and collector characteristics. Due to mainly transient conditions in solar operated facilities and integration of the thermal buffer in the solar system, the input energy to the HDH cycle cannot be based on a short time such as hourly or daily calculations. Thus it is possible to express the *GOR* as an integrated value over a fairly long time period or one year by the ratio between total fresh water production and total energy input. As radiation data is only available on hourly basis for one year (8760 hr/year), thus $t = 0$ to 8760 is taken into the integral. The cumulated yearly *GOR* can then be written as:

$$GOR = \frac{\int_{t=0}^{8760} \dot{m}_d(t) h_{fg} dt}{\int_{t=0}^{8760} \dot{Q}_{in}(t) dt} \quad (4.84)$$

Energy recovery is achieved in two different ways, brine recirculation and recovery of latent heat of condensation:

$$Q_{rec} = M_r c_w (T_{w5} - T_{amb}) + M_{hw} c_w (T_{w7} - T_{w6}) \quad (4.85)$$

Where M_{hw} is the hot seawater water load required for the evaporator and M_r is the recirculated brine.

4.5.8 Salt and mass flow balances

Assuming that the distillate water is free of salt, the overall mass and salt balances can be applied on the HDH system. As a starting point, the mass of the brine blow down M_b can be related to the feed seawater make-up M_f through a salt balance on the evaporator:

$$r_c = \frac{M_f}{M_b} = \frac{S_b}{S_f} \quad (4.86)$$

where r_c is the salt concentration ratio, S_b , and S_f are the corresponding salt concentrations for rejected brine and feed seawater respectively. The amount of rejected and recirculated brine M_r can be determined respectively as:

$$M_b = \frac{M_d}{r_c - 1} \quad (4.87)$$

$$M_r = M_{hw} - M_f \quad (4.88)$$

The cumulated *GOR* and daily fresh water production will be used for investigating the performance and transient behavior of the PCM-supported HDH system under varying weather conditions of El-Arish city on the Mediterranean Sea north of Egypt.

4.6 Representation of the MEHH and MECD phenomena

The section begins by listing some fundamental points towards laying out the approach to the representation of MEHH by the mathematical mode. The representation approach should answer a key question, which is deemed to be important to an understanding of the connections between the mathematical formulations presented in the previous sections and the coupled multi-physics of dual phase change phenomena involved on both micro and macro scale levels. The intention is to provide a logical conceptual foundation for the subsequent numerical analysis. This foundation will adopt a clear separation between three levels of parameters, which can be identified as “constants”, “state variables”, and “dependent or solution parameters”. This separation offers an easy and straightforward implementation of mathematical formulations at hand.

4.6.1 Fundamental points

1. The first level (or constants) is defined as those parameters, which can be derived directly from the boundary and geometrical conditions (i.e. the independent parameters) and remain constant at their average values along the packing height. For example:
 - The void and solid fractions (equations 4.40, and 4.41), the specific surface area (equation 4.45), the packing permeability (equation 4.21), as well as the effective thermal properties of the solid phase (equations 4.55 to 4.57) can be derived directly from the geometry of the column and packing size.

- Given the liquid and gas mass flow rates, then the liquid and gas hold up (equations 4.42 to 4.44), average pore velocities (equation 4.17 and equation 4.18 for liquid and gas respectively), relative permeabilities (equations 4.24 to 4.29), as well as the effective thermal properties of the liquid and gas phases (equations 4.56 to 4.57), and pressure drop (equations 4.10 and B1 to B8 in appendix B) can be calculated.
- Given the characteristics of packing materials (together with the liquid and gas mass flow rates), the interfacial areas between each pair of solid and fluid phases (equations 4.46 to 4.47), effective heat and mass transfer coefficients (equations 4.48 to 4.54 followed by equation 4.9) can be estimated.

It has to be pointed out that the parameters mentioned above remain constant as long as the boundary and geometric conditions don't change. Once one or more of these conditions is changed, values of these parameters will be updated accordingly in the model. Although the saturation permeabilities are only needed for calculations of the pressure drop when the packing size is too small (very dense porous media) or for derivation of the gas flow velocity when operating the system under natural convection, they are always calculated by the model. When operating the system under forced convection, which is the operation mode adopted in the present study, the approach of Stichlmair et al. [29], as described in Appendix (B), is followed.

2. The second level (or state variables) is commonly well known as the thermophysical properties of the involved phases, which are appreciatively affected by or have mutual dependencies on the solution parameters. For instance:
 - The density of the gas phase depends on its temperature and humidity content as described by equation (4.19).
 - The heat capacity of the PCM as described by the apparent heat capacity formulation in equation (4.63) and equations (4.65) to (4.68) depends on its temperature.
 - Other state variables for the gas and liquid phases are estimated at the respective average temperatures in the bed.
3. The third level stands for those parameters, which are derived from the solution of the one dimensional energy and mass balance equations and vary both in space and time (i.e. 4.7 to 4.8 for the external PCM thermal, 4.11 to 4.14 for the evaporator, and 4.32 to 4.35 for the condenser).

4.6.2 Capturing the MEHH and MECD phenomena

What immediately follow are the fundamental ideas and calculations strategy on how to evaluate the solution parameters to capture the MEHH and MECD phenomena

that form the study logical foundation. In reference to figures (3.2) and (3.3), three levels of this foundation are of paramount importance: microscale level, macroscale level, and coupling physics on these two levels along the packing height. Within the simulation strategy, the dual phase change phenomena described in this chapter (including the set of governing heat and mass balance equations together with the apparent heat capacity formulation) can be treated in two ways or as a sequential combination of the two: on a micro level, followed by a macro level.

4.6.2.1 Microscale level

At the microscale, the interfaces between all phases serve as particular locations where boundary or flux conditions must be applied to capture the coupled interaction between all phases in the form of source and sink terms (i.e. q_{ls} , q_{gs} , q_{lg} , and q_{latent}). Regarding the micro level, the physical phase change problem within PCM beads is literally similar to the case of evaporation of a falling water or fuel droplet. Here, the droplet, surrounded by air is gradually heated, giving rise to a change in evaporation, which uses a latent heat formulation. For the PCM beads, the resultant heat transfer from the surrounding water and gas phases is transferred to the beads, where at a moment in time, the phase is changed from solid to liquid.

This can either be treated as local within the bead or as an integrated value at each point along the packing height in the 1-D model. The later approach has been adopted as mentioned earlier using the apparent heat capacity model. The dominant heat transfer mechanism inside the PCM beads is assumed to be by conduction at the thermal conductivity of the solid state including the phase change of melting/freezing.

4.6.2.2 Macroscale level

At the macroscale, the wetting phase is described in terms of its average properties within a small volume, i.e. the volume averaging technique. Thus, at each point, a macroscale phase is characterized as occupying a fraction of the available volume and to have a certain interface per unit volume with other phases. Each phase in the system is described in a similar way. Precise definition of the interface shape is neither required nor possible to obtain at the macroscale.

On the macro level, the continuous solid approach for modeling phase change regenerators (PCR) is applied using the apparent heat capacity formulation. Here, the latent heat is defined at the melting/freezing front, which moves in space and time under the continuously updated apparent heat capacity. For the PCM phase change, the jump in the heat capacity, which takes place at sharp melting points (i.e. the singularity problem), is regularized by introducing a temperature range or mushy region over which the phase change occurs.

For liquid-gas phase change problems, the gas phase is assumed to be saturated at its local temperature, since the air circulates in a closed loop. This implies that the water vapor concentration (or vapor pressure) at the liquid-gas interface and in the bulk gas phase can be calculated as a function of the interface and gas temperatures respectively. Hence the driving forces for heat and mass transfer are coupled together through equations (4.36) to (4.39). The bulk gas concentration is calculated according to Dalton's law and equation of state for ideal gas mixture, assuming saturation conditions and the total pressure of the water vapor-air mixture equals to the atmospheric pressure. It can also be calculated using equation (2.11).

All sensible and latent heat rates are defined at the common interfaces based on the local temperatures of all phases, which are coupled together and updated as a function of space and time. Thus, heating/cooling the gas and liquid phases by the solid phase at a certain point or packing height, is directly influencing their local temperatures and mass transfer rates at the next point of the numerical calculations scheme.

Those overall characteristics of the MEHH and MECD phenomena on both micro and macro scale levels could be captured through the implementation strategy adopted (as will be proved and validated against experimental measurements in chapter 6) while the computational efforts and cost are incomparably much better than a detailed micro scale analysis using for instance a CFD simulation platform.

For simulation of the natural flow system, the model couples the momentum balance to energy and mass balances through a bouyant force term, dependant on temperature and concentration gradients (i.e. equation 4.31). The bouyant forces are directly introduced into the source term for the momentum balance.

5 Experimental Analysis

This chapter discusses the results of the experimental studies on the PCM-supported HDH system. The main objective of the experimental investigations is to examine the performance and viability of applying PCM components in the HDH cycle comprising the evaporator and condenser under steady state conditions. Since the multiple-effects of heating and humidification phenomena of interest are believed to have an impact on the system performance under steady state conditions, they will be focused throughout the present analysis in comparison with nonconductive packing media.

Transient effects will be discussed in chapter 8 under real weather conditions using the numerical simulation model for the HDH plant as a whole. Experiments, not only on laboratory scale but also as a prototype, were designed and performed to measure fundamental time dependent variables and critical parameters affecting the system performance. A system parameters analysis will be presented.

Description of the main features of the experimental set up together with the measuring techniques, and test procedures used in obtaining data for the HDH process are presented. An example of the conducted experiments is discussed to show the functionality of the experimental set up and behavior of the system.

5.1 Experimental setup and procedures

5.1.1 Design objectives

Generally, experimental studies are needed to ensure that a real system behaves according to the theoretical approach represented by conservation equations and thermodynamic relations. Therefore, the main design objectives of the experimental apparatus are to provide support and verification of the developed theoretical approach and performing direct experimental investigations on the system performance and heat and mass transfer processes. It is important also to recognize that the developed theoretical approach in chapter 4 is fundamentally computational in nature. The corresponding physical experiments do not necessarily have to follow the same perspective as the theoretical approach. This is because much of the desired information at the pore scale would be hard to obtain or measure physically in a real apparatus.

Thus, it is intended to experimentally measure the main changing independent and dependent variables and critical parameters affecting the processes of the present investigations. The system independent variables to be measured are hot and cold water temperatures and mass flow rates, and air temperatures and mass flow rate at the inlet of the evaporator and condenser. It is also of interest to measure the PCM temperature at different positions along the packing height. The dependent variables

to be measured are the outlet temperatures of fluid phases as well as the distillate rate and gas phase pressure drop or alternatively gas velocity has to be measured in case of natural convection operation.

5.1.2 Experimental Facility

The basic elements of the proposed HDH desalination units are: the evaporator, the condenser, and heat supply system combining a solar collector with PCM thermal storage tank as described in chapter 3. The test apparatus is designed with the same main features as the proposed system, but replacing the flat plate solar collector with an electric heater, using tap water instead of seawater, and stratified hot water storage tank without PCM elements.

The set-up consists of three parts, which are separated by water piping and valves: the main HDH apparatus comprising the evaporator and condenser columns, a hot water storage tank with an electrical heater and a cold water storage tank as presented by the block diagram in figure (5.1). The main HDH experimental apparatus is shown photographically in figure (5.2). It consists of two cylindrical transparent columns to permit good visual observation of the evaporator and condenser processes during plant operation. The transparent columns support two T-section tubes and are connected together in a symmetrical and closed loop arrangement. The transparent columns for the evaporator and condenser have 0.4m inner diameter, 0.9m height, and 2mm thickness.

For laboratory purposes, a controllable heating system of 15 kW is used to heat the evaporator inlet water up to the targeted temperature. The evaporator and condenser columns are packed with PCM elements encapsulated in 75 mm diameter spheres. The PCM which was chosen for this application is a proprietary mixture of organic and inorganic salts which have melting points of 58°C and 34°C for the evaporator and condenser respectively. Table (A.1) in the Appendix presents the thermo-physical properties of the selected PCM elements.

Hot water storage tank with a capacity of 0.5 m³ is used for brine recirculation. Two cold water storage tanks of 1 m³ capacity each are arranged in parallel such that they can be switched alternatively at any time of plant operation to keep the pumped cold water temperature within appropriate limits for achieving higher condensation performance.

Water distribution systems in the evaporator and condenser were designed as simple shower heads, which were produced in the laboratory by boring small holes on a sector of two empty plastic spheres that were used for PCM capsulation.

5.2 Measuring Techniques

K-type thermocouples were used for the temperature measurement. All thermocouples were calibrated under same conditions with an accuracy of ± 2 °C (or uncertainty of ± 5 %). Water, air, PCM, and plant wall temperatures were measured at different locations in the test setup using 34 thermocouples. Surface and core temperatures inside PCM spheres were measured at five different equidistance layers along the packed height in both evaporator and condenser.

The temperature measurement locations are shown in figure (5.3); (i) temperature of the hot water before and after electrical heater, (ii) temperatures of liquid water and gas at top and bottom of both the evaporator and condenser columns, (iii) wall temperature of the stainless steel upper elbows, and (iv) surface and core temperatures inside the PCM spheres at five locations along the packed height in both evaporator and condenser. In addition, ambient temperature was measured by a digital display thermometer and recorded for each experiment.

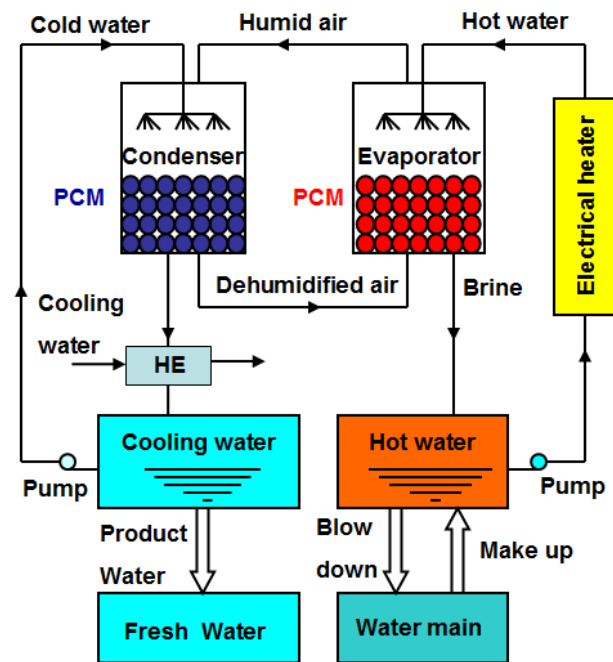


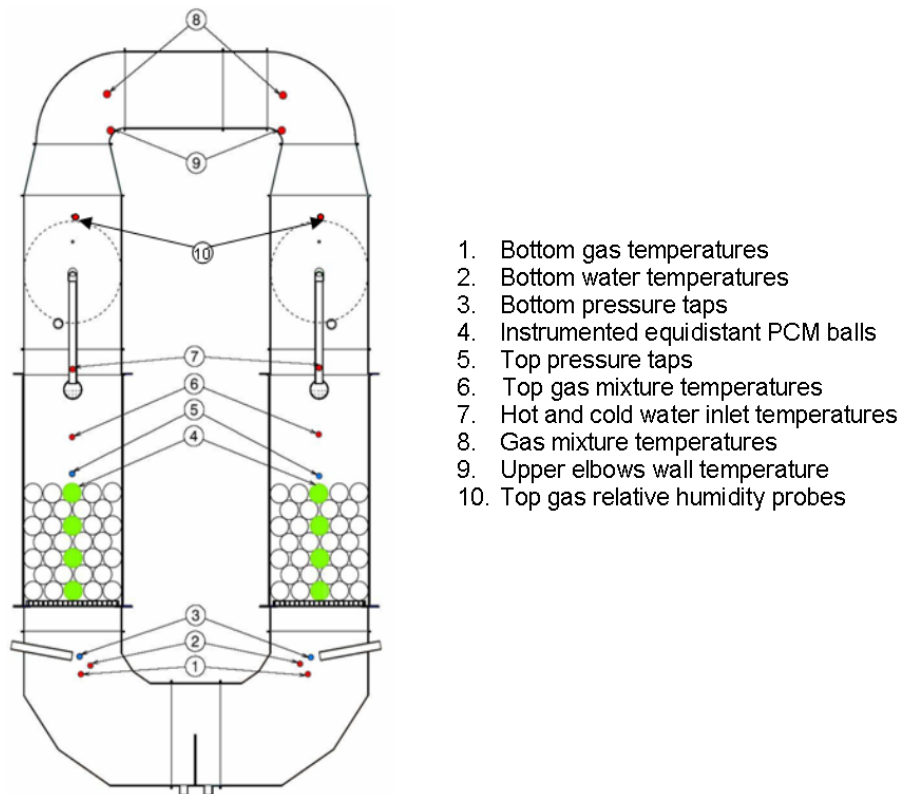
Figure 5.1: Block diagram for the test setup



Figure 5.2: Test apparatus and prototype of PCM based HDH system

For measuring the mass flow rate of hot water at the evaporator inlet, two rotameters are used upstream and downstream the electrical heater with an accuracy of ± 5 %. The inlet mass flow rate to the condenser was measured using electronic flow meters with an accuracy of ± 3 % for a wide range of operational flow rates. Humidity

of air was measured at top of the evaporator and condenser and found to be always saturated. Since water vapor was condensing on the humidity measurement sensors, we were unable to obtain humidity measurements in the same frequency as the temperature measurements. To overcome this difficulty, the humidity probes were taken out every 15 minute for a short time and dried by a hot air fan and then were inserted back into their hosting holes.



1. Bottom gas temperatures
2. Bottom water temperatures
3. Bottom pressure taps
4. Instrumented equidistant PCM balls
5. Top pressure taps
6. Top gas mixture temperatures
7. Hot and cold water inlet temperatures
8. Gas mixture temperatures
9. Upper elbows wall temperature
10. Top gas relative humidity probes

Figure 5.3: Locations of measured parameters

It was not possible to use typical hot wire anemometry for measuring air velocity because of the strong effect of the humidity on the measurements. Therefore, air velocity was directly measured by a digital anemometer on dry basis and the ventilator AC control device was precalibrated at different air velocities for plant operation during forced convection experiments. Measuring uncertainty range of air velocity is estimated within $\pm 8\%$. In case of natural air draft, it was decided to derive the air velocity from the energy balance on the condenser. Since pressure drop is not at all a crucial parameter for these investigations due to large packing size, it was measured by single reading of pressure difference between the two ends of a calibrated water U tube manometer.

The product condensed water was measured hourly in calibrated plastic jars. Before fully operating the rig, the water level inside the cold storage tanks was adjusted to a certain level beyond which water overflows to the calibrated plastic jars through 12 mm diameter pipes. The quantity of condensate accumulated in the measuring jars was noted every hour. From this, the mass flow rate of the output condensate produced by the plant was easily measured within uncertainty range of $\pm 5\%$. This range of uncertainty results from the fact that water surface in the condensate tank is concaved due to surface tension, while the small diameter of the overflow pipe causes a hydraulic resistance resulting in partly accumulation of 5% of the condensate from one hour to the next. However, comparing the accumulated condensate over 4 operation hours under constant boundary conditions between different experiments guarantees fair assessment of different setups and boundary conditions.

An error analysis was performed to clearly define the uncertainty margins for the measured parameters and how measuring errors propagate and how (quantitatively) they impact the calculated variables. Relevant error bars that are useful for quantitative qualification of the results will always appear on the comparative graphs throughout the present analysis.

The thermocouples were inserted into the rig through small diameter pipes which were welded in the tubes and lower elbows. Small umbrellas were used for protecting the tips of thermocouples, used for measuring the gas temperatures against falling water droplets to ensure right reference of the measured data. On the other hand, the thermocouple tips for measuring outlet cold and hot water temperatures at the lower elbows were immersed in a small sponge supported by a little water collection plate to ensure measuring water temperatures. Gas temperature sensors are also protected by small umbrellas at the top of the evaporator and condenser while water temperature sensors are inserted into the water mains directly upstream the shower heads.

5.3 Functional description

The test rig configuration comprises three closed loops as shown in figure (5.1); the air loop, the hot water loop, and the cooling water loop. The plant works on a similar operation cycle which has been described by figure (4.1). The test runs were performed over a time span of 4 hours under steady boundary conditions. The condensate is discarded and measured using calibrated jars. During the plant operation, mass flow meters were checked regularly and the output distillate was measured every one hour.

The start-up procedures for the experimental apparatus are described as follows:

1. Based on the previous calibration data, the water pumps and ventilator (in case of forced convection runs) are adjusted by their regulating appliances at the required flow rates.
2. Water in the hot storage tank is warmed up to 50-60 °C through a complete recirculation between the tank and the electrical heaters. This is important for maintaining the desired inlet water temperature of 65-85 degrees prior to entering the evaporator with minimum fluctuation margins.
3. At the beginning, the condenser pump discharge is sprayed individually for quite sufficient time until fully developed recirculation of the cold water to the cold water storage tank in the condenser loop is observed. Water level in the cold storage tank is reduced due to operating (dynamic and static) liquid holdup in the packed bed and through supply and return pipes. Thereafter, additional amount of cold fresh water is added to the working cold water storage tank for compensation of the liquid hold up until a little overflow takes place to the calibrated measuring jars.
4. Once this water level is reached, the hot water is directed to the evaporator shower head to start full operation of the plant. Due to difference in hydraulic resistances between the warming-up loop and the full hot water closed loop cycle on the evaporator side, the frequency regulator is readjusted to maintain the hot water flow rate at the desired level.
5. At the same moment of starting full operation of the plant, the data acquisition system is started to scan and record measured data. The scanning interval is preset at 10 seconds to allow good control on the evaporator inlet water temperature.
6. Ambient temperature as well as water manometer and velocimeter readings are noted and recorded.

The test run was expanded over a 4 hours of operation time under invariant inlet and boundary conditions. During experimentation the mass flow meters were checked regularly every 30 minutes and the output distillate was noted and recorded every one hour.

5.4 Design of experiments and potential influences of boundary conditions

In order to create different scenarios for different combinations of input parameters, each input variable is investigated at high and low levels. Although there are several factors that affect the efficiency of the plant, the parameters chosen to vary in this experiment are the most crucial and most easily controlled and adjusted. Table (5.1) presents the chosen independent parameters to vary and their lower and upper

operating limits. In light of the literature survey in chapter 2, the varying parameters include mainly inlet hot water temperature to the evaporator, mass flow rates of hot water and air, and packing height.

Moreover, the experiments are designed to examine both natural convection conditions and using Non-PCM (Empty plastic spheres having the same size as PCM spheres, and Hiflow industrial packing elements) elements for comparative tests.

In the very early stage of the experiments, the effect of inlet cooling water mass flow rate to the condenser on plant productivity was examined under six types of boundary conditions using PCM packing without distillate cooler. The results showed that this influence is very small within the planned range of mass flow rates. Thus, the inlet cooling water mass flow rate and temperature were constantly maintained at a higher level of 670 l/h, and around 21°C respectively to exclude the effect of cooling water conditions on plant productivity. However, the effect of inlet cooling water mass flow rate and temperature as crucial parameters under real operation conditions of the HDH system will be studied numerically in the next chapters.

Based on the previous calibration data, the water pumps and ventilator are accurately adjusted at the predefined flow rates to guarantee fixed boundary conditions for similar tests. Moreover, eight repeatability-prove tests were conducted on both PCM and Non-PCM packing types and found repeatable within less than 5%.

The subsequent sections compare and discuss the results obtained by employing different packing types to show the influence of operation parameters on the plant performance. First of all, the thermal behavior of PCM evaporator and condenser will be discussed in comparison with the empty spheres packing through one sample of experimentation runs. The six cases or combinations of boundary conditions which are indicated in table (5.2) were selected from the experimental plan in table (A.2) in the Appendix (A). The selected experiments were conducted on both PCM and empty spheres at two levels of packing height for studying the effect of PCM compared to Non-PCM packing. Additionally, the same set of experiments were conducted on industrial packing elements called “Hiflow packing” at lower packing height under forced and natural convection.

In the first and fourth case of boundary conditions in table (5.1), both of them have a higher inlet water temperature (83 °C). The first case has high inlet mass flow rate of water (500 l/h) to the evaporator, and high air velocity (0.55 m/s), while the fourth case has the lower levels of both inlet water mass flow (250 l/h) and air velocity (0.23 m/s) in the system. This means that the first case has the highest heat capacity flow rates, while the fourth case has the lowest for both water and air in the system, but air to water mass flow ratio is nearly the same.

In the second case, water heat capacity flow is decreased due to lower inlet hot water mass flow rate, while the air flow rate is maintained high. When Air flow rate has two impacts on the system performance, where the energy transfer rate through dry batches between solid and air (i.e. MEHH) increases with increasing air flow rate, both sensible and latent heat transfer at the air-liquid interface increases until reaching an optimum value of air/water mass flow ratio. Beyond this point the high sensible heat transfer rate negatively influences (i.e. comes at the expense) of the mass transfer rate at the interface. Moreover, most of the heat and mass transfer take place at the upper region of the evaporator, which causes the solid packing in the lower part of the column to be colder than the gas phase.

Table 5.1: Chosen variable parameters for experiments and range of values

Parameter	Units	Low level	High level
Mass flow of hot water " m_{hw} "	l/h	250	500
Corresponding water mass flux " L "	kg /m ² .s	0.55	1.1
Temperature of inflow hot water " T_{w2} "	°C	65	83
Mass flow of cold water " m_{cw} "	l/h	370	670
Air velocity " v_a "	m/s	0.23	0.55
Corresponding air mass flux " G "	kg /m ² .s	0.25	0.59
Packing height " Z "	m	0.38	0.78

Table 5.2: Basic sets of designed experiments according to boundary conditions

Parameter	Case No.					
	1	2	3	4	5	6
Air velocity " v_a " (m/s)	0,55	0,55	0,23	0,23	0,55	0,23
Mass flow of hot water " m_{hw} "	500	250	500	250	500	500
Temperature of inlet hot water " T_{w2} " (°C)	83	83	83	83	65	65
Mass flow of cold water " m_{cw} " (l/h)	670	670	670	670	670	670

When lowering the water mass flow rate the gas-solid interfacial area increases, while the wetted area (between water and solid) decreases. At constant inlet hot water temperature and constant air flow rate, this has two opposing effects; as it leads to higher rate of energy retrieval from solid to gas, but decreasing the water heat capacity flow rate decreases all sensible and latent heat transfer components in the system as well as thermal stratification along the packing height.

In the third case of boundary conditions, water heat capacity flow rate is maintained at the highest level, while air velocity is low which lowers all sensible and latent heat components between the gas phase and both solid and liquid phases.

In the last two cases, the inlet hot water temperature was decreased to the lower level while maintaining the hot water mass flow rate high. In the fifth case the air flow rate was also maintained high, while in the last case it was reduced to the lower level (the same as the first and third cases but under low inlet hot water temperature). The inlet hot water temperature potentially has a pronounced impact on heat and mass transfer components at all interfaces as well as thermal stratification in the bed.

These potential influences of operational and design parameters have been introduced and discussed to a certain depth both on micro and macro scale levels in chapter 3, however it might be helpful for interpreting the experimental results and subsequent discussions to provide a qualitative expectation of the temperature profiles plotting them over the height of the bed. These qualitative profiles would make it possible to predict the transported mechanisms and their feedback influences on distillation rates.

Given axial stratification along the packed height, the solid temperature at the top layers of the bed is higher than that of the gas phase, while the reverse may hold true at the bottom layers when the heat capacity flow of hot water is low. Thus, the expected behavior of the system in this case is that there is heat flow from gas to solid in the lower part of the column (i.e. cooling effect) and from solid to gas in the upper part. This implies that there should be a certain height of the bed at which the heat flow between gas and solid is zero (balancing point), as depicted in figure (5.4). Thus, if the system design is to be optimized so that at every specific location along the packing height there would be always heat flow from solid beads to the gas mixture in the evaporator to avoid cooling effects (and to the cooling water in the condenser), this will result in a more profound multi stage heating/humidification in the evaporator or cooling/dehumidification in the condenser. These idealized temperature profiles are illustrated qualitatively in figure (5.5) for the evaporator and condenser respectively. Under such circumstances, the conductive packing would have more profound impact on the distillate yield.

5.5 Results and discussions

Since the size and thermal storage capacity of PCM packing in the evaporator and condenser are relatively small when compared to those of the used hot water storage tank, unexpected effects when comparing PCM with Non-PCM packing during steady state operation conditions led to a new focus of the study. The experimental measurements revealed a productivity enhancement of PCM packing. The interesting phenomena of locally established multiple-effects of heating/humidification and cooling/dehumidification in the evaporator and condenser respectively, as discussed in detail in chapter 3, seemed to play the main role behind these effects. Hence steady state operation became more crucial and interesting than the transient conditions, and therefore will be focused throughout the present analysis.

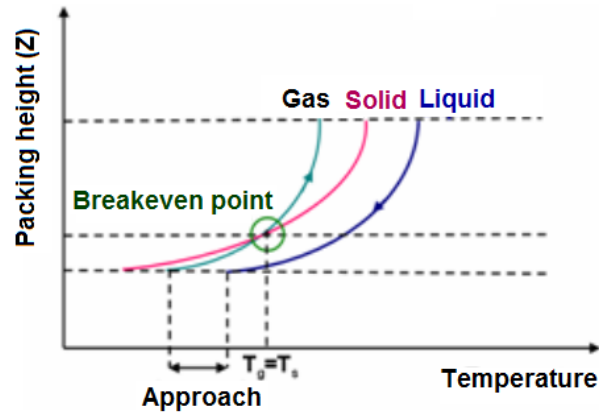


Figure 5.4: Qualitative illustration of temperature profiles in the evaporator

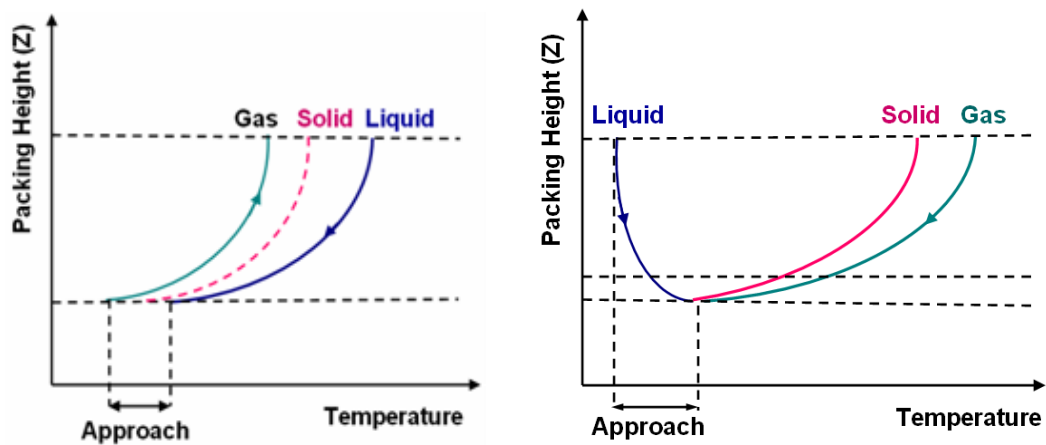


Figure 5.5: Qualitative illustration of ideal temperature profiles, Left: evaporator, Right: condenser

The main indicator to be considered throughout the evaluation and comparison between various operation scenarios and packing types is the productivity. Since the present system is a prototype unit developed to examine the comparative performance and reliability of the PCM based system, there is no energy recovery mechanism implemented in the setup. Thus the gained output ratio (GOR) in this case has no physical significance, as it is rather a measure for the plant thermal

performance and its threshold value shouldn't exceed unity. Realistic units would include an energy recovery system for lower energy consumption, as was described in the previous chapters, and will be investigated numerically in chapter 8 when considering the complete solar driven HDH plant.

5.5.1 Behavior of the PCM-supported HDH cycle

Figure (5.6) shows the evolution of inlet water temperature, the outlet water and gas temperatures as well as PCM temperatures at the top, middle, and bottom layers for the evaporator and condenser as one example of the PCM system thermal behavior. As can be seen from the figure, the outlet gas, water, and PCM temperatures are increasing with time until they all approach each other at the point of steady state or thermal equilibrium after nearly two hours. Along its pass through the evaporator, hot water transfers part of its energy with the solid phase and other part with the gas mixture. Energy transport to the gas mixture includes sensible and latent heat (evaporative) components which is strongly dependent on the liquid-gas temperature difference. Energy transport to the solid phase includes two sensible heat (convection) components at the liquid-solid and gas-solid interfaces, which depend on the binary temperature differences as described in chapter 4.

At the beginning of plant operation, the temperature of PCM beads is the same as ambient temperature and the differences between water temperature and both solid and gas temperatures are at its maximum values. In this early stage, one would expect a heat transfer in the direction from gas to solid phase, since the gas temperature increases very quickly compared to the solid phase due to the latent heat of evaporation. Marching in time at every specific location along the packed height, the temperature of PCM increases while the liquid-solid and gas-solid temperature differences decrease until they reach a certain limit at which the energy flows into and out of the solid phase at liquid and gas interfaces respectively are balanced.

Having reached thermal balance at one point, it will move forward to the next point along the packing height from top to the bottom until full steady state conditions are reached. The same scenario takes place in the condenser with the gas phase as the heat source. It can be clearly seen that the outlet gas temperature from the evaporator is very close to the PCM top layer temperature. The outlet gas temperature from the condenser (and inlet to the evaporator), outlet water temperature from the evaporator, bottom PCM layer temperature in the condenser and bottom PCM layer temperature in the evaporator are very close to each other.

Thermal stratification in the evaporator is higher than that of the condenser because of the lower heat source (gas) temperature in the condenser in comparison with the heat source (hot water) temperature in the evaporator and due to the concurrent flow in the condenser. In the concurrent flow in the condenser, it is anticipated that most

of the condensation takes place in the first top layers of the bed where the cooling water temperature is at its lowest level while the gas temperature is at its maximum level. Hence, the water temperature increases downwards due to condensation and cooling of humid air. This causes the temperature of the middle PCM layer to be higher than that at the top layer, as depicted in figure (5.6b), due to absorption of a large portion of the latent heat of condensation by the middle PCM layer. The middle PCM layer reaches steady state conditions earlier than PCM layers at top and bottom of the condenser, since the middle layer acts as a thermal buffer before the bottom layer. While the inlet and outlet gas temperatures approaching steady state conditions, the inlet cooling water temperature was gradually increasing over time during this experiment, which causes the retardation of the top PCM layer to reach steady state. However, it can be seen in figure (5.6) that the intermediate PCM layer temperature lies between both inlet and outlet gas temperatures in both components under the specified boundary conditions.

Figure (5.7) shows the evolution of water and gas temperatures at top and bottom of the empty spheres packing unit. It can be seen that the Non-PCM system achieves steady state sooner than the PCM based one. This is self-evident due to the fact that the hollow plastic spheres have a negligible thermal storage capacity compared to PCM spheres. The plots on figure (5.8) and table (5.3) illustrate that the differences between inlet and outlet gas and inlet and outlet liquid temperatures in the evaporator and condenser of the PCM packing are higher than those of the Empty spheres packing.

Table 5.3: Average values for inlet and outlet liquid and gas temperatures and productivities during steady state operation conditions (refer to figure 4.1)

	T_{w2}	T_{w1}	T_{w3}	T_{w4}	T_{a1}	T_{a2}	ΔT_{hw}	ΔT_a	ΔT_{cw}	Productivity (l/h)
PCM	83.2	54.5	26.6	51.9	50.1	66.7	28.7	16.6	25.3	23.5
ES	82.9	57.8	21.1	47	49.8	65.3	25	15	26	20.5

Although the boundary conditions were typically the same on the evaporator side, the outlet water temperature for the PCM packing was about 3 °C lower than that of the empty spheres. On the condenser side the inlet cooling water temperature of the PCM system was higher than that of the empty spheres, nevertheless the PCM productivity was 14.6% higher than that of the empty spheres.

The plots on figure (5.9) illustrate the improvement of productivity and GOR for PCM system in this experiment under steady state conditions due to increased temperature difference between top and bottom gas states. Moreover, the performance analysis indicates that the effectiveness of PCM evaporator and condenser has increased by 3 and 6% respectively compared with the empty spheres packing.

It could be interpreted that this particular behavior of PCM based system represents some first signs on the potentially important role of establishing multiple effects of heating and humidification due to existence of thermally conductive elements in the system. It is worth to mention that this behavior can also be realized using other kinds of sensible heat storage or conductive media since it is not associated with the solid-liquid phase change phenomenon inside the packing medium but rather related to its thermal conductivity.

The phenomena of multiple effects of heating/humidification and cooling/dehumidification have been elaborated in chapters 3 and 4. For the PCM packing there is complex interaction between various boundary conditions and the geometrical parameters. For instance, increasing the water mass flow rate increases the wetted area, enhances axial thermal stratification in all phases in the bed, and increases the solid-gas temperature difference while decreasing the dry interfacial area between solid and gas phases.

On the other hand, for a specific inlet hot water temperature and mass flow rate, the heat transfer between air and both water and solid phases depend on the air mass flow rate, which in turn has effects on the heat flow between water and solid. As mentioned earlier, there is a trade-off between direct contact heat and mass transfer at the liquid-gas interface and indirect heat and mass transfer resulting from the MEHH phenomena. When the water vapor diffusion at the liquid-gas interface dominates, for instance due to large interfacial area or high mass transfer coefficient or both, this will come at the expense of the MEHH and vice versa.

The energy flow between all and each pair of phases plays the major role in plotting the system behavior under each specific boundary and geometrical conditions. For instance, the energy flows in the evaporator are mainly dependent on:

- The heat capacity flow of inlet hot water,
- Air to water mass flow ratio,
- Interfacial areas,
- Packing height, and
- The thermal conductivity of the packing (i.e. Biot numbers).

The maximum sensible heat transfer rates between solid and gas occur if the PCM is infinitely conductive and fluid-solid heat transfer coefficients are infinite. In this case the temperature of the PCM will be always at the heat source temperature (i.e. water in the evaporator or gas in the condenser), which may give rise to the MEHH to dominate. These particular characteristics have to be seen as the basic background for describing and reading the comparative results between PCM (as a conductive medium) and Non-PCM packing types.

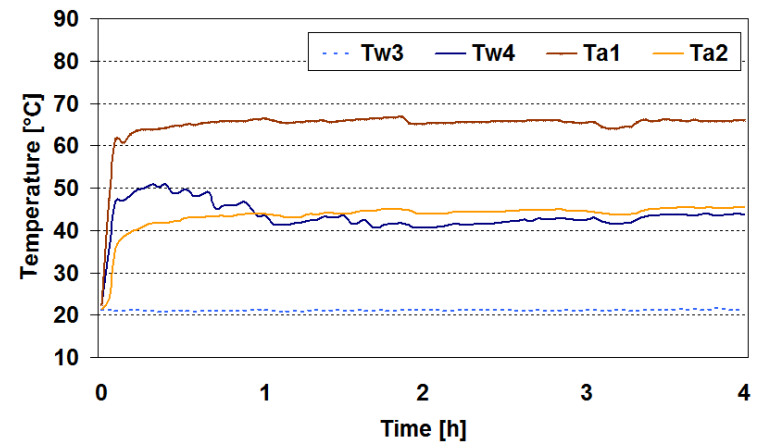
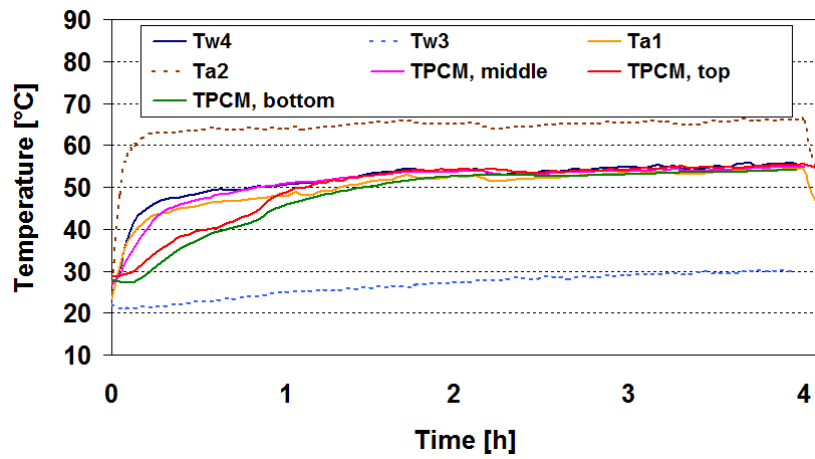
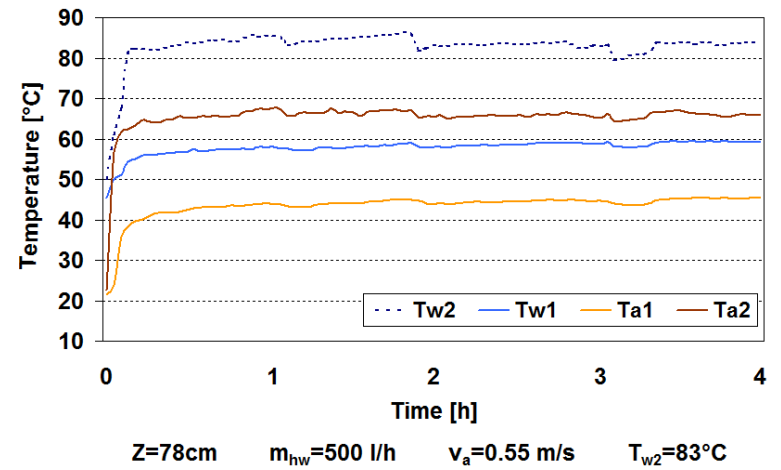
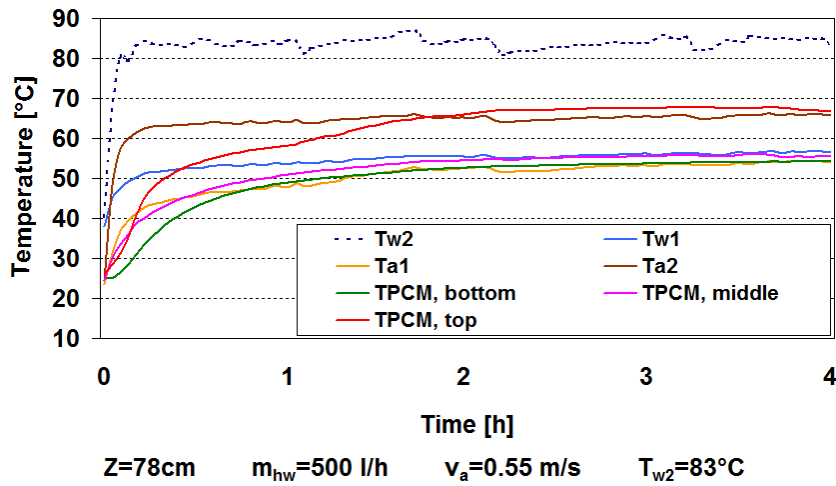


Figure 5.6: Thermal behavior of PCM system, top: evaporator, bottom: condenser

Figure 5.7: Thermal behavior of empty spheres system, top: evaporator, bottom: condenser

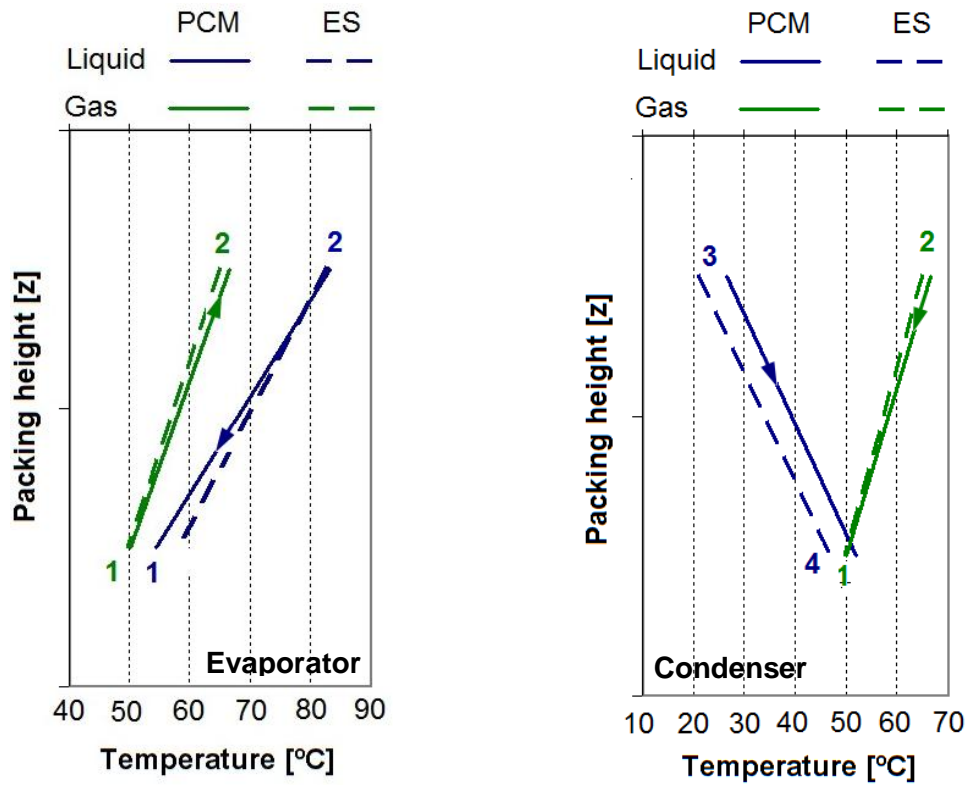


Figure 5.8: Average inlet and outlet liquid and gas temperatures for experiment case (1), Left: Evaporator, Right: Condenser

5.5.2 Comparison between conductive and non conductive packing

Overall comparative distillate output for the two packing types under similar boundary conditions for an operation period of two hours after reaching steady state are shown in figure (5.10). For the higher level of packing height as shown in figure (5.10a), the positive impact of conductive packing (PCM beads) on the productivity can be seen more clearly in the first and fourth cases of boundary conditions (i.e. first and fourth case from the left hand side on figure 5.10 or as listed in table 5.2). Both of them have a higher inlet water temperature (83 °C). The first set has higher inlet mass flow rate of water (500 l/h) to the evaporator, and higher air velocity (0.55 m/s) while the fourth set has the lower levels of both inlet water mass flow (250 l/h) and air velocity (0.23 m/s) in the system as pointed out earlier. In the first case, there are both good direct contact diffusion and MEHH in the PCM system, which results in 14.5% higher distillate rate than the empty packing system.

The fourth case of boundary conditions (case of low water mass flow rate, low air velocity, and high inlet water temperature) is more interesting. We can not see

any effect of PCM at the lower packing height as shown in figure (5.10b), while the PCM system productivity enhancement reaches its maximum value amongst all several sets of experiments at the higher level of packing height.

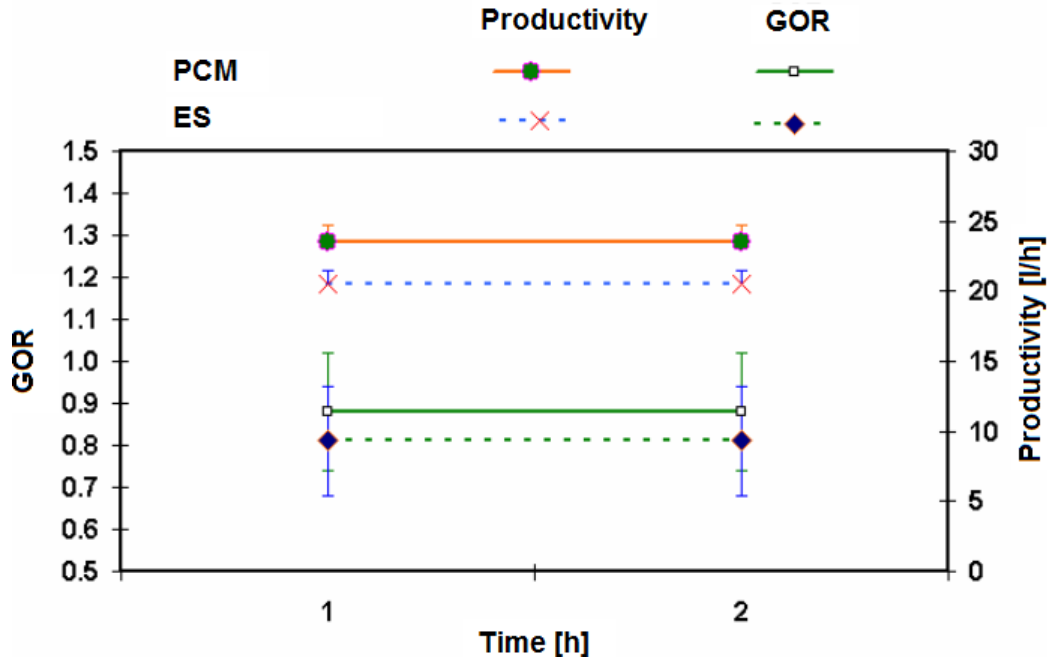


Figure 5.9: Evolution of productivity and GOR for PCM and Empty balls packing elements

In this case, direct contact diffusion is drastically damped due to the lower levels of both inlet water mass flow (less wetted and interfacial areas, see equations 4.46 and 4.47) and air velocity (i.e. less mass transfer coefficient at the interface, see equation 4.49). The PCM system achieves 42.9% higher distillate rate than the empty packing system. When decreasing the packing height by 50% as in figure (5.10b) for both first and fourth sets of boundary conditions, the difference in productivity between PCM and empty packing systems nearly vanishes since the number of PCM layers (i.e. the number of effects) is also decreased by 50%, which hinders the MEHH.

The second set of boundary conditions is another example of the trade-off between the direct latent and sensible heat transfer at different interfaces. At the high packing height, lowering inlet hot water mass flow rate to 250 l/h has a negative impact on the PCM compared to the empty packing system due to the cooling effect in the lower part of the bed, which has been illustrated qualitatively in figures (5.4) and (5.5). This negative impact turns out to be positive at the lower packing height under same conditions, where the cooling effect is avoided by lowering the packing height. In contrast, GOR values are nearly the same

within the inaccuracy margins. The reasons behind these findings are elaborated below.

For the higher packing height, the surface area for direct contact heat and mass transfer for both packing types (i.e. PCM and empty spheres) is reduced due to reducing the mass flow rate of water (wetted area is reduced, see equation 4.47) but still higher than the low packing height while the mass transfer coefficient is still high since the air mass flow rate is maintained at the high level (see equation 4.49). Furthermore, since the wetted area is reduced by 50%, as a result the parallel path of heat flow from the liquid to gas phase through the solid phase is cut by half. This gives rise to the direct mass diffusion since the mass transfer coefficient is still high due to higher air mass flow rate as just mentioned above. Lowering the packing height by 50%, the total interfacial area for direct diffusion in the bed is also halved which gives rise to the MEHH, thus the PCM system produces 26.2% more fresh water than the empty packing.

Increasing the packing height increases the surface area for heat and mass transfer between all phases for a given liquid and gas loads. Thus, higher boundary conditions are necessary for higher packing heights to avoid cooling effects while satisfying the favorable temperature profiles and heat flow directions.

In contrary, higher packing height would have negative impact on system performance under lower boundary conditions because it will act only as a heat sink for both liquid and gas phases due to cooling effects in the lower part of the evaporator which hinders the productivity. Under steady state, the break even point will be located vertically at a distance where the net heat flow between gas and solid phase in the bed could be in the direction from gas to solid.

This explains the comparative behavior of the PCM system under the first and last set of boundary conditions for both packing height levels in figure (5.10). Under the same higher boundary conditions (first set) the positive impact of PCM in the system decreased with decreasing the packing height due to lower surface interfacial areas and lower number of MEHH (half number of packing layers). In contrary, under lower inlet water temperature the negative impact of PCM at higher packing level turns out to be positive at the lower level due to low mass transfer rate at the water-gas interface in both PCM and empty spheres. Nevertheless in PCM the MEHH effect starts to appear due to the trade off between sensible and latent heat transfer at different interfaces as elaborated earlier.

In the third case of boundary conditions (reference is still made to figure 5.10 and table 5.2), the packing height plays no major role and the positive effect of PCM is not remarkably high because the air velocity is low which lowers the gas-solid heat transfer coefficient and hence the role of MEHH is not well activated although the inlet hot water temperature and mass flow rate are kept at the higher level. Here direct heat and mass transfer at the liquid gas interface

dominates due to both high temperature and concentration gradients and low heat transfer rate from liquid to gas through the solid phase.

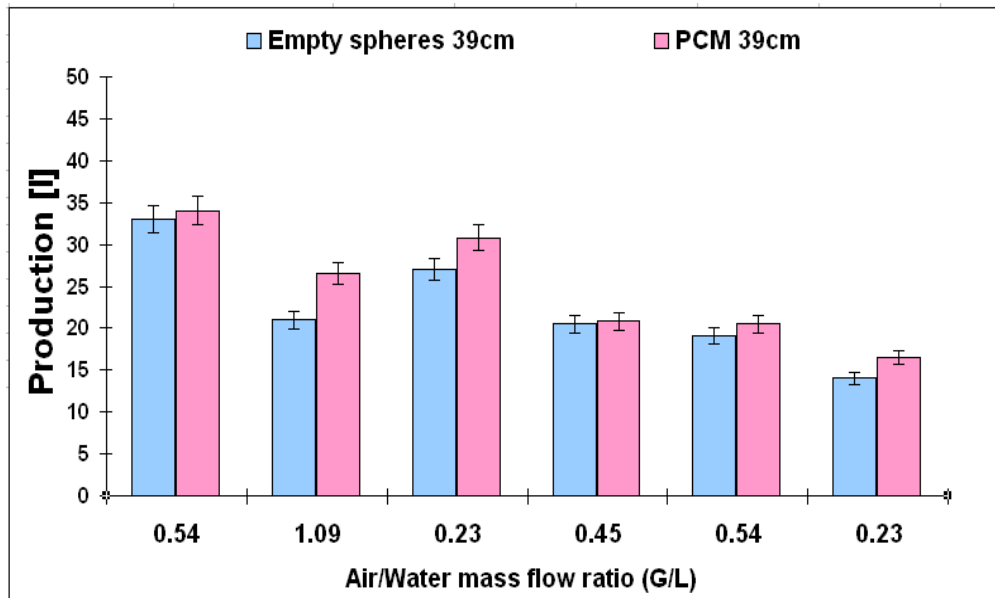
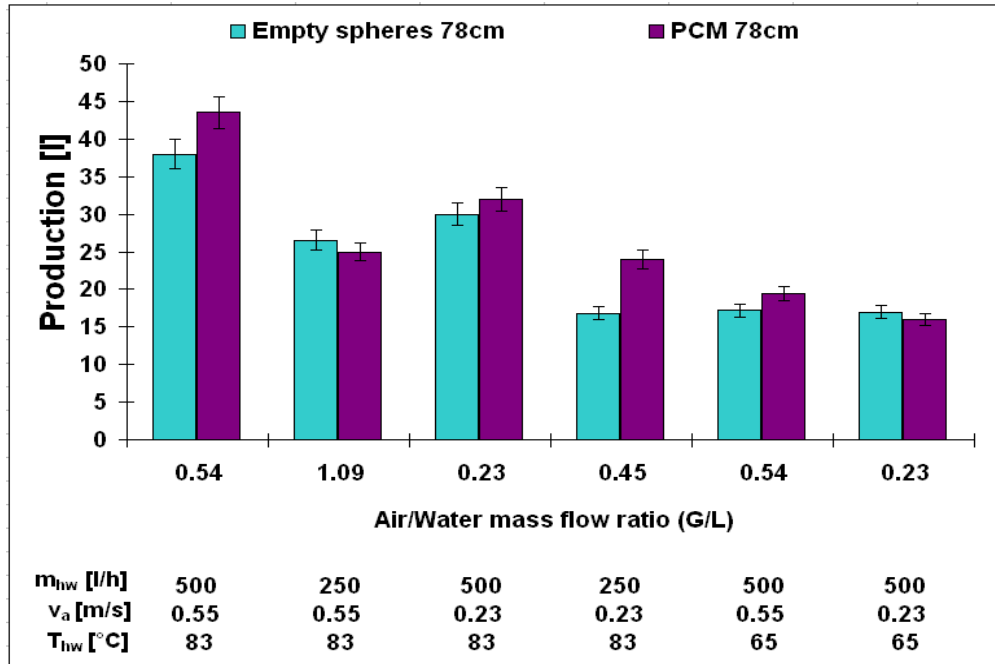


Figure 5.10: Comparative productivity; (Top) 78cm packed height, (Bottom) 39cm packed height

The last two cases of boundary conditions (5 and 6) are devoted to lower inlet hot water temperature of 65 °C at higher water mass flow rates and low and high air mass flow rates. The results clearly reveal the importance of maintaining high inlet water temperature for the system productivity regardless of the packing type. However a minor role of conductive packing can be noticed, in dependency on the packing height due to difference in the specific interfacial surface areas, and number of layers active in the MEHH process.

It can be said that at a constant thermal conductivity of the packing medium, the influence of the conductive packing on the system performance is strongly dependent on the magnitude of the binary solid-gas and solid-liquid interactions, which is governed by the specific dry/wet areas on the outer surface of beads, quality of the inlet hot water temperature to the system, packing height or number of active packing layers in the MEHH process, and associated heat and mass transport coefficients or mass flow rates.

5.5.3 Effect of packing specific area

Further questions arise whether the PCM thermal conductivity and stratification effects, which induce the MEHH phenomenon, would have a higher impact on the system performance or enhancing the direct contact diffusion at the liquid-gas interface, using e.g. smaller packing elements would lead to same or better performance.

In order to follow this question, results are furthermore compared between PCM and Hiflow Rings, which is a commercially packing material being used in industrial stripping columns. Extra six experimentation runs were conducted using Hiflow packing elements. Four experiments were conducted under the same first four sets of boundary conditions that are listed in table (6.2) and presented in figure 5.10. The last two experiments were conducted under natural draft operation at high inlet hot water temperature and different inlet hot water mass flow rates of 250 and 500 l/h to get more insight on the effect of the MEHH.

The Hiflow Rings with size 20 mm that have been used, have a specific surface area of 291 (m^2/m^3), and porosity of 0.75 compared to 46.6 (m^2/m^3) and 0.42 for those of the PCM spheres respectively. For a packed height of 0.39m, the total surface areas available for heat and mass transfer (i.e. wetted area and dry patches) are 2.26 and 13.9 m^2 for the PCM spheres and Hiflow rings, respectively (i.e. the Hiflow rings area is 6 times larger than that of the PCM spheres).

Figure (5.11) exhibits the total distillate output through 2 hours of steady state operation for the three packing types under different boundary conditions and natural draft air flow. It can be seen from the first case that when the high mass flow rate of hot water is combined with high air velocity in the system, increasing the specific surface area of packing (i.e. Hi-flow Rings) gives strong rise to direct

latent heat transfer over the influence of MEHH. In this case we can see that Hiflow packing produces 36% more distillate than the PCM packing, while the specific surface area of Hi-Flow Rings is 600% that of the PCM spheres. At higher air velocities and high wetted area, direct heat and mass transfer between water and gas dominates, which reduces the energy flow from water to the PCM beads. Thus results in damping the MEHH over the packing height.

It can be easily seen from the second, third, and fourth cases that lowering water mass flow rate and/or air mass flow rate has an influence on decreasing the direct contact heat and mass transport, and thus gives rise to the MEHH through the liquid-solid-gas parallel heat path accompanied by thermal stratification in the bed. In the third case, which is already more interesting from the previous section, the MEHH influence is more pronounced here and this is clear from the fact that empty spheres produce almost the same distillate as Hiflow Rings and the productivity of both of them is 16% lower than that of the PCM packing.

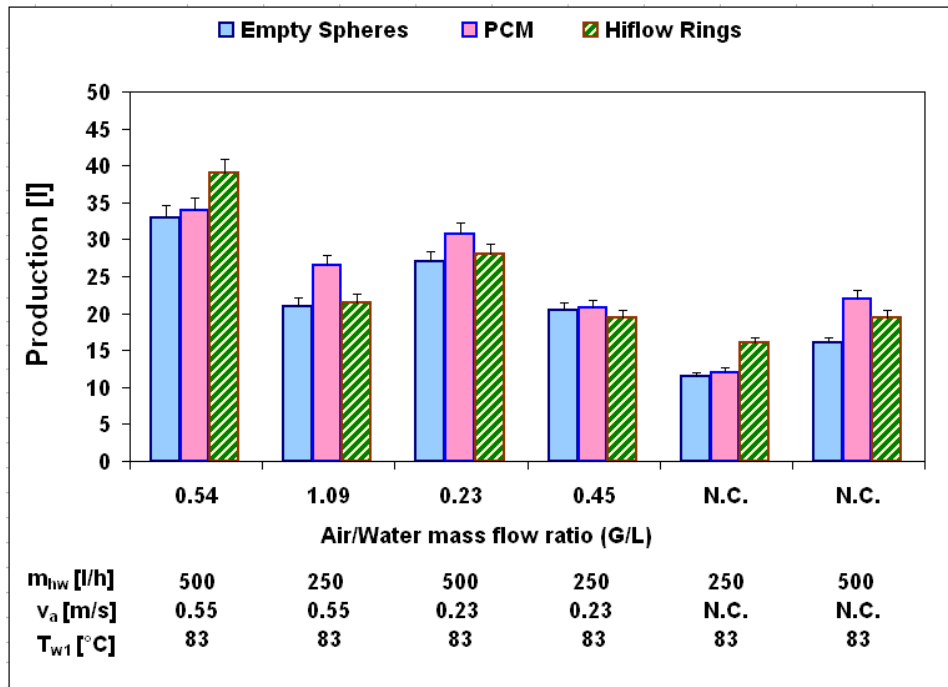


Figure 5.11: Comparative productivities for PCM, Empty spheres, and Hiflow rings packing media for 0.38m packing height (for two hours of steady state operation)

The last two cases under natural convection (V.C.), reveal that the influence of MEHH increases under the high input energy to the system ($m_{hw}=500$ l/h and $T_{w1}=83^\circ\text{C}$) resulting in a higher production of 13% more than that of the Hi-flow Rings in the last case. Under natural convection where air flow is induced by the double diffusion effects (density and humidity gradients), the MEHH boosts the

natural air flow in the system. In the fifth case under natural air mass flow, increasing the specific surface area as of the Hiflow packing compensates and outpaces the role of MEHH, due to low mass flow rate of hot water, resulting in a higher production of 25% more than that of the PCM packing. On comparison with empty spheres, it is evident from this case, where air velocity is very low estimated at 0.1 m/s, that MEHH are nearly absent at very low hot water mass flow rates and low specific packing area.

5.6 Conclusions

The performance of air humidification-dehumidification system utilizing phase change materials (PCM) as packing media both in the evaporator and condenser under forced and free convection has been studied experimentally. Performance of the PCM based system was evaluated in comparison with Non-PCM elements including empty plastic spheres having the same size as PCM spheres, and Hiflow Rings which is a commercial industrial packing. The effect of various parameters on the plant performance and productivity has been investigated.

From the previous analysis it is clear that there is a strong and complex interaction between four main parameters, air to water mass flow ratios in the evaporator and condenser, packing height, heat capacity flow of inlet hot water, and thermal conductivity and PCM communication with the surrounding fluid phases which can be characterized by their respective Biot numbers. The axial thermal stratification is established in the bed due to the interaction between these parameters, which is essential for creating the multiple-effect mechanisms.

Under most of the boundary conditions, PCM elements generally have positive impact on the productivity rate of the plant compared to Non-PCM packing elements. However, this impact can be seen more clearly under higher inlet water mass flow rate and higher inlet water temperature on the evaporator, and higher mass flow rate of air in the system due to low thermal conductivity and large size of the PCM elements. Although this enhancing effect of PCM elements under such higher boundary conditions is more pronounced for higher packing height, it holds also true for the lower packing height but with lower impact as well.

The comparative analysis revealed that the main reason behind enhancing the system productivity with PCM elements at steady state is attributed to the potential role of establishing multiple-effects of heating/humidification and cooling/dehumidification mechanisms in the evaporator and condenser respectively as compact heat and mass exchangers. The experimental analysis has demonstrated a strong and complex interaction between four main parameters, air to water mass flow ratios in the evaporator and condenser, packing height, heat capacity flow of inlet hot water, and thermal conductivity or PCM communication with the surrounding fluid phases which can be characterized by their respective Biot numbers. The axial thermal stratification is

established in the bed due to the interaction between these parameters, which is essential for creating the multiple-effect mechanisms.

The solid phase thermal conductivity represents the key parameter that controls local heat and mass transfer not only at solid-liquid and solid-gas interfaces, but also at liquid gas interface. The multiple-effect mechanism depends on the thermal conductivity of the packing elements but has no relationship with solid-liquid phase change in the PCM media. The present analysis indicated that the potential role of multiple-effect mechanisms can also be realized by employing other conductive media rather than PCM media which usually have poor conductivity. However, since only one PCM candidate was examined in the present study, theoretical analysis has been carried out in parallel to clearly explore the effect and limits of solid thermal conductivity. These results will be presented in the next chapter. Packing media which have optimum thermal conductivity, smaller size, and lower cost would be ideal candidates for the present application. Nevertheless, incorporation of PCM media in the hot water storage tank could have a potential role for realizing 24 hours operation of the HDH plants.

Experimental results suggest that forced convection remarkably enhances the productivity of HDH plants compared to natural draft operation for all packing types. However, the conductive packing elements have a positive impact on the natural draft operation as well especially at higher heat capacity flow of hot water. Under natural convection where air flow is induced by double diffusion effects (density and humidity gradients), the MEHH boosts the natural air flow in the system, and hence increases its productivity. Increasing the specific surface area of the packing can compensate and outpace the role of MEHH at low mass flow rates of hot water. The role of MEHH in naturally drafted flow is nearly absent at very low hot water mass flow rates and low specific packing area. Conductive packing media may have a potential that could be utilized to improve the natural flow characteristics in other important applications such as cooling towers.

6 Model Implementation and Validation

Suitable correlations and volume averaging technique for conceptualization of the complex packed bed geometry to one dimensional domain has been presented in chapter 4. Obviously, the use of such engagement between one dimensional CS model and inter-penetration continua approach might produce a consistent and simple simulation model for prediction of heat and mass transfer phenomena inside the single and dual phase change regenerators.

This chapter presents the numerical solution of the mathematical model developed in chapter 4. All the single models were first resolved and refined against experimental data using COMSOL due to its friendly and powerful graphical user interface and numerical solvers. Then MATLAB was used to solve for the same individual components and for the HDH system as a whole. MATLAB was helpful when solving for the whole system where all the single models are structured and coupled together in an interactive simulation platform. The main facilities provided by MATLAB implementation are; importing yearly meteorological data on hourly basis from spread sheets, exporting solution results directly to spread sheets, less computational time and cost, and more varieties of interfacing with other simulation platforms. Therefore, the MATLAB implementation will only be presented.

Due to the similarity between the evaporator and condenser designs, and considering the single phase flow generator as a simplified case of the evaporator and condenser, the numerical solution procedures for the nearly-similar sets of coupled non-linear partial differential equations as well as other state variables equations can be explained by implementation of one of the dual phase change regenerators. Therefore the evaporator model was selected to represent the solution approach of the three physical problems.

Validation of the model has been performed upon realizing a wide variety of experimentation results. However, for sake of brevity, only the most relevant examples of simulation results and validation against experimental data will be presented.

6.1 Implementation of the evaporator model with MATLAB

A one-dimensional transient numerical simulator was constructed to predict the simultaneous transport of heat and moisture in an isothermal two phase countercurrent flow with a low level of mass diffusion and solid-liquid phase change. The hydrodynamics in the packed bed are coupled with the heat and mass transfer (as described in detail by the equation systems in chapter 4) and the system is solved using MATLAB to predict the temperature, velocity, humidity, and pressure fields for arbitrary boundary conditions (temperature, flux, pressure and concentration).

The simulation model uses one of the MATLAB specialized tool boxes as a simulation platform. This tool box has been originally developed for solving all types of coupled partial differential equations. The present mathematical model consists of a set of parabolic partial differential equations (PDEs) that are all coupled and should be solved simultaneously. MATLAB provides a special function called “*pdepe*” to solve such coupled nonlinear kinds of partial differential equations. The MATLAB implementation follows the same strategy, assumptions, and implementation approach of the COMSOL model. Therefore, the next sections will only focus on the implementation using the “*pdepe*” built-in function.

The “*pdepe*” function offers the possibility to numerically solve initial-boundary value problems for systems of parabolic and elliptic PDEs in one space dimension and time. The general form of the PDEs is defined as:

$$c\left(x,t,u,\frac{\partial u}{\partial x}\right)\frac{\partial u}{\partial t} = x^{-m}\frac{\partial}{\partial x}\left(x^m f\left(x,t,u,\frac{\partial u}{\partial x}\right)\right) + s\left(x,t,u,\frac{\partial u}{\partial x}\right) \quad (6.1)$$

Where u is the solution variable, x and t are distance and time respectively. The PDEs hold for $t_0 \leq t \leq t_f$ and $a \leq x \leq b$. The interval $[a, b]$ must be finite, m can be 0, 1, or 2, corresponding to slab, cylindrical, or spherical symmetry, respectively. If $m > 0$, then a must be ≥ 0 . Where $f(x,t,u,\partial u/\partial x)$ is a flux term and $s(x,t,u,\partial u/\partial x)$ is a source term. The coupling of the partial derivatives with respect to time is restricted to multiplication by a diagonal matrix $c(x,t,u,\partial u/\partial x)$.

In this equation c corresponds to the energy accumulated in the system, f is a flux term and s is a source term. The boundary conditions at points $x = a$ and $x = b$ for all times t and the interval $[a, b]$ to be finite, are stated in the form:

$$p(x,t,u) + q(x,t,u) \cdot f(x,t,u,\partial u/\partial x) = 0 \quad (6.2)$$

In a system of coupled PDEs, it can be expressed in a matrix form for the boundary conditions at point a

$$\begin{bmatrix} p_a(x=a,t,u)(1) \\ p_a(x=a,t,u)(2) \end{bmatrix} + \begin{bmatrix} q_a(x=a,t)(1) \\ q_a(x=a,t)(2) \end{bmatrix} \cdot \begin{bmatrix} f(1) \\ f(2) \end{bmatrix} = \begin{bmatrix} 0 \\ 0 \end{bmatrix} \quad (6.3)$$

and similarly at point b

$$\begin{bmatrix} p_b(x=b,t,u)(1) \\ p_b(x=b,t,u)(2) \end{bmatrix} + \begin{bmatrix} q_b(x=b,t)(1) \\ q_b(x=b,t)(2) \end{bmatrix} \cdot \begin{bmatrix} f(1) \\ f(2) \end{bmatrix} = \begin{bmatrix} 0 \\ 0 \end{bmatrix} \quad (6.4)$$

Initial conditions are stated in the form

$$u(x, t_0) = u_0(x) \quad (6.5)$$

and for a system of equations:

$$\begin{bmatrix} u_1(x, t = 0) \\ u_2(x, t = 0) \end{bmatrix} = \begin{bmatrix} u_{1,0}(x) \\ u_{2,0}(x) \end{bmatrix} \quad (6.6)$$

In order to implement the PDEs system of the evaporator (as an example) in the “pdepe” function, the system of equations arranged to fit the terms of equation (6.1) as shown in table 6.1.

6.2 Solution of the HDH plant lumped model

The primary reason for creating a computer model of a solar desalination system is to determine how much distillate water the system will supply over a long period of time, usually over the whole year. Long term system performance is important in determining the economic viability of its particular design due to the transient nature of continuously varying weather conditions. As with any simulation model, the design characteristics of the components and operation parameters may be varied to help optimizing the system in terms of its performance and cost.

A complete but simplified system model has been developed to simulate the proposed solar distiller based on the governing equation systems, which have been developed in chapter 4 (i.e. equations 4.7 to 4.88). The model was developed in MATLAB, since it is an integrated package and helpful engineering tool. With the simulation model, the system performance can virtually be tested in different environments by altering the meteorological data. The model predicts the system’s transient behaviour and therefore uses an explicit calculations scheme for different parameters of interest.

Concerning the boundary conditions, the inlet feed seawater temperature, ambient conditions and hourly solar irradiation data are given as input parameters. The water vapor concentration in the air can be determined as a function of the gas temperature assuming saturation conditions, since the air circulates in a closed loop cycle. The temporal and spatial evolution of temperature and concentration fields of fluid and solid phases are then derived from the solution.

The model comprises three main modules; the evaporator, condenser, and solar water heater consisting of a solar flat plate collector (FPC) and PCM thermal storage tank (also referred to as the thermal buffer). Each module was developed using a “pdepe” function, tested and refined separately to solve the coupled partial differential equations governing each component as described in details in

chapter 4. Then the three modules were incorporated into a main structure which masters the three modules by calling different "pdepe" functions to constitute the simulation model of the PCM-supported HDH system. Figure (6.1) shows the flow diagram and the control logic of the model.

The solar water heater module receives water mass flow rate and metrological records as input data. It defines the number of time increments (one-hour time increments are used here as the meteorological data are recorded hourly) for the control loops and the inlet water temperature to the thermal buffer. The same module also entirely solves the governing equations for the thermal buffer (i.e. equation 4.7 to 4.10 together with equations 4.63 to 4.68 and 4.78 to 4.80) and defines the outlet water temperature (i.e. the inlet water temperature to the evaporator).

The evaporator module receives the inlet boundary water temperature from the solar water heater module, the inlet gas temperature and concentration from the condenser, and the water mass flow rate as input data. It calculates the hourly average evaporation rate and outlet brine and gas temperatures (i.e. equation 4.11 to 4.31, equations 4.36 to 4.57, and equations 4.63 to 4.68).

The condenser module receives the outlet gas temperature, mass flow rate, and concentration of the evaporator together with the cooling water mass flow rate and ambient temperature as input data. It calculates the hourly distilled water, outlet gas temperature, and concentration, and outlet cooling water temperature (i.e. equation 4.32 to 4.35 to 4.57, equations 4.17 to 4.31, and equations 4.63 to 4.68).

The energy balance of the heat exchanger downstream of the condenser (equation 4.81) is performed based on the outlet cooling water temperature from the condenser, outlet brine temperature from the evaporator, and ambient temperature of feed seawater (as described in chapter 4) to determine the inlet water temperature to the solar collector in the next time step. Once the average hourly values for different parameters have been determined for the time increment used, the program then goes to an integration mode. The instantaneously, hourly, and daily values are summed up over the operation period to determine the total values. The hourly and daily yield, GOR, different component efficiencies, and the yearly accumulated yield and GOR are calculated.

6.3 Model validation

The numerical simulation predictions of the HDH unit hourly and accumulated distillate production were compared with the experimental measurements under the first two sets of boundary conditions in table (5.2) for the two packing heights of 78cm and 39cm, respectively (i.e. the first two cases from left hand side in figures 5.10a and 5.10c respectively). The main indicators used for the model

validation were the hourly distillate rate, inlet and outlet liquid and gas temperatures, and PCM temperatures at three locations along the packing height.

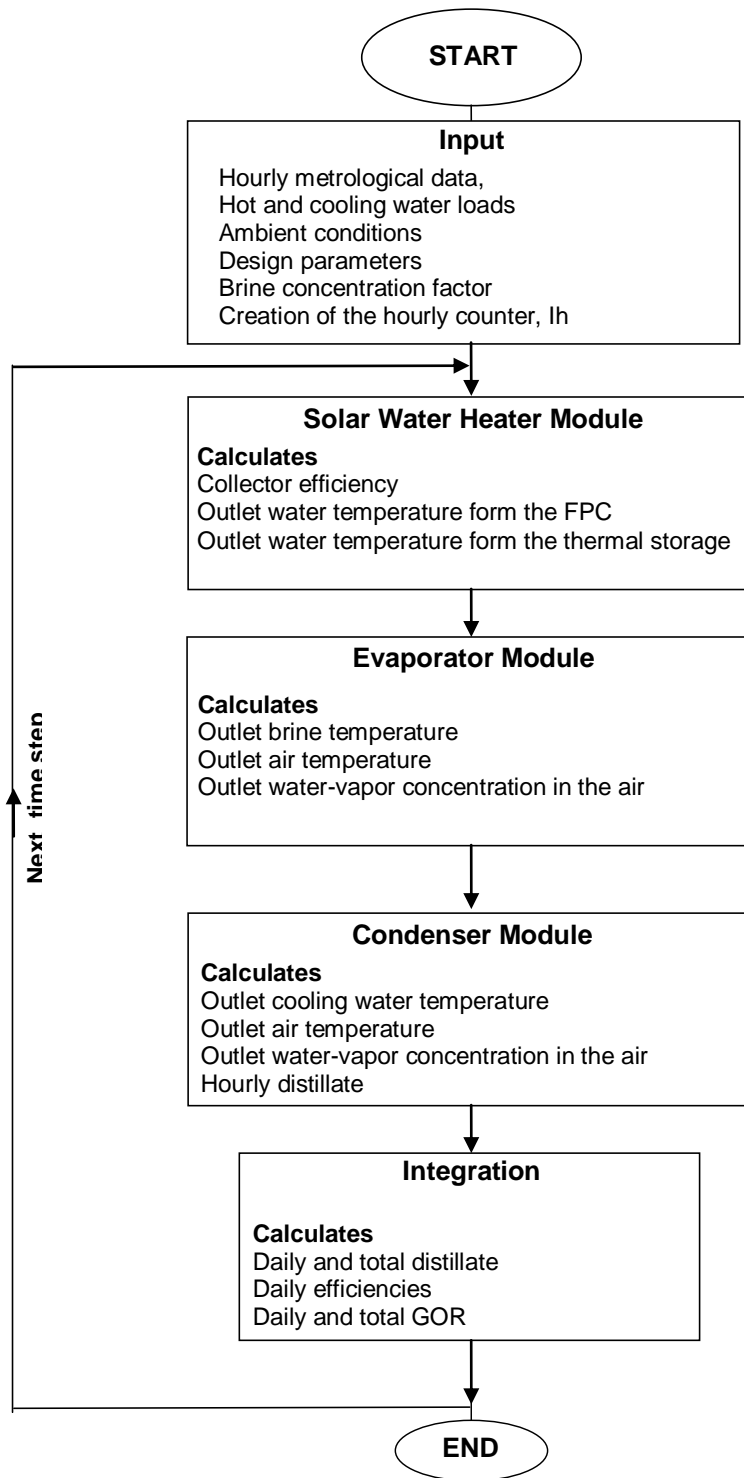


Figure 6.1: Flow diagram and control logic of the simulation model

Table 6.1: Implementation of energy and mass balance equations using the "pdepe" MATLAB function

Equations	Accumulation term $c\left(x, t, u, \frac{\partial u}{\partial t}\right) \frac{\partial u}{\partial t}$	Convection and diffusion terms $x^m \frac{\partial}{\partial x} \left(x^m f\left(x, t, u, \frac{\partial u}{\partial x}\right) \right)$ $m=0$	Sink and source terms $s\left(x, t, u, \frac{\partial u}{\partial x}\right)$
Gas energy balance	$\varepsilon_g c_{p,g} \frac{\partial(\rho_g T_g)}{\partial t}$	$\varepsilon_g k_g \frac{\partial^2 T_g}{\partial z^2} - \varepsilon_g c_{p,g} v_g \frac{\partial(\rho_g T_g)}{\partial z}$	$h_{g_s} a_{g_s} [T_g - T_s] + h_{l_g} a_e [T_l - T_g] + \dot{m}_{evap} h_{fg}$
Liquid energy balance	$\varepsilon_l \rho_l c_l \frac{\partial T_l}{\partial t}$	$\varepsilon_l k_l \frac{\partial^2 T_l}{\partial z^2} - \varepsilon_l \rho_l c_l v_l \frac{\partial T_l}{\partial z}$	$h_{l_s} a_w [T_l - T_s] - h_{l_g} a_e [T_l - T_g] - \dot{m}_{evap} h_{fg}$
Solid energy balance equation	$\varepsilon_s \rho_s c_{app,s} \frac{\partial T_s}{\partial t}$	$k_{s,eff} \frac{\partial^2 T_s}{\partial z^2}$	$h_{l_s} a_w [T_l - T_s] + h_{g_s} a_{g_s} [T_g - T_s]$
Gas mass balance	$\varepsilon_g \frac{\partial c}{\partial t} \varepsilon_g$	$\varepsilon_g \frac{\partial(c v_g)}{\partial z} - \varepsilon_g D \frac{\partial^2 c}{\partial z^2}$	\dot{m}_{evap}

The evaporator and condenser both were packed with the respective PCM spheres HS58 and HS34 as mentioned earlier. Similar tests were performed with empty spheres packing of the same size (air capsules). Table 6.2 presents the specific boundary and operating conditions for these four test cases. The measured initial temperatures, inlet cooling water, and hot air temperatures as a function of time were used as input data for the simulation model.

Table 6.2: Specified boundary and operating conditions for model validation

Parameter	Units	Value
Mass flow of hot water " M_{hw} "	l/h	500
Corresponding hot water mass flux " L_{hw} "	kg /(m^2 .s)	1.1
Temperature of inflow hot water " T_{w2} "	°C	83
Mass flow of cold water " M_{cw} "	l/h	670
Corresponding cold water mass flux " L_{cw} "	kg /(m^2 .s)	1.48
Air superficial velocity " V_{asup} "	m/s	0.55
Corresponding air mass flux " G "	kg / m^2 .s	0.59

Figures (6.2), (6.3) and (6.4) show the evolution of inlet and outlet temperatures of each phase in comparison with experimental measurements for PCM packing and empty spheres packing respectively at a packing height of 78cm.

From figures (6.2), (6.3) and (6.4), it is observed that the results obtained from the present model are in fairly good agreement with the measured data. However, the simulation results for the PCM temperature profiles deviate relatively from the results obtained by experiments due to segregation problems occurred in the PCM packing in a number of spheres during experiments. This certainly influences the real thermophysical properties of PCM candidates while the simulation model makes use of the ideal prescribed properties set by the PCM supplier. The characteristic knee for phase change appears clearly during the phase change process in the simulation results in figure (6.3) but not at all in the experiments for both the evaporator and condenser. Consequently, the outlet gas and liquid temperatures in experiments approach the steady state more quickly than the simulation, which could be due to the considering the phase change heat capacity of PCM packing in the simulation model, while there is no phase change in the experiment due to segregation, which happened randomly in sporadic packing elements in most of layers. During transient periods, the temperature profile for the solid phase, and consequently temperature profiles for liquid and gas phase, in the simulation is different from that in experiments due to segregation, as can be clearly seen in the first hour in figure (6.3). Once the system reaches steady state, the deviation between experimental measurements and numerical predictions for the outlet liquid and gas temperatures

decreases. The percentage deviation for the evaporator and condenser lies within $\pm 5\%$ at low and high operating temperatures.

However, it can be observed that all the temperature fields for fluid phases follow the PCM temperature trends, as they remain constant during the isothermal phase change processes. Up to this point, the PCM role as a temporary heat storage and heat exchanger become obvious both experimentally and theoretically regardless whether it has negative or positive effects under the present boundary and geometrical conditions and thermophysical properties of designated PCM beads.

Figure (6.4) shows that the outlet liquid and gas temperatures of simulations are in better agreement with those of experiments for empty spheres than with PCM spheres. The maximum temperature deviation between simulation and experimental results for empty spheres packing is less than 3K at steady state for the outlet liquid temperature. Compared with the empty spheres packing, the system of PCM packing took longer time to reach steady state due to the huge heat capacities of PCM. However, this huge heat capacity should have an impact only during the transient period or startup of the plant. Therefore, the deviation between measured and simulated temperatures decreases when the system approaches steady state conditions.

Table 6.3: Measured and simulated total productivities [l]

	High packing, H=0.78m		Low packing, H=0.39m	
	PCM	Empty spheres	PCM	Empty spheres
Experiments	90.5	79.0	72.0	67.5
Simulations	90.9	79.4	73.7	67.6

The accumulated productivities over time and final total productivities for each case including the start-up period are shown in Figure (6.6) and Table (6.3), respectively. The accumulated productivities are linearly related with the operation time both for simulations and experiments, which means the fresh water production rates are almost constant for each case.

The total fresh water productivities for simulations are in good agreement with experiment for all cases. From the present results, the positive impact of PCM beads on the productivity can be seen clearly especially for the higher packing height. The PCM packing increases the productivities by 6.7% and 13.3% for lower (39cm) and higher (78cm) packing heights respectively in comparison with empty spheres packing. Moreover, when the packing height is doubled under same boundary conditions for each packing type, the productivity increases by 25.7% and 17.0% for PCM packing and empty spheres packing respectively.

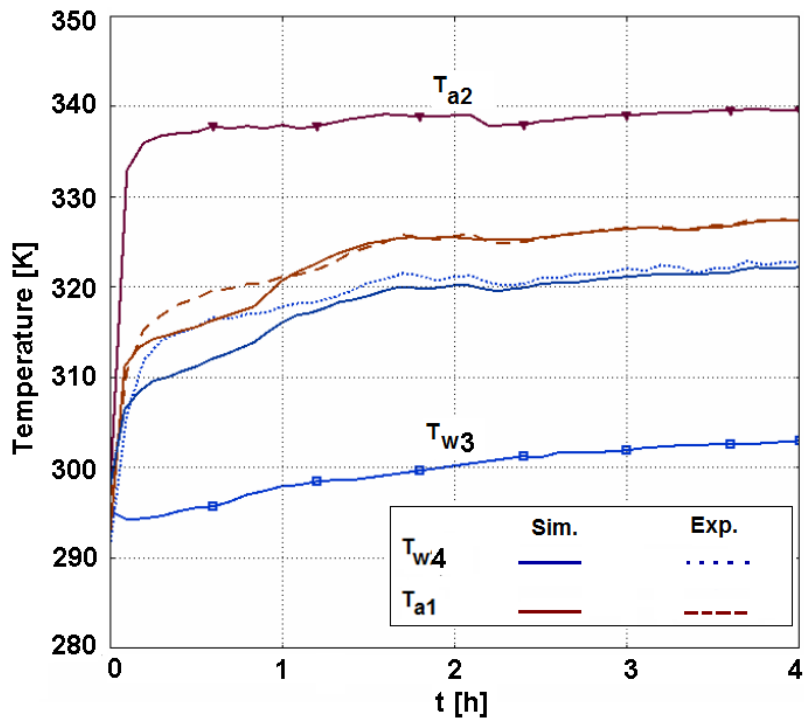
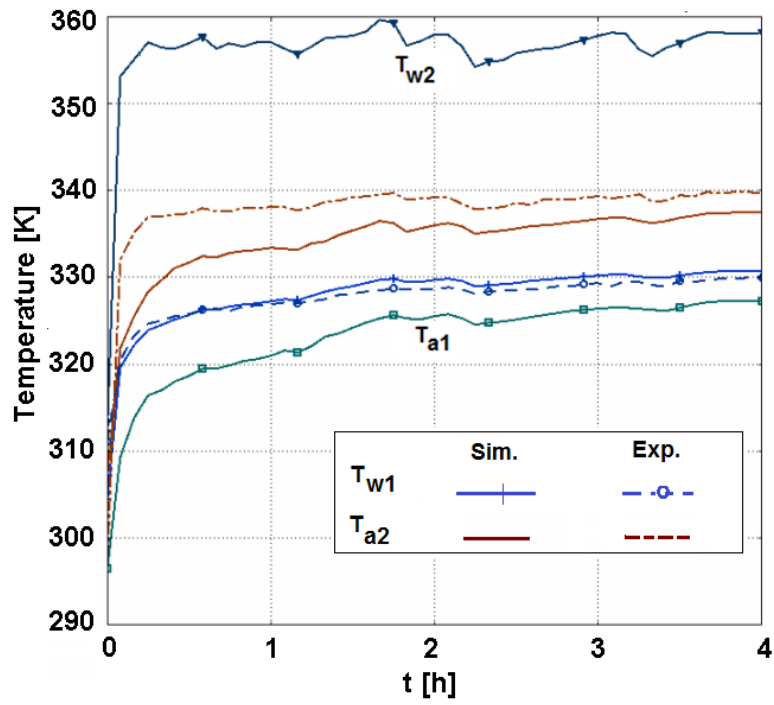


Figure 6.2: Evolution of inlet and outlet liquid and gas temperatures for PCM packing height 78cm; Top: evaporator, (b) Bottom condenser

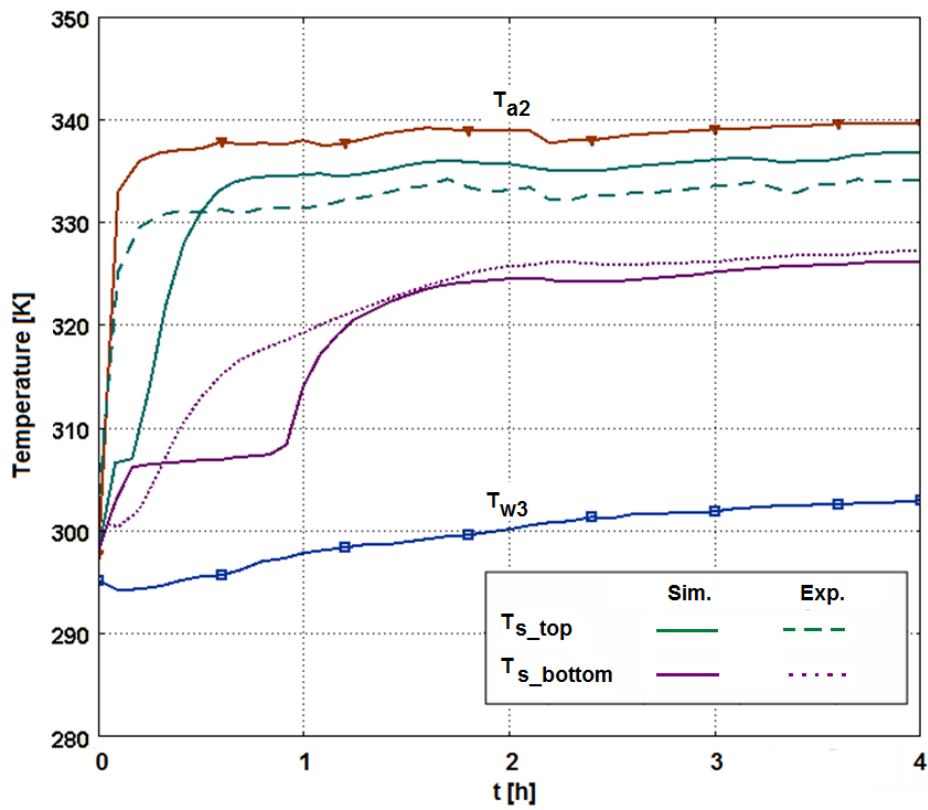
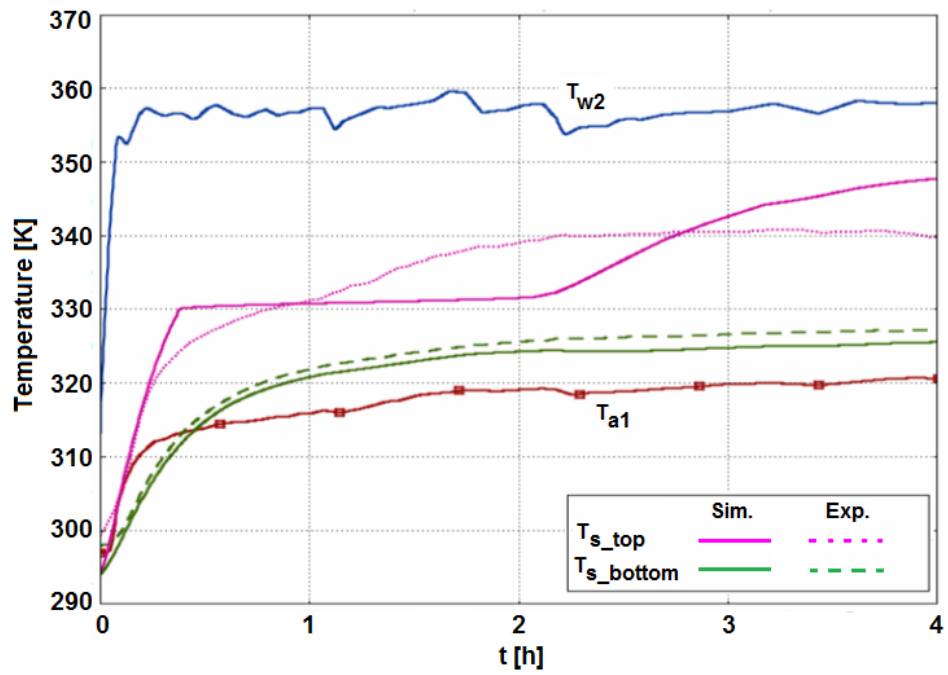


Figure 6.3: Evolution of solid phase temperatures for PCM packing height 78cm; Top: Evaporator, Bottom: Condenser

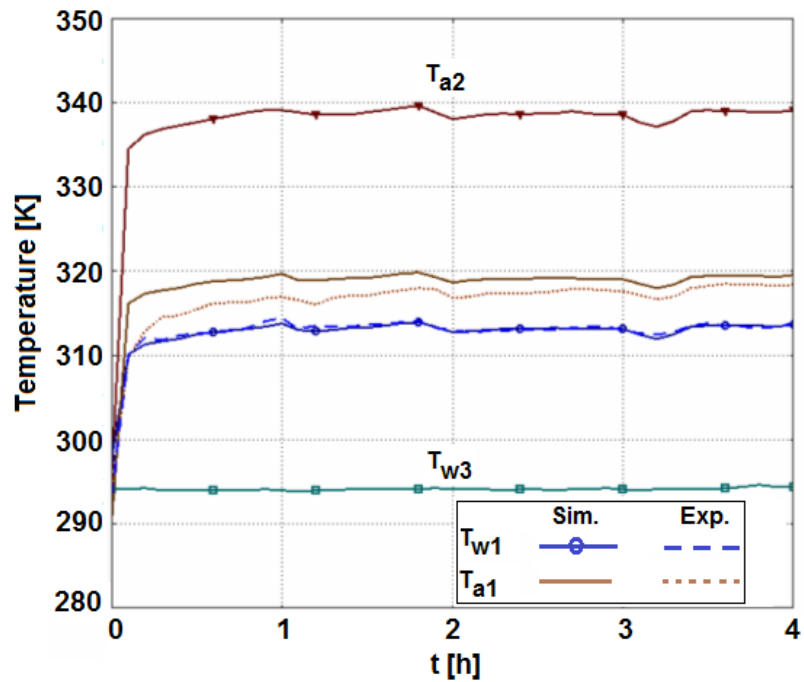
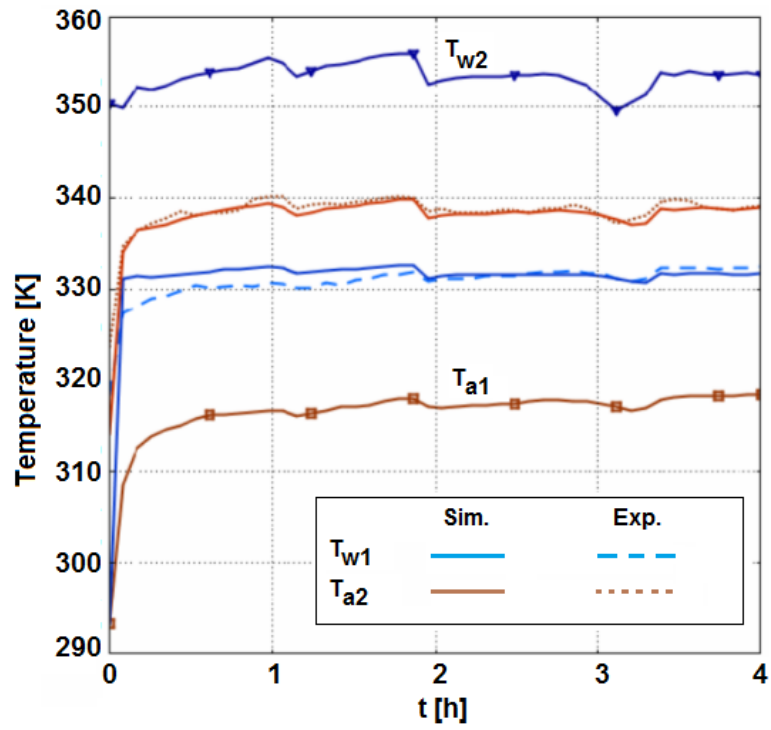
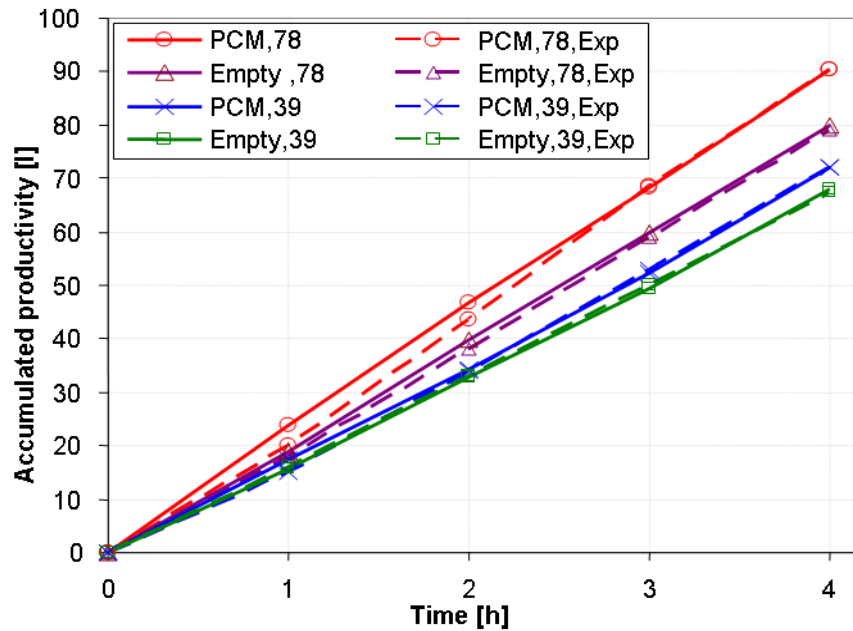


Figure 6.4: Evolution of inlet and outlet liquid and gas temperatures for empty spheres packing height 78cm; Top: Evaporator, Bottom: Condenser



'78' and '39' represent the packing heights in cm

Figure 6.5: Comparison between measured and simulated accumulated hourly productivities

6.4 Sample of simulation results

This section intends to provide more insight into the temporal and spatial developments of different field parameters of interest for better understanding of the PCM regenerator behaviour and its effect on the evaporator performance. It is believed that this extra explanation could be useful for supporting the study approach and core messages. Table (6.4) provides the input operational and geometrical parameters that have been considered for the present run. The air superficial velocity in this numerical experiment, which was one of the early trials to investigate the effect of natural flow, is far lower than that of the validation experiments stated in table (6.2). The lower packing height and slightly lower mass flow rate of hot water have been considered.

Figure (6.6) depicts the temporal evolution of PCM temperature along the packing height of the evaporator. Constant melting temperature as well as the stratification behaviour can be observed. The PCM temperature increases until it reaches the melting point at 330K, and remains constant until complete melting takes place in all layers. The melting front starts from the upper layers, where the inlet hot water

temperature is at its maximum level, and moves downwards due to stratification of both liquid and gas phases as well as the low effective thermal conductivity of PCM along the packing height. Thereafter, a sensible heat component increases the PCM temperature until reaching the steady state conditions. Since the melting front moves in time downward in the bed, this looks like propagating waves or a “sea snake” rising up from the bottom. Little peaks of temperatures above the melting range can be observed near the top of the bed, these may represent some locations just around the breakeven points during the transient period with the gas phase temperature profile (reference is made to figure 5.4), and perhaps also due to melting of PCM over a mushy region rather than a sharp melting front.

Table 6.4: Inlet and geometrical parameters within a sample simulation run

Parameter	Value	Units
Inlet water temperature	358	K
Water flow rate	400	l/hr
Packed height	0.39	m
Column diameter	0.4	m
Inlet and initial air temperature	298	K
Initial PCM temperature	298	K
Air velocity	0.13	m/s

Figure (6.7) shows the temperature history of liquid water along the packing height. The water temperature decreases through its path from top to bottom, where it reaches the minimum. The outlet water temperature increases over time due to continuous decrease in the temperature difference and heat transfer rates between water and both gas and solid phases. Figures (6.8) and (6.9) represent the temperature and concentration fields respectively of the gas phase during simultaneous heating and humidification processes. It can be seen from the figure that the concentration also increases with time and packed bed height, to reach its maximum value of 21mol/m^3 . The time evolution and final profiles of the fluid temperatures and concentration fields is really governed by the existence of a conductive packing medium and its thermophysical properties, otherwise the system would behave stationary and reach steady state in a very short time like other distillation columns and cooling towers packed with non-conductive media.

6.5 Conclusions

In this chapter, the numerical solution procedures and strategy were introduced and applied for solving the governing energy and mass balances of the evaporator mathematical model as an example. Geometric representation of the complex packed bed geometry was replaced by representation of uni-dimensional domain. This enabled to solve the mathematical model both in COMSOL Multiphysics and

MATLAB using the approach of “*Inter-penetrating Continua*” based on the “*volume averaging technique*”. The simulation models for different components have been verified upon realizing a wide variety of experimentation results.

Comparison with the experimentation results indicated good agreement between predicted and measured parameters. Some important lessons have been learned from the validation experiments. Based on the experimental results, the most appropriate empirical correlations for the model have been defined. This allowed more control on various influencing parameters and was projected on the main HDH system’s model which will be used as the main tool for numerical optimization. The individual components models as well as the lumped simulation model for the HDH plant may be regarded as real predictive models for their associated physical systems. On the other hand, for getting more insight and better understanding of various transport phenomena that take place in the system, extra sample of the numerical results were presented. Analysis of the sample results gave more insight in the system behavior and ascertained the role of thermal energy management of the conductive packing media.

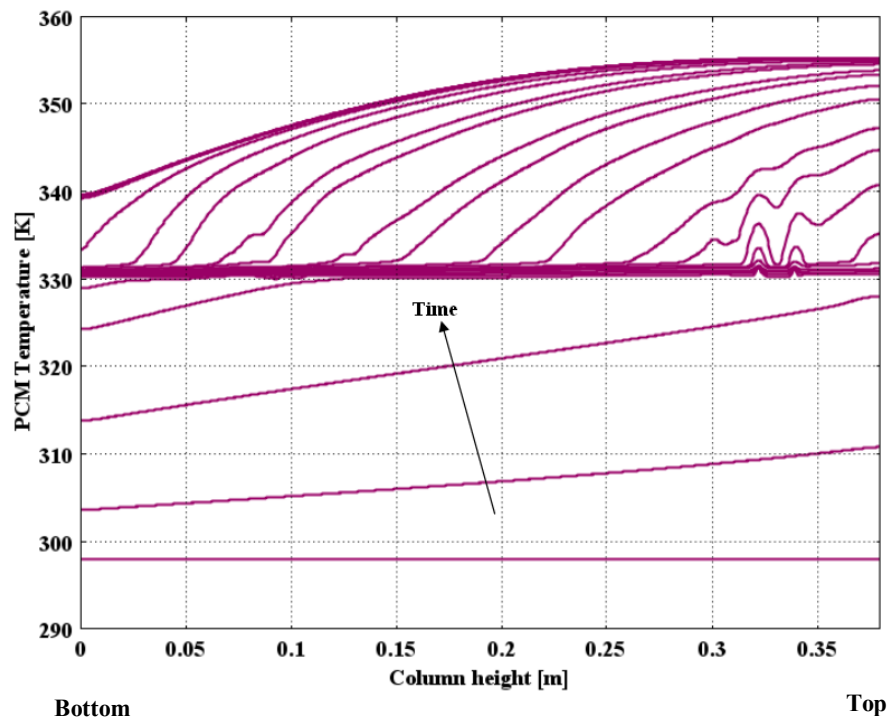


Figure 6.6: Time evolution of PCM temperature along the packed height

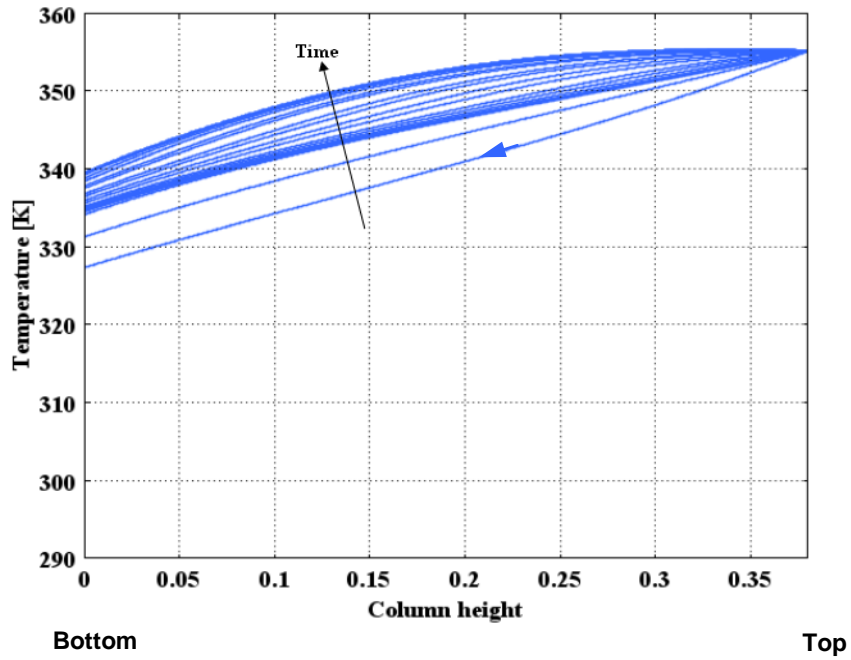


Figure 6.7: Evolution of liquid temperature along the packed height

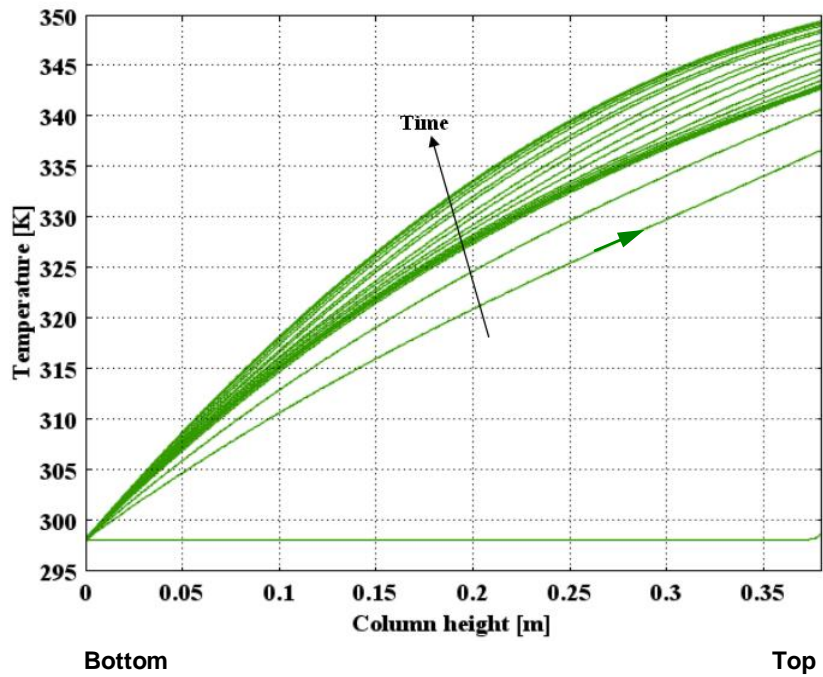


Figure 6.8: Time evolution of gas temperature along the packed height

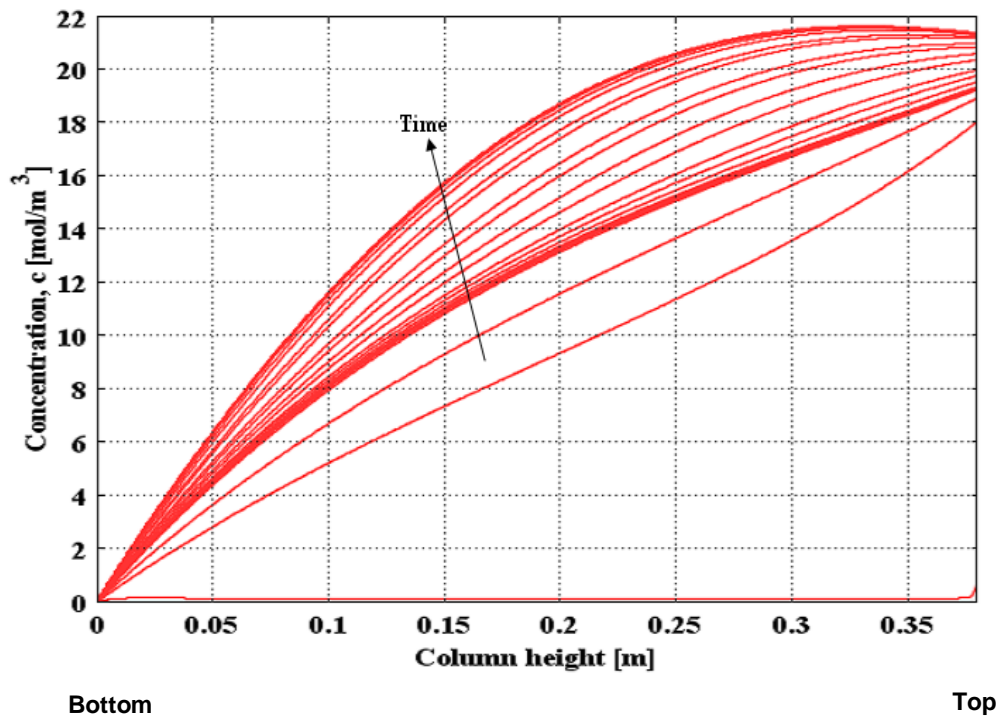


Figure 6.9: Time evolution of water vapor concentration along the packed height

7 Parameters Analysis of the Evaporator and Condenser

This chapter presents the results of the numerical study conducted by using the MATLAB models that quantifies the potential for heat and mass transfer efficiency and optimization parameters for the evaporator and condenser. The aim of this work is to characterize the optimum design of the evaporator and direct contact condenser packed with spherical phase change material (PCM) elements as a conductive media in the humidification-dehumidification (HDH) system. The external thermal buffer will be optimized as an integral part of the HDH plant under real weather conditions and will be presented separately in the next chapter. The stimulus for this analysis derives from recognition that any improvement in the performance of individual components and subsystems might lead to better ways of increasing the fresh water productivity of energy use.

The investigated parameters are:

- Inlet hot and cooling water temperatures and flow rates,
- Packing thermal conductivity,
- Packing size and column aspect ratio,
- Water to air mass flow rate ratio, and
- Inlet air temperature to each component

Here the evaporator and condenser packed beds, unless stated, have the dimensions of 0.6m diameter and 1m packing height, where they are filled with 40mm spherical PCM elements. The reference boundary conditions used for the present computer simulation are listed in table 7.1 and partly on each figure. Table A.1 in the appendix presents the thermophysical properties of PCM candidates in the evaporator and condenser.

The simulation time was extended over 4 hours to guarantee the system reaches steady state. The results of the only last hour were considered for evaluation of all systems under investigation to refer to the analysis when the system works at steady state regime.

7.1 Boundary conditions

The evaporator and condenser performance depends on many parameters, which have mutual influences and combined effects. In order to quantify the effects of several parameters, parametric studies have been carried out numerically with the aim of maximizing the evaporation and condensation rates. Hereby various parameters have been varied to examine their impact on the system performance, mainly the output distillate rate.

Table 7.1: Reference boundary conditions for the evaporator and condenser

Parameter	Units	Value
Mass flow of hot water " M_{hw} "	kg/h	1000
Mass flow of cold water " M_{cw} "	kg/h	1000
Velocity of air " v_a "	m/s	0.55
Temperature of hot seawater water " T_{w2} "	°C	83
Temperature of cooling water " T_{w3} "	°C	25
Temperature of inlet air to the evaporator " T_{a1} "	°C	25
Temperature of inlet air to the condenser " T_{a2} "	°C	66

7.2 Evaporator Performance

Fundamental variables and critical parameters mentioned above and the effect of using different types of packing media will be discussed and analysed. For each case, only the value of each targeted parameter was varied, while other parameters were kept constant at the specified value.

7.2.1 Effect of packing size

It is known that there is an inverse relationship between packing diameter and specific surface area (i.e. packing area per unit volume of the bed; m^2/m^3), as depicted in figure (7.1). For a specific column diameter, all heat and mass transfer coefficients depend on the specific area of the packing (a), as well as the packing diameter itself, according to equations (4.43) and (4.48) to (4.50). As the flow rate and diameter of spherical particles are increased under a given diameter of the packed column, the mean heat and mass transfer coefficients increase, while the interfacial areas of contact decrease, such that it becomes difficult to optimize the bed characteristics.

In conventional packed beds, a is inversely related to both the porosity (ε) and particle size through equation (4.48), while the porosity in turn is directly related to the particle diameter as suggested by equation (4.43). Combination of all of these considerations with energy and mass balance equations (4.14) to (4.17) shows the opposing effects that the particle size and specific surface area have on the thermal performance of the system. The effect of packing diameter on the evaporation rate is demonstrated in figure (7.2), which clearly explains why heat and mass transfer rate densities do not increase substantially in consistence with figure (7.1) as the dimension of the sphere diameter (d) becomes smaller especially under lower mass flow rates of hot water. The productivity decreases on increasing the packing diameter, but this effect becomes more significant at higher mass flow rates. However, it is excepted that smaller packing size leads to a higher heat capacity flow between hot water and air, but it seems that its effect is not the predominating one.

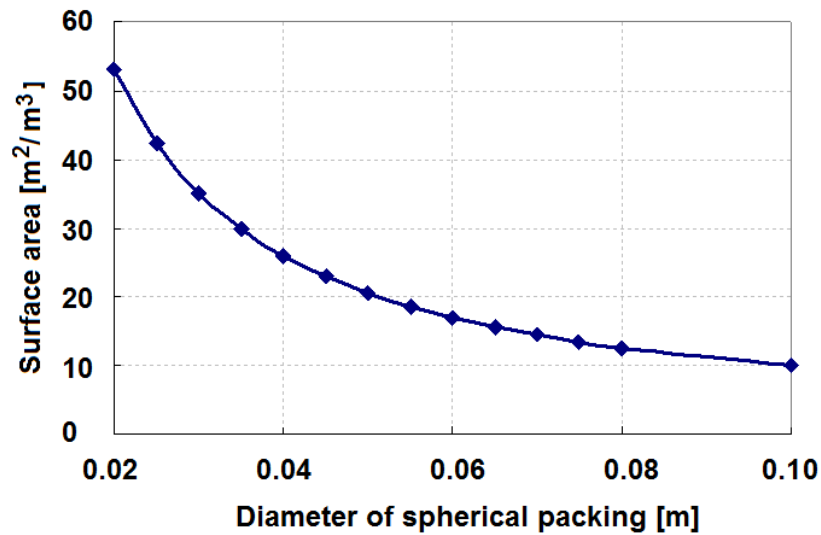


Figure 7.1: Effect of packing size on specific surface area of the packed bed

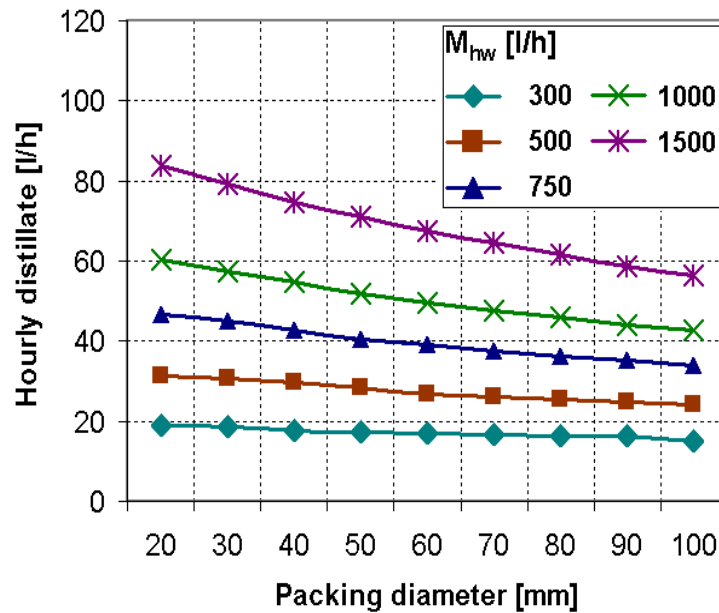


Figure 7.2: Effect of packing size on the evaporation rate

On the other side, the effect of the packing size on pressure drop through the bed is of primary importance in the design of the column. Packing of small sized elements requires a large pressure drop for uniform fluid flow through the bed, which causes a

large amount of energy to propel the air in the column. Packing of large size would be desired to reduce the pressure drop.

Figure (7.3) shows the pressure drop of the gas mixture under different hot water mass flow rates. However, due to relatively big size of PCM spherical capsules considered in the study (i.e. the commercially available PCM spheres size) and low airflow velocity range commonly used in HDH cycles, the maximum pressure drop is approximately limited to 2 kPa for a particle diameter larger than or equal to 40mm, which represents only 2% of the ambient air pressure. The pressure drop increases considerably when the packing diameter decreases below 40mm. Thus the electric energy required to induce the air flow also increases, which represents a major problem in non-electrified areas of developing countries, where the electric energy may be supplied by PV panels. In addition, operating the system under high pressure drops requires more expensive and robust structure than that operating at nearly ambient conditions.

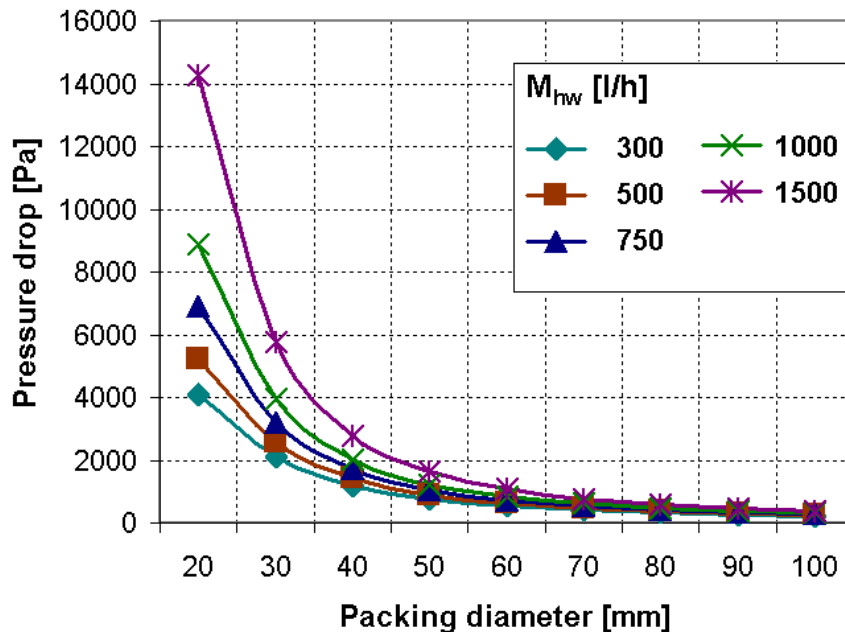


Figure 7.3: Effect of packing size on the pressure drop of the gas

The pressure drop is strongly dependent on air to water mass flow ratio. However, for a 1000 kg/h water mass flow rate, or water mass flux of $2.2 \text{ kg/m}^2 \cdot \text{s}$ and 75mm packing diameter, the pressure drop under natural convection is estimated from experimental data as 0.35 kPa, while it is around 0.5 kPa for the forced convection at air to water mass flow ratio of 0.3. For the 40mm diameter packing it is estimated to

be 0.45 kPa under natural convection and 2 kPa under forced convection as pointed out above. These values correspond to an electric power consumption of 0.15 kWh per m³ of fresh water production under natural convection (virtual energy saving due to overcoming the pressure drop by natural convection), while it is around 0.4 kWh/m³ real consumption for the forced convection.

As a result, the influence of gas-mixture pressure drop on the energy input to the HDH system as well as its performance can be safely neglected in comparison with the thermal energy input requirements when the packing size is equal to or greater than 40mm. However, for the mass flow rates considered in this study, on comparing figures (7.2) and (7.3) and considering the cost and available sizes of PCM packing in the market, the packing diameter of 40mm can be considered as the optimum size and, therefore, will be fixed throughout the parametric analysis.

7.2.2 Effect of column aspect ratio

The optimum void fraction is not only strongly dependent on the ratio between packing and column diameters (i.e. equation 4.43) but also on the ratio between column diameter (D_{bed}) and height (H), which is called the column aspect ratio due to the MEHH phenomenon. For a given packing diameter, the packed height and column diameter can combine differently to yield the same overall volume. The general design strategy is to minimize the fluid flow path length in contact with the porous medium to minimize the friction losses in the bed while simultaneously maximizing the distillation rate due to the MEHH and avoiding cooling effects which may result in the lower part of the bed as mentioned earlier in chapter 5.

In order to study the impact of the column geometrical aspect ratio on fresh water productivity, first the packing volume was kept constant at $V_{bed}=0.3\text{m}^3$ (which was close to the packing volume of the prescribed column dimensions 0.6m diameter and 1m packing height) and the packing height was kept constant. The column diameter was varied in both cases. Figures (7.4) and (7.5) show the effect of column geometrical aspect ratio on the hourly distillation under different hot water mass flow rates for both cases. At a lower column aspect ratio, the diameter of the tank gets smaller and hence the cross sectional area is reduced, which increases the superficial flow rate and as a result the heat and mass transfer coefficients increase. Thus, for both cases the effect of the aspect ratio parameter becomes more sensible under higher mass flow rates of hot water.

In the first case at constant packing volume, as the aspect ratio increases the packing height decreases, which reduces the favourable thermal stratification in the bed and hence the evaporation rate decreases. For constant packing height, in the second case, the results reveal that increasing the aspect ratio improves the performance of the system, until a saturation point is reached. The general tendency is that an enlargement of the column diameter increases the packed volume and the

interfacial areas active in heat and mass transfer to the air which enhances the evaporation rate.

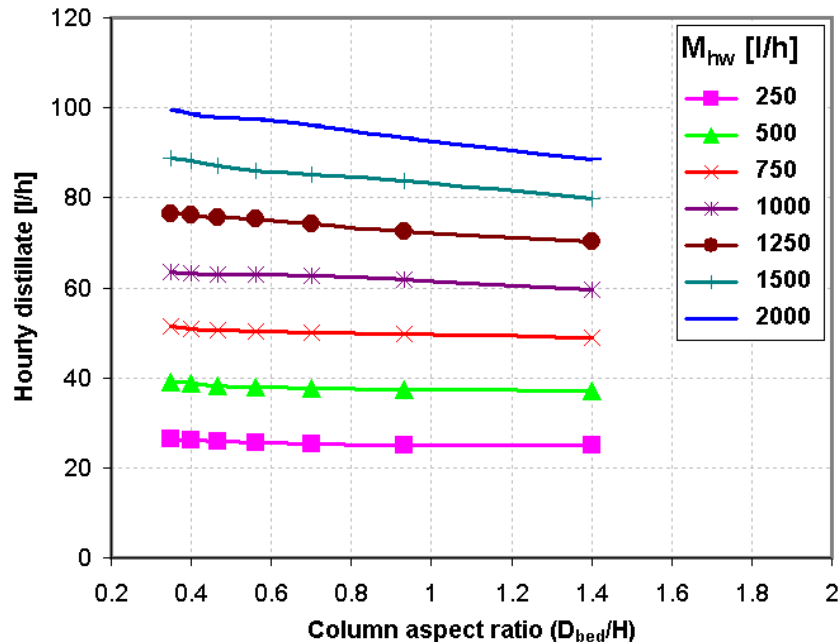


Figure 7.4: Effect of column aspect ratio on the evaporation rate, $V_{bed}=\text{const.}$

However, when the maximum saturation potential of the outlet air is reached, additional enlargement of the column diameter has no positive effect any more. This means that there is an optimum diameter of the column for a certain water mass flow rate. Increasing the column diameter beyond this optimum value leads to a decrease in the thermal stratification which decreases the distillation rate. It is apparent from figure (7.5) that the optimum performance can be obtained at an aspect ratio between 0.8 for low mass flow rates and 1 for higher mass flow rates.

Nevertheless, the effect of aspect ratio was further examined at a higher packing height of 2m as shown in figure (7.6). This plot obviously shows that the aspect ratio is not the sole determinant factor in column sizing but also the packing height by itself plays an important role in the evaporator performance due to the MEHH phenomenon. Moreover, the packing height has a significant influence on the optimum column aspect ratio as well. In this case, as the packing height is increased, the thermal stratification in the bed increases and the dependency of the optimum aspect ratio becomes more strongly tied to the hot water mass flow rate. Two distinct groups of mass flow rates can be classified as; below and above 1000 [l/h]. Below a mass flow rate of 1000 [l/h], the trend is fairly similar to effect of column

aspect ratio under constant bed volume in figure 7.4. For the higher mass flow rates, there is a clear optimum aspect ratio lies between 0.4-0.5 at which the evaporation rates peak. These findings indicate that no generalization can be made regarding the optimum aspect ratio, but should be rather regarded as a case specific.

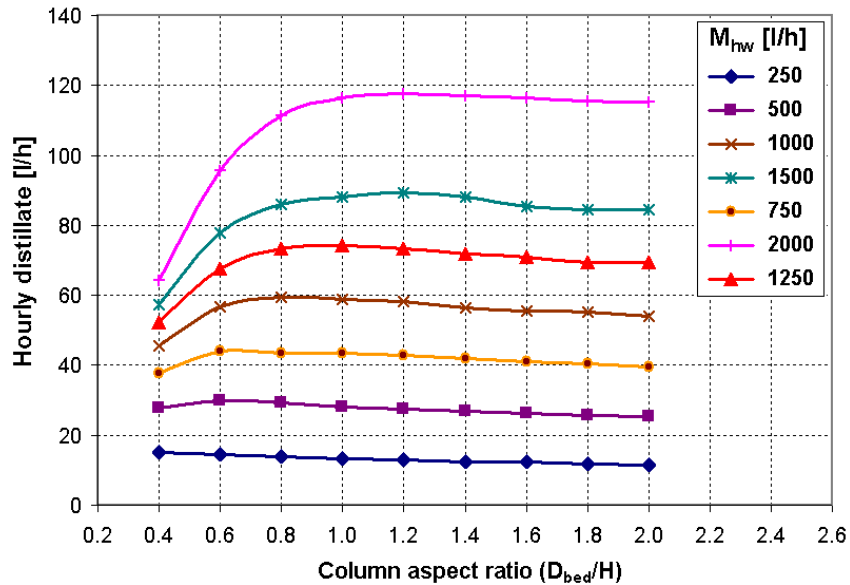


Figure 7.5: Effect of column aspect ratio on the evaporation rate, $H=1\text{m}$

7.2.3 Effect of inlet hot water temperature

The gas-solid heat flow direction depends on the quality of inlet heat capacity flow of hot water relative to the heat capacity of the packing and the state of inlet gas temperature to the column. As the ratio between water heat capacity and packing heat capacity increases, evaporation rate is enhanced. This is because, as the water to solid heat capacity ratio increases, both T_s and thermal stratification increase and the rate of heat transfer from the hot solid surface to the gas increases. Figure (7.7) presents results for the influence of inlet hot water temperature on the evaporation rate. This figure illustrates the dramatic difference between the behaviour of high and low inlet hot water temperatures. As it can be seen in this figure, the response of the system becomes more profound as the water load increases. The influence of increasing the water load is three folds; the interfacial areas are changed due to increasing the wetted area, the heat and mass transfer coefficients increase due to varying the liquid and gas hold up, and the liquid-solid heat capacity ratio increases as well. It can be clearly observed from the slopes, that the inlet hot water temperature has the most significant effect on the evaporation rate with respect to other parameters.

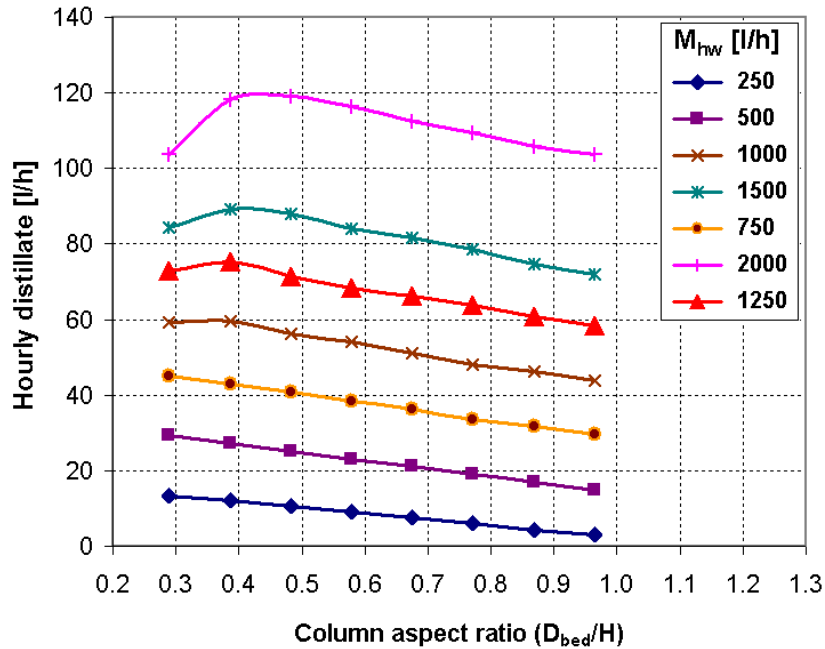


Figure 7.6: Effect of column aspect ratio on the evaporation rate, $H=2\text{m}$

The evaporation rate, as expected, increases as the inlet hot water temperature increases and, as a consequence, the solid temperature T_s increases as well. As the T_s increases, the rate of heat transfer from the solid to the humid air (i.e. the gas) increases, which superheats the gas and increases its capacity to carry more water vapour across the successive, stratified packing layers. At low inlet hot water temperature, the mean value of T_s may be lower than the mean gas temperature along the packing, and the direction of resultant heat flow between solid and gas phases may be reversed as well.

7.2.4 Effect of inlet saturated air temperature

The inlet air temperature to the evaporator is another fundamental parameter for the evaporator effectiveness. Figure 7.8 shows the results of varying the inlet air temperature. One can clearly see the declining trend of the evaporation rate with increasing the inlet air temperature particularly at sufficiently high water mass flow rates. The reason behind this trend is attributed to the fact that, for a closed air loop cycle, the air is always saturated at the local temperature everywhere in the HDH cycle, and its humidity content varies exponentially with the temperature.

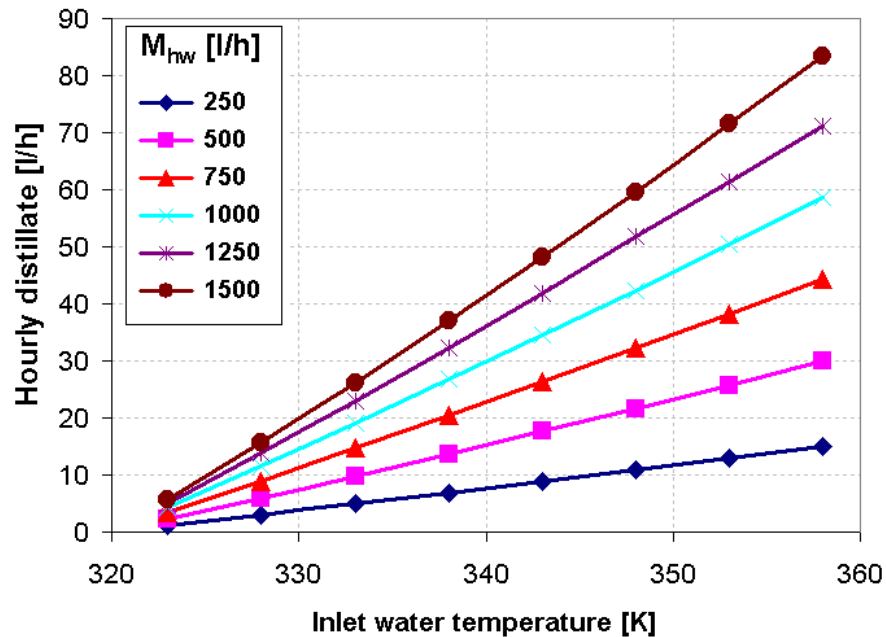


Figure 7.7: Effect of inlet hot water temperature on the evaporation rate

Under such conditions, the optimum effectiveness of the evaporator would be obtained when the inlet/outlet temperature difference can be maximized. Since the outlet air temperature is limited thermodynamically by the inlet hot water temperature, increasing the air temperature at the inlet of the evaporator decreases the exploitable potential. Practically, in a closed air loop HDH cycle, the inlet air temperature to the evaporator is determined by the condenser effectiveness and vice versa.

7.2.5 Effect of water to air flow ratio

A crucial parameter in the performance of an air-water system is the air mass flow through the direct contact heat and mass exchanger. An increase in the mass flow results in an increase of the effective heat and mass transfer coefficients. This is a positive aspect; however a higher air mass flow also decreases the temperature and humidity rise that is achieved within the evaporator, which in turn has a negative impact on the condenser performance in a closed air loop HDH cycle. As a result, the air mass flow rate in the HDH cycle not only influences the individual thermal effectiveness of the evaporator or condenser by itself but also has strong mutual impacts on both of them. Thus, a compromise between the evaporator and the condenser efficiencies has to be made. This is a fundamental aspect that needs to

be considered, as the evaporator and condenser are coupled together in the HDH cycle. Therefore, it could be more practical to perform the same analysis when dealing with the performance optimization of the HDH plant as a whole. Thus, this context will be presented in the next chapter under real weather conditions of a selected geographical location.

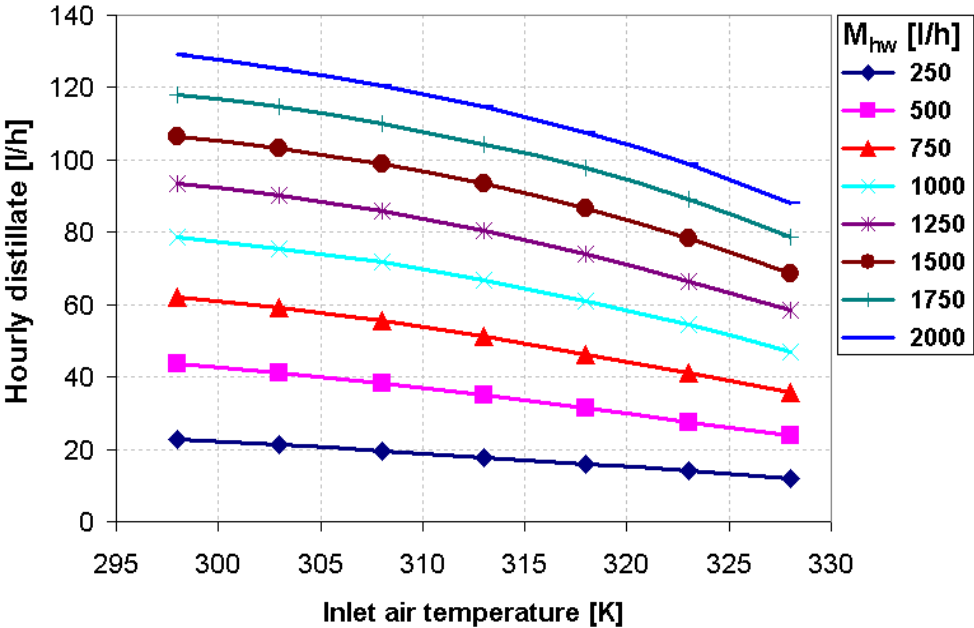


Figure 7.8: Effect of inlet air temperature on the evaporation rate

When the increase in air mass flow rate is accompanied by an increase in hot water mass flow rate, as it can be seen in figure (7.9), the effect is amplified and the optimum air/water flow ratio increases until reaching a saturation point. It can be said that an air/water flow ratio of 1.0 is fairly adequate for reaching the optimum saturation point for the different mass flow rates considered in the analysis.

7.2.6 Effect of packing thermal conductivity

In order to choose an appropriate packing media for the evaporator, the effect of thermal conductivity was investigated. Since real application will utilize real materials available, the later two factors shall be analyzed through utilization of different packing media such as PCM and sensible heat storages (e.g. water, air spheres, aluminum, iron, Pyrex glass, and fired clay brick). The PCM latent heat of fusion is one of the most important properties for PCM that determines its capacity to store energy. However, the energy storing and releasing processes occur during transient states, and the latent heat of fusion can affect the performance of transient state as

well as the time required to reach a steady state, but will never affect the system once it reaches steady state or when passing through low transient periods.

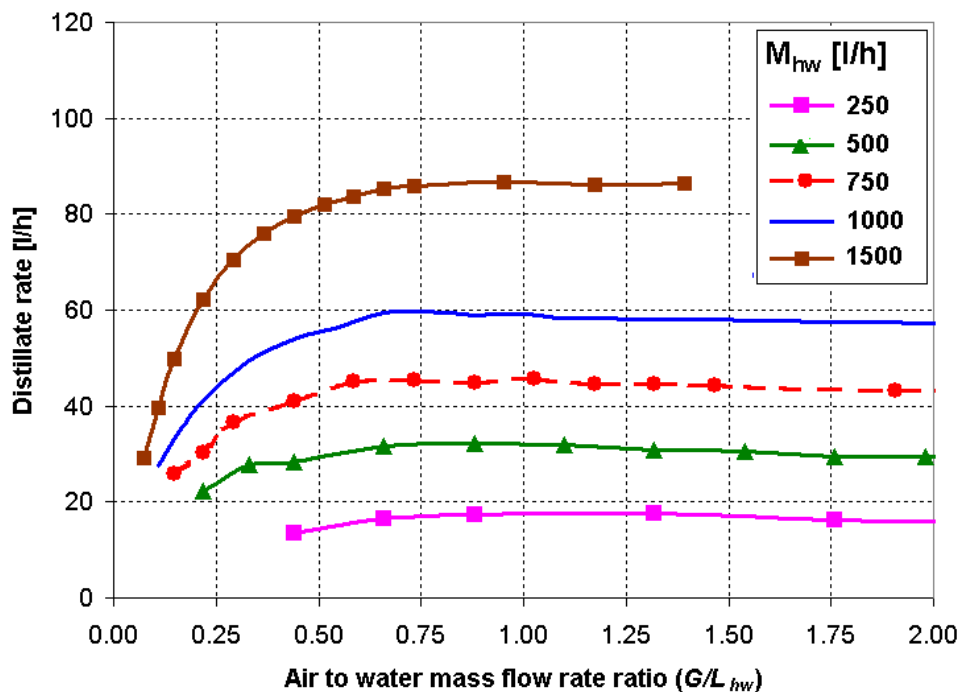


Figure 7.9: Effect of air/water mass flow ratio on the evaporation rate

As pointed out earlier in the experimental analysis, the thermal conductivity of the packing is an important factor, which influences the thermal performance of the dual phase change regenerators. The analysis indicated that thermal conductivity controls local heat and mass transfer not only at solid-liquid and solid-gas interfaces but also at liquid-gas interface. At steady state conditions, the energy flow from liquid to solid phase equilibrates with the energy flow from gas to solid and the local temperatures of all phases remain constant. Therefore, numerical analysis has been carried out to have deep insight about the extent of this effect. The effect of thermal conductivity is expressed mathematically not only in the heat balance equations of the solid phase as described in chapter 4, (e.g. equation 4.2, and 4.4) but also in the energy balances of both liquid and gas phases through the introduction of the Jefferson degradation factors in the heat transfer coefficients with the solid phase (i.e. equation 4.9).

Figures (7.10) and (7.11) illustrate the difference between the evaporation rates of high and low thermal conductivity materials. The effect of thermal conductivity is depicted in figure (7.10). Figure (7.11) demonstrates the dependency of the

evaporation rate on the hot water load with reference to air as a very poor conductive medium.

As it can be seen in these figures in comparison with air, it is clear that the evaporation rate increases at higher solid thermal conductivity. Nevertheless, the proportionality of evaporation rate is neither uniform with k_s nor linear with the water mass flow rate. It is also important to point out that maximum evaporation rate occurs when k_s is around $1.14 \text{ W.m}^{-1}.\text{K}^{-1}$ as for the case of Pyrex glass and fired clay brick as listed in table (7.2) . It seems that around this value of k_s , the best balance between sensible and latent heat components at different interfaces can be obtained. This means that the evaporation rate is enhanced at the expense of the sensible heat component at the liquid-gas interface due to increasing the sensible heat transfer at the solid-gas interface with better stratification in the bed. As the thermal conductivity is further increased, this optimum balance is broken down and evaporation rate is decreased.

On comparing the productivities of the Pyrex glass and fired clay bricks, it is recommended that, using smaller size (40-50 mm diameter) of spherical fired clay bricks and would be the ideal candidate for the present application due to its lower cost, rather than the Pyrex glass which is quite expensive, heavy, and has high vulnerability for breaking.

In figure (7.11), the highly conductive media such as aluminium and iron show a declining trend for the percentage improvement in the evaporation rate over the air, as an approximately non-conductive medium, when increasing the water load. The lower conductive media show a peak at 500 l/h, and then follow the same declining trend as the water load is further increased. Although increasing the water load increase the productivity due to increasing the wetted area and heat and mass transfer coefficients at water-air interface, the area of dry patches decrease with the same magnitude of increasing the wetted area which decreases the heat transfer at the solid-air interface and hence the percentage improvement over the air spheres decreases as well. The phenomenological process known as the MEHH, which is an important topic addressed in the current study, stands behind this interpretation.

Table 7.2: Effect of different packing media on the evaporation rate ($M_{hw}=1000 \text{ [l/h]}$)

Medium Properties	Glass, Pyrex	Brick (fired clay)	Iron	Aluminum	Water	PCM (HS 58)	Air
$k \text{ (W/m.K)}$	1.14	1.13	70	229	0.64	0.6	0.027
$\rho \text{ (kg/m}^3\text{)}$	2240	2310	7880	2701.1	1000	1280	1.084
$c \text{ (J/kg)}$	840	922	511	938.3	4180	2.51E+05	1015
$M_d \text{ [l/h]}$	62.52	62.38	60.87	59.92	60.73	59.82	56.89
$M_d \text{ Increase (\% relative to air)}$	9.9%	9.65%	6.99%	5.32%	6.74%	5.14%	0.00%

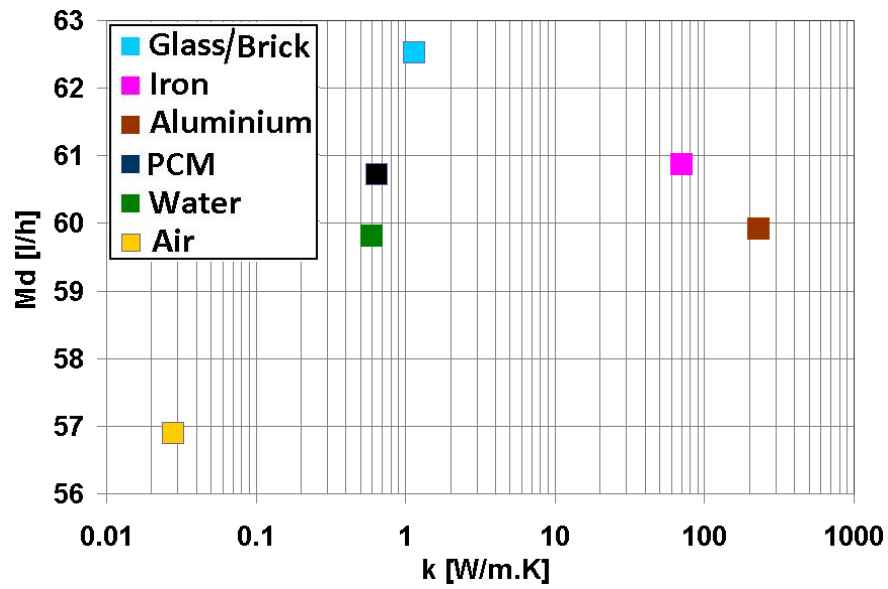


Figure 7.10: Effect of packing media properties on the evaporation rate

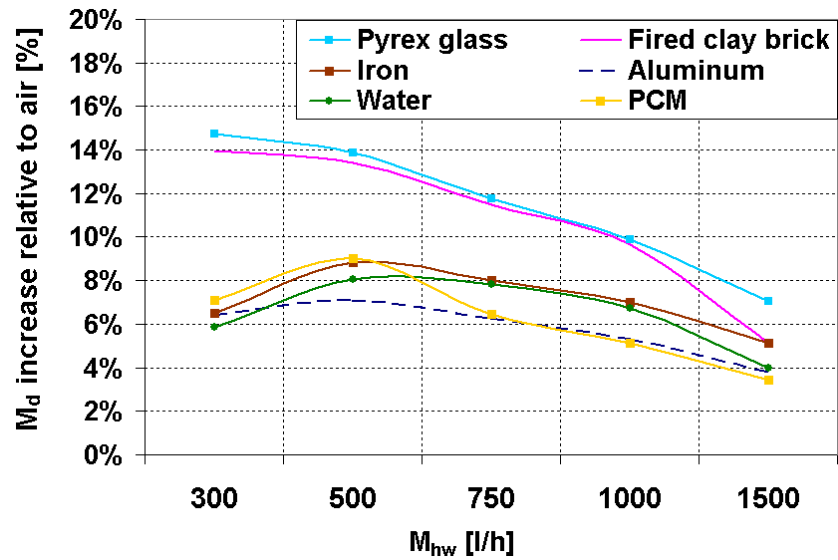


Figure 7.11: Effect of hot water flow rate on the evaporation rate of different packing media

7.2.7 Concluding remarks

It has been demonstrated that the productivity of an evaporator can be noticeably enhanced by the use of a conductive packing media. The thermal conductivity represents an influencing parameter that controls local heat and mass transfer rates. The effect of thermal conductivity on the evaporator effectiveness and distillate rate has been analyzed through utilization of different packing media. It was found that the proportionality of evaporation rate is neither uniform with the thermal conductivity k_s nor linear with the hot water mass flow rate. It is also important to point out that the maximum evaporation rate was obtained when k_s is around $1.14 \text{ W.m}^{-1}.\text{K}^{-1}$ as for the case of Pyrex glass and fired clay brick. The study concluded that, using smaller size of spherical fired clay bricks as a conductive media with optimum thermal conductivity, and due to its lower cost would be the ideal candidate for the present application, rather than PCM media that usually have poor thermal conductivity and high cost. The present analysis indicated that air to water mass flow ratio is one of the most crucial operational parameters and its optimum value lies around 1.0.

7.3 Condenser Performance

Due to similarity between the evaporator and condenser, the previous discussions and interpretations of the effect of various influencing parameters on the evaporator performance can serve as a common background to understand the condenser behaviour.

7.3.1 Effect of inlet cooling water temperature

As pointed out earlier, under steady state conditions the energy and mass balances imply that the liquid phase will be the final destination (i.e. the sole sink) of all the energy and mass transfer from gas to both solid and liquid phases. Effect of cooling water temperature and mass flow rate or the heat sink capacity can be considered both of self-evident and fundamental importance on the energy flow between all phases in the system under each specific boundary and geometrical conditions. As shown in figure (7.12), the lower inlet cooling water temperature and higher cooling water mass flow rate, the more fresh water that can be produced under given conditions.

Following the same trend, the condenser performance has more pronounced response to the inlet cooling water temperature under higher cooling water mass flow rates. This appears clear from the steeper slopes for higher cooling water mass flow rate in figure (7.12). Given certain boundary conditions, cooling water mass flow rate can be adjusted with the inlet cooling water temperature to attain a specific cooling effect (i.e. condensation rate). For example, to get a condensation rate of 40l/h, three different combinations of cooling water mass flow rates and inlet temperatures can be used; 750l/h with 20°C, 1000l/h with 30°C, and 1500l/h with

40°C respectively. This gives flexibility in optimization of the system operation conditions depending on the site specific conditions with respect to the prevailing climatic conditions and seasonal variations of local cooling feed water source.

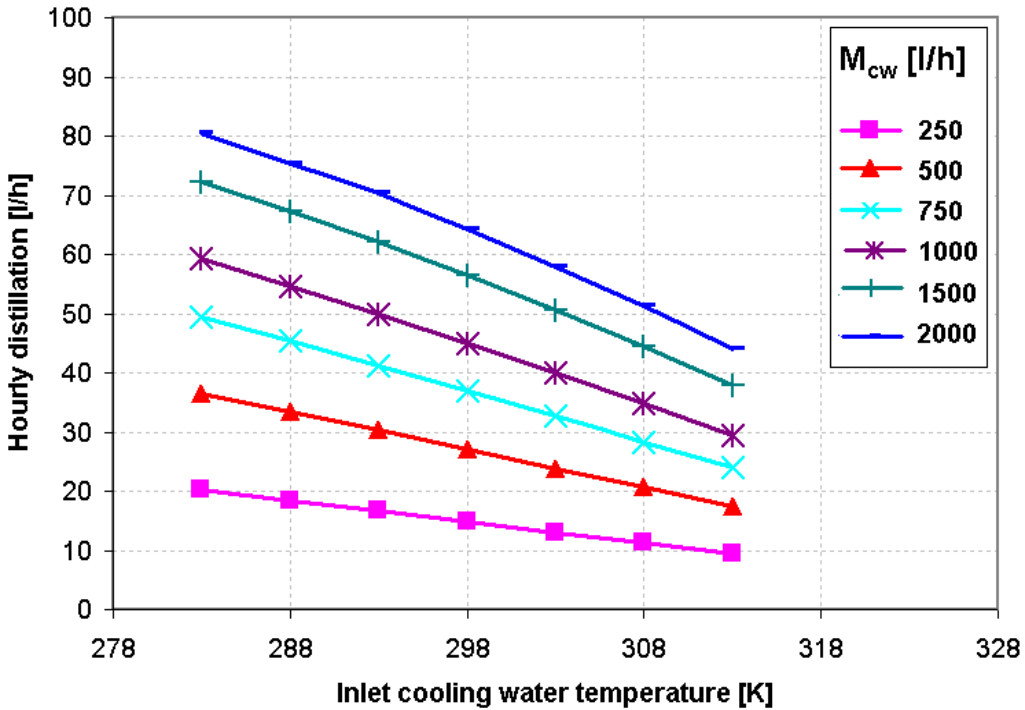


Figure 7.12: Effect of inlet cooling water temperature on the condensation rate

7.3.2 Effect of inlet saturated air temperature

Assuming saturation conditions (valid assumption for closed air loop cycles), increasing inlet air temperature will, of course, result in a higher water vapor content per kg of dry air and will increase the temperature and vapor pressure differences between the gas phase on one side and both PCM and liquid phases on the other side (i.e. increasing heat and mass transfer potentials). Therefore, the inlet air temperature is a very important parameter for the condenser performance. Figure (7.13) depicts the effect of inlet saturated air temperature on the hourly condensation rate. It seems that the condensation rate approximately varies linearly with the inlet air temperature at very low mass flow rate of cooling water and higher range of inlet air temperatures beyond 65-70°C regardless of the mass flow rate. The higher the cooling water mass flow rate, the stronger effect of the inlet air temperature is. While the inlet hot air is the heat source, increasing its sensible and latent heat capacities, the heat sink capacity should be enhanced with the same magnitude to meet the

condensation load. Increasing the mass flow rate of cooling water perhaps could be the easiest way to provide such extra heat sink capacity. Nevertheless, the outlet cooling water temperature will decrease, which certainly would have a negative impact on the effectiveness of heat recovery down stream of the condenser as was described in figure (4.1).

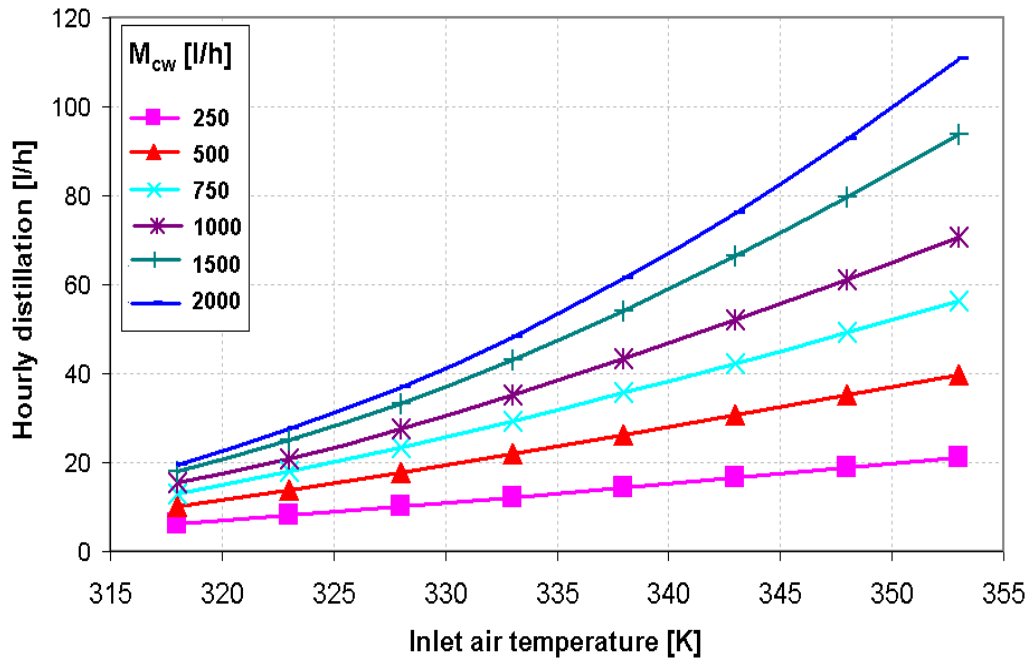


Figure 7.13: Effect of inlet air temperature on the condensation rate

From figure (7.13), it can be seen that to handle a specific condenser load, different combinations of inlet air temperature and matched cooling water mass flow rate can be applied under given boundary conditions. However, to get more insight into the effect of the ratio between source and sink heat flow capacities, the cooling water to air mass flow rate ratio has to be carefully studied as a crucial operational parameter.

7.3.3 Effect of cooling water to air mass flow ratio

The ratio between cooling water to air mass flow rate is widely expressed in terms of liquid flux and gas fluxes (i.e. L/G ratio) to exclude the effect of column cross sectional area. To perform this analysis, the air superficial velocity was varied from 0.1 to 2m/s while the cooling water mass rate was varied from 250 to 1500l/h. The variations of air to water mass flow rate ratio and the cumulative hourly condensate are shown in figure (7.14) and figure (7.15). It can be realized from these figures that

the condensate rate, productivity factor, and number of transfer units (NTU) are highly influenced by the variation of G/L ratio. On comparing the two figures, it could be stated that the optimum air to water mass flow ratio lies around 0.5.

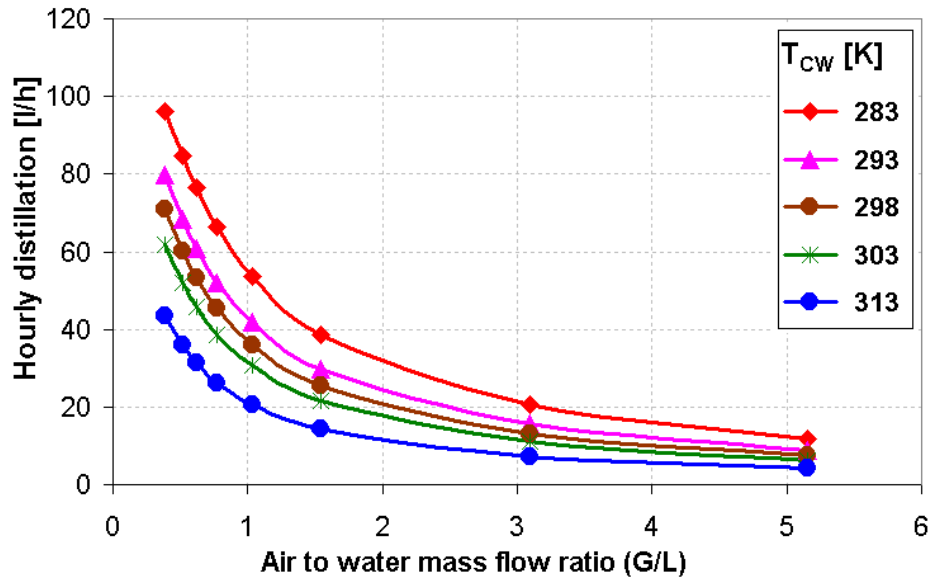


Figure 7.14: Effect of air to water mass flow ratio on the condensation rate

7.3.4 Effect of packing thermal conductivity

In order to choose an appropriate packing media for the condenser, the effect of thermal conductivity was investigated similar to the evaporator through examining the same group of packing media. The thermophysical properties of PCM packing in the condenser were kept the same as those of PCM 34.

The packing thermal conductivity is a fundamental factor, which influences the thermal performance of the condenser. At the liquid-solid interface the rate and direction of heat flow becomes part of the energy and mass balances at the liquid-gas and solid-gas interfaces as mentioned earlier. The condensed water at the solid-gas interface trickles down and may or may not collide with the cooling water somewhere along its down flow through the packing.

Figure (7.16) gives the hourly productivity as a function of thermal conductivity for different packing media. There is essentially no big difference for each packing material other than air. Comparing the productivity of all materials, as presented in table (7.3), at a cooling water flow rate of 1000 l/h, aluminium and iron packing produce nearly the same and highest condensation rate with 64.97 and 64.95 l/h,

respectively, followed by glass (63.874 l/h), brick (63.866 l/h) and water capsules (63.19 l/h), then PCM (62.77 l/h), and finally air capsules (60.23 l/h). Observing this result and the media properties listed in table (7.3), we find that the packing media with higher thermal conductivities produces more condensate. Moreover, for all media, the rank of productivities at any cooling water mass flow rate is coincidentally the same as the rank of their thermal conductivities.

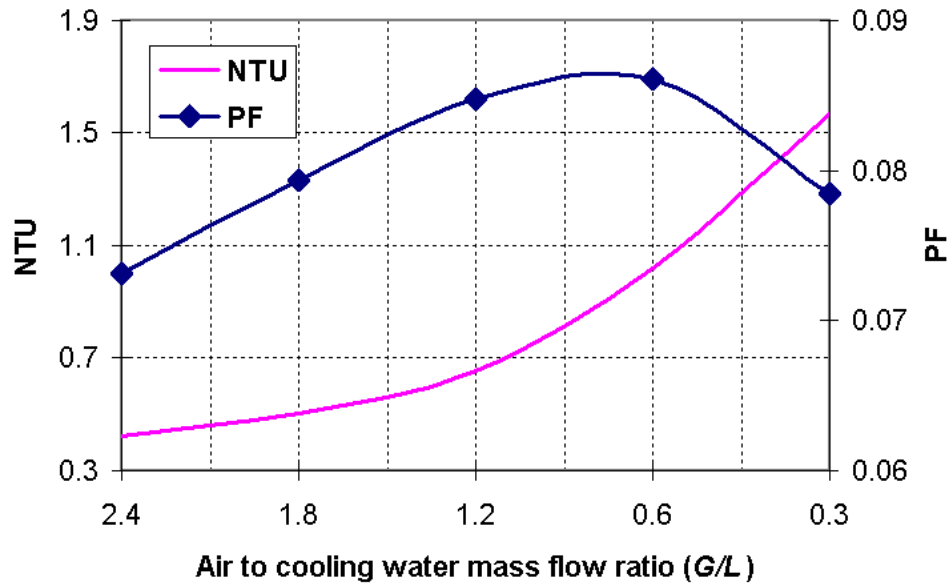


Figure 7.15: Effect of water to air mass flow ratio on the PF productivity factor and NTU

That is the order of aluminum, iron, brick, glass, water, PCM 34 and air. Although the productivity differences between them are relatively small (excluding air capsules), this order never changes under given conditions. Consequently, the thermal conductivity is the most important property when choosing packing media. The higher the thermal conductivity, the better the condensation rate will be, without consideration of other factors, such as economical factors, packing weight, corrosion and aging, etc.

The present analysis indicates that, among all thermo-physical properties of packing medium, the thermal conductivity represents an influencing parameter that controls local heat and mass transfer not only at solid/liquid and solid/gas interfaces but also at liquid/gas interface. Starting from ambient conditions at the beginning of plant operation, the PCM has a capacity to store some latent heat of condensation and produce some more fresh water during this early transient period. Marching in time the PCM temperature increases until it reaches steady state during which the cooling rate plays the main role to keep PCM dry patches active in condensation. As a

result, rather than PCM media which usually suffer from poor thermal conductivity, other conductive media with high thermal conductivities, smaller size, and lower cost would be ideal candidates for the present application.

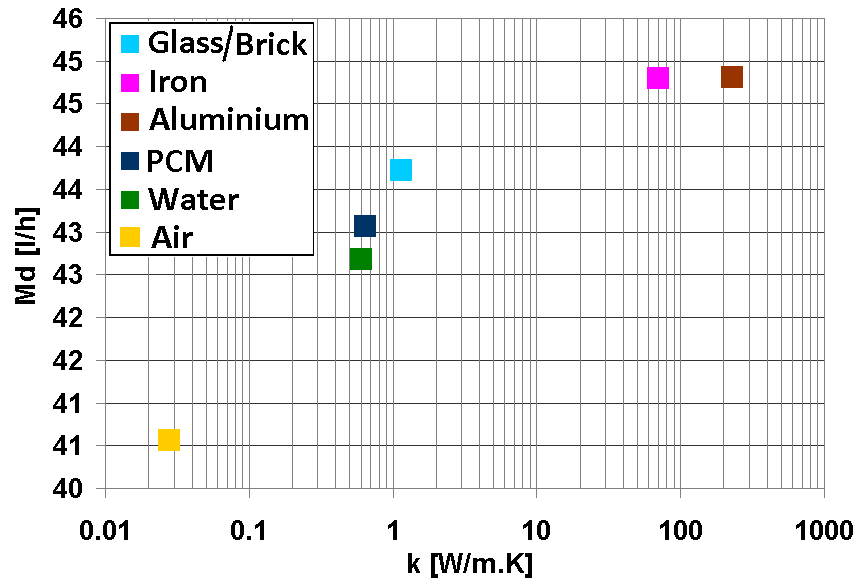


Figure 7.16: Effect of solid packing media on hourly productivity

On the other hand, when condensation depends on the interfacial vapour pressures, the sensible energy flow components impact the film temperature at the liquid-gas and solid-gas interfaces and consequently affects the latent heat components. At steady state conditions, the energy flow from liquid to solid phase equilibrates with the energy flow from gas to solid and the local temperatures of all phases remain constant. However, numerical analysis has been carried out to have deep insight about the extent of this effect.

Table 7.3: Effect of different packing media on the condensation rate ($M_{cw}=1000$ [l/h])

Medium Properties	Glass, Pyrex	Brick (fired clay)	Iron	Aluminum	Water	PCM (HS 58)	Air
k (W/m.K)	1.14	1.13	70	229	0.64	0.6	0.0278
ρ (kg/m ³)	2240	2310	7880	2701.1	1000	1280	1.084
c (J/kg)	840	922	511	938.3	4180	2.51E+05	1015
M_d [l/h]	44.81	44.79	43.72	43.72	43.07	42.69	40.56
M_d Increase (%) relative to air	10.5%	10.4%	7.8%	7.8%	6.2%	5.2%	0.0%

Figure (7.17) and (7.18) demonstrate the effect of thermal conductivity at different cooling water mass flow rates and different inlet cooling water temperatures, respectively. The results show that the effect of thermal conductivity of PCM has a considerable effect on the condensation rate. This effect appears much stronger when its value is less than 2 [W/m/K], moderately between 2 and 10, and slightly above 10 for the given mass flow rate of air.

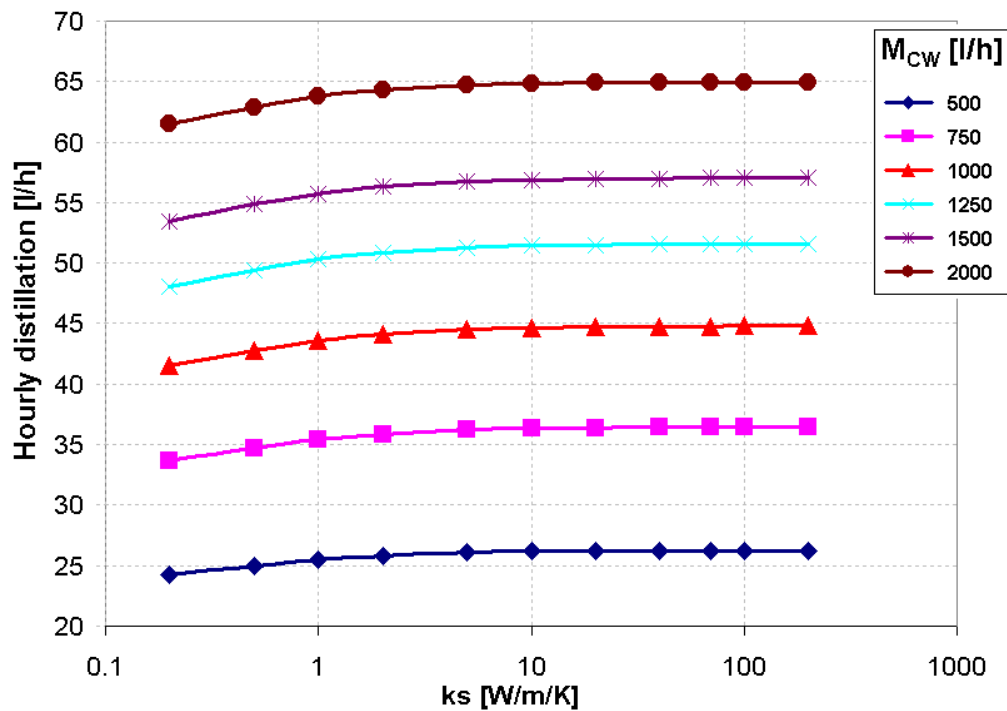


Figure 7.17: Effect of PCM thermal conductivity on condensation rate under different cooling water mass flow rates

7.3.7 Concluding remarks

The present analysis indicated that water to air mass flow ratio is one of the most crucial operational parameters and its optimum value lies around 1.5. However, the thermal conductivity represents an important parameter that controls local heat and mass transfer rates. The thermal conductivity of the packing media should not be less than 2W/m/K for better performance of the condenser. The study concluded that, conductive media with high thermal conductivity, smaller size, and lower cost would be the ideal candidates for the present application, rather than PCM media that usually have poor thermal conductivity and high cost.

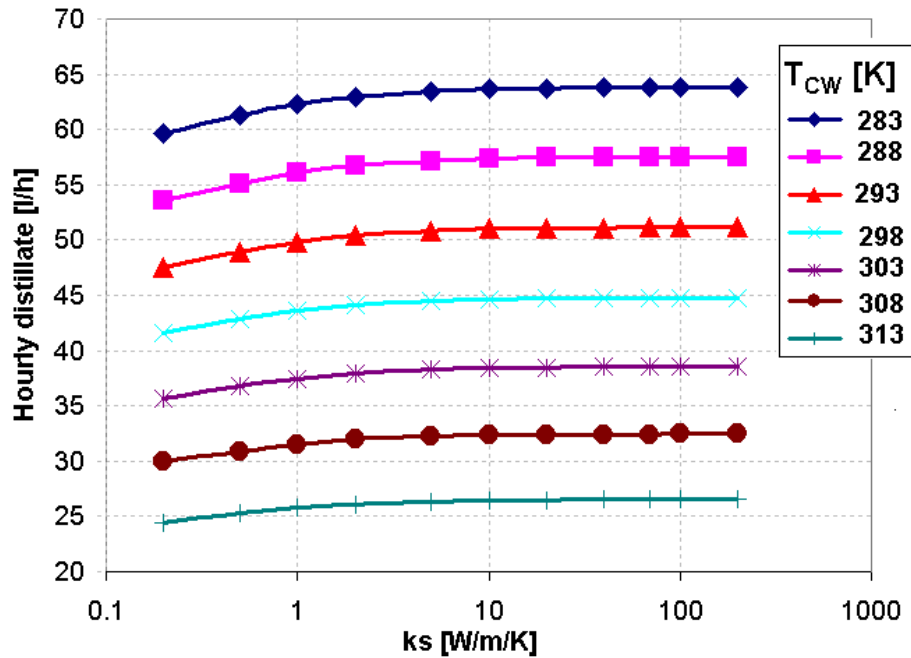


Figure 7.18: Effect of PCM thermal conductivity on condensation rate under different inlet cooling water

7.4 Conclusions

A numerical study has been carried out to optimize the design of the evaporator and direct contact condenser utilizing spherical PCM elements as packing media in a solar driven humidification-dehumidification (HDH) desalination plant. Fundamental variables and critical parameters affecting the system performance such as the effect of column geometrical aspect ratio, packing size, air to water mass flow rate ratio, PCM thermal properties, and the effect of different types of packing media were studied. A system parameters analysis and characteristic guidelines for the optimum parameters and operation conditions have been obtained and presented. Comparative performance of the system is clearly documented using PCM and Non-PCM packing elements. Table (7.4) summarizes the recommended design parameters to produce 1000 [l/day] fresh water when the inlet hot water temperature is maintained at 83°C. The study concluded that, conductive media with optimum thermal conductivity (as indicated in table 7.4), 40mm packing diameter, and lower cost would be the ideal candidates for the present application, rather than PCM media that usually have poor thermal conductivity and high cost.

Table 7.4: Design recommendations for the evaporator and condenser to produce 1000 [l/day] fresh water, inlet hot water temperature= 83°C

Parameter	Column aspect ratio (D_{bed}/H)	Air to water mass flow ratio (G/L)	Packing diameter [mm]	Packing thermal conductivity [W/m.K]	Water flow rate [l/h]
Evaporator	0.5	1.0	40	1-2	750
Condenser	1.0	0.5	40	>10	1000

8 Optimization of HDH plant

In this chapter, simulation of a complete HDH plant with periphery will be performed in order to identify suitable plant configurations and operating parameters. Given specific meteorological data for continuously varying weather conditions, the design characteristics and performance of the desalination plant can be optimized for every location and environment. The results obtained in this chapter follow the overall mass and salt balance analysis, which has been discussed in chapter 4 considering the same plant layout and operation strategy.

8.1 Geographical locations

Two locations in Egypt were selected as representative sites for application of the simulation model, namely: Al-Arish and Al-Kahrga as depicted on the map in figure 8.1. Al-Arish city is located on the northern coast of the Mediterranean Sea whilst Al-Kharga is located in the western desert south of Egypt. The solar irradiation intensity is less than 5.4 kWh/m²/day and highly transient for Al-Arish especially in winter, while it is 6.7-6.8 kWh/m²/day and with very smooth daily and seasonal variations for Al-Kharga. On the other side, Al-Khrga is characterized by desert climatic conditions, where marginal discrepancy in daily ambient temperature is noticeable, some examples are shown in figure 8.2. As a coastal city, Al-Arish doesn't exhibit such high fluctuation in daily temperatures due to the huge heat capacity of the Mediterranean Sea.



Figure 8.1: Selected geographical locations in Egypt

8.2 Boundary conditions and input parameters

Al-Arish city will be considered as the main site for optimization of the HDH plant with a targeted fresh water production capacity around 1000 l/day. The local weather data used for the simulation is extracted from the Meteornorm database. It is a climate database using either weather station records or satellite data. The input weather data is generated based on averaged hourly values.

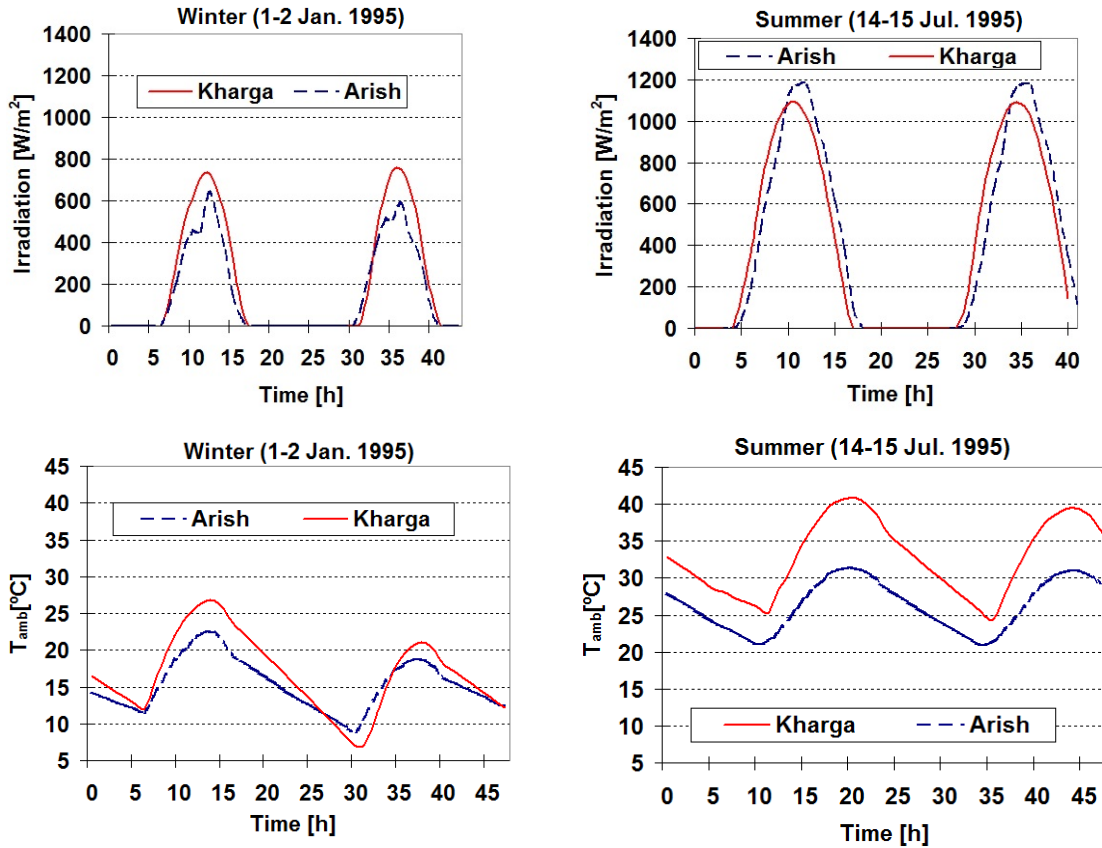


Figure 8.2: Daily and seasonal variations of weather conditions in Al-Arish and Al-Kharga, Egypt

The meteorological input parameters are the dry bulb temperature and the global solar radiation. The solar radiation determines the thermal energy input, while the ambient temperature determines the inlet feed seawater temperature as well as the inlet cooling water temperature to the condenser.

8.3 Parametric Analysis

In order to study the influence of parameters on the considered system layout, yearly simulation and predictions for the system performance were considered as the basis for the optimization procedures. Various geometrical, thermophysical properties of PCM in the external thermal buffer, and operation conditions of the HDH cycle coupled with the solar collector field, as described in figures (3.1) and (4.1), will be discussed and analyzed. MATLAB implementation was used to solve for the single components as well as for the system as a whole.

The MATLAB model describes how the solar power components are combined with the desalination block in one structure to simulate the complete plant based on the coupling strategy shown in figure 4.1. The above description assumes no heat losses during fluid flow through the HDH unit. The solar collector efficiency is modelled through introduction of an empirical correlation in equation (4.84). As mentioned previously, this correlation summarily includes the heat losses through the connecting pipes with the HDH plant and the flow mal-distribution in the collector absorber. Hence rather conservative amounts of fresh water production can be expected.

Control criteria and mechanisms were implemented in the simulation model to guarantee positive entropy production in the system. For instance, the solar collector should be bypassed during night or cloudy hours to avoid heat losses to ambient during these times, the outlet temperature from the solar collector must not exceed 95°C to avoid boiling of seawater and scale formation, and the inlet hot water temperature to the evaporator must not fall below the inlet cooling water temperature to the condenser. These two temperatures represent the margin for the time variation of temperature fields in the system. The inlet cooling water temperature to the condenser was assumed constant at ambient.

Both the evaporator and condenser packed beds have diameter 0.8m and height 1.6m. The spherical PCM packing size was 40mm for both the evaporator and condenser, and 75mm for the thermal buffer. The baseline boundary conditions are listed in table 8.1 and partly on each figure. Table A.1 in the appendix presents the thermophysical properties of different types of PCM used for the present computer simulation corresponding to the evaporator, condenser, and thermal buffer.

Table 8.1: Specified baseline boundary and operating conditions

Parameter	Units	Value
Mass flow of hot water " M_{hw} "	kg/h	1000
Solar collector area " A_{coll} "	m ²	220
Temperature of cooling and seawater water " T_{cw} "	°C	T_{amb}
Mass flow of cold water " M_{cw} "	kg/h	2600
Brine concentration factor " r_c "	-	2
Mass flow rate of air " M_a "	kg/h	1300
Geographical location	-	Al-Arish

Various parameters have been varied to see their impact on the system performance. System performance is evaluated in terms of the GOR (see equations 2.4 and 4.84 to 4.89) and output distillate rate (ODR) as a function of cooling water to air flow rate ratio, hot water to air flow rate ratio, size of the solar collector field,

size of the thermal buffer, melting temperature of PCM in the thermal buffer, and brine concentration factor. The computation time was setup for the whole year with a time step 120 seconds using interpolation techniques to smoothly develop a time evolution of the average hourly input weather conditions over the entire time steps between the successive hours.

The effects of transient weather conditions and climate on the system performance have been examined comparing between the two different locations in Egypt; Al-Arish, and Al-Kharga.

8.3.1 Effect of brine concentration factor (r_c)

Figure 8.3 shows the variations of distillation rate and GOR under same operation conditions with the brine concentration factor for a solar collector area of 220 m². The results reveal that the GOR increases as the brine concentration factor increases due to better heat recovery while the rate of distillate decreases at the same time. In closed water loop HDH processes, mixing of feed seawater and recirculated brine causes the degradation of the solar collector's thermal efficiency due to increasing the inlet brine temperature to the collector, and hence the inlet heat capacity flow rate to the HDH system decreases. The distillate rate peaks at a value of $r_c=2$ while the GOR peaks at a value of $r_c=3$ beyond which the GOR saturates while the distillate rate continues to drop. Thus operating the plant at a value of $r_c>3$ is not recommended under these circumstances.

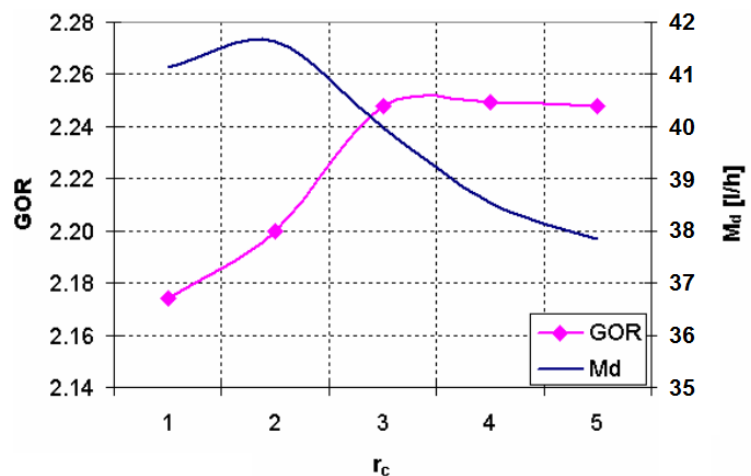


Figure 8.3: Effect of brine concentration ratio on the average-yearly distillate rate and GOR

Further, scale formation is an important limiting factor to be considered when talking about brine circulation. The tendency of scale formation increases with increasing the recirculated fraction due to increasing the brine salinity. The threshold limit for this factor decreases in inverse proportion to the top brine temperature which can be reached in the plant. For instance, the threshold value for r_c has been set at 1.5 for Multi-Stage Flash desalination plants working at a top brine temperature around 110°C to avoid serious scale formation problems. Since the top brine temperature level in HDH systems is designed at a maximum value of 85°C, a higher threshold limit of r_c up to 3 probably can be tolerated. However, since the variation of GOR is

less steep than that of the distillate rate in Figure 11, and to minimize the potential risk of scale formation, the optimum value of r_c is suggested to be 2. This value will be considered throughout the analysis and discussions in the subsequent sections.

8.3.2 Effect of thermal buffer storage capacity

The capacity of the storage has a significant effect on the operation and overall performance of the HDH system. A smaller storage unit operates at a higher mean temperature, but supports the plant operation for a shorter time period in the night or during cloudy weather. The first effect results in a higher inlet hot water temperature to the evaporator, higher potential of heat and mass transfer within and between the evaporator and condenser, and more fresh water output as compared to a system having a larger storage unit.

The effectiveness of a thermal energy storage, and so the optimum storage capacity, depend on both quality and quantity of the input thermal energy as well as the thermophysical properties of the storage medium. When the collector area is under-designed or when the solar intensity is low, the optimum storage size gets smaller. For Al-Arish city, the insolation intensity and sunshine hours are both lower than for Al-Kharga. Thus, a solar collector area of 60m^2 is not sufficient to support the thermal storage,

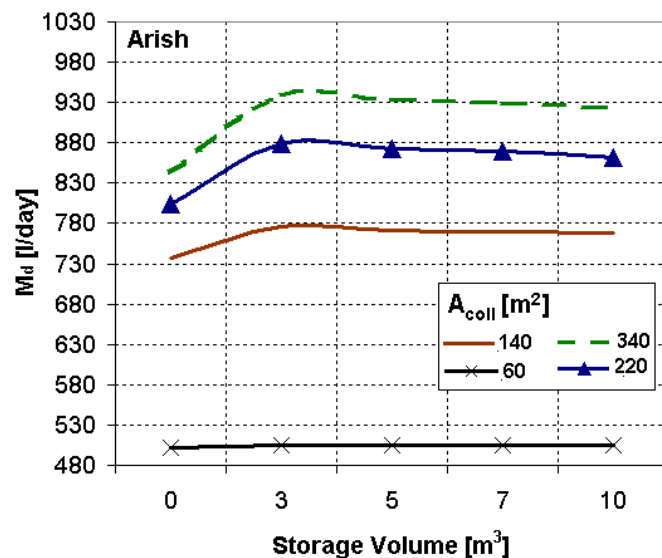


Figure 8.4: Effect of PCM thermal buffer volume on the average-yearly daily distillate for Al-Arish

even with a small capacity as shown in figure 8.4. Therefore, storage capacity has a tiny effect on the fresh water production rate. Having the collector area increased for Al-Arish city, the optimum storage volume shows up at 3m^3 . On the contrary, the optimum storage capacity can be determined under the same small collector area of 60m^2 as 3m^3 at Al-Kharga due to high solar intensity all over the year, but shifts to a higher value of 5m^3 by increasing the collector area as shown in figure 8.5. Due to high solar irradiation intensity at Al-Kharga, the performance of the HDH systems becomes very sensitive to the variation in the storage volume at smaller collector area of 60m^2 , which could be the reason for the noticeable peak at 3m^3 capacity.

The general observation which can be made regarding optimum storage capacity is that short-term storage units, which can meet fluctuations over a period of few hours or one day thermal load, have been generally found to be the most productive and economic for the present application as shown in figures 8.4 and 8.5.

8.3.3 Effect of solar collector area

Furthermore, the collector area plays an important role in enhancing the HDH plant performance. It can be clearly observed from figure 8.6. that the gap in distillate rate between Al-Arish and Al-Kharga shrinks as the collector area increases. For a given thermal load of the desalination plant, it appears that increasing the collector area beyond a certain value makes the effect of storage volume more pronounced, in particular for the highly transient weather conditions in Al-Arish. The reason behind that could be attributed to the lower ambient temperature in Al-Arish, which enhances the condenser performance, since the cooling water temperature was set at ambient in the model as mentioned earlier. Thus the effect of increasing the inlet hot water temperature to the evaporator with larger collector areas is magnified in Al-Arish by the enhanced performance of the condenser. These findings suggest that the effect of highly transient solar irradiation can be better mitigated by increasing both the collector field area and storage volume rather than increasing one of them alone.

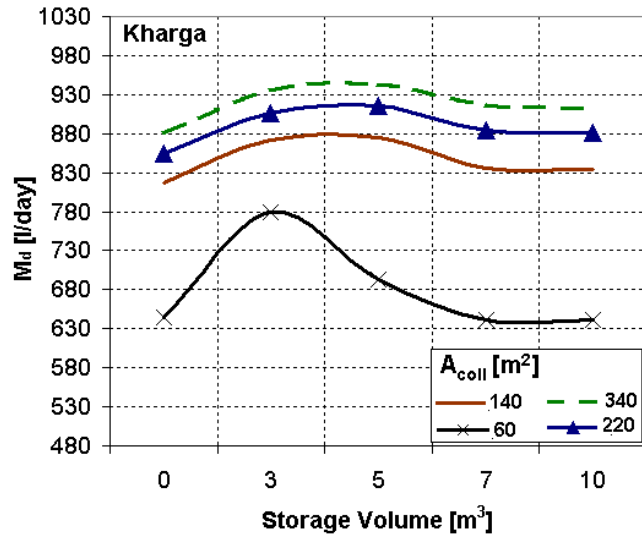


Figure 8.5: Effect of PCM thermal buffer volume on the average-yearly daily distillate for Al-Kharga

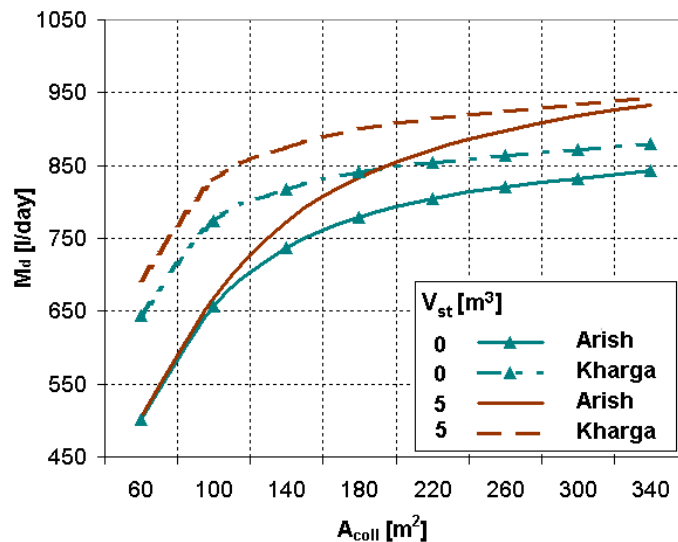


Figure 8.6: Effect of solar collector area on the average-yearly daily distillate rate under different climatic conditions

8.3.4 Effect of hot water flow rate

A crucial parameter in the performance of solar collectors is the mass flow rate of the working medium through the collector. With a higher mass flow, the absorber temperature decreases because of the better cooling effect rate. The decrease of the absorber temperature leads to a decrease in the heat losses to the ambient, which in turn results in a higher efficiency of the collector. It shows that the efficiency can be increased by increasing the mass flow through the collector. However, a higher mass flow also decreases the temperature rise that can be achieved through the collector. Thus, a compromise between the temperature rise and the efficiency has to be made since a high mass flow with insignificant temperature rise is generally not practical for real applications.

Therefore, the influence of inlet air mass to hot water flow ratio is important to be investigated for the HDH system as a whole, due to its combined effects and opposing trends on the performance of the single components. Increasing the mass flow rate of feed seawater increases the energy efficiency of both the condenser and solar collector, while it decreases the evaporator efficiency due to lowering the operating inlet hot water temperature, which reduces the distillate rate.

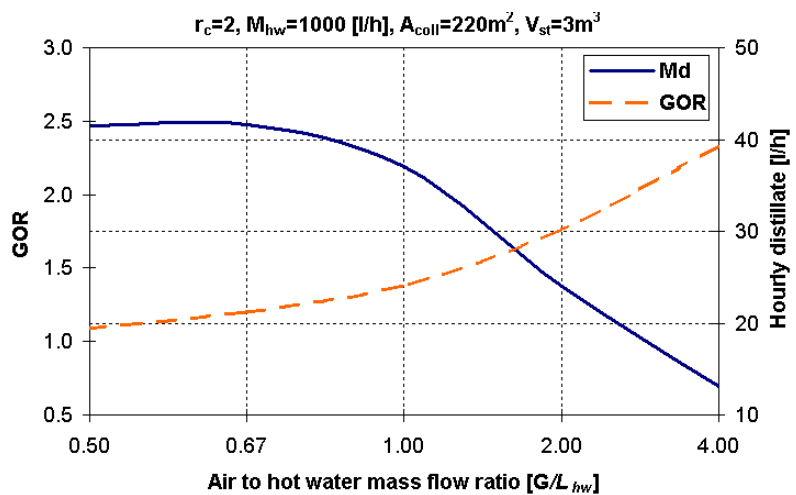


Figure 8.7: Effect of air to hot water mass flow rate ratio on the average-yearly daily distillate rate and GOR

On the other hand, increasing hot water flow rate increases the wetted and effective interfacial areas in the evaporator, and hence improves the mass transfer rate at the liquid-gas interface as discussed earlier.

However, it is expected from earlier results that the hot water mass flow rate is not the predominating factor in comparison with the effect of inlet hot water temperature on the evaporator effectiveness. Figure 8.7 shows the combined effects of hot feed water mass flow rate on the distillate rate and GOR. The maximum fresh water production rate peaks at an air to water mass flow ratio of 0.67, which is close to the optimum ratio found for the evaporator when it was studied alone (0.75). It is clearly observed that there is an opposite trend for GOR which increases with increasing the G/L_{hw} ratio. The GOR reaches the maximum at $G/L_{hw}=4$ and depicts a minimum value at $G/L_{hw}=0.5$ which means that this operation point should be avoided under

the specified boundary and weather conditions, especially that the distillate rate also decreases below the optimum point at $G/L_{hw}=0.67$. The optimum theoretical mass flow ratio would be selected as the intersection point at $G/L_{hw}=1.8$. However, it is believed that the right decision depends on the energy source and cost, for instance if the energy is supplied through a waste heat source or has a very low cost the decision then maybe to adopt the highest distillation rate as the main criterion. It can also be observed that the impact of increasing G/L_{hw} is more pronounced on the distillate rate than the GOR between the intersection point and the maximum distillation rate. Thus the optimum point would be selected as the mean value between $G/L_{hw}=0.67$ and $G/L_{hw}=1$, i.e. $\approx 0.8-0.9$.

8.3.5 Effect of cooling water flow rate

Due to existence of an additional heat exchanger at inlet of the condenser to bring the cooling water temperature down to the ambient conditions, the condenser performance is expected to be always better at higher mass flow rates of the coolant. But the mass flow rate has a strong effect on the outlet cooling water temperature, which in turn is extremely important since it determines the amount of latent heat recovery through the main heat exchanger downstream of the condenser. In addition, the cooling water mass flow rate should be optimized in order to reduce the pumping power required for the coolant and the cooling seawater in the additional heat exchanger upstream of the condenser. The overall thermal performance of HDH system was found to be optimized at a cooling water flow rate double the air flow rate in the system as shown in figure 8.8. The optimum water to air flow rate ratio can also be considered as the same optimum ratio found for a stand-alone condenser.

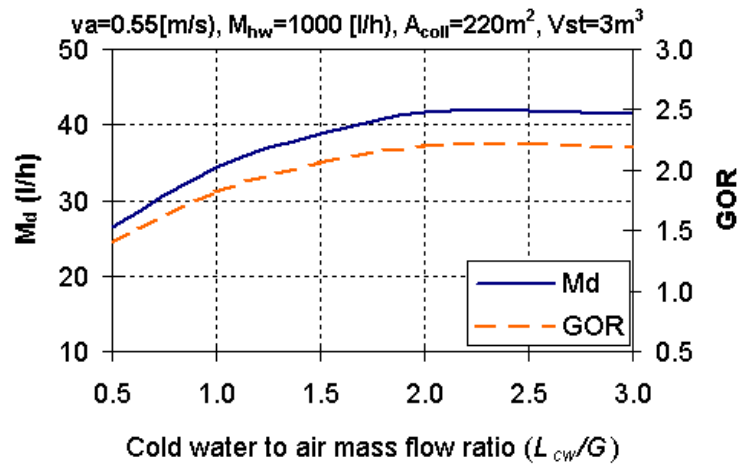


Figure 8.8: Effect of cooling water to air flow rate ratio on the average-yearly hourly distillate production and GOR

8.3.6 Effect of storage medium type

Characterization of the ideal thermal storage medium for a certain application is a complex task. Numerical simulation can be used to predict different effects of certain

storage materials and thus it can help to find the optimum thermophysical properties of the storage medium (e.g. optimum melting point range, heat capacity, heat of fusion, etc.).

In order to study the influence of the storage material, one entire year was simulated and weather data for Al-Arish city was set as boundary conditions. Both sensible and latent heat storage media were simulated, see figure 8.9. The effect of using water as a sensible heat storage in the external thermal buffer is compared with that of PCM spheres with a melting point 70°C and other thermophysical properties indicated in table A.1 in the appendix.

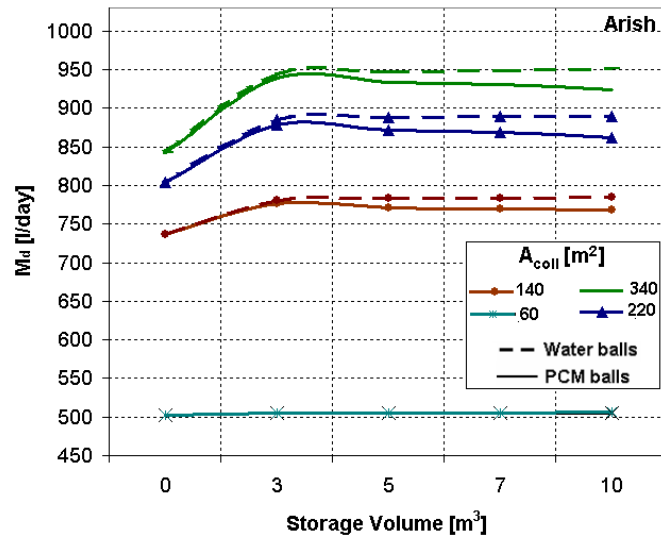


Figure 8.9: Comparison between water and PCM as a storage medium

It is evident that the distillate rate using water spheres is typically the same as the PCM storage for small collector area of 60 m² and small storage capacity up to 3m³. Increasing the storage volume beyond the optimum capacity of 3m³ with increasing the solar collector area, the distillate rate of the HDH plant equipped with water spheres provides more distillate rate than a PCM storage.

This behavior is explained as follows. Fixed-bed heat regenerators are usually cycled between heat storing and heat releasing modes. First, a stream containing charging heat is passed through the bed, where the heat is transferred to the packing. Later a cold stream is passed through the hot bed in the reverse direction, thereby heating the stream in the retrieval cycle. In this ideal arrangement, the packing with the highest temperature in the regenerator contacts the fluid at the exit from the store. Thus, temperature stratification is always desired to achieve high thermal performance of the cyclic regenerators as it allows the highest attainable inlet fluid temperature at the interface with the load.

Due to the proposed unidirectional or once-through flow arrangement through the storage tank, the collector output continuously charges storage and energy is simultaneously withdrawn to handle the demand for the HDH cycle. Under the transient and low solar irradiation intensity at Al-Arish, the daily average inlet hot water temperature to the storage is relatively low compared to the melting

temperature of the PCM (70°C) while the operation temperature range of the storage (i.e. between the inlet hot water during sunny hours and inlet cooling water during night and cloudy hours) is wide. These conditions result in two effects. First, most of the stored heat will be sensible, which is in favour of water as the best sensible storage medium. Second, water store has less stratification since the phase transition of PCM will take place only in the first layers at the highest temperature of inlet hot water to the store during sunny (charging) hours. During cloudy or night hours, the cold water contacts the highest packing layer at the entrance of the store in contrary to the cyclic regenerators.

This type of operation damps the thermal quality of the working medium at the entrance during sunny hours and hence, increases the temperature gradients inside the store which is a counter-productive effect in this arrangement since the working medium contacts the coolest layers at the exit.

As mentioned earlier, the general behaviour of a HDH system is that a higher inlet hot water temperature leads to a higher efficiency. This implies that a phase change or sensible storage medium which increases the average operating temperature during day and night will increase the system performance. However, when the achieved temperature rise through the collector is too small (e.g. due to underestimation of the collector area, low efficiency of the collector, or low intensity of solar radiation), the obtained heat quality might be useless for the practical application.

Furthermore, the temperature range over which heat is added or retrieved to/from the thermal storage is crucial for the thermal storage efficiency as illustrated in figure (8.10). When the temperature operation range is wide compared with the melting range of PCM, a good sensible heat storage such as water would become comparable of even more efficient than a latent heat storage, since the major part of energy storage will be accomplished as a sensible component. The worst efficiency

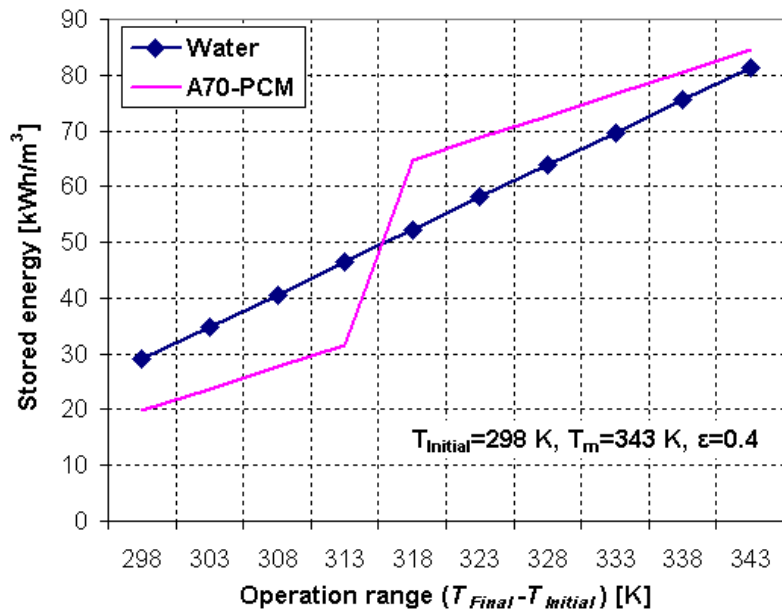


Figure 8.10: Effect of operational temperature range on sensible and latent heat storage

for latent heat storage would be obtained when the melting point or range of a PCM lies outside the operation range. Figure (8.11) shows a histogram of the hourly variation of outlet hot water temperature from the solar collector, which represents the inlet temperature to the PCM storage tank.

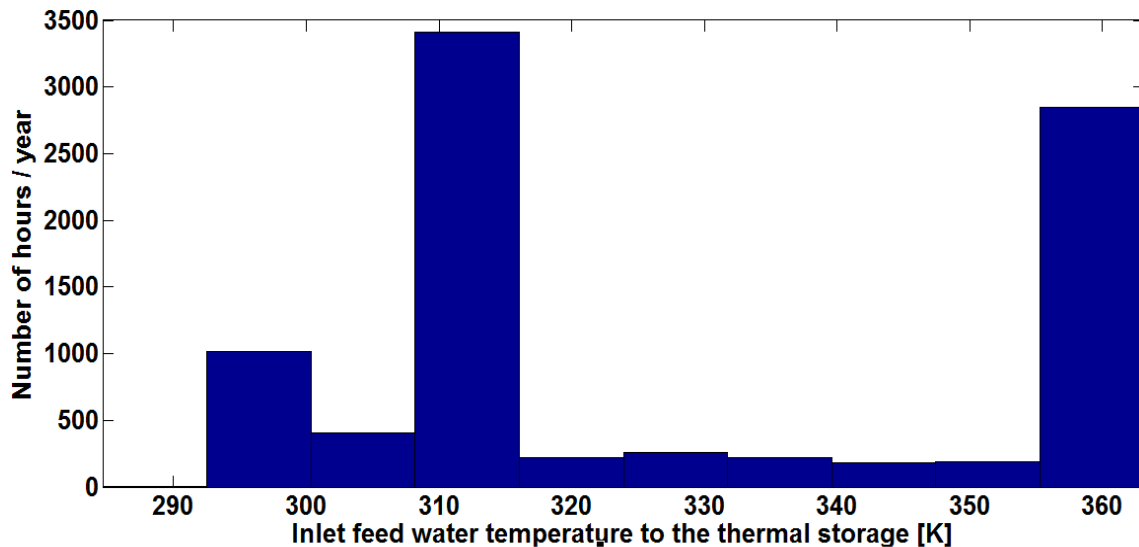


Figure 8.11: Histogram of hourly variation of inlet water temperature to the PCM-storage over one year for Al-Arish city with 3m³ thermal storage

It is clear from the figure how wide the fluctuation margin in the collector outlet water temperature. The useful heat output from the collector under the local influencing meteorological quantities and the specified load structure is indeed not favourable of a latent heat store. The *Stefan number* (*Ste*) materializes these facts; it is the ratio of the PCM sensible heat to latent heat per unit mass:

$$Ste = \frac{c_{pcm}(T_{i,h} - T_{i,c})}{\Delta H_m} \quad (8.1)$$

Where $T_{i,h}$, and $T_{i,c}$ represent the inlet fluid temperature during the heating (energy storing) period, and the inlet fluid temperature during the cooling (energy releasing) period respectively. The symbols c_{pcm} is the heat capacity of the PCM, and ΔH_m is the latent heat of phase change.

As Stefan number tends to infinity ($Ste \rightarrow \infty$), sensible heat storage dominates, while when the Stefan number approaches zero ($Ste \rightarrow 0$), latent heat storage dominates. For optimal PCR operation, the latter limiting case is preferred. These effects are clearly observed and elaborately discussed by both Erk and Dudukovic [83] and Modarresi and Sadrameli [84]. The physical properties of useful phase change

compounds, and the usable temperature ranges generally limit Ste to σ (10^{-2}). However, the practical average yearly limit of Ste is σ (1) for the present case, which means that with this larger value of Ste the amount of sensible heat is much higher than the latent heat.

8.3.7 Effect of PCM melting temperature (T_m)

For examining the effect of different melting points, the specific heat capacities (i.e. solid, liquid and apparent heat capacity) of all simulated PCM candidates are assumed to be equal and the same as the PCM A-70. Only the melting point of the PCM was changed individually. Thus, the influence of the melting temperature shall become evident even if a PCM with these characteristics does not exist in reality.

Figure (8.12) shows the effect of T_m on the plant hourly distillate rate for both Al-Arish and Al-Kharga locations at two different collector areas. For low and high values of $T_m = 40$ and 80°C , the distillate rate is higher than the intermediate melting points. As the T_m at intermediate points of 50, 60, and 70°C becomes more closer to the inlet hot water temperature, the distillate rate is reduced.

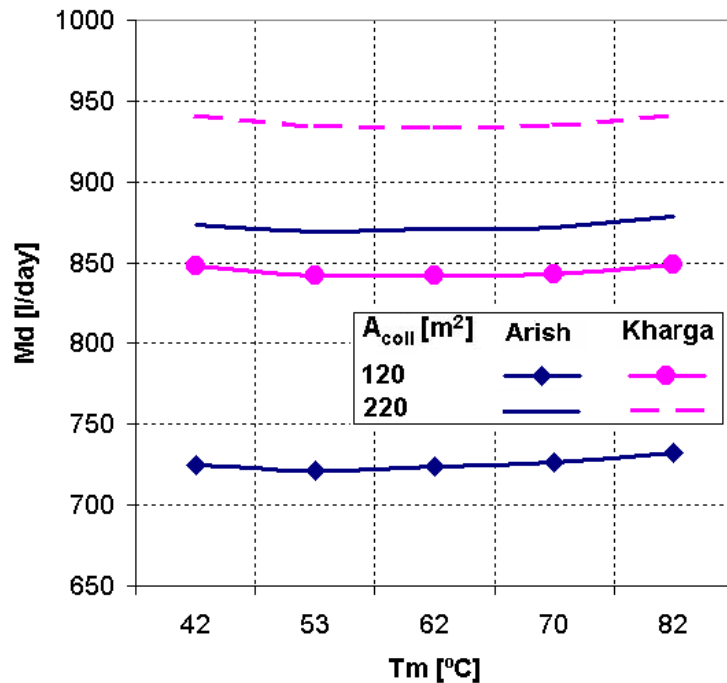


Figure 8.12: Effect PCM melting temperature in the external thermal buffer

When T_m becomes sufficiently lower than the inlet hot water temperature to the store, i.e. at $T_m=40^\circ\text{C}$, it represents a mostly latent heat storage in the response since most

of the PCM layers will be in a molten state for many hours a day. This implies that the thermal storage will behave as a sensible storage during these molten hours and the storage axial temperature profile will become more homogeneous (i.e. less stratified). Thus, the outlet fluid temperature gets better as one gets away from discontinuity in the storage temperature.

When T_m becomes sufficiently higher than the inlet hot water temperature to the store, i.e. at $T_m=80^\circ\text{C}$, the PCM storage behaves as a sensible heat storage. Of course, when this happens, the regenerator is not operating efficiently in the sense of the thermal storage concept due to the adopted once-through arrangement in the simulated system.

When T_m at intermediate points of 50, 60, and 70°C becomes more close to the inlet hot water temperature, phase transition of PCM will take place only in the first layers at the highest temperature of inlet hot water to the store during sunny (charging) hours. As pointed out in the previous section, this type of operation damps the thermal quality of the working medium at the storage entrance during sunny hours and hence, increases the temperature gradients inside the store which is a counter-productive effect in the once-through arrangement.

However, the advantages of the once-through setup is its simplicity both in construction and operation, and lower investment and operation costs, since only one tank is needed in comparison with the cyclic generators, in which at least two tanks with a sophisticated control mechanisms are necessary. In spite of the fact that the simple system considered in the study proved to have a quite limited performance as stratification cannot be utilised effectively, simplicity and reduced costs remain major aims in realizing decentralized small-scale desalination units. One is worth noting that the once-through storage will be superheated and supercooled much more often than a cyclic regenerator, which will also result in higher stresses on the material and an overall degradation of the storage efficiency in a short life time.

One possible measure to mitigate these negative consequences and improve the overall efficiency of both thermal storage and HDH system is to use a simple concentrating solar power collector (e.g. evacuated tube collector; ETC) instead of the flat plate collector FPC suggested in the study.

FPC have low cost but low exit temperatures and efficiencies are low for the required temperature quality of the present application when compared with the ETC. Evacuated tube collectors are more expensive than FPC, thus the initial capital costs are high but operational costs are relatively low. Nevertheless, the improved efficiency of the ETC results in a lower collector area and hence the investment costs are partly compensated.

However, it is believed that the final judgement and selection of the best overall plant setup and ideal components should be based on a comprehensive techno-economical analysis.

8.4 Conclusions

The results obtained from the parametric study on the HDH system indicates that the crucial parameters have been rigorously defined for practical purposes under real weather conditions. The ideal HDH performance is approached for: brine concentration factor (r_c)=2, air to hot water mass flow ratio=1.5, cooling water to air mass flow ratio=2, thermal storage volume 3-5 m³ per m³ of daily fresh water production capacity depending on the local climatic conditions.

The once-through flow arrangement in the external PCM thermal buffer with a flat plat collector has a limited efficiency when combined with the HDH plant in comparison with water storages with the same volumetric capacity.

For optimal operation of the external PCM thermal buffer, Stefan number must be small enough, as this means that there is a great amount of latent heat that can be stored (relative to sensible heat). The physical properties of useful phase change compounds, and the usable temperature ranges generally limit Ste to $O(10^{-2})$. However, the practical average yearly limit of Ste in the present application is $O(1)$, which means that with this larger value of Ste the amount of sensible heat is much higher than the latent heat.

Utilization of PCM in the thermal storage is recommended only for high energy density and in applications where there is a narrow operational temperature change around the melting range, as the latent heat becomes much larger than the sensible heat. It is therefore of interest to look in future studies at the techno-economical aspects for different simulation scenarios and coupling setups of the external thermal buffer and concentrating solar power collectors with the HDH system.

9 Summary and conclusions

9.1 Summary

This work discusses the results of experimental and numerical studies on a humidification-dehumidification (HDH) system utilizing conductive packing media in the evaporator and condenser. The objective of using conductive packing is to achieve multiple-effects of heating/humidification (MEHH) and cooling/dehumidification (MECD) while air passing through the successive packing layers in the evaporator and condenser respectively. The major objective of this study is to examine the innovative approach for locally creating MEHH and MECD and to determine the technical and economic feasibility of applying conductive packing media in the evaporator and condenser and PCM thermal storage in HDH solar desalination plants under both steady state operation conditions.

A mixed micro-macro balance transient simulation model has been established and validated against experimental measurements using COMSOL Multiphysics and MATLAB for solving fluid flow and heat and mass transfer phenomena in one spatial dimension for different components in such a loop. At the macroscale, the wetting phase is described in terms of its average properties within a small volume by using the interpenetration continua and volume averaging technique. Thus, at each point, a macroscale phase is characterized as occupying a fraction of the available volume and to have a certain interface per unit volume with other phases. Each phase in the system is described in a similar way. Precise definition of the interface shape is neither required nor possible to obtain at the macroscale. On the macro level, the continuous solid approach for modeling phase change regenerators (PCR) is applied using the apparent heat capacity formulation. All sensible and latent heat rates are defined at the common interfaces based on the local temperatures of all phases, which are coupled together and updated as a function of space and time. Thus, the MEHH and MECC can be captured at successive points along the packing height.

Using the simulation tools, a detailed heat and mass transfer analysis for the dynamic performance of a PCM-supported HDH system over a wide range of operation conditions has been undertaken. Experiments, not only on laboratory scale but also as a prototype, were designed and performed to measure fundamental time dependent variables and critical parameters affecting the system performance. A system parameters analysis for the main single components as well as for the whole HDH plant with its supporting solar collector field and PCM thermal energy storage has been performed under varying weather conditions over one year for Al-Arish City on the eastern north coast of Egypt. The analysis focuses on the optimum coupling and operation conditions of the HDH system with the solar collector field and the external thermal buffer. Special attention has been paid to the effect of thermo-physical properties of the packing media and heat recovery enhancement.

9.2 Conclusions

Under most of the boundary conditions, conductive packing elements generally have positive impact on the productivity rate of the plant compared to non-conductive packing. However, this impact is more profound under higher inlet water mass flow rate and higher inlet water temperature on the evaporator, and higher mass flow rate of air in the system due to low thermal conductivity and large size of the PCM elements. Although this enhancing effect of conductive packing elements under such higher boundary conditions is more pronounced for higher packing height, it holds also true for the lower packing height but with lower impact as well.

The comparative analysis revealed that the main reason behind enhancing the system productivity with conductive packing elements at steady state is attributed to the potential role of establishing multiple-effects of heating/humidification MEHH and cooling/condensation MECC mechanisms in the evaporator and condenser respectively as compact heat and mass exchangers. The experimental analysis has demonstrated a strong and complex interaction between four main parameters, air to water mass flow ratios in the evaporator and condenser, packing height, heat capacity flow of inlet hot water, thermal conductivity and packing communication with the surrounding fluid phases, which can be characterized by their respective Biot numbers. The axial thermal stratification is established in the bed due to the interaction between these parameters, which is essential for creating the multiple-effect mechanisms.

Experimental results suggest that forced convection remarkably enhances the productivity of HDH plants compared to natural draft operation for all packing types. However, thermally conductive packing elements have a positive impact on the natural draft operation as well, especially at higher heat capacity flow of hot water. Under natural convection where air flow is induced by the double diffusion effects (density and humidity gradients), the MEHH boosts the natural air flow in the system, and hence increases its productivity.

The solid phase thermal conductivity represents an influencing parameter that controls local heat and mass transfer not only at solid-liquid and solid-gas interfaces but also at liquid gas interface in the evaporator and condenser. Theoretical analysis has been carried out to clearly explore the effect and limits of solid thermal conductivity. It has been demonstrated that the productivity of the evaporator can be enhanced by the use of a conductive packing media. It was found that the proportionality of evaporation rate is neither uniform with the thermal conductivity k_s nor linear with the hot water mass flow rate. The maximum evaporation rate was obtained when k_s is around $1.14 \text{ W.m}^{-1}.\text{K}^{-1}$ as for the case of Pyrex glass and fired clay brick, beyond this value the distillate rate decreases.

For the condenser it was found that the packing media with higher thermal conductivities produces more condensate. Moreover, for all media, the rank of

productivities at any cooling water mass flow rate is coincidentally the same as the rank of their thermal conductivities. The thermal conductivity of the packing media should not be less than 2W/m/K for better performance of the condenser.

The role of MEHH is nearly absent or even negatively influencing the distillate rate at very low hot water mass flow rates and low temperature due to cooling effects on the air in the lower part of the evaporator. Both experimental and theoretical analysis indicated that increasing the specific surface area of the packing can compensate and outpace the role of MEHH, as the conductive packing has rather limited influence under such conditions. Therefore, when operating HDH plants under forced convection, industrial packing media which have high specific surface area and lower cost would be ideal candidates for the evaporator and condenser. However, conductive packing media may have a potential that it could be utilized to improve the natural flow characteristics in other important applications such as cooling towers.

Moreover, the study revealed that the inlet hot water temperature and air to water mass flow ratio have rather stronger influence on the system performance than the thermal conductivity of the packing. The numerical analysis indicated that the optimum value of water to air mass flow ratio is lies between 1.3 and 1.5 for the evaporator and between 1.5 and 2 for the condenser.

The results obtained from the parametric study on the complete solar HDH system indicates that the crucial parameters have been identified for practical purposes under real weather conditions. The ideal HDH performance is approached for: brine concentration factor (r_c)=2, air to hot water mass flow ratio=1.5, cooling water to air mass flow ratio=2, thermal storage volume 3-5 m³ per m³ of daily fresh water production capacity depending on the local climatic conditions.

The once-through flow arrangement in the external PCM thermal buffer with a flat plat collector has a limited efficiency when combined with the HDH plant in comparison with water storages with the same volumetric capacity. For optimal operation of the external PCM thermal buffer, the Stefan number must be small enough, as this means that there is a great amount of latent heat that can be stored (relative to sensible heat). Utilization of PCM in the thermal storage is recommended only for high energy density, and in applications where there is a narrow operational temperature change around the melting range. It is therefore of interest to look in future studies at the techno-economical aspects for different simulation scenarios and coupling setups of the external thermal buffer and concentrating solar power collectors with the HDH system.

References

- [1] Huges C.N., Tompson T.I., Groh J.E., and Frieling D.H., Solar distillation utilizing multiple-effect humidification., U.S. Dept. of Interior Research and Development, Report No. 194, 1966.
- [2] Al-Hallaj S. and Selman J.R. (2002). A comprehensive study of solar desalination with humidification-dehumidification cycle. MEDRC Series of R&D Reports, Project: 98-BS-032b.
- [3] Al-Hallaj S., Parekh S., Farid M.M. and Selman J.R. (2006). Solar desalination with humidification-dehumidification cycle: Review of economics. *Desalination* 195: 169-186.
- [4] Müller-Holst H., Engelhardt M. and Scholkopf W. (1999). Small-scale thermal seawater desalination simulation and optimization of system design. *Desalination* 122: 255-262.
- [5] Müller-Holst H., Engelhardt M., Herve M. and Scholkopf W. (1998). Solar thermal seawater desalination systems for decentralized use. *Renewable Energy* 14(1-4): 311-318.
- [6] Gajbert H. and Fiedler F. (2003). Solar combisystems, State of the Art Report. In: *Solar Energy State of the Art*. Denmark Tekniske Universitet, Internal Report BYG-DTU SR-03-14 2003, Editors: Furbo S., Shah L.V. and Jordan U., ISSN 1601 – 8605.
- [7] Knudsen S. and Dennis M. (2003). Thermal storage for small solar heating systems, state of the art report, In: *Solar Energy State of the Art*. Danmark Tekniske Universitet, Internal Report BYG-DTU SR-03-14 2003, Editors: Furbo S., Shah L.V. and Jordan U., ISSN 1601 – 8605.
- [8] Nagano K. (2003). Development of a high performance solar hot water supply system using evacuated solar tubes and latent thermal energy storage. *Proceedings of International Solar Energy Society, Gotegorg, 2003*.
- [9] Hassabou A., Spinnler M., Hanafi A., Polifke W. Experimental analysis of PCM-supported humidification-dehumidification desalination system. *IDA Word Congress–Atlantis, The Palm-Dubai, UAE November 7-12, 2009*. REF:IDAWC/DB09-289.
- [10] Schlunder E.U., Equivalence of one- and two-phase models for heat transfer processes in packed beds: one-dimensional theory, *Chem. Eng. Sci.* 30 (1975) 449-452.
- [11] Kaviany M., *Principles of Heat Transfer in Porous Media*, second ed., Springer, New York, 1995, pp. 391:424.
- [12] Arkar C., Medved S. Influence of accuracy of thermal property data of a phase change material on the result of a numerical model of a packed bed latent heat storage with spheres. *Thermochimica Acta* 438 (2005) 192-201.

- [13] Vafai K., Sozen M. An investigation of a latent heat storage porous bed and condensing flow through it. *ASME Journal of Heat Transfer*, 112 (1990) 1014-1022.
- [14] Jeffreson C.P., Prediction of breakthrough curves in packed beds: I. Applicability of single parameter models & II. Experimental evidence for axial dispersion and intraparticle effects (p 416-420) *AIChE J.* 18 (1972): 409–420.
- [15] Wakao N., Kaguei S. Heat and mass transfer in packed beds. Gordon and Breach Science Publishers, (1982) New York, London, Paris.
- [16] Ismail K.A.R., Stuginsky R. A parametric study on possible fixed bed models for PCM and sensible heat storage. *Applied Thermal Engineering* 19 (1999) 757-788.
- [17] Vafai K. and Sozen M. (1990). An investigation of a latent heat storage porous bed and condensing flow through it. *ASME Journal of Heat Transfer* 112: 1014-1022.
- [18] Civan F. and Sliepcevich C.M. (1987). Limitation in the apparent heat capacity formulation for heat transfer with phase change. *Proceedings of the Oklahoma Academy of Science* 67: 83-88.
- [19] Bird B.R., Stewart W.E, and Lightfoot E.N. Transport phenomena. Second Edition, John Wiley & Sons, Inc. New York.
- [20] Nield, D.A. and Bejan A. (1999). Convection in porous media. 2nd edn. Springer-Verlag, New York.
- [21] Carbonell R.G. Multiphase Flow Models in Packed Beds. *Oil & Gas Science and Technology – Review IFP*, 55 4 (2000):417-425.
- [22] Sáez A.E., and Carbonell R.G. Hydrodynamic parameters for gas-liquid cocurrent flow in packed-beds. *AIChE J.*, 31 (1985): 52.
- [23] Holub R.A., Dudukovic M.P., and Ramachandran P.A. Pressure drop, liquid holdup and flow regime transition in trickle flow. *AIChE J.*, 39 (1993): 302.
- [24] Hassabou A., Spinnler M., Polifke W.. Experimental and theoretical studies on integration of new PCM-based components in solar desalination. 2nd periodic report. Project No. 05-AS-003. (2007) The Middle East Desalination Research Center (MEDRC).
- [25] Voller V.R. An overview of numerical methods for solving phase change regenerator system. *Heat Transfer Engineering* 25(4) (1997) 45-53.
- [26] Slattery JC (1972) *Momentum, energy and non transfer in continua*. McGraw-Hill
- [27] Torab H., Beasley D.E. Optimization of a packed bed thermal storage unit. *Transaction of the ASME, Journal of Solar Energy Engineering* 109 (1987) 171-175.
- [28] Carbonell R.G. Multiphase Flow Models in Packed Beds. *Oil & Gas Science and Technology – Review IFP*, 55 4 (2000):417-425.
- [29] Stichlmair J., Bravo J. L., and Fair J. R. General model for prediction of pressure drop and capacity of countercurrent gas/liquid packed columns. *Gas*

- Sep. Purif. (3)1989: 19-27.
- [30] Bauer H. Dechema Monographie, 37 (1960): 7/78.
 - [31] Klerk A. Liquid holdup in packed beds of low mass flux. R&D Note, AIChE J., 49 6 (2003): 1597-1600.
 - [32] Kister H.Z. (1992). Distillation Design. McGraw-Hill, New York.
 - [33] Engel V., Stichlmair J., and Geipel W. Fluid dynamics of packings for gas-liquid contactors. Chemical Engineering Technology 24 5 (2001): 495-462.
 - [34] Shi M. G., and Mersmann A. Effective Interfacial Area in Packed Columns. Chem.-Ing.-Tech. 1964, 56, 404.
 - [35] Onda K., Takeuchi H., Okumoto Y. Mass transfer coefficients between gas and liquid phases in packed columns. J. Chem. Eng. Jpn. 1968b, 1, 56.
 - [36] Strigle R.F. (1987). Random packings and packed towers. Gulf publishing company, Houston, Texas.
 - [37] Woerlee G.F., Berends Z.J. and Jan de Graauw O. (2001). A comprehensive model for the pressure drop in vertical pipes and packed columns. Chemical Engineering 84: 367–379.
 - [38] Shulman H.L., Ullrich C.F. and Wells N. (1955). Performance of packed columns III Hold-up for aqueous and non-aqueous systems. AIChE 1: 259.
 - [39] Stemmet C.P., Jongmans J.N., van der Schaaf J, Kuster B.F.M. and Schouten J.C. (2005). Hydrodynamics of gas–liquid counter-current flow in solid foam packings. Chemical Engineering Science 60: 6422 – 6429.
 - [40] Wagner I, Stichlmair J, and Fair J.R. Mass transfer in beds of modern, high-efficiency random packings. Industrial Engineering Chemistry Resources 36 (1997): 227-237.
 - [41] Gandhidasan P. Estimation of the Effective Interfacial Area in packed-bed liquid desiccant contactors. Industrial Engineering Chemistry Resources 42 (2003): 3420-3425.
 - [42] Cornell, D.; Knapp, W. G.; Fair, J. R. Mass transfer efficiency of packed columns. *Chem. Eng. Prog.* 1960, 56, 68.
 - [43] Bravo, J. L.; Fair, J. R. Generalized correlation for mass transfer in packed distillation columns. Industrial Engineering Chemical Processes Design Development 21 (1982): 162.
 - [44] Bolles, W. L.; Fair, J. R. Improved mass transfer model enhances packed-column design. *Chem. Eng.*, 89 14 (1982): 109.
 - [45] Klausner J.F. and Mei R.Y. (2006). Evaporative heat and mass transfer for the diffusion driven desalination process. *Heat and Mass Transfer* 42: 528–536.
 - [46] Klausner J.F. and Mei R.Y. (2005). Diffusion driven desalination, an innovative approach to fresh water production from seawater. Presentation in ASME-ZSIS International Thermal Science Seminar ITSS II.
 - [47] Yi Li, Klausner J.F., Mei R., and Jessica Knight J. Direct contact condensation in packed beds. *International Journal of Heat and Mass Transfer* 49 (2006): 4751–4761.

- [48] Crone S., Bergins C., and Straus K. Multiphase Flow in Homogeneous Porous Media with Phase Change. Part I: Numerical Modeling. *Transport in Porous Media* 49 (2002): 291–312.
- [49] Krupiczka, R. 1967. Analysis of thermal conductivity in granular materials. *Int. Chem. Eng.* 7(1): 122-144.
- [50] Sun .J., and Besant RW., 2005. Heat and mass transfer during silica gel-moisture interactions. *Int. J. of Heat and Mass Transfer* 48: 4953-4962.
- [51] Dullien, F.A.L., 1992. *Porous Media: Fluid Transport and Pore Structure*. Second Edition, Academic Press, New York, NY.
- [52] Ergun, S., 1952. Fluid flow through packed columns. *Chemical Engineering Process*, 48(2): 89-94.
- [53] Baker D., 1984. *Cooling Tower Performance*. Chemical Publishing Co., Inc., New York.
- [54] Merkel F., 1925. "Verdunstungshuhlung," *Zeitschrift des Vereines Deutscher Ingenieure (V.D.I.)*, Vol. 70, pp. 123-128.
- [55] Sutherland J.W., 1983. Analysis of mechanical draught counterflow air/water cooling towers, *Journal of Heat Transfer*, 105: 576-583.
- [56] Singham J. R., 1998. Cooling towers, the packing region. In *Heat Exchanger Design Handbook*, Part 3, Library of Congress Cataloging-in-Publication Data, Begell House, Inc., New York, USA.
- [57] Thomas K. D., Jacobs H. R., and Boehm R. F., (1978). Direct contact condensation of immiscible fluids in packed beds. *Mechanical Engineering*, University of UTAH.
- [58] Braun, J.E., 1988. *Methodologies for the Design and Control of Central Cooling Plants*. Ph.D. Thesis, University of Wisconsin.
- [59] Al-Hallaj S. (1994). *Solar desalination by humidification-dehumidification cycle*. M.Sc. Thesis, Jordan University of Science and Technology.
- [60] Polifke W, and Kopitz J., 2005. *Wärmeübertragung/Grundlagen, analytische und numerische Methoden*. Pearson Studium, München, ISBN 3-8273-7104-X.
- [61] Treybal, R. E., *Mass Transfer Operations*. McGraw Hill, 2nd edition, 1968.
- [62] Gahin, S., and Ghazi, M. A. Engineering analysis for solar operated humidification-dehumidification plant. *Solar World Forum*, Brighton, UK; Vol. 2, pp; 1097-1104, August 1981.
- [63] Gleick , P. H., 1993. *Water in Crisis*. First Edition, Oxford University Press, Inc., 200 Madison Avenue, New York 10016, USA, ISBN 0-19-507627-3, P 69-372.
- [64] Miller J. E. Review of Water Resources and Desalination Technologies. SAND 2003-0800, Unlimited Release Printed March 2003. http://www.sandia.gov/water/docs/MillerSAND2003_0800.pdf, last accessed 13-08-2010.
- [65] Winter Pannell D.J. and McCann L., *The economics of desalination and its potential application in Australia, Sustainability and economics in agriculture working paper*, Agricultural and Resource Economics, University of Western Australia, 2001, pp. 1-7.

- [66] Kalogirou S. Use of parabolic trough solar energy collectors for sea-water desalination. *Applied Energy* 60 (1998): 65-88.
- [67] Abdel-Jawad M. Energy sources for coupling with desalination plants in the GCC countries. Consultancy report prepared for ESCWA, (September 2001).
- [68] Dabbagh, T., Sadler, P., Al-Saqabi, A., and Sadeqi, M. Desalination, an Emergent Option. In: Peter Rogers and Peter Lydon, eds, *Water in the Arab World*. 1996, First Edition, The American University in Cairo Press, 113 Sharia Kasr el Aini, Cairo, Egypt, ISBN 977-424-412-5, P 203-241.
- [69] El-Dessouky H., and Ettouney H. *Fundamentals of salt water desalination*. First edition 2002, ELSEVIER SCIENCE B.V., Sara Burgerhartstraat 25, P.O. Box 211, 1000 AE Amsterdam, The Netherlands.
- [70] Loupasis s., 2002. Technical analysis of existing renewable energy driven desalination schemes. Commission of the European Communities, Directorate General for Energy and Transport, ALTENER Program, Contract number 4.1030/Z/01-081/2001.
- [71] Silver, R.S. (1983). *Seawater Desalination*. In *Desalination Technology-Development and Practice*. A. Porteous, London, Applied Science Publishers, PP 1-30.
- [72] Middle East Desalination Research Center (MEDR). *Matching Renewable Energy with Small-Scale Desalination Plants*, Literature review and analysis of the state of the art of renewable energy.
- [73] Abu-Zeid M. (1997). Egypt's water policy for the 21st century. IXth World Water Congress of IWRA, *Water Resources Outlook for the 21st Century: Conflict and Opportunities*, Montreal, Canada, 1-6 September 1997, PP 1-7.
- [74] Karagiannis I. C., and Soldatos P. G. Water desalination cost literature: review and assessment. *Desalination* 223 (2008), PP:448–456.
- [75] ProDes (Promotion of Renewable Energy for Water production through Desalination) project partners. *Roadmap for the development of desalination powered by renewable energy*. pre-final version, October 2009, a project co-financed by the Intelligent Energy for Europe programme (contract number IEE/07/781/SI2.499059).
- [76] F. Trieb, C. Schillings, S. Kronshage, P. Viebahn, N. May, C. Paul, U. Klann, M. Kabariti, A. Bennouna, H. Nokraschy, S. Hassan, L. Georgy Yussef, T. Hasni, N. Bassam and H. Satoguina. *Concentrating Solar Power for the Mediterranean Region (AQUA-CSP)*. German Aerospace Center (DLR), Study for the German Ministry of Environment, Nature Conversation and Nuclear Safety, November 2007.
- [77] Fath H.E.S. (1998). Solar distillation: A promising alternative for water provision with free energy, simple technology and a clean environment. *Desalination* 116: 45-56.
- [78] Kalogirou, S. (2005). Seawater desalination using renewable energy sources. *Progress in Energy and Combustion Science* (31): 242–281.

- [79] Tiwari G.N. and Yadav Y.P. (1987). Comparative designs and long-term performance of various designs of solar distiller. *Energy Conservation and Management* 27 (3): 327-333.
- [80] Rizzuti, L., Ettouney, H. M., and Cipollina, A. (2006). *Solar desalination for the 21st century*. Springer.
- [81] NRC review of the desalination and water purification technology roadmap. Washington DC; National Research Council/The National Academies Press, 2001.
- [82] Bejan A. (2004). Designed porous media: maximal heat transfer density at decreasing length scales. *International Journal of Heat and Mass Transfer* 47: 3073–3083.
- [83] Erk HF, Dudukovic MP. (1996). Phase-change heat regenerators: modeling and experimental studies. *AIChE* 42(3): 791 - 808.
- [84] Modarresi A., and Sadrameli S.M. (2004). Modeling and Simulation of a Phase Change Regenerator System. *Heat Transfer Engineering* 25(4): 45–53.
- [85] El-Sayed M. (1997). Experimental and theoretical study of a heat storage system utilizing new phase change materials. M.Sc. Thesis, Faculty of Engineering, Cairo University, Egypt.
- [86] Hale D.V., Hoover M.J. and O'Neill M.J. (1971). Phase change materials Handbook. Report no. HREC-5183-2LMSC-HREC D225138. NASA, Marshall Space Flight Center, Alabama.
- [87] Muller-Holst H., Koessinger F., Kollmansberger H. and Al-Hainai H. (2001). Small scale thermal water desalination system using solar energy or waste heat. MEDRC Series of R&D Reports, Project: 97-AS-024b.
- [88] Sayed M.T., Kumar S., Moallami K.M. and Naraghi M.N. (1997). Thermal storage using form-stable phase- change materials. *ASHRAE Journal* 36 (5): 45-50.
- [89] Abe Y., Takahashi Y., Sakamoto R., Kanari K., Kamimoto M. and Ozawa T. (1984). Charge and discharge characteristics of a direct contact latent heat thermal energy storage unit using form stable high density Polyethylene. *ASME Journal of Solar Energy Engineering* 106: 465-474.
- [90] Kamimoto M., Abe Y., Sawata S. Tani, T. and Ozawa T. (1986). Latent thermal storage unit using form stable high density Polyethylene, Part I: Performance of the storage unit. *ASME Journal of Solar Energy Engineering* 108: 282-289.
- [91] Kamimoto M., Abe Y., Takahashi Y., Tani T. and Ozawa T. (1986). Latent thermal storage unit using form stable high density Polyethylene, Part II: Numerical analysis of heat transfer. *ASME Journal of Solar Energy Engineering* 108: 290-297.
- [92] Garg., H. P., Mullick, S. C., and Bhargava, A. K. (1985). *Solar thermal energy storage*. D. Reidel Publishing Company.
- [93] Stritih U. An experimental model of thermal storage system for active heating or cooling buildings. University of Ljubljana, Aškerčeva 6, 1000 Ljubljana, Slovenia, e-mail: uros.stritih@fs.uni-lj.si, <http://www.fskab.com/Annex17/Workshops/EM2>.

- [94] Abhat A. (1978). Investigation of physical and chemical properties of phase change materials for space heating/cooling applications. Proceedings of the International Solar Energy Congress, New Delhi, India.
- [95] Buddhi D. and Sawhney R. L. (1994). Proc: Thermal energy storage and energy conversion. School of Energy and Environmental Studies, Devi Ahilya University, Indore, India.
- [96] Hiran S., Suwondo A., Mansoori G. (1994). Characterization of alkanes and paraffin waxes for application as phase change energy storage medium. *Energy Sources* 16: 117-128.
- [97] Abhat A. (1983). Low temperature latent heat thermal energy storage; heat storage materials. *Solar Energy* 30 (4): 313-331.
- [98] Sharma S., Kitano D., and Sagara H.K. (2004). Phase change materials for low temperatures solar thermal applications. *Res. Rep. Fac. Eng. Mie Univ.*, 29: 31-64.
- [99] Lane G. (1983). *Latent heat materials. Volume 1*, CRC Press, Boca Raton, Florida.
- [100] Veraj R., Seeniraj B., Hafner B., Faber C. and Schwarzer K. (1998). Heat transfer enhancement in a latent heat storage system. *Solar Energy* 65: 171-180.
- [101] Hasnain S.M. (1998). Review on sustainable thermal energy storage technologies, Part I: heat storage materials and techniques. *Energy Conversion and Management* 39: 1127-1138.
- [102] Lane G. (1983). *Solar heat storage; latent heat materials. Volume 1*, CRC Press Inc, Boca Raton, Florida, USA.
- [103] Nielsen K. (2003). Thermal energy storage, a state-of-the-art. A report within the research program "Smart Energy-Efficient Buildings", at NTNU and SINTEF 2002-2006, Department of Geology and Mineral Resources Engineering NTNU, Trondheim.
- [104] Hauer A. (2001). Thermal energy storage with zeolite for heating and cooling applications. Proc. ZAE-Symposium 2001. ZAE Bayern (Zentrum für angewandte Energieforschung), TU Bayern, Garching, Munich. (Presentation 14).
- [105] Maier-Laxhuber P. (2001). Cold storage with zeolite systems. Proc. ZAE-Symposium 2001, ZAE Bayern (Zentrum für angewandte Energieforschung). TU Bayern, Garching, Munich.(Presentation 6).
- [106] Padmanabhan P. V., and Murthy M. V. (1986). Outward phase change in a cylindrical annulus with axial fins on the inner tube. *International Journal of Heat and Mass Transfer* 29 (12): 1855-1868.
- [107] Lamberg P. and Siren K. (2003). Approximate analytical model for solidification in a finite PCM storage with internal fins. *Applied Mathematical Modeling* 27: 491-513.
- [108] Siegel R. (1977). Solidification of low conductivity material containing dispersed high conductivity particles. *International Journal of Heat and Mass Transfer* 22: 1087-1089.

- [109] Mehling H., Hiebler S. and Ziegler F. (2000). Latent heat storage using a PCM graphite composite material. Proc. of Terrastock 8th international conference on Thermal Energy Storage, 28 August – 1 September 2000, Vol. 1: 375-380.
- [110] Stritih U. and Novak, P. (2000). Heat transfer enhancement of phase change process. Proc. of Terrastock 8th international conference on Thermal Energy Storage, 28 August – 1 September 2000, Vol. 1: 333-338.
- [111] U.S. Department of energy, Energy Efficiency and Renewable Energy, Energy Savers. Phase change materials for solar heat storage. National Technical Information System (NTIS), info@ntis.gov.
- [112] Bajnoczy G., Palffy E. G., Prepostffy E. and Zold A. (1999). Heat storage by two grade phase change material", Periodica Polytechnica Ser Chem. Eng., 43(2): 137-147.
- [113] Farid M. and Yacoub K. (1989). Performance of direct contact latent heat storage unit. Solar Energy 43(4): 237 –51.
- [114] Sokolov M. and Keizman Y. (1991). Performance indicators for solar pipes with phase change energy storage. Solar Energy 47(5): 339- 346.
- [115] Trelles J.P. and Duffy J.P. (2003). Numerical simulation of porous latent heat thermal energy storage for thermoelectric cooling. Applied Thermal Engineering 23: 1647 - 1664.
- [116] Watanbe T., Kikuchi H. and Kanzawa A. (1993). Enhancement of charging and discharging rates in a latent heat storage system by use of PCM with different melting temperatures. Heat Recovery Systems CHP 13 (1): 57- 66.
- [117] Galloway T.R. and Sage B.H. (1970). A Model of the mechanism of transport in packed, distended and fluidized beds. Chemical Engineering Science 25: 495.
- [118] Kuwahara F., Shirota M. and Nakayama A. (2001). A numerical study of interfacial convective heat transfer coefficient in two-energy equation model for convection in porous media. International Journal of Heat and Mass Transfer 44: 1153-1159.
- [119] Anathanarayanan V., Sahai Y., Mobley C.E. and Rapp R.A. (1987). Modelling of fixed bed heat storage units utilizing phase change materials. Metallurgical and Materials Transactions B. 18B: 339-346.
- [120] Saito M.B. and De Lemos M.J. (2005). Interfacial heat transfer coefficient for non-equilibrium convective transport in porous media. International Communications in Heat and Mass Transfer 32: 666–676.
- [121] Singh R., Saini R.P. and Saini J.S. (2006). Nusselt number and friction factor correlations for packed bed solar energy storage system having large sized elements of different shapes. Solar Energy 80: 760-771.
- [122] Standish, N. and Drinkwater, J.B. (1970). The effect of particle shape on flooding rates in packed columns. Chemical Engineering Science 25: 1619-1621.
- [123] Gauvin W.H. and Katta S. (1973). Momentum transfer through packed beds of various particles in the turbulent flow regime", AIChE Journal 19(4): 775-783.

- [124] Barba A. and Spiga M. (2003). Discharge mode for encapsulated PCMs in storage tanks. *Solar Energy* 74: 141–148.
- [125] Marzo M. (1995). Drop wise evaporative cooling. Mechanical Engineering Department, University of Maryland, College Park, MD 20817, Reprinted from ATTI 13 Congresso Nazionale Sulla Trasmissione Del Calore, 13 Unione Italiana, Di Termofluidodinamica, National Heat Transfer Conference, 22-23 Giugno 1995, Bologna, Italy.
- [126] Ettouney H., El-Desouky H. and Al-Ali A. (2005). Heat transfer during phase change of Paraffin wax stored in spherical shells. *Solar Energy Engineering* 127: 357-365.
- [127] Weislogel M.M. and Chung J.N. (1991). Experimental investigation on condensation heat transfer in small arrays of PCM-filled spheres. *International Journal of Heat and Mass Transfer* 34: 31-45.
- [128] Bourouni K., Martin R., Tadrist L., Chaibi M.T.. Heat transfer and evaporation in geothermal desalination units. *Applied Energy*, Elsevier, 64(1) 1999: 129-147.
- [129] Bourouni K., Chaibi M.T. and Tadrist L. (2001). Water Desalination by humidification and dehumidification of air: state of the art. *Desalination* 137: 167-176.
- [130] Khedr M. (1993). Techno-economic investigation of air humidification-dehumidification desalination process. *Chemical Engineering* 16: 270-274.
- [131] Garg S.K., Gomkale S.D., Datta R.L. and Datar D.S. (1968). Development of humidification-dehumidification technique in arid zones of India. *Desalination* 5: 55-63.
- [132] Al-Hallaj S., Farid M.M. and Tamimi A. (1998). Solar desalination with a Humidification – dehumidification cycle: performance of unit. *Desalination* 120: 273-280.
- [133] Abu Arabi M.K. and Reddy V.K. (2003). Performance evaluation of desalination processes based on the humidification/dehumidification cycle with different carrier gases. *Desalination* 156: 281-293.
- [134] Nawayseh, N.K., Farid, M.M., Omar, A.Z., Sabrin, A. (1999). Solar desalination based on humidification process-II: Computer simulation. *Energy Conversion and Management* 40: 1441-1461.
- [135] Younis M. A, Darwish M. A. and Juwayhel F. (1993). Experimental and theoretical study of a humidification-dehumidification desalting system. *Desalination* 94: 11-24.
- [136] Klausner J.F. and Mei R.Y. (2006). Evaporative heat and mass transfer for the diffusion driven desalination process. *Heat and Mass Transfer* 42: 528–536.
- [137] Klausner J.F. and Mei R.Y. (2005). Diffusion driven desalination, an innovative approach to fresh water production from seawater. Presentation in ASME-ZSIS International Thermal Science Seminar ITSS II.
- [138] Samad M.A. (1993). Operational problems in the solar desalination plant and its remedies. *Desalination* 93: 615-624.

- [139] Belessiotis V, Delyannis E (2001). Water shortage and renewable energies (RE) desalination-possible technological applications. *Desalination* 139: 133-138.
- [140] Haddad O.M., Al-Nimr M.A. and Maqableh A. (2000). Enhanced solar still performance using a radiative cooling system. *Renewable Energy* 21: 459-469.
- [141] Miyatake O., Koito Y., Tagawa K. and Maruta Y. (2001). Transient characteristics and performance of a novel desalination system based on heat storage and spray flashing. *Desalination* 137: 157–166.
- [142] Al-Enezi G., Ettouney H. and Fawzy N. (2006). Low temperature humidification dehumidification process. *Energy Conversion and Management* 47: 470-484.
- [143] Lex M.F., Sattelmayer T., Spinnler M. and Blumenberg J. (2003). Solar thermal distillation evaporation over a packed bed. Diploma Thesis, Lehrstuhl für Thermodynamik, Technische Universität München.
- [144] Gahin S., Darwish M.A. and Ghazi M.A. (1980). Solar powered humidification-dehumidification desalination system. *Proceedings of the 7th International symposium on Fresh Water from the Sea, Athenes, Greece, 1980*: 399-406.
- [145] Abdel Moneim M.A. (1989). Theoretical and experimental studies of a humidification-dehumidification desalination system. Ph.D. Thesis, Faculty of Engineering, Cairo University, Egypt.
- [146] Kheder M.M (1988). Desalination by air humidification. Ph.D. Thesis, Faculty of Engineering, Cairo University, Egypt.
- [147] Swift A.H.P, Huanmin, L. and Becerra H. (2002). Zero discharge waste brine management for for desalination plants. *Desalination Research and Development Program Report No. 89, Final Report, University of Texas at El Paso El Paso, Texas*.
- [148] Dawoud, B., Zurigat, Y.H., Klitzing, B., Aldoss, T. and Theodoridis, G. (2006). On the possible techniques to cool the condenser of seawater greenhouses. *Desalination* 195(1-3): 119-140.
- [149] Narayan G. Prakash, Sharqawy M. H., Summers E. K., Lienhard J. H., Zubair S. M., Antar M.A., (2010). The potential of solar-driven humidification-dehumidification desalination for small-scale decentralized water production. *Renewable and Sustainable Energy Reviews* 14(4): 1187-1201.
- [150] Galen E. V. and Van den brink G. V. (1986). Energy storage in phase change materials for solar applications. *International Journal of Ambient Energy* 7: 31.
- [151] De Maria G., D'Alessio L., Coffari E., Paolucci M. and Tiberio C. A. (1985). Thermo-chemical storage of solar energy with high temperature chemical reaction. *Solar Energy*, 35(5): 409-416.
- [152] Fujii I., Tsuchiya K., Higano M. and Yamada J. (1985). Studies on an energy system by use of the reversible chemical reaction. *Solar Energy* 34(4-5): 367-377.
- [153] Abhat A. (1981). Short term thermal energy storage. *Revue Physique Applique* 15: 477-501.

- [154] Brendel T., Solare Meerwasserentsalzungsanlagen mit mehrstufiger Verdunstung, Betriebsversuche, dynamische Simulation und Optimierung., Ph.D. Thesis, Fakultät für Maschinenbau der Ruhr-Universität Bochum, 2003.
- [155] Chafik E, "A new seawater desalination process using solar energy," *Desalination*, 2002, pp. 153:25–37.
- [156] Orfi, J., Laplante, M., Marmouch, H., Galanis, N., Benhamou, B., Nasrallah S. B., Nguyen, C.T.. Experimental and theoretical study of a humidification dehumidification water desalination system using solar energy. *Desalination* 168 (2004):151.
- [157] Beasley D.E. (1983). Dynamic response of packed bed for thermal energy storage. Ph.D. Thesis, University of Michigan.
- [158] International Atomic Energy Agency. Desalination Economic Evaluation Programme, Version DEEP-3.1; Draft version of the user's manual, Vienna, September 2006.
- [159] Nawayseh, N.K., Farid, M.M., AL-Hallaj, S. and Tamimi, A.R., 1999; Solar desalination based on humidification process-I evaluating the heat and mass transfer coefficients. *Energy Conversion and Management*, 1999a, 40:1423-1439.

Appendices

Appendix A

A1. PCM Thermo-physical properties

Table A.1. Thermo-physical properties of PCM media

Properties	HS 34 (Condenser)	HS 58 (Evaporator)	ICE-A70 (PCM Storage)
Appearance colour	Grey/Brown liquid/crystals	White crystals/powder	Red Rubbery
Description	Proprietary mixture of inorganic salts	Proprietary mixture of inorganic salts	Blend of heavy cut hydrocarbons
Phase Change Temp. (°C)	32-34	57-59	69-71
Operating Temp. Range (°C)	29-39	55-61	65-75
Density (Kg/m ³)	1500	1280	890
Latent Heat (kJ/kg) (<i>Calorimetry</i>)	145	351	220
Thermal conductivity (W.m ⁻¹ K ⁻¹)	0.46	0.6	0.23
Specific heat – Solid (kJ.kg ⁻¹ .K ⁻¹)	1300	2.1	2.2
Specific heat – Liquid (kJ.kg ⁻¹ .K ⁻¹)	2200	3.6	2.2
Congruent Melting	Yes	Yes	Yes
Sub Cooling	No	No	No
Flammability	No	No	>150°C
Stability (cycles)	>1100	>1000	>1000
Max. Operating Temp. (°C)	~80	~90	~90

A2. Factorial design of experiments and experimental plan

Table A.2. Factorial design of experiments and experimental plan

Packed height	M_{cw} (l/h)	M_{hw} (l/h)	$T_{hw, in}$ (83°C)	$T_{hw, in}$ (65°C)
	M_{air} (m/s)			
0.38 m	370	500	Day no (1, 2, and 3)	Day no (4)
	0.55	250		
	370	250	Day no (5)	Day no (6)
	0.55	500	Day no (7)	Day no (8)
	370	500	Day no (7)	Day no (8)
	0.28	250	Day no (9)	Day no (10)
	370	250	Day no (9)	Day no (10)
	0.28	500	Day no (11)	Day no (12)
0.78 m	670	500	Day no (11)	Day no (12)
	0.55	250	Day no (13)	Day no (14)
	670	250	Day no (13)	Day no (14)
	0.55	500	Day no (15)	Day no (16)
	670	500	Day no (15)	Day no (16)
	0.28	250	Day no (17)	Day no (18)
	670	250	Day no (17)	Day no (18)
	0.28	500	Day no (19)	Day no (20)
0.78 m	370	500	Day no (19)	Day no (20)
	0.55	250	Day no (21)	Day no (21)
	370	250	Day no (21)	Day no (21)
	0.55	500	Day no (23)	Day no (24)
	370	500	Day no (23)	Day no (24)
	0.28	250	Day no (25)	Day no (26)
	370	250	Day no (25)	Day no (26)
	0.28	500	Day no (27)	Day no (28)
0.78 m Empty sphere	670	500	Day no (27)	Day no (28)
	0.55	250	Day no (29)	Day no (30)
	670	250	Day no (29)	Day no (30)
	0.55	500	Day no (31)	Day no (32)
	670	500	Day no (31)	Day no (32)
	0.28	250	Day no (33)	Day no (34)
	670	250	Day no (33)	Day no (34)
	0.28	500	Day no (39)	Day no (40)
0.78 m PCM spheres	670	500	Day no (39)	Day no (40)
	0.28	250	Day no (41)	Day no (42)
0.78 m PCM spheres	670	500	Day no (41)	Day no (42)
	0.55	250	Day no (43)	Day no (44)
0.78 m PCM spheres	670	500	Day no (35)	Day no (36)
	Natural draft	250	Day no (37)	Day no (38)
0.78 m PCM spheres	670	250	Day no (37)	Day no (38)
	Natural draft	500	Day no (39)	Day no (40)

A3. Constants and Thermo-physical properties of air and water

Table A.3: Constants and Thermo-physical properties of air and water

Properties	Water	Air	Units
Thermal conductivity	0.62	0.0264	W/m.K
Dynamic viscosity at 50 °C.	2.4 e-03	1.87 e-05	N.s/m ²
Density at 50 °C.	998	1.177	kg/m ³
Surface tension	6.6 e- 02	-	N/m
Molecular weight	18.015e-3	28.97e-3	kg/mol
Specific heat	4180	1006	J/kg.K
Specific heat of water vapour & Humid air	1872	1015.952	J/kg.K
Kinematic viscosity	-	1.53 E-05	m ² /sec
Coefficient of volumetric thermal expansion (average for 0-80 °C)	-	0.003193358	K ⁻¹
Coefficient of concentration expansion (average for 0-80 °C)	-	0.0023	% ⁻¹
Binary diffusion coefficient at 50 °C.	2.77e-5	2.77e-5	m ² /s
The universal gas constant	-	8.31447	J/mol.K
Reference temperature	-	273	K
Reference density of air at 273 °K	-	1.29	kg/m ³
Reference humidity of air at 273 °K	-	0.00376	kg /kg
Reference water vapour pressure at 273 °K	618.9	-	Pa
Latent heat of evaporation	45050		J/mol

Appendix B

B1. Pressure drop calculations (Stichlmair et al. [29])

Stichlmair et al. [29] shows the advantages of the particle model. In this model structure, the real packing is replaced by a system of spherical particles which have the same surface and void fraction as the original packing. With these equivalence conditions, the equivalent diameter of the particle d_p is:

$$d_p = 6 \frac{1 - \varepsilon}{a} \quad (\text{B.1})$$

Thus, the originally random structure of the packing is made accessible to calculation. Stichlmair et al. [29] show that the correlations for fluidized beds can also be applied to a system of fixed particles. The analysis of the pressure drop on the air side in a packed column was based on the computation of the dry column pressure drop and a correction term to account for the effect of liquid flow rate. Equation (27) describes the basic equation of the particle model. The dry column pressure drop per unit height that utilizes the single particle friction factor as well as the bed porosity ε is given by the following correlation [29]:

$$\nabla P_d / Z = 3/4 f_0 [(1 - \varepsilon) / \varepsilon^{4.65}] (\rho_g V_g^2) / d_p \quad (\text{B.2})$$

where V_g is the air superficial velocity and f is the friction factor given by the following equation:

$$f_0 = C_1 / \text{Re}_g + C_2 / \text{Re}_g^{0.5} + C_3 \quad (\text{B.3})$$

where the friction factor f_0 for a single particle is a function of gas Reynold's number:

$$\text{Re}_g = \rho_g V_g d_p / \mu_g \quad (\text{B.4})$$

The friction factor f_0 is derived from the dry pressure drop of the original packing. Therefore, it is one of the characteristic parameters of a random and structured packing, together with the geometric surface a and the void fraction ε . The constants C_1 , C_2 and C_3 in equation (B.3) are available in Stichlmair et al [29] for different packing elements other than spherical packing. As long as the friction factor can be expressed in the same form of equation (B.3), the model can be applied for spherical packing (or any other packing geometry).

Bird et al. [19] provides a simple and useful empirical expression for the friction factor for creeping flow around a sphere that matches the form of equation (B.3):

$$f_0 = \left(\sqrt{24 / \text{Re}_g} + 0.5407 \right)^2 \quad \text{for } \text{Re} < 6000 \quad (\text{B.5})$$

From the above correlation, the constants of equation (B.3) were determined from equation (B.5) as listed in table B.1.

The pressure drop in the irrigated bed is higher than that of dry bed, then the change in friction factor for a single wet particle will be different from that of the dry particle since the actual gas Reynolds number depends on the actual wet particle diameter. Thus, the irrigated friction factor will be [29]:

$$f'_0 = f_0 \left\{ \left[1 - \varepsilon \left(1 - \frac{h_l}{\varepsilon} \right) \right] / (1 - \varepsilon) \right\}^{C/3} \quad (\text{B.6})$$

where h_l is the liquid holdup and

$$c = \frac{[-C_1/\text{Re}_g - C_2/(2\text{Re}_g^{1/2})]}{f_0} \quad (\text{B.7})$$

The irrigated pressure drop can then be expressed as a ratio to the dry pressure drop [29]:

$$\nabla P_{irr} / \nabla P_d = \left\{ \left[1 - \varepsilon \left(1 - \frac{h_l}{\varepsilon} \right) \right] / (1 - \varepsilon) \right\}^{(2+C)/3} (1 - h_l/\varepsilon)^{-4.65}$$

Table B.1. Constants of equation (B.3) for spherical packing.

C_1	24
C_2	5.29776
C_3	0.2923565

Appendix C

C1. Literature correlations for heat transfer coefficient between bed packing and working fluid

The heat transport between the storage material and the heat transfer fluid within packed bed is caused by convective processes and can be described in terms of heat transfer coefficient, h_{sf} [$\text{W}\cdot\text{m}^{-2}\cdot\text{K}^{-1}$]. However, most studies for evaluation of the heat transport within PCM packed bed focus on air-PCM packed beds. In practice, some results from sensible heat storage are also applicable to analogous PCM packed beds. Correlation for a randomly packed, distended and fluidized beds has been developed by Galloway and Sage [117]. The constants in the correlation were re-determined by Beasley [157] based on measurements in an air/glass packed bed and by comparison with measured temperature distributions in rock beds. The resulting equation is:

$$Nu = 2.0 + 2.0Re_0^{\frac{1}{2}}Pr^{\frac{1}{3}} + 0.05Re_0Pr^{\frac{1}{2}} \quad (\text{C.1})$$

Where Re_0 is superficial Reynolds number, defined as $u_0 d_p / \nu$; where d_p is the particle diameter [m], u_0 is the superficial velocity [$m\cdot s^{-1}$], and Pr denotes the Prandel number, defined as $\nu c_p / k$. The *superficial velocity* is defined as the volumetric flow rate divided by the whole cross sectional area (both fluid and solid).

Intraparticle conduction (Biot number) effects on the axial thermal dispersion can be included by correcting the heat transfer coefficient. The effect of intraparticle conduction is to reduce the effective heat transfer coefficient in the following manner [27]:

$$h_{eff} = h_{sf} / [1.0 + 0.2Bi] \quad (\text{C.2})$$

Where Bi is the Biot number, defined as $Bi = hd/2k_b$, and subscript b denotes to bed solid packing.

The heat transfer coefficient for heat exchange between the fluid and the PCM spheres could also be calculated according to the following expressions [117].

$$J_h = aRe_0^z \quad (\text{C.3})$$

Where a and z are given in Table (C.1).

The Ergun analogy factor J_h represents an analogy between the friction factor and the heat transfer coefficient. In fact, J_h is proportional to the friction factor. Accordingly, the heat transfer coefficient is expressed as:

$$h = J_h U_f \rho_f C_f / \text{Pr}^{0.67} \quad (\text{C.4})$$

Moreover, to obtain an effective convective film heat transfer coefficient h_{eff} that accounts for the effect of intraparticle conduction and can be used with Schumann model [119] for modeling transient one dimensional flow in packed beds:

$$1/h_{\text{eff}} = \frac{1}{h} \left(1 + \frac{Bi}{5.0}\right) B^2 + \frac{d_p}{L Pe} \quad (\text{C.5})$$

Where Bi is the Biot number, defined as $Bi = hd/2K_b$, B is the thermal capacity ratio $B = V_H/(1+V_H)$, V_H is the heat capacity ratio between the bed or storage medium and the working fluid, defined as $V_H = \rho_b c_b (\varepsilon - 1) / \rho_f c_f \varepsilon$; where b and f denote to bed and fluid respectively, and Pe is the Peclet number, defined as $Pe = (\rho_f c_f u_p) 2AL\varepsilon / k_f A_b$.

Table C.1. Constants used in the calculation of J_h [66]

D_{st}/d_p	a	z
10.7	1.58	-0.40
16.0	0.95	-0.30
25.7	0.92	-0.28
>30	0.9	-0.28

Wakao and Kaguei [15] have experimentally examined the results on h_{sf} for both steady and transient behaviors and reached to a reliable correlation. They have found the following correlation for h_{sf} for spherical particles (or the dimensionless form of it; the Nusselt number):

$$Nu_a = \frac{h_{sf} d_p}{k_f} = 2.0 + 1.1 Re^{0.6} Pr^{\frac{1}{3}} \quad \text{for spherical particles} \quad (\text{C.6})$$

Where $Re = \varepsilon u_p d_p / \nu = u_D d_p / \nu$, where u_p and u_D are the average pore velocity (bulk mean velocity) and the Darcian velocity of the fluid respectively. However, Wakao and Kaguei correlation neglects the axial diffusion effects and is valid only for packed beds with ($\varepsilon \approx 0.4$).

Kuwahara et al. [118], has conducted a numerical experiment to determine the interfacial convective heat transfer coefficient in the two-energy equation model for conduction and laminar convection in porous media packed beds. For determining h_{sf} they considered a porous medium with an infinite number of solid square rods of size d , arranged in a regular triangular (staggered) pattern. A universal correlation for the Nusselt number, which agrees well with experimental data of Wakao and Kagueli [15], has been established using the results obtained for a wide range of porosities, Prandtl, and Reynolds numbers. Thus, the following expression has been established from their numerical experiments based on the two-dimensional model.

$$\frac{h_{sf} d_p}{k_f} = \left(1 + \frac{4(1-\varepsilon)}{\varepsilon} \right) + \frac{1}{2} (1-\varepsilon)^{\frac{1}{2}} Re^{0.6} Pr^{\frac{1}{3}} \quad \text{valid for} \quad 0.2 < \varepsilon < 0.9 \quad (\text{C.7})$$

Where the definition of $Re = \varepsilon u_p d_p / \nu = u_D d_p / \nu$, is still valid and this correlation is based on porosity dependency for backed beds with particle diameter d .

An extension of the same physical model of Kuwahara et al. [118] has been formulated by Saito et al. [120] to treat turbulent heat transfer modeling in porous media under the local thermal non-equilibrium assumption. Macroscopic time-average equations for continuity, momentum and energy were presented for an infinite medium over which the fully developed flow condition prevails. Interfacial heat transfer coefficient h_{sf} were determined numerically by calculating a heat balance for a unit cell and an expression was given as:

$$h_{sf} = \frac{Q_{tot}}{A_i \Delta T_{ml}} \quad (\text{C.8})$$

Where $A_i = 8 d_p \times 1$. The overall heat transferred in the cell, Q_{tot} is given by:

$$Q_{tot} = (D - d_p) \rho_f C_f u_p (T_{fo} - T_{fi}) \quad (\text{C.9})$$

Where D , ρ_f , C_f , u_p , T_{fo} , and T_{fi} are the distance between consecutive centers of two neighbor cells, the density, specific heat capacity, the bulk mean velocity of the fluid, and the bulk mean fluid temperatures at the outlet (o), and inlet (i) of the pore channel respectively. The symbol ΔT_{ml} represents the logarithm mean temperature difference and is expressed as a function of the cell outer surface temperature (T_s), T_{fo} , and T_{fi} :

$$\Delta T_{ml} = \frac{(T_s - T_{fo}) - (T_s - T_{fi})}{\ln(T_s - T_{fo}) / (T_s - T_{fi})} \quad (\text{C.10})$$

Equation (C.7) represents an overall heat balance on the entire cell and associates the heat transferred to the fluid to a suitable temperature difference ΔT_{ml} . Quantitative agreement was obtained when comparing the preliminary results of this model with simulation results by Kuwahara et al. [118].

From the above review on the heat transfer coefficient correlations between a working fluid and packed bed studied and summarized in table (C.2), it can be stated that both Wakao and Kaguei [15] and Kuwahara et al. [118] correlations are more general and much reliable for a range of porosities up to 0.4, and greater than 0.4 respectively for the present study.

C2. Summary of some heat transfer coefficient correlations between fluids and packed beds

Table C.2. Summary of some heat transfer coefficient correlations between fluids and packed beds

AUTHOR	FORMULA	CONDITIONS	EQN	REF
Galloway and Sage proposed the correlation	$Nu = 2.0 + 2.0Re \frac{1}{2} Pr^{\frac{1}{3}}$ $+ 0.05Re Pr^{\frac{1}{2}}$	Heat transfer fluid was Air	C.1	117
Constants were determined by Beasley	Accounting for intraparticle conduction effect $h_{eff} = h_{sf} / [1.0 + 0.2Bi]$ $Bi = hd/2k_b$			27 27
Baumeister and Bennet	$h = J_h U_f \rho_f C_f / Pr^{0.67}$ $J_h = a Re^z$ Constants a and z are given in Table (2.3) Accounting for intraparticle conduction effect $1/h_{eff} = \frac{1}{h} (1 + \frac{Bi}{5.0}) B^2 + \frac{d_p}{L * Pe}$ $B = V_H / (1 + V_H)$ $V_H = \rho_b c_b (\varepsilon - 1) / \rho_f c_f$ $Pe = (\rho_f C_f U_i) 2AL\varepsilon / k_f A_b$	Forced convection (2.22)	C.2 C.3	119
		(2.21)		
		(2.23)	C.4	119
Wakao and Kaguei	$Nu_d = \frac{h_{sf} d_p}{k_f} = 2.0 + 1.1 Re^{0.6} Pr^{\frac{1}{3}}$	Spherical particles 0.2 < ε < 0.4	C.6	15

Kuwahara et al.	$\frac{h_{sf} d_p}{k_f} = \left(1 + \frac{4(1-\varepsilon)}{\varepsilon} \right) + \frac{1}{2}(1-\varepsilon)^{\frac{1}{2}} Re^{0.6} Pr^{\frac{1}{3}}$	Laminar flow $0.2 < \varepsilon < 0.9$	C.7	118
Saito et al	$h_{sf} = \frac{Q_{tot}}{A_i \Delta T_{ml}}$ $Q_{tot} = (D - d_p) \rho_f C_f u_p (T_{fo} - T_{fi})$ $\Delta T_{ml} = \frac{(T_s - T_{fo}) - (T_s - T_{fi})}{\ln(T_s - T_{fo}) / (T_s - T_{fi})}$	Turbulent flow $0.2 < \varepsilon < 0.9$	C.8 C.9 C.10	120

Appendix D

D1. Cooling tower theory and performance

D.1.1 Merkel's equation

The practical theory of cooling towers operation was, perhaps, first developed by Merkel [3]. This theory has been presented and discussed in detail throughout numerous heat and mass transfer textbooks as the basis of most cooling tower analysis and design rating. Excessively large number of scientific research and publications cover the theoretical and experimental analysis of wet cooling towers over its long history which has led to a common understanding and technical maturity. Baker [53] presented a complete review on the technical papers dealing with cooling tower and assessed different suggestions of coupling heat and mass transfer in a single driving force.

Merkel's theory has lumped both sensible and latent heat transfer due to interface-bulk temperature and humidity differences in a single driving force for total heat transfer and equivalent single transfer coefficient. This driving force is the difference between the enthalpy of the saturated air at the interface and the enthalpy of the bulk humid air. Considering a small element of the packing region in counter flow as illustrated in figure D.1, the heat transfer rate from water to air can be expressed as [56]:

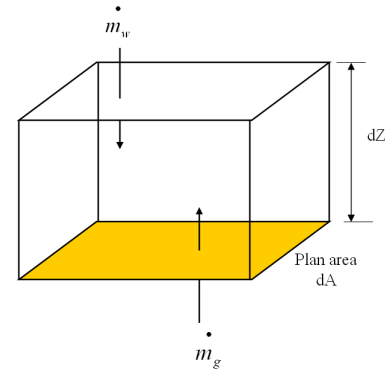


Figure D.1: Counter flow through an element of the packing region [5]

$$d\dot{Q}_{lg} = \dot{q}_{lg} a_e dV \quad (D.1)$$

where a_e is the specific (per unit volume) water-air interfacial area, dV is the element volume, and \dot{q}_{lg} is the heat flux at the interface, given by:

$$\dot{q}_{lg} = \gamma (h_{g,int} - h_g) \quad (D.2)$$

where

$h_{g,int}$ = the specific enthalpy of moist gas at the interface

h_g = the specific enthalpy of the local bulk moist air

γ = Reynolds flux; an empirical coefficient with the units ($\text{kg}\cdot\text{m}^{-2}\cdot\text{s}^{-1}$) and approximated by:

$$\gamma \approx \frac{h}{c_{p,g}} \quad (\text{D.3})$$

where h is the surface heat transfer coefficient in a dry flow that is similar geometrically and in other respects (56).

Merkel has based his theory on the following basic postulations and approximations that may be summarized as:

- Negligible heat transfer resistance in the liquid film,
- Constant mass flow rate of water per unit of cross sectional area of the tower (water loss due to evaporation is neglected),
- Specific heat of the air-vapor mixture at constant pressure is the same as that of the dry air, and
- Lewis number for humid air is unity.

All of the preceding assumptions were subjected to examinations by other researchers. Rigorous analysis by Sutherland [55] indicated that counter-flow cooling towers could be undersized between 5 to 15% due to Merkel's assumptions and that the underestimation of tower volume increases with increasing value of water to air mass flow rate ratio. In contrary, Baker [53] mentioned that the effect of water evaporation is relatively small and produces a value for number of transfer units (NTU) of 1.34 percent lower than reality.

Heat transfer in packed bed and cooling towers is commonly presented in terms of the height of transfer unit (HTU) and number of transfer units (NTU). These parameters have been defined as a result of integrating the energy balance equations across the packing region from air entry to air exit referring to the small element illustrated in figure (D.1). The final form of integral after rearranging is expressed as follows [56]:

$$\int_{h_{w,out}}^{h_{w,in}} \frac{dh_w}{h_{g,int} - h_g} = \int_{Z_1}^{Z_2} \frac{\gamma a_e}{m_w} AdZ \quad (\text{D.4})$$

or $I_M = I_P$

where I_M and I_P stand for the left and right hand sides of equation (D.1), and

dh_w = change in the specific enthalpy of water in its flow direction ($\approx c_{pw}dT_w$)

A = the plan or cross sectional area of the column

\dot{m}_w = the mass flow rate of water

After Singham (56), equation (D.4) will be considered as the basic formulation of Merkel's equation. The main designer task is to ensure equality of the two sides of this equation (i.e. I_M and I_P).

D.1.2 Number of transfer units (NTU)

Two closely related expressions for the right hand side integrand I_P are commonly used for practical purposes. The first practice expresses the performance of the packing as the number of transfer units (NTU), while the second measures the heat transfer performance as a packing dimensionless characteristic quantity (KaV_{sp}/L), where K is the overall mass transfer coefficient between water and air based on the enthalpy difference ($\text{kg}\cdot\text{m}^{-2}\cdot\text{s}^{-1}$), a is the packing specific surface area, V_{sp} is the packed bed volume per unit cross sectional area, and L is the water superficial mass flux per unit cross sectional area ($\text{kg}\cdot\text{m}^{-2}\cdot\text{s}^{-1}$).

According to the first practice, definitions of the effectiveness (NTU) is in close similarity with those used for the heat exchanger design, hence is defined by [56]:

$$NTU = \frac{\gamma}{G} a_e \quad (D.5)$$

where G is the gas superficial mass flux per unit cross sectional area ($\text{kg}\cdot\text{m}^{-2}\cdot\text{s}^{-1}$), and the dimensionless quantity γ/G , which is a function of Reynolds number, is a form of nondimensional heat transfer coefficient **Stanton number** defined as:

$$St = \frac{h_{1g}}{Gc_{p,g}} \quad (D.6)$$

Thus NTU can be regarded as the product of Stanton number and a geometric feature of the packing a (56). A modified Stanton number based on the effective wetted area a_w instead of the total specific packing area a is also used [57]:

$$St^* = \frac{h_{1g} a}{Gc_{p,g} \left(\frac{a_w}{V} \right)} \quad (D.7)$$

where $h_{1g} a$ is the volumetric heat transfer coefficient, and V is the packed bed volume. The relationship between the two performance measures was shown to be [56]:

$$\int_{h_{w,out}}^{h_{w,in}} \frac{dh_w}{h_{g,int} - h_g} = \frac{KaV_{sp}}{L} = \frac{G}{L} NTU = \frac{\dot{m}_g}{\dot{m}_w} NTU \quad (D.8)$$

Advantage of the first practice is the recognition of the packing performance NTU as a form of Stanton Number with its familiarity in dry heat transfer processes. NTU is a measure of the difficulty of separation, which relates the change in the bulk phase composition to the average driving force [32]. It is, therefore, a measure of the cooling tower size and water recovery ratio. The lower the NTU , the higher the specific productivity per unit volume of the cooling tower and consequently the higher the water recovery ratio. The left hand side of equation (D.8) reveals this concept. Smaller NTU means that the separation column is more efficient when smaller energy input to the system (dh_w) produces high driving force for heat and mass transfer ($h_{g,int} - h_g$). This means that for a cooling tower size and under same inlet conditions, the mechanical energy for pumping water as well as the input heat energy is inversely proportional to the NTU . Advantage of the second practice is the elimination of gas to water mass flow ratio G/L from Merkel's equation [56].

D.1.3 Height of transfer unit (HTU)

The height of transfer unit (HTU) is defined as the height of packing which gives a change in composition equivalent to one transfer unit and therefore it is a direct measure for the column efficiency [32]. It can be related to the NTU and hence to the Stanton number by:

$$H = HTU \times NTU \quad (D.9)$$

$$\text{or} \quad HTU = \frac{C}{St \ a} \quad (D.10)$$

where H is the total packing height, and C is the liquid-gas heat capacity flow ratio;

$$C = \frac{\dot{m}_l c_{p,l}}{\dot{m}_g c_{p,g}} \quad (D.11)$$

For a detailed development and derivation of equations (D.1) to (D.8) which spells out the pertinent assumptions, Singham [56], Thomas et al [57], and Kister [32], should be consulted.